BIOPHYSICAL AND STRUCTURAL CHARACTERIZATION OF PROTEINS IMPLICATED IN GLAUCOMA AND GAUCHER DISEASE

A Dissertation
Presented to
The Academic Faculty

by

Susan D. Orwig

In Partial Fulfillment
of the Requirements for the Degree
Doctor of Philosophy in the
School of Chemistry and Biochemistry at Georgia Insitute of Technology

Georgia Institute of Technology
December 2011

COPYRIGHT 2011 BY SUSAN ORWIG

BIOPHYSICAL AND STRUCTURAL CHARACTERIZATION OF PROTEINS IMPLICATED IN GLAUCOMA AND GAUCHER DISEASE

Approved by:

Dr. Raquel L. Lieberman, Ph.D. , Advisor
School of Chemistry and Biochemistry
Georgia Institute of Technology

Dr. Roger Wartell, Ph.D.
School of Biology
Georgia Institute of Technology

Dr. Nicholas V. Hud, Ph.D.
School of Chemistry and Biochemistry
Georgia Institute of Technology

Dr. Loren D. Williams, Ph.D.
School of Chemistry and Biochemistry
Georgia Institute of Technology

Dr. Al Merrill, Ph.D.
School of Biology
Georgia Institute of Technology

Dr. A. (Yomi) K. Oyelere, Ph.D.
School of Chemistry and Biochemistry
Georgia Institute of Technology

Date Approved: August 17th, 2011

To Gwedolyn Baker Orwig and Scooby Doo, this is for you.

ACKNOWLEDGEMENTS

I would like to thank my family for the continual love and support they have provided over the years; my father for always being there, my mother for always listening, Lauren for keeping me grounded, Steven for being my foot slave, and Jackie for her amazing stories. I also wish to thank my grandmother for opening her home and setting me on this journey. I would like to particularly thank my minions, Chris and Pamela, for their amazing attitudes and all their work towards helping me succeed. I wish to thank my thesis committee for their useful feedback over the years. Finally, I will be forever grateful to my thesis advisor, Dr. Raquel L. Lieberman, for providing me the opportunity to study in her lab and for sculpting me into the scientist I am today.

TABLE OF CONTENTS

LIST OF TABLES

LIST OF FIGURES

LIST OF SYMBOLS AND ABBREVIATIONS

4MU-βGlc	4-methylumbelliferyl-β-glucopyranoside
4-PBA	4-phenylbutyrate
α	alpha
AD	Alzheimer's disease
APP	amyloid precursor protein
Aβ	amyloid-β peptide
β	beta
BME	β-mercaptoethanol
C	Celsius
$CaCl_2$	calcium chloride
cal	calorie
CD	circular dichroism
c	centi
CHES	*N*-cyclohexyl-2-aminoethanesulfonic acid
CHO	Chinese hamster ovary
CMC	critical micellar concentration
CNS	central nervous system
core-OLF	compact structural core of myoc-OLF
CV	coefficient of variation
Da	Dalton
°	degree
Δ	change
ΔT_m	change in melting temperature

Dex	dexamethasone
DMSO	dimethylsulfoxide
DSC	differential scanning calorimetry
DSF	differential scanning fluorimetry
DTT	dithiothreitol
ECM	extracellular matrix
EDTA	ethylenediaminetetraacetic acid
ER	endoplasmic reticulum
ERAD	ER-associated degradation
ERSD	ER storage disorder
ERT	enzyme replacement therapy
FDA	Food and Drug Administration
G	Gibb's free energy
g	gram
γ	gamma
GAG	glycosaminoglycan
GCase	acid β-glucosidase
GD	Gaucher disease
GlcCer	glucosylceramide
Gnd HCl	guanidine hydrochloride
H	enthalpy
HEK	human embryonic kidney
HEP	heparin
Hepes	4-(2-hydroxyethyl)-1-piperazineethanesulfonic acid
hr	hour

HTM	human trabecular meshwork
HTS	high-throughput screening
IFG	isofagomine
IOP	intraocular pressure
IPTG	isopropyl β-D-1-thiogalactopyranoside
ITC	isothermal titration calorimetry
JOAG	juvenile open-angle glaucoma
k	kilo
K	Kelvin
L	liter
LOPAC	Library of Pharmacologically Active Compounds
m	milli
m	meter
M	molar
MALDI-TOF/TOF	matrix assisted laser desorption ionization time of flight
MBP	maltose binding protein
MBP-OLF	maltose binding protein-olfactomedin fusion protein
MES	2-(N-morpholino)ethanesulfonic acid
min	minute
MMPs	matrix metalloproteases
mol	mole
Myoc-OLF	C-terminal olfactomedin domain of myocilin
n	nano
NaCl	sodium chloride
NB-DNJ	N-butyldeoxynojirimycin

NMR	nuclear magnetic resonance
NN-DNJ	N-(n-nonyl)deoxynojirimycin
OAG	open angle glaucoma
OLF	olfactomedin domain
PBS	phosphate-buffered saline
PC	pharmacological chaperone
PCD	protein conformational disorder
PEG	polyethylene glycol
PK	proteinase K
PMSF	phenylmethanesulfonylfluoride
POAG	primary open-angle glaucoma
R^2	coefficient of determination
RGC	retinal ganglion cell
rmse	root-mean-square erro
RT-PCR	real-time polymerase chain reaction
S	entropy
S/B	signal-to-background
SDS	sodium dodecyl sulfate
SDS-PAGE	sodium dodecyl sulfate polyacrylamide gel electrophoresis
SEC	size-exclusion chromatography
SRT	substrate replacement therapy
TCEP	tris(2-carboxyethyl)phosphine HCl
TEM	trabecullar extracellular meshwork
TEM	transmission electron microscopy
$[\theta]$	molar ellipticity

ThT	Thioflavin T
TIGR	Trabecular Meshwork Inducible Glucocorticoid Response
TM	trabecular meshwork
T_m	melting temperature
TMAO	trimethylamine N-oxide
TX	Triton X-100
μ	micro
UPR	unfolded protein response
WDR36	WD repeat domain 36
WT	wild-type

SUMMARY

The inherited form of primary open angle glaucoma, a disorder characterized by increased intraocular pressure and retina degeneration, is linked to mutations in the olfactomedin (OLF) domain of the myocilin gene. Disease-causing myocilin variants accumulate within trabecular meshwork cells instead of being secreted to the trabecular extracellular matrix thought to regulate aqueous humor flow and control intraocular pressure. Like other diseases of protein misfolding, we hypothesize myocilin toxicity originates from defects in protein biophysical properties. In this thesis, the first preparative recombinant high-yield expression and purification system for the C-terminal OLF domain of myocilin (myoc-OLF) is described. To determine the relative stability of wild-type (WT) and mutant OLF domains, a fluorescence thermal stability assay was adapted to provide the first direct evidence that mutated OLF is folded but less thermally stable than WT. In addition, mutant myocilin can be stabilized by chemical chaperones. Together, this work provides the first quantitative demonstration of compromised stability among identified OLF variants and placing myocilin glaucoma in the context of other complex diseases of protein misfolding.

Subsequent investigations into the biophysical properties of WT myoc-OLF provide insight into its structure and function. In particular, myoc-OLF is stable in the presence of glycosaminoglycans (GAGs), as well as over a wide pH range in buffers with functional groups reminiscent of such GAGs. Myoc-OLF contains significant β-sheet and β-turn secondary structure as revealed by circular dichroism analysis. At neutral pH, thermal melts indicate a highly cooperative transition with a melting temperature of ~55°C. A compact core structural domain of OLF was identified by limited proteolysis

and consists of approximately residues 238-461, which retains the single disulfide bond and is as stable as the full myoc-OLF construct. This construct also is capable of generating 3D crystals for structure determination. This data, presented in Chapter 3, inform new testable hypotheses for interactions with specific trabecular extracellular matrix components.

To gain further insight into the biological function of myoc-OLF, a facile fluorescence chemical stability assay was designed to identify possible ligands and drug candidates. In the assay described in Chapter 4, the target protein is initially destabilized with a chemical denaturant and is tested for re-stabilization upon the addition of small molecules. The assay requires no prior knowledge of the structure and/or function of the target protein, and it is amendable to high-throughput screening. Application of the assay using a library of 1,280 compounds revealed 14 possible ligands and drug candidates for myoc-OLF that may also generate insights into myoc-OLF function.

Due to the high β-sheet content of monomeric myoc-OLF and presence of an aggregated species upon myoc-OLF purification, the ability of myoc-OLF to form amyloid fibrils was suspected and verified. The fibril forming region was confirmed to reside in the OLF domain of myocilin. Kinetic analyses of fibril formation reveal a self-propagating process common to amyloid. The presence of an aggregated species was confirmed in cells transfected with WT myocilin, but to a greater extent in cells transfected with P370L mutant myocilin. Both cell lines stained positive for amyloid. Taken together, these results provide further insights into the structure of myocilin and suggest a new hypothesis for glaucoma pathogenesis.

Finally, in a related study, small molecule drug candidates were investigated to treat acid β-glucosidase (GCase), the deficient lysosomal enzyme in Gaucher disease, another protein conformational disorder. Three new GCase active-site directed 3,4,5,6-tetrahydroxylazepane inhibitors were synthesized that exhibit half inhibitory concentrations (IC_{50}) in the low millimolar to low micromolar range. Although the compounds thermally stabilize GCase at pH 7.4, only one of the synthesized analogs exhibits chaperoning activity under typical assay conditions. This successful pharmacological chaperone is also one in which GCase is in its proposed active conformation as revealed by X-ray crystallography. Probing the plasticity of the active-site of GCase offers additional insight into possible molecular determinants for an effective small molecule therapy for GD.

CHAPTER 1

INTRODUCTION

1.1 Glaucoma

Glaucoma is an irreversible, chronic, degenerative optic neuropathy affecting 70-80 million people world-wide and is second only to cataracts as a cause of blindness [1]. A patient is considered to have glaucoma when at least one eye has both typical structural and functional defects, that is to say damage to the optic disc and subsequent visual field loss [2]. Damage to the optic disc is visualized by ophthalmologists as a topical deepening and widening of the cup due to loss of retinal ganglion cell (RGC) axons along with supporting glial and vasculature, and the deformation of connective tissues supporting the optic disk [3]. Injury to RGC axons occurs by a variety of factors, only some of which are understood. In its initial phase, glaucoma is asymptomatic and painless. Patients with glaucoma typically lose peripheral vision first and may lose all vision if not treated early.

Classification of glaucoma is based on three factors: (1) etiology, depending on if the symptoms present themselves on their own (primary) or if the symptoms are a result of disease or injury to the eye (secondary), (2) anatomy of the anterior chamber, open angle or closed angle, and (3) by the age of onset. Based on these classifications, glaucoma may be broken down into three categories: primary open angle glaucoma (POAG), primary acute closed angle glaucoma, and primary congenital glaucoma. Of these, POAG is the most common [4].

Glaucoma is a heterogeneous disorder and is frequently associated with elevated intraocular pressure (>21 mm Hg, IOP). However, increased IOP is neither necessary nor sufficient for onset or progression of the disease [5], and it is not clear how elevated IOP leads to visual field loss [6]. The anterior chamber of the eye is where the increase in IOP

occurs. Since the lens and cornea lack a blood supply, the anterior chamber has its own circulatory system and is filled with aqueous humor. This clear fluid is produced in the ciliary body and circulates throughout the anterior chamber (Fig. 1.1).

Aqueous humor outflow is regulated by the trabecular meshwork (TM) in the iridocorneal angle (angle formed by the iris and cornea) and drainage occurs through the Schlemm's canal [7]. The TM is a filter-like structure composed of trabecular beams of extracellular matrix (ECM) and endothelial cells (TM cells). TM cells help regulate eye pressure by controlling the drainage of the fluid from the eye as new fluid is produced [8], and structural abnormalities in the TM are believed to obstruct aqueous humor outflow and lead to elevated IOP. Therefore, increased IOP does not result from an increased production of aqueous humor, but rather from a reduced outflow. Since the optic nerve damage cannot be treated directly, focus in the field has been directed to treat the only known risk factor that can be modified, elevated IOP. Clinical trials have shown that reducing IOP slows the onset and progression of glaucoma [9-10] and current research focuses on identifying the site of resistance within the TM and the mechanism that changes the overall resistance.

1.1.1 Myocilin Linked with POAG

Myocilin was first discovered as a result of research directed towards understanding steroid-induced glaucoma. Corticosteroids are widely used as anti-inflammatory agents for the treatment of ocular inflammatory conditions. However, a link between the exogenous administration of corticosteroids and elevated IOP has been known since the 1950's, and can lead to secondary glaucoma [11-13]. Treatment of TM cells *in vitro* with corticosteroids, in particular dexamethasone (Dex), induced the expression of a 55 and 66 kDa protein in a time and dose-dependent manner similar to the elevated IOP observed in patients [14-16]. These protein products were determined to

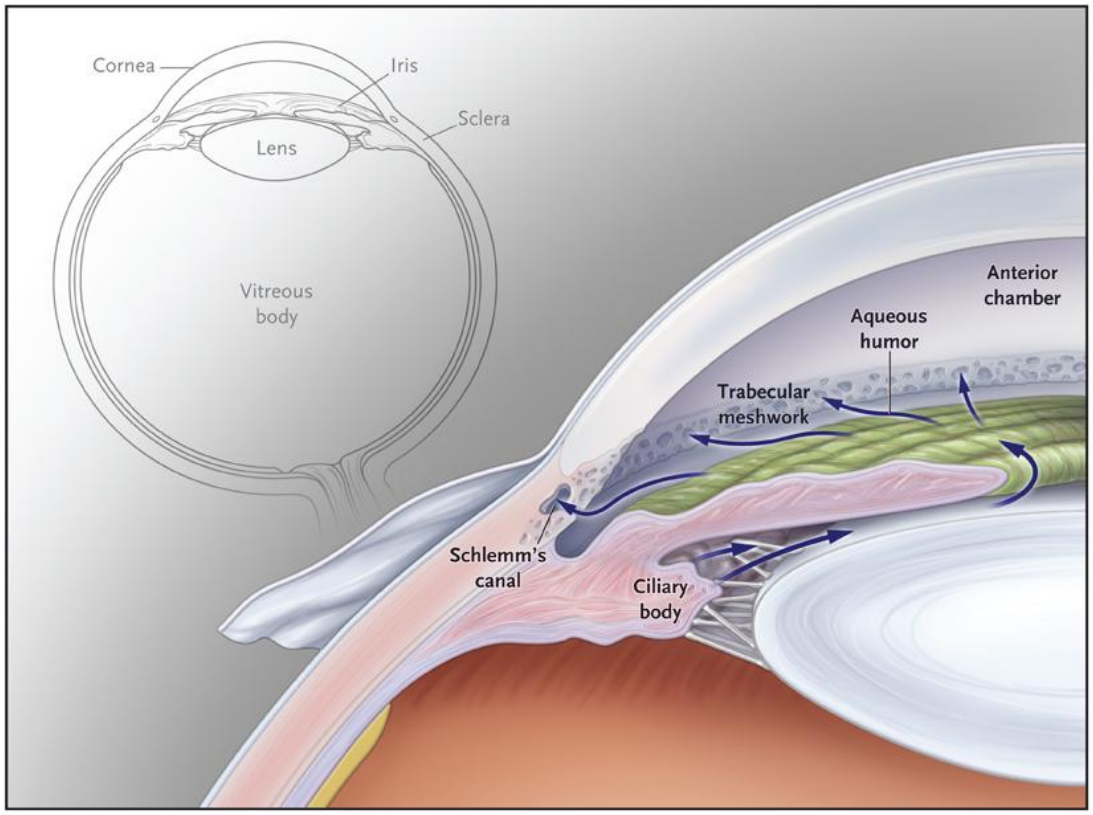

Figure 1.1 Circulation of the aqueous humor. This anterior segment of the eye shows the circulation of the aqueous humor from the ciliary body through the pupil into the anterior chamber. The aqueous humor then passes through the trabecular meshwork into Schlemm's canal and travels from there into the episcleral venous system. A smaller amount of aqueous humor leaves the eye through the face of the ciliary body, just below the trabecular meshwork. Figure was reprinted with permission from [17].

arise from the same gene which was named Trabecular Meshwork Glucocorticoid Responsive (TIGR) gene [18-19] and is now known as myocilin (see below).

Attempts to identify promoter elements in the TIGR gene to explain the hypersensitivity of individuals to the corticosteroids and the up-regulation of TIGR were unsuccessful [20], and the finding of a delayed response (8-16 hrs) to induction by Dex suggested that TIGR's transcriptional regulation by glucocorticoids is a secondary response and not a direct stimulation [21]. However, genetic linkage studies conducted in a single large Caucasian family in USA with an autosomal dominant pedigree for early-onset POAG (juvenile OAG, JOAG) localized a genetic defect in GLC1A, mapped to chromosome 1q21-1q31 [22]. This gene was confirmed by subsequent studies with other families diagnosed with JOAG. The TIGR gene was soon identified within chromosome 1q [23], and its location was confirmed in an unrelated study [24]. The gene product was permanently renamed myocilin based on its homology to the N-terminal domain with non-muscle myosin, as well as the identification of the gene product in the connecting cilium of photoreceptor cells [24].

To date, at least 20 genetic loci associated with POAG have been reported [25], but only three genes have been confirmed to be linked to POAG so far: myocilin (*MYOC*) [23], optineurin (*OPTN*) [26], and WD repeat domain 36 (*WDR36*) [27]. Only myocilin is established as directly glaucoma causative, while the roles of optineurin and WD36 remain unclear due to conflicting evidence. Mutations in the myocilin gene are attributed to 4% of adult-onset POAG cases and 10-33% of juvenile-onset cases [28-30].

1.2 Myocilin

Myocilin (gi accession: 4557779, geneID 4653) is a 504 amino acid glycoprotein (~55 kDa) [18, 24] consisting of three structural domains: a 32 residue N-terminal signal sequence for secretion [18], a myosin-like coiled-coil region (residues 111-184), and a C-terminal olfactomedin (OLF) domain (residues 244-504) (Fig. 1.2) [31]. Interestingly,

myocilin possesses a uniquely bipartite secondary structure, α-helical N-terminus and β-sheet in the C-terminal domain, and is believed to have evolved from two separate proteins [32]. The coiled-coil domain contains two leucine zippers, which are found in a wide variety of proteins and have the ability to form homo- or heteromeric complexes. It is this region that is responsible for multimerization [33-34] and interactions with certain extracellular matrix proteins [33, 35-36]. Current knowledge of the function of myocilin is primarily restricted to this region. Very little is known about the function of OLF domains, which are highly conserved across higher eukaryote species. More than 90% of glaucoma-associated mutations are found within the myocilin OLF domain.

1.2.1 Localization and Function

The normal function and localization of myocilin are topics of active and controversial research, as myocilin is expressed in almost every ocular tissue, and, depending on the tissue, it is observed extra- or intracellularly [37]. Within the eye, myocilin is expressed in the trabecular meshwork, cornea, lamina cribosa, ciliary body, iris, retina, post laminar optic nerve head, vitreous and aqueous humor [31, 33-34, 37-39]. Of these tissues, the highest level of expression is within the TM, the region of the eye believed to regulate IOP [40-41]. Moreover, myocilin is found in a variety of tissues outside the eye and, of these, its highest levels were found in the skeletal muscle and heart [18, 29, 31].

Myocilin is a secreted protein (Fig. 1.3A), confirmed by the isolation of recombinant myocilin from conditioned medium of cultured TM cells [19, 42]. Given that secreted proteins are generally synthesized, folded, and processed through the endoplasmic reticulum (ER) and golgi apparatus, it is not surprising that myocilin has also been found within organelles associated with the secretory pathway [43-46]. Myocilin has been reported to be cleaved in the ER by calpain II into two fragments; a 20

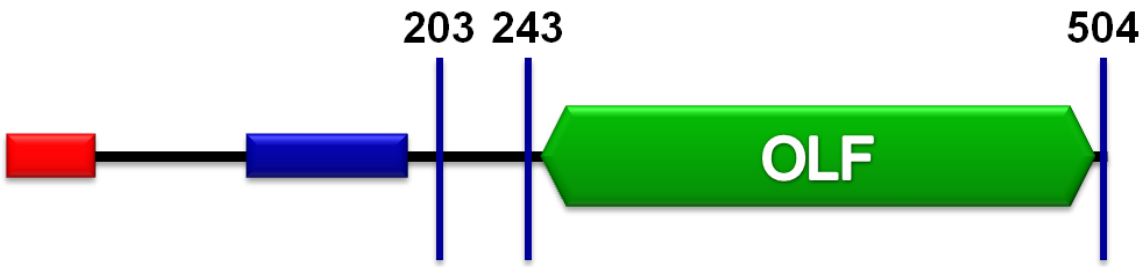

Figure 1.2. Scheme of myocilin protein domains. Myocilin contains an N-terminal signal sequence (red), coiled-coil domain (blue), and a C-terminal olfactomedin domain (green). Numbers 203 and 243 correspond to the amino acid sequence of the linker domain contained in exon 2, whereas 504 marks the last residue of myocilin.

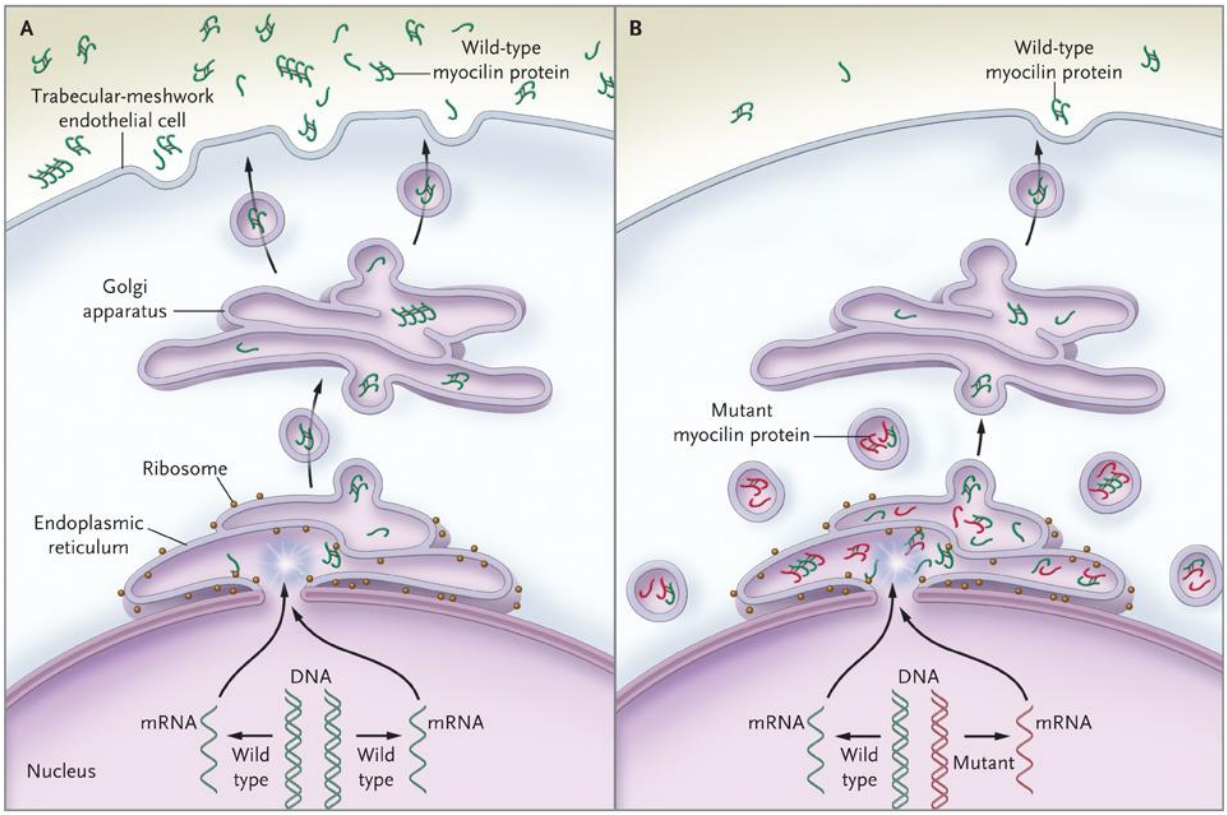

Figure 1.3. Proposed pathways for normal secretion of myocilin into the aqueous humor and for secretion reduced by a *MYOC* mutation. In Panel A, wild-type myocilin protein (green symbols) is produced in the endothelial cells of the trabecular meshwork and passes through the secretory pathway to reach the extracellular space. In the first step in this process, messenger RNA (mRNA) is transcribed from the gene encoding myocilin (*MYOC*) and is delivered to ribosomes at the endoplasmic reticulum, where the mRNA directs the synthesis of myocilin. Next, transport vesicles convey myocilin to the cell membrane through the Golgi apparatus. These vesicles fuse with the cell membrane and release myocilin into the extracellular space and aqueous humor. Along the secretory pathway, molecules of myocilin may associate with each other and form multimers (dimers and tetramers are depicted). In Panel B, heterozygous mutations of the *MYOC* gene are associated with an autosomal dominant form of glaucoma. The

wild-type copy of *MYOC* encodes normal myocilin protein (green symbols), and the mutant *MYOC* copy encodes mutant myocilin protein (red symbols). Myocilin protein forms multimers that may be composed of both wild-type and mutant subunits. Secretion of mutant myocilin protein and multimers containing mutant subunits is greatly reduced, leading to the retention of the mutant protein in the endoplasmic reticulum and intracellular vesicles of trabecular-meshwork cells. This figure was reprinted with permission [17].

kDa N-terminal fragment and a C-terminal 35 kDa olfactomedin containing fragment [47]. Both the 35 kDa fragment and full-length myocilin have been reported to be secreted to the ECM and are present in aqueous humor and select monolayer cells engineered to over express myocilin, and thus hypothesized to maintain a normal ECM structure [34, 48-49].

Despite the evidence supporting myocilin as a secreted protein that would normally function in the ECM, myocilin is also believed to play an intracellular role [24, 37]. Sakai *et al.* and others have shown that myocilin associates with mitochondria membranes [50-52]. However, these interactions appear to be cell-type specific as they are only observed in trabecular meshwork and astrocyte cells, but not in corneal fibroblasts [52-53]. Finally, myocilin has been shown to interact with microtubules [54]. Karali *et al.* argue that while the observed intracellular staining patterns suggest some intracellular localization, it is not clear whether some of the staining represented extra- or intracellular staining and whether some of the intracellular staining represents cells synthesizing large amounts of myocilin for secretion to the extracellular space [37].

During the subsequent 14 years since the linkage of myocilin to early and late-onset POAG, considerable effort has been invested to determine its function in normal eyes, and how changes in myocilin expression or mutations may lead to glaucoma. It is critical to determine the function of myocilin to see if it is important in the regulation of IOP and normal trabecular meshwork function. Myocilin is likely a multifunctional protein, as it has been identified both intra- and extracellularly. Inside the cell, myocilin may influence mitochondrial function as over-expression in TM cells reduced mitochondria respiration, which sensitizes cells and triggers apoptotic events [50]. This is consistent with the observed loss of TM cells in POAG [55]. Overall, in spite reports of potential intracellular functions, myocilin is believed to be largely an ECM protein. Full-length myocilin associates with components of the ECM via interactions with the Heparin (Hep) II domain of fibronectin, laminin, decorin, and collagens types I, III, IV, V and VI

[36, 51, 56-58]. These interactions lead to a possible role in cell-matrix interactions and regulation of these interactions in the TM [36]. Myocilin is thought to modify cell signaling events mediated by the Hep II domain of fibronectin, which impaires cell attachment and migration of human skin fibroblasts [59]. Myocilin is also hypothesized to control the adhesive properties of the cell, as over-expression in TM cells results in a loss of cellular adhesion [60]. Myocilin is also presumed to play a role in stress response, which is consistent with the expression being inducible by environmental factors such as steroid treatment with Dex, heat-shock, mechanical stretch, and oxidative stress [19, 40, 45, 61]. In support of this hypothesis, targeted deletion of the myocilin gene does not result in glaucoma [6], which suggests myocilin may not be critical for normal eye function and that a stress response may be needed to see a disease-causing phenotype.

Taken together, myocilin shares many features of ECM or "matricellular" proteins that display diverse functions including the ability to bind to the ECM, influence cell-matrix interactions, and serve as stress and injury response proteins. Matricellular proteins can function both intra- and extracellularly [62-63]. For example, similar to myocilin, tenascin-C has de-adhesive effects when presented as soluble proteins to cells in a strong adhesive state [64]. However, myocilin differs from tenascin-C because it does not block cell attachment to fibronectin [59]. Whether or not myocilin functions as a extracellular matricellular protein remains to be confirmed, as well as its roles in other regions of the eye and other organs.

1.2.2 Myocilin-Associated POAG

The first hypothesis regarding association of myocilin to POAG was that elevated IOP may be caused by increased levels in myocilin, which in turn leads to a reduction of outflow facility either by physically obstructing the outflow path and/or affecting cell-mediated processes that control outflow [36]. The basis of this notion is founded on studies in which human TM cells treated with Dex displayed increased myocilin

production in a dose-dependent manner that correlated with the timing and increase of IOP [14, 45]. Immunohistochemical staining of POAG eyes showed an increase in myocilin levels [65]. More recently, the levels of myocilin have been found to be statistically elevated in human aqueous humor of POAG patients [66] further supporting the connection between increased myocilin levels and POAG. Nguyen *et al*. hypothesized that increased levels of myocilin may accumulate within the TM and interfere with normal flow patterns, thus resulting in increased IOP [18]. This hypothesis was corroborated by a study in which human eyes treated with recombinant myocilin showed an increase in IOP over 12 hours, increasing outflow resistance 94% [67]. Cultured anterior segments of porcine and human eyes perfused with recombinant OLF domain of myocilin did not result in changes of outflow facility, indicating the observed elevations in IOP may be the result of the N-terminal myosin-like domain interactions in the ECM [49].

A complicating factor in studies involving animal models is that only a couple species are genetic carriers for POAG, including rats [68] and some canine breeds [69-70]. Rats that spontaneously develop increased IOP had a 3.2-fold increase in myocilin transcription [68]. Conversely, rats treated with Dex display elevated IOP, but the protein and mRNA levels of myocilin in the trabecular meshwork and around Schlemm's canal in the steroid-treated eyes were the same as the controls [71]. However, in canine models, aqueous humor levels of myocilin were elevated in dogs with either primary or secondary OAG [69] and beagles had increased levels of myocilin in the aqueous humor proportionate to the severity of the disease [70]. To further complicate the matter, transgenic mice heterozygous (+/-) and homozygous (-/-) for the null *MYOC* mutation were both viable and fertile and no ocular abnormalities were observed indicating myocilin is not required for normal development [6].

As highlighted by the animal model studies, the hypothesis that increased levels of myocilin lead to decreased aqueous humor outflow, and ultimately POAG, remains

controversial. Human anterior segment cultures over-expressing the recombinant N-terminal domain of myocilin resulted in a construct that was sequestered in the cell, but displayed an increase in outflow facility resulting in decreased IOP [72], which is contrary to previous reports that the N-terminal domain is responsible for elevated IOP as mentioned above [49]. Based on the conflicting data, it is unclear if the differences that were observed are due to species variations (i.e. mice do not naturally acquire POAG) or due to the mode of delivery of the over-expressed myocilin. In humans, hemizygous deletion of myocilin [73] or the presumed homozygous null mutation (R46Stop) [74] does not result in POAG, which suggests that elevated myocilin levels may be a secondary effect of elevated IOP and not the primary cause. Therefore, increased levels of myocilin would not cause the elevated IOP, but may be the result of it. Taken together, evidence supports involvement of high myocilin levels in POAG, but the mechanism is unclear.

1.3 Mutant Myocilin and POAG

The most common inherited form of POAG is linked to point mutations in the myocilin gene, accounting for 4% of adult-onset cases and ~10% of juvenile forms of the disease [23, 75-76]. The vast majority (>90%) of mutations are missense mutations in the C-terminal OLF domain, highlighting the functional importance of this domain in POAG pathogenesis (Fig. 1.2) [77] . Mutations in the first exon containing the coiled-coil domain account for the remaining glaucoma-inducing mutations, and no mutations are located in the second exon, which encodes a linker region between the two domains (Fig. 1.2) [77]. According to the myocilin allele specific phenotype database (www.myocilin.com), there are currently 79 known disease-causing mutations located in the OLF domain alone [78]. These mutations are generally associated with a juvenile or early-onset form of POAG [79], but patients with Q368Stop mutation typically have a later adult-onset [73]. Myocilin mutations lead to high IOP that frequently requires

surgical intervention to manage the glaucoma. It is interesting to note that although myocilin is such widely distributed in many tissues throughout the body as discussed above, it is only associated with POAG, an eye disease.

Mutations in myocilin reduce its secretion *in vitro* and *in vivo*, resulting in a reduction or absence of myocilin in the TM of patients with glaucoma-associated *MYOC* mutations [80]. Myocilin variants accumulate in the ER either as homo-oligomers or hetero-oligomers when coexpressed with WT myocilin (Fig. 1.3B) [72, 81-86], resulting in a significantly reduced level of functional myocilin in the ECM of the TM [80, 82-83, 86]. However, the reduced myocilin levels in these tissues are not believed to cause the POAG phenotype, as both myocilin knock-out mice [6] and patients with the R46Stop mutation do not acquire POAG [74]. Instead, sequestration of myocilin mutants in the ER likely results in a toxic gain-of-function, unrelated to the normal function of myocilin [6]. These aggregates have been shown to be detergent insoluble [87].

Under normal homeostasis in the cell, molecular chaperones are present in the ER to carefully monitor and assist proteins to their native conformations and continue on their path to maturity and cellular trafficking. ER quality control mechanisms ensure that nascent proteins that fail to fold or assemble correctly are retained in the ER [88]. It is believed that the quality control machinery of the ER recognizes general biophysical properties shared by incompletely folded proteins, including exposed hydrophobic patches, mobile loops, and a lack of compactness [89]. If the protein continues to misfold after multiple attempts of refolding, it is generally targeted for degradation and transported to the cytosol where it is rapidly degraded by an ubiquitin-mediated proteolytic pathway [90].

In this ER associated degradation (ERAD) process, the aberrant protein must first be extracted from the ER lumen to be degraded by the proteasome, a barrel-shaped structure which requires the substrate to be unfolded to gain access into the active site [90-91]. However, if the rate of synthesis of a protein exceeds the folding and

degradation rates of a cell, accumulation of the protein will occur [92]. Mutations, as in the case of myocilin, that interfere with protein folding as well as environmental factors may exacerbate this problem and trigger ER stress responses. In particular, the unfolded protein response (UPR) induces the upregulation of genes encoding ER resident chaperones [93-94] such as GRP78 (also called BiP) [95] or protein disulfide isomerase (PDI) [96]. Ultimately, programmed cell death is initiated if ER stress is not alleviated.

In myocilin-associated POAG, disease-causing variants of myocilin apparently possess a folding defect and lead to aggregation in cells. For example, large myocilin juxtanuclear aggregates have been observed within the ER of HEK and differentiated primary human TM cells [97]. Sequestration of mutant myocilin triggers the UPR and the apoptotic pathway [83, 86, 98] characteristic of an ER storage disease. Both the molecular chaperone GRP78 and the folding enzyme PDI have been shown to be up-regulated in HTM cells expressing mutant myocilin [43, 84]. Aggregation of mutant myocilins in cultured HTM cells leads to a deformed cellular morphology and diminished cell proliferation [84]. The subsequent breakdown of TM cell structure leads to obstruction of aqueous humor outflow pathway [99], ocular hypertension, and, ultimately, POAG [17].

1.3.1 Potential Myocilin-POAG Therapy

Many diseases are the result of amino acid substitutions in a protein leading to either a lack of functional protein (the result of ERAD) and/or due to toxic effects of the misfolded protein or aggregates. This may directly or indirectly influence the ability of the cell to function properly and can lead to cell death through apoptosis. Disorders that fall into this general pattern are referred to as ER storage disorders (ERSDs) or, more broadly, protein conformational disorders (PCDs) [100]. Furthermore, both intra- and extracellular protein aggregates are hallmarks of many neurodegenerative disorders as

well, including Alzheimer's disease, Parkinson's disease, multiple sclerosis, and loss-of-function disorders such as lysosomal storage disorders [101].

PCDs are primarily the result of missense mutation(s) in a gene that leads to altered protein behavior, aberrant cellular or extracellular activity, and detrimental downstream effects that ultimately manifest in disease. However, many of these disease-causing mutations do not seriously compromise the global fold of a protein, but rather lead to local perturbations that are recognized by the ER quality control system, as is predicted to be the case for myocilin. We, and others [76, 97], have hypothesized that if myocilin aggregation in the ER can be alleviated, either by stabilization of mutant protein to facilitate folding and secretion or to promote a more efficient degradation mechanism, the dysfunction of TM cells due to cytotoxicity could be relieved and delay the onset of clinical symptoms. Support for this therapeutic approach comes from cell-based assays where growth at lower temperatures allowed secretion of certain mutant myocilins, suggesting that when protein production is slowed, toxicity is reduced [76, 97]. In conjunction, addition of nonspecific chemical chaperones such as glycerol, 4-phenylbutyrate [102], and trimethylamine *N*-oxide (TMAO) [103] improves secretion of mutant myocilin.

Pharmacological chaperones (PCs) hold promise as drug candidates since they are developed as selective and potent binders to their target protein. They are effective at lower concentrations than chemical chaperones [104]. These small molecules are typically substrates, inhibitors, ligands, or variations thereof. They are designed to be cell-permeable and capable of binding to endogenous mutant protein to confer enhanced thermodynamic or kinetic stability, and allow increased trafficking from the ER, thus alleviating ER stress and restored protein function. PC therapy has been proposed and investigated as a potential treatment for many genetic disorders that result from misfolded and/or unstable proteins [105], and partial or complete restoration of thermal stability by PCs have been shown for numerous types of mutant protein, including secreted proteins,

transcription factors, ion channels, G protein-coupled receptors, and lysosomal enzymes [106]. A similar approach for myocilin may lead to a therapeutic compound, but is currently unachievable due to limited structural and functional studies of which to base PC design.

1.4 Thesis Objectives

1.4.1 Chemical Chaperone Rescue of Mutant Myocilin Stability

Although one of the major challenges to studying molecular properties of myocilin has been the difficulty in recombinant expression of a soluble, well-behaved species, we have overcome this limitation. We developed a new high-yield expression and purification system for the C-terminal region of myocilin (myoc-OLF) comprising the OLF domain fused to maltose binding protein (MBP) and representative glaucoma causing mutants. We also developed a facile fluorescence thermal stability assay without removal of MBP to gain insight into the biophysical characteristics of WT and mutant myocilins. This system was also employed to identify chemical chaperones that thermally stabilize the mutant proteins. Our results provide the first direct evidence that mutated OLF is folded but less thermally stable than WT. Taken together, our results set the stage for studies to further evaluate the nature of the aggregated myocilin species as well as to identify therapeutic compounds that both exert a specific stabilizing effect on myocilin and enhance mutant myocilin secretion in cells.

1.4.2 Biophysical Characterization of the Olfactomedin Domain of Myocilin

The objective of this study is to probe the molecular properties of myoc-OLF to gain insight into its function and structure, and we report the first detailed solution biophysical characterization. This work places the OLF domain for the first time in the context of other known proteins. The data presented here inform new testable hypotheses

for interactions with specific trabecular extracellular matrix components, and may assist in design of therapeutic agents for myocilin glaucoma.

1.4.3 Application of SYPRO® Orange, a Fluorescent Hydrophobic Dye, for a High-Throughput Ligand Binding Assay for Proteins of Unknown Structure and/or Function, such as Myocilin

Due to the lack of specific knowledge of the function and structure of myocilin, we sought to develop and validate a high-throughput chemical stability assay to identify ligands and potential drug candidates based on the premise that ligand binding confers conformational stability to its target protein. Since this ligand-induced stability is a general property of proteins, our assay may be adapted essentially to any soluble protein, regardless of prior knowledge of structure and/or function. The chemical stability assay was verified using MBP as a model protein, and stabilization upon ligand binding occurred in a dose-dependent fashion. Myoc-OLF, the protein of therapeutic interest, was stabilized in a similar manner with the TMAO, a known osmolyte. Our assay not only has identified the first potential therapeutic compounds, but may also generate insights into myoc-OLF function.

1.4.4 Characterization of Amyloid Fibrils Formed by Myocilin

Although emerging clues to the pathogenesis of myocilin-induced inherited forms of glaucoma have come to light in the past decade, little progress has been made towards understanding the molecular mechanisms that lead to sporadic glaucoma, which may be due in part to the heterogeneity of the disorder. In this work, we initially sought to characterize the aggregated form of myoc-OLF and found that both WT and mutant forms of the protein form amyloid fibrils, similar to proteins in other PCDs described above. These fibrils may be created under a variety of conditions *in vitro* and fibrillization occurs in a nucleation dependent, self-propagating manner. Furthermore,

mutant myocilin expressed in mammalian cells forms intracellular aggregates containing amyloid fibrils. Taken together, this work provides new insights into myocilin and suggests a novel molecular based hypothesis for pathogenesis.

1.4.5 The Acid β-Glucosidase Active Site Exhibits Plasticity in Binding 3,4,5,6-Tetrahydroxyazepane-based Inhibitors

In a related study, small molecule drug candidates were investigated to treat acid β-glucosidase (GCase), the deficient lysosomal enzyme in Gaucher disease, another protein conformational disorder. These small molecules, called pharmacological chaperones, have largely been active-site-directed inhibitors of acid β-glucosidase (GCase), the deficient lysosomal enzyme, usually containing five- or six-membered rings, such as modified azasugars. Here we extend the scaffold to seven-membered nitrogen-containing heterocycles (3,4,5,6-tetrahydroxyazepanes) with or without alkyl ether substructures. Comparison of crystal structures reveals that the core azepane stabilizes GCase in its proposed active conformation, whereas binding of an analog with a hydroxyethyl tail creates a conformation of GCase in which the active site is covered. Although all compounds thermally stabilize GCase at pH 7.4, reflective of the pH in the ER, only the core azepane is a micromolar competitive inhibitor and exhibits increased activity for the neuronopathic G202R- and the non-neuronopathic N370S- mutant GCase enzymes in an intact cell assay. Thus, the core azepane scaffold is a candidate for pharmacological chaperone development. The plasticity of the active site of GCase observed in binding azepanes offers a structure-based route to the design of second-generation azepanes and more generally, insight into the possible molecular determinants for an effective pharmacological chaperone for Gaucher disease.

CHAPTER 2

CHEMICAL CHAPERONE RESCUE OF MUTANT MYOCILIN STABILITY

2.1 Introduction

Open angle glaucoma (OAG) is a recent addition to the family of protein conformational disorders that includes cystic fibrosis, Alzheimer disease, p53-related cancers, and lipid metabolism disorders such as Gaucher and Fabry diseases, among others [107]. OAG, the most common form of glaucoma that affects ~70 million people worldwide, is a complex and heterogeneous disease characterized by irreversible vision loss often associated with elevations in intraocular pressure [108-109]. The molecular and physiological mechanisms that lead to intraocular pressure increase are poorly understood, but are thought to occur in the anterior region of the eye within the anatomical pathway for outflow of aqueous humor, which includes the trabecular meshwork [110-111]. In the last 10 years, significant progress has been made in identifying causative genes that account for inherited, autosomal-dominant glaucoma cases. Genes for three protein products, myocilin, optineurin, and WD36, have been linked to familial forms of OAG. Of these, mutations in myocilin are by far the most common, accounting 10-33% of the juvenile (35 years of age and younger) and 3-4% of all adult-onset OAG cases [108].

Myocilin is a ~55 kDa glycoprotein expressed in ocular tissues, as well as throughout the human body [110]. Myocilin contains four main regions: (1) a secretion signal sequence, (2) a linker with a putative N-glycosylation site, (3) a coiled-coil/leucine zipper for multimerization [112] and interactions with certain extracellular matrix proteins [113-115], and (4) a ~30 kDa olfactomedin (OLF) domain in which the majority of genetic lesions leading to OAG are located. The explicit biological functions of

myocilin and the OLF domain in any human tissue have not been identified, but a major proposed function for myocilin in the eye is structural participation in the trabecular meshwork extracellular matrix believed to limit the migration of human trabecular meshwork (HTM) cells [116]. Accordingly, myocilin is expressed at relatively high levels in [117], and is secreted from [110], HTM cells. More generally, emerging roles of OLF domains include involvement in adhesion as well as neuronal growth, as well as in development in the mammalian brain [118-119]. The prevalence and sequence conservation (~60-80% identity among mammals) [120] of OLF domains among higher eukaryotes underscores the need for additional structural and functional studies.

Recent evidence supports a toxic gain-of-function disease mechanism for mutant myocilin. Mice heterozygous and homozygous for a myocilin knock-out allele [121] and human individuals with myocilin truncation mutations near the N-terminus [122] do not exhibit ocular abnormalities. Instead of secretion to the extracellular matrix, mutant myocilins have been shown to accumulate in the endoplasmic reticulum (ER) of HTM cells with toxic consequences [123-124]. In cell-based assays, growth at lower temperatures enables secretion of mutant myocilins, suggesting that when protein production is slowed, toxicity is reduced [124-126]. In addition, the ability to rescue secretion of mutant myocilins at permissive temperatures indicates that these myocilin variants likely retain a native-like three-dimensional structure, but have compromised stability due to a local perturbation caused by the mutation. At lower temperatures, conformational variability is expected to decrease, as the protein is further away from its temperature of unfolding.

Proteins like mutant myocilins that are folded in the ER are prevented from continuing further along the path to protein maturation and cellular trafficking if they are not folded correctly. A collection of proteins defined as “ER quality control” recognize features/flaws in a newly folded protein, such as those in disulfide bonds, and a misfolded protein is then either refolded to its native state, or targeted for degradation [127]. Even

minor defects in structure remote from a functional site of the protein cannot escape the highly redundant, tightly regulated ER quality control system that can detect exposed hydrophobic patches in soluble proteins, mobile loops, and general reduced compactness, i.e. biophysical properties [128]. ER quality control does not test newly folded proteins for function, which may be preserved for a missense mutant that retains a native-like structure.

If mutant proteins are not cleared efficiently from the ER and instead are accumulated, cellular stress responses are provoked, which may predispose cells to additional pathological events. In particular, ineffective clearing of mutant myocilins leads to aggregation, cell stress and eventually death [123, 125, 129-131]. HTM cell dysfunction death is thought to lead to a compromised matrix unable to properly control eye pressure, and eventually, the retinal degeneration characteristic of glaucoma. Thus, the pathophysiology is not linked directly to abolished intrinsic function, but first to a defect in protein stability, then to a defect in cellular trafficking, ER stress, and finally to reduced function of the trabecular meshwork.

Mechanisms that stabilize a mutant protein in its native state or accelerate the rate of folding and enable it to meet ER quality control standards hold promise as therapy for protein misfolding diseases [132-133]. The ability to traffic mutant protein with residual function out of the ER is hypothesized to reduce toxicity and cell stress, allowing for partial restoration of function, which will ultimately delay the onset of clinical symptoms [134]. In the case of mutant proteins without a known ligand or molecular structure, such as myocilin, screening for tailored small molecules that accomplish these goals requires a top-down approach, i.e. without knowledge of specific surface binding patches.

To lay the foundation for identification of small molecules capable of stabilizing mutant myocilin, we developed a high-yield expression and purification system for the C-terminal region of myocilin (myoc-OLF) comprising the OLF domain and corresponding representative glaucoma-causing mutants. One of the major challenges to studying the

structural and biophysical properties of myocilin to date has been the difficulty in recombinant expression of a soluble, well-behaved species. We also developed a facile fluorescence thermal stability assay and used this system to gain insight into the biophysical characteristics of wild-type and mutant myocilins and to identify chemical chaperones that thermally stabilize the mutant proteins. Taken together, our results set the stage for studies to further evaluate the nature of the aggregated myocilin species, as well as to identify therapeutic compounds that both exert a specific stabilizing effect on myocilin and enhance mutant myocilin secretion in cells.

2.2 Results and Discussion

2.2.1 Expression and Purification of Wild-Type Myoc-OLF

We have focused on the myocilin OLF domain primarily because this is the location of 90% of all known glaucoma-causing mutations (http://www.myocilin.com/variants.php). Other benefits to studying the isolated, compact OLF domain include lack of oligomerization due to the presence of the coiled-coil/leucine zipper region and complex disulfide patterns [112]. Myoc-OLF domain harbors no predicted glycosylation sites and has a single disulfide bond [112, 135], supporting the hypothesis that the domain expressed in a soluble recombinant form in *E. coli* will be structurally similar to that of the human protein produced in trabecular meshwork cells.

A major challenge to the study of myocilin is its known propensity to aggregate. Insoluble myocilin inclusions have been observed for both overexpressed wild type myocilin in *Drosophila* eyes [131] as well as mutant myocilin in mammalian cell culture [129], suggesting that myocilin aggregation may be relevant to both sporadic and inherited forms of glaucoma. Poor yield and solubility is common among previous reports of in vitro expression, purification and characterization of myocilin and/or the

OLF domain in a soluble form using heterologous hosts such as *P. pastoris* [135], *Sf9* insect cells [136], 293 EBNA cells [113], or refolded from *E. coli* inclusion bodies [137-138]. Thus, to date, experiments conducted on myocilin and/or OLF were limited to concentrations of 0.05-0.1 mg/ml, and aggregation was observed at higher concentrations [113].

We overcame the challenge of recombinant expression and generated a soluble OLF construct that can be produced at high yield (~2 mg purified protein /L culture), purified to homogeneity, and concentrated to at least 10 mg/mL (Fig. 2.1A) by fusion to MBP via an 8 amino acid linker. The linker was designed with a Factor Xa cleavage site, enabled by subcloning myoc-OLF from the pET-30 Xa-LIC vector (see Methods). Thus, the linker length and position of the cleavage site are different from the commercial pMAL vector. The ability of MBP to facilitate proper folding and improve expression levels of difficult proteins in *E. coli* is well documented [139], and the short linker design can help prevent aggregation of a fused protein without affecting its three dimensional structure [140]. Indeed, our final MBP-OLF fusion protein proved superior to other longer-linker fusion constructs we tested, in which the purified protein was co-eluted with the *E. coli* folding chaperone GroEL (identified by Western blot and trypsin digest/mass spectrometry). Expression levels of wild-type (and mutant MBP-OLF, see below) were increased, and GroEL was eliminated, with the use of the rare-codon correcting Rosetta-gami 2 *E. coli* strain, rich media, and growth after induction at 18°C.

Cytosolic MBP-OLF, purified initially by amylose affinity chromatography, is a mixture of aggregated, monomeric MBP-OLF, and MBP (identified by Western blot and trypsin digest/mass spectrometry) likely from cleavage by cellular proteases or incomplete translation. Fractionation by size-exclusion chromatography (Fig. 2.1B) reveals these three species. An elution peak with a retention time corresponding to the ~ 72 kDa MBP-OLF monomer is isolated. This fusion protein retains a disulfide bond

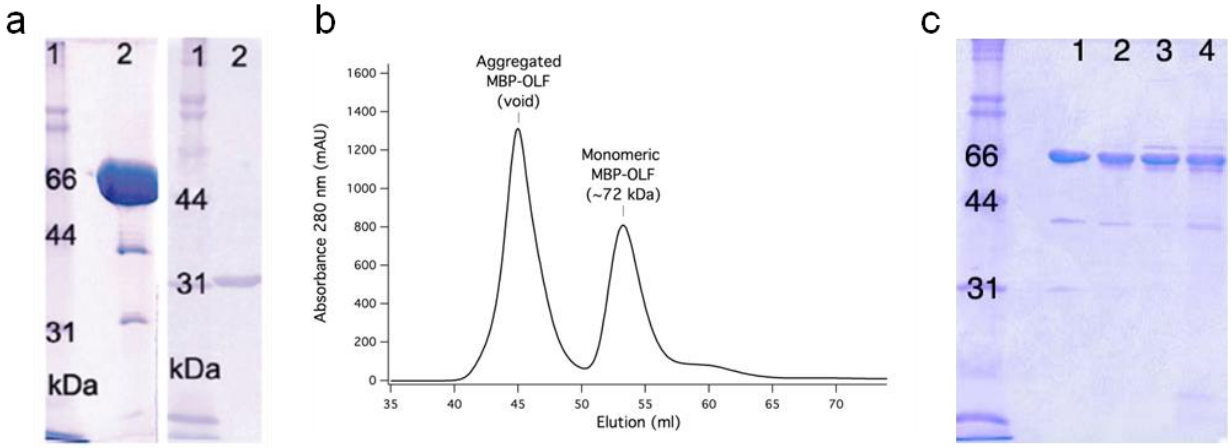

Figure 2.1. Protein purification. A) SDS-PAGE analysis of purified MBP-OLF (WT) and cleaved myoc-OLF. Left: lane 2, purified, concentrated (monomeric) MBP-OLF (WT) (72 kDa, ~10 mg/mL). Right: lane 2, cleaved myoc-OLF (~31 kDa, ~0.5 mg/mL). B) SEC of MBP-OLF WT) displaying aggregated MBP-OLF and monomeric MBP-OLF. C) SDS-PAGE analysis of purified MBP-OLF mutants. Lane 1, MBP-OLF (D380A); lane 2, MBP-OLF (I477S); lane 3, MBP-OLF (I477N); and lane 4, MBP-OLF (K423E). Low levels of MBP (~40 kDa) do not impede thermal stability measurements (see text). Gels include molecular mass standards as lane 1.

(Table 2.1) composed of the only two cysteine residues, which are found in the OLF domain.

The second distinct peak is in the void volume, indicating an aggregated species is present. The relative intensity of this cytosolic aggregate peak compared to monomer is not sensitive to time incubated at 4 °C, a freeze-thaw cycle, or concentration (not shown). In addition, neither the monomer nor aggregate re-equilibrates to the other species if each is reloaded separately onto the size exclusion column (Fig. 2.2). By SDS-PAGE under reducing conditions, the aggregates appear identical to monomeric MBP-OLF (Fig. 2.2, inset). The aggregated material comprises a broad spectrum of molecular mass as assessed by fractionation on a Sephacryl S-400 column designed to fractionate significantly larger macromolecules. The relationship of this high molecular weight aggregate species isolated from *E. coli* cytosol to inclusions observed in cellular glaucoma studies [131, 141] is not known at this time, but could be further evaluated in the context of improper disulfide bond formation as well as the observed high β-sheet content for OLF [135], and its predicted amyloid propensity [142].

Finally, as a consequence of the shorter link, accessibility of Factor Xa to the cleavage site is somewhat compromised. Efficient cleavage for monomeric, wild-type MBP-OLF is observed after overnight incubation at 37°C, whereas almost no cleavage occurs at room temperature. Cleaved wild-type OLF can be isolated from uncleaved MBP-OLF and MBP by amylose affinity chromatography, and appears as a purified monomer (~ 31 kDa) after gel filtration (Fig. 2.1A). Cleaved wild-type OLF is well-behaved. No visible precipitation is observed for monomeric cleaved OLF concentrated to over 5 mg/mL, and no appreciable aggregation or degradation is observed by either size exclusion chromatography or SDS-PAGE, even after prolonged incubation at 4 °C (Fig. 2.2).

Table 2.1. Characterization of disulfide bonds in OLF-containing proteins in this study. The thiol-modifying reagent ThioGlo® 1 only reacts with OLF-containing proteins when the reducing agent TCEP is added. Thus, OLF retains the single disulfide bond in all proteins characterized.

Sample	Fluorescence Intensity (513 nm)
Cleaved myoc-OLF	0.5 ± 0.3
Cleaved myoc-OLF + TCEP	55.7 ± 2.6
MBP-OLF	0.9 ± 0.1
MBP-OLF + TCEP	46.6 ± 3.1
MBP-OLF (D380A)	0.9 ± 0.2
MBP-OLF (D380A) + TCEP	45.0 ± 2.0
MBP-OLF (I477S)	0.7 ± 0.4
MBP-OLF (I477S) + TCEP	60.9 ± 1.9
MBP-OLF (I477N)	1.5 ± 0.3
MBP-OLF (I477N) + TCEP	71.9 ± 1.5
MBP-OLF (K423E)	0.6 ± 0.2
MBP-OLF (K423E) + TCEP	60.5 ± 2.8

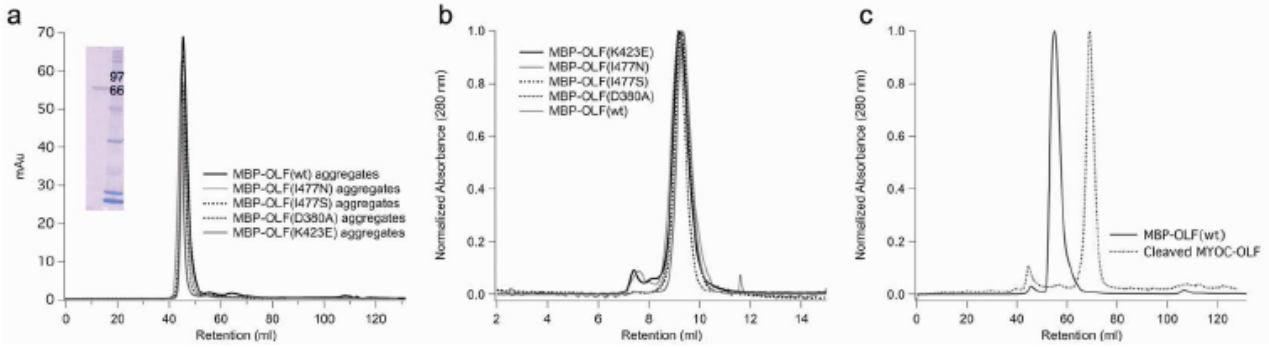

Figure 2.2. **Characterization of OLF and mutants by SEC.** A) Aggregates purified as in Methods that are reloaded onto preparative Superdex 75 column do not disaggregate into monomers. Inset: Fractionation of aggregates on SDS-PAGE under reducing conditions yields monomer MBP-OLF (~ 72 kDa). Right: molecular mass markers (kDa). B) MBP-OLF monomers purified as in Methods that are reloaded onto analytical Superdex 75 column do not equilibrate to aggregates to any appreciable extent. C) MBP-OLF(wt) and cleaved MYOC-OLF incubated at 4 °C for over a month do not aggregate to any appreciable extent.

2.2.2 Expression and Purification of Mutant Myoc-OLF

The four mutant myocilins selected for this study are well documented in the literature both in terms of prevalence among glaucoma patients as well as aggregating behavior in cells. The myocilin mutants selected represent mild (D380A) [143], moderate (I477S) [144], and severe phenotypes ((I477N[145], K423E [146]), as well as changes in size, polarity and charge. The locations of these mutations within the three dimensional fold of OLF are not currently known, but they do not interfere with disulfide bond formation (Table 2.1). In cellular studies [125-126], both D380A- and I477S- mutant myocilin secretion could be rescued by low temperature culture, whereas little or no secretion could be rescued with I477N- or K423E-mutant myocilin. The latter two mutants are also observed as aggregates in the ER, and induce the unfolded protein response [123, 131] (Summarized in Table 2.2).

Given previous cellular studies on these mutant myocilins, it was not clear from the outset whether soluble, recombinant expression of any mutants would be achievable, but expression and purification of MBP-OLF mutants followed closely that of wild-type MBP-OLF (Fig. 2.1c), with similar yields (~1 mg purified mutant MBP-OLF/ L culture). All experiments with MBP-OLF mutants were conducted well within a week of purification. Like wild-type MBP-OLF, three species were isolated by gel filtration, but based on peak height, the amount of aggregate mutant MBP-OLF in the void volume relative to that isolated in a monomeric form, varied from ~ 1.8 ± 0.4 for wild type MBP-OLF, 3.4 ± 0.2 for the D380A OLF domain mutant (MBP-OLF(D380A)), 12.1 ± 2.1 for the I477N (MBP-OLF(I477N) and 14.2 ± 2.0 for the I477S mutant (MBP-OLF(I477S), and 33.4 ± 3.6 for the K423E OLF domain mutant (MBP-OLF(K423E)). Like wild-type MBP-OLF, these ratios were unaffected by protein handling or concentration loaded onto the Superdex 75 column. After purification, prolonged incubation at 4 °C leads to degradation of the OLF domain of the MBP-OLF mutants as observed by SDS-PAGE (not shown). Furthermore, we do not observe appreciable interconversion between

Table 2.2: Summary of solubilization and secretion behaviors reported for select mutant myocilins of relevance to the current study[a].

Mutation	Glaucoma phenotype	*In vitro* solubilization [147]	Secretion from 37 °C culture HEK293 [125]/HTM [126]	Secretion from 30 °C culture HEK293 [125]/HTM [126]	ER retention [84, 131]
D380A	Mild	+	+/-	+/+	n.d.
I477S	Moderate	-	-/n.d.	+/n.d.	n.d.
I477N	Severe	-	-/-	+/-	+
K423E	Severe	-	-/-	-/-	+

soluble aggregates and monomer (Fig. 2.2). Taken together, there appears to be considerable inherent aggregation propensities in spite of isolation from the *E. coli* cytosol. After incubation with Factor Xa using conditions used for MBP-OLF, only the cleaved MBP could be isolated, suggesting mutant OLF had degraded at 37°C. To date, Factor Xa cleavage could not be further optimized to isolate the mutant OLFs. Circular dichroism spectra of the purified monomeric MBP-OLF mutants exhibit the expected mixture of the predominantly α-helical MBP (minima at 208, 222 nm) and predominantly β-sheet previously reported for OLF [135](minimum at 217), with some variation in overall intensity indicative of primarily local changes in structure (Fig. 2.3).

2.2.3 Thermal Stability Assay

The ability to express and purify site-directed MBP-OLF mutants in *E. coli* similar to wild-type, combined with similar CD signatures, suggests that these mutants are folded and retain a native-like three dimensional structure at or below room temperature. Thus, we developed a stability assay to compare wild-type OLF with that of mutants using a method that could be applied in a high-throughput fashion to test many mutants and stabilizing compounds. For this reason, we also preferred an assay that minimized protein amount and concentration requirements. The fluorescence thermal shift assay described originally for screening buffer conditions and stabilizing compounds [148] meets these criteria and was adapted to compare wild-type to mutant OLF.

The fluorescence thermal shift assay uses a real time (RT)-PCR instrument to conduct a slow melt while measuring fluorescence. The excitation and emission settings of the RT-PCR instrument are compatible with Sypro Orange, a dye known to bind to hydrophobic regions of proteins, which become increasingly exposed as the temperature of the protein-dye solution is raised. The T_m is determined as the midpoint of the transition given the upper and lower limits of the fluorescence signal, and assumes a two-state transition. Although other studies using fluorescence thermal shift assays have

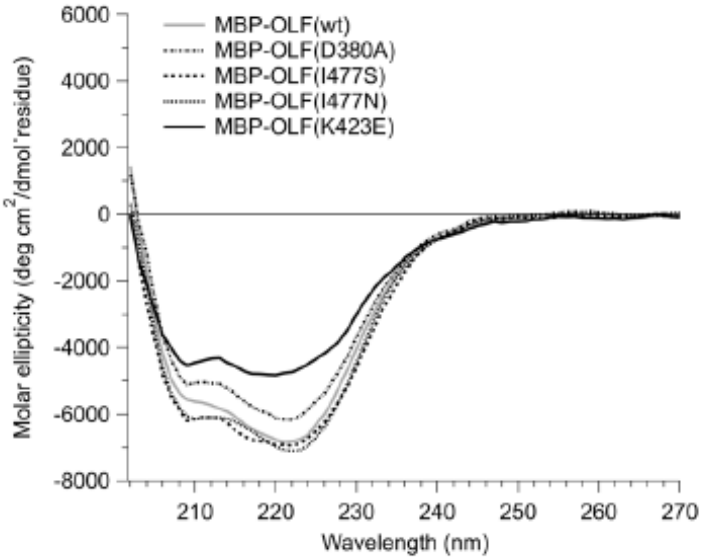

Figure 2.3. Characterization of MBP-OLF and mutants by CD. Overall, the shapes of the mutants are similar to MBP-OLF(wt), exhibiting a mixture of α-helical and β-sheet signatures expected of the fusion protein. Changes in intensity indicate some local perturbations, however.

explored protein stability as a function of buffer conditions or ligand [149-150], and a variant library of Rop, a well studied 14 kDa four-helix bundle [151-152], our study appears to be a novel application of the fluorescence stability assay to an explicitly aggregation-prone domain with disease relevance. This was accomplished by adapting the fluorescence thermal stability assay to the MBP-OLF fusion protein.

The fluorescence stability assay provides a reproducible, precise (~ ± 1 °C; Table 2.3), and convenient way to measure relative protein stability. The assay was used first to evaluate the melting temperature (T_m) of cleaved, wild-type OLF, which exhibits a reproducible transition at 52.7 ± 0.3 °C at neutral pH (Fig. 2.4A). To expand the assay to include mutant MBP-OLF fusion proteins, which cannot be cleaved with Factor Xa, we examined next the thermal stability of MBP alone (Fig. 2.4B) and compared wild-type MBP-OLF and cleaved OLF each with and without maltose (Fig. 2.4A, C). Apo MBP, which was isolated after Factor Xa cleavage of wild-type MBP-OLF, exhibits a transition at 56.1 °C, and the addition of excess maltose shifts the T_m to 67.1 °C. These values are somewhat lower than those obtained for MBP from *E. coli* K-12 by differential scanning calorimetry (~ 64 °C without and ~ 72 °C with maltose at neutral pH) [153-154], but two amino acid sequence differences and the additional C-terminal linker may contribute to this discrepancy. Wild-type MBP-OLF without maltose exhibits a broad melting transition with a T_m of 51.8 °C. With maltose, two discrete transitions are observed for wild-type MBP-OLF, one at 52.7 °C and the other at ~67 °C. The former transition overlaps well with cleaved OLF (Fig. 2.4A), and indicates that the first transition in the MBP-OLF fusion protein corresponds to the OLF domain. Compared to results with MBP, the second transition in MBP-OLF with maltose present is likely MBP with bound maltose. Notably, addition of maltose to the cleaved wild-type OLF sample does not alter the T_m (Fig. 2.4A). Taken together, these experiments establish that in the presence of maltose at pH 7, the melting of MBP is independent of the OLF domain, and the T_m of the OLF domain is not affected by the presence of either MBP or maltose.

Table 2.3. Effects of osmolytes on proteins investigated in this study.

	Protein only	**+Betaine**	ΔT_m	**+Glycerol**	ΔT_m	**+4-PBA**[a]	ΔT_m	**+Proline**	ΔT_m	**+Sarcosine**	ΔT_m	**+Sucrose**	ΔT_m	**+TMAO**	ΔT_m
MBP-OLF	52.7 ± 0.80	59.6 ± 0.8	6.9	56.0 ± 1.2	3.3	55.5 ± 0.5	2.8	57.2 ± 0.3	4.5	65.2 ± 0.6	12.5	64.3 ± 0.1	10.6	64.1 ± 0.7	11.4
MBP-OLF(D380A)	46.7 ± 0.5	50.8 ± 0.2	4.1	49.5 ± 0.2	2.8	47.2 ± 0.1	0.5	49.9 ± 0.2	3.2	58.3 ± 0.6	11.6	54.2 ± 0.7	7.5	55.6 ± 0.9	8.9
MBP-OLF(I477S)	41.9 ± 0.5	48.0 ± 0.6	6.1	45.1 ± 0.2	3.1	42.6 ± 0.1	0.7	45.3 ± 0.3	3.4	54.0 ± 0.4	12.0	50.7 ± 0.2	8.7	52.7 ± 0.8	10.7
MBP-OLF(I477N)	40.1 ± 0.8	45.1 ± 0.7	4.9	43.7 ± 0.4	3.5	41.4 ± 0.4	1.3	43.8 ± 0.9	3.7	52.5 ± 0.3	12.4	50.3 ± 0.9	10.2	50.1 ± 0.8	9.9
MBP-OLF(K423E)	40.5 ± 0.1	45.9 ± 0.6	5.4	42.6 ± 0.2	2.0	38.9 ± 0.4	-1.6	42.7 ± 0.7	2.1	48.6 ± 0.6	8.1	46.3 ± 0.5	5.7	48.8 ± 0.7[b]	8.3
MBP	67.1 ± 0.3	71.3 ± 0.6	4.2	68.2 ± 0.4	1.1	66.2 ± 0.1	-0.9	69.8 ± 0.6	2.7	75.1 ± 1.0	8.0	72.6 ± 0.8	5.5	74.4 ± 0.1	7.3

[a]5 mM 4-PBA. [b]5 M TMAO.

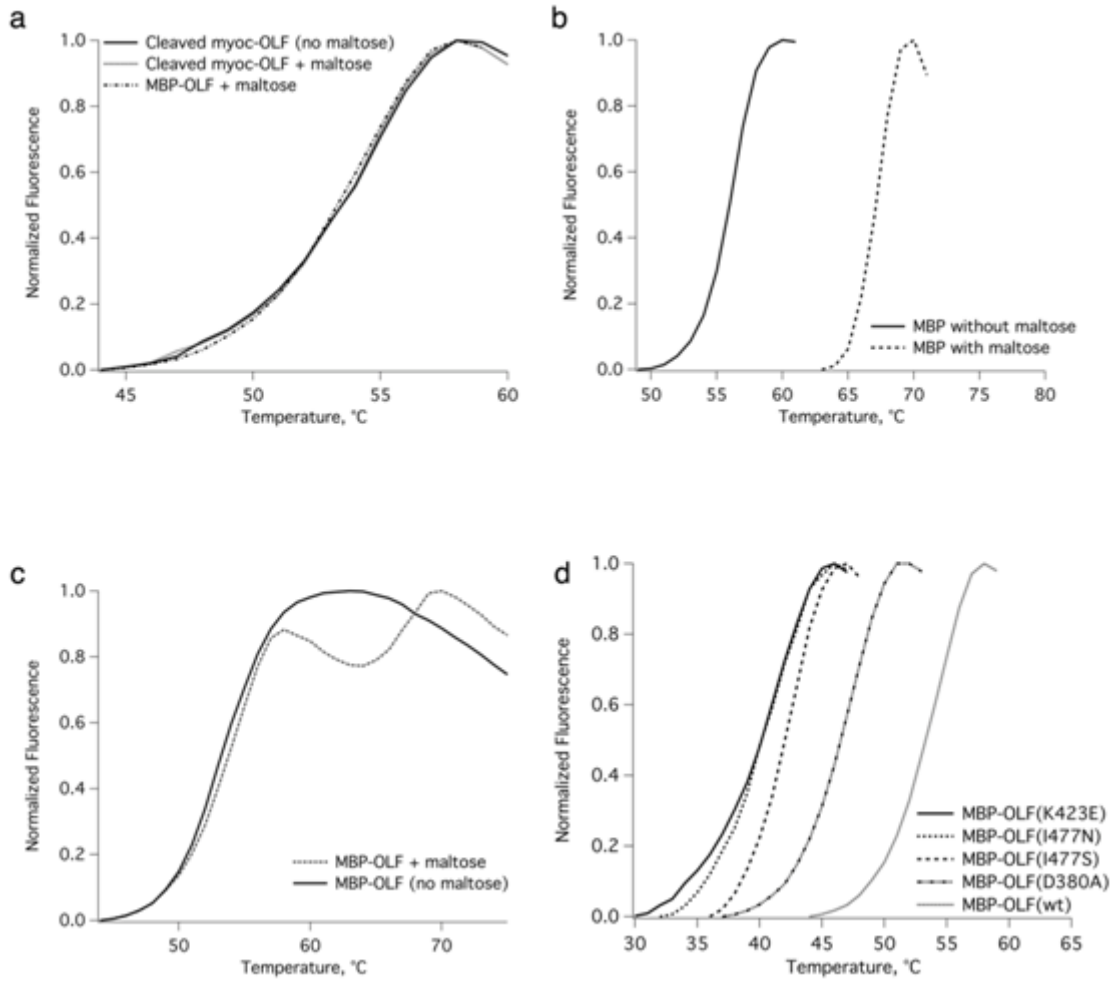

Figure 2.4. Melting curves. A) Cleaved myoc-OLF with and without maltose. B) MBP melting with and without excess maltose. C) MBP-OLF with and without maltose. D) Comparison of mutant MBP-OLF stability.

In comparison to wild-type MBP-OLF, all four MBP-OLF mutants tested were destabilized, but retained a discrete melting transition expected for a folded protein (Fig. 2.4D, Table 2.3). The transitions for MBP overlap well (not shown), reinforcing the independence of the two protein domains in the assay. MBP-OLF(D380A), which is associated with a mild glaucoma phenotype, exhibited the highest melting temperature (46.1 °C) of those tested in this study. This result is consistent with the observation that MBP-OLF(D380A) was expressed and purified in the highest yield among the mutants, and in cell studies is partially secreted at 37 °C [125] and largely secreted at 30 °C [125-126]. MBP-OLF(I477S), associated with a moderate myocilin glaucoma phenotype, showed the next highest T_m of 41.9 °C, while the remaining two mutant proteins exhibit similar melting temperatures to each other, near 40 °C. Given that the temperature of the anterior eye is ~ 35 °C [155], a significant population of unfolded, aggregation prone mutant OLF domain is expected to be present. MBP-OLF(K423E) exhibits a weak pre-transition prior to the major unfolding transition, which may have origins in extra instability conferred by charge inversion at this location in the OLF domain. The trend in T_m appears to follow generally the severity of aggregation and disease, although a strong correlation with disease phenotype will require the assessment of the stability of numerous other disease-causing myoc-OLF mutants, which is beyond the scope of this study.

2.2.4 Stabilization of Wild-Type and Mutants of MBP-OLF with Osmolytes

A shift of the population to a more stable, native-like, folded state of myocilin could be an effective therapeutic intervention for myocilin glaucoma. One practical therapeutic avenue would be to stabilize mutant myocilin with small molecules delivered topically to the anterior region of the eye. Compounds of therapeutic interest for myocilin could include those with general stabilizing ability called chemical chaperones, or those that are tailored to bind a particular target, which are called pharmacological

chaperones [156]. There are several ways that a chaperone may help trafficked proteins, both wild-type and mutant, meet the ER quality control requirements, which include both thermodynamic- and kinetic-based mechanisms. For example, the chaperone could (1) accelerate folding, reducing the chance that it will be recognized as unfolded; (2) bind and stabilize a fully folded protein so that it is less likely to unfold or to be recognized as misfolded; (3) stabilize the protein for post-translational modification (e.g., glycosylation) or interaction with a binding partner required for proper trafficking; or (4) all or some combination of the above.

Numerous studies on potential pharmacological chaperones are focused on thermodynamic stabilization [157-160]. Even transthyretin, in which the chaperones ultimately decrease the rate of pathogenic amyloid fibril formation, the tetrameric state of protein is stabilized [161]. Thus, drawing upon these examples, we believe that an important feature of a therapeutic compound for myocilin glaucoma will be restoration of mutant myocilin stability to near wild-type levels. We further suggest that therapeutic agents should not just enable mutant myocilin to pass ER quality control and be secreted from HTM cells, but should also prevent myocilin from aggregating in the ECM. The latter effect could also include promoting proper protein-protein interactions that maintain ECM integrity.

As a starting point for this approach, and for proof-of-principle that mutant myocilins can be stabilized, we selected a subset of chemical chaperones called osmolytes, low molecular weight agents found in nature that improve protein homeostasis in eukaryotic cells in response to osmotic stress [162]. Osmolytes exert a stabilizing force on proteins not by direct ligand interaction but by destabilizing the unfolded state of the protein relative to that of the native, an effect thought to be due largely to unfavorable interactions of the protein backbone with the osmolyte-rich environment [163-166]. Osmolytes are of particular interest for forced folding of biologically important proteins that are intrinsically unfolded [167]. In this study, we examined the effects of betaine,

glycerol, proline, sarcosine, sucrose, trimethylamine N-oxide (TMAO), and 4-phenylbutyrate (4-PBA) on myoc-OLF and MBP-OLF mutants (Fig. 2.5). TMAO in particular is known to counteract urea unfolding [168]. The last compound, 4-PBA, is not explicitly an osmolyte, but is a chemical chaperone originally identified for treatment of urea cycle disorders. 4-PBA has also been evaluated as a treatment for cystic fibrosis because it enables cellular trafficking of a mutant transporter caught in an intermediate folding state [133, 169]. Although these compounds do not necessarily bind to myoc-OLF as ligands, any that are found to stabilize myocilin are in principle of therapeutic potential, and are therefore good test cases for evaluating the effects of small molecules on myocilin using the fluorescence stability assay.

First, we compared the effects of these stabilizing agents on MBP alone, wild-type MBP-OLF, and myoc-OLF, at several concentrations of chemical chaperones. As expected, there is a concentration dependence of the chaperone on the extent of stabilization. We chose to focus on assays in the presence of 3 M chaperone, except for 4-PBA and TMAO where indicated, based on previous *in vitro* studies [167-168, 170-171], ease of preparing solutions, and significant stability enhancement observed (Table 2.3, Fig. 2.5). Comparison of wild-type MBP-OLF and cleaved OLF (not shown) reveals only a small difference (~0.3°C) in melting temperature for all compounds tested; thus, we report in Table 2.3 only the results for MBP-OLF and corresponding mutants. In addition, compared to MBP-OLF, the extent of MBP stabilization is generally lower magnitude (Table 2.3). In sum, the comparison of mutant MBP-OLF stability reflects the effect on the myoc-OLF domain alone.

The effects of the seven chemical chaperones on wild-type myoc-OLF rank as follows: sarcosine ~ TMAO ~ sucrose (8-10°C) >> proline ~ betaine ~ glycerol (2-4 °C) > 4-PBA (~ 0 °C) (Table 2.3, Fig. 2.5). Given that osmolytes confer only limited stability to proteins via side chain effects [163], the degree of stabilization of the mutants should be relatively consistent with that of wild-type myoc-OLF. Notably, sarcosine, a

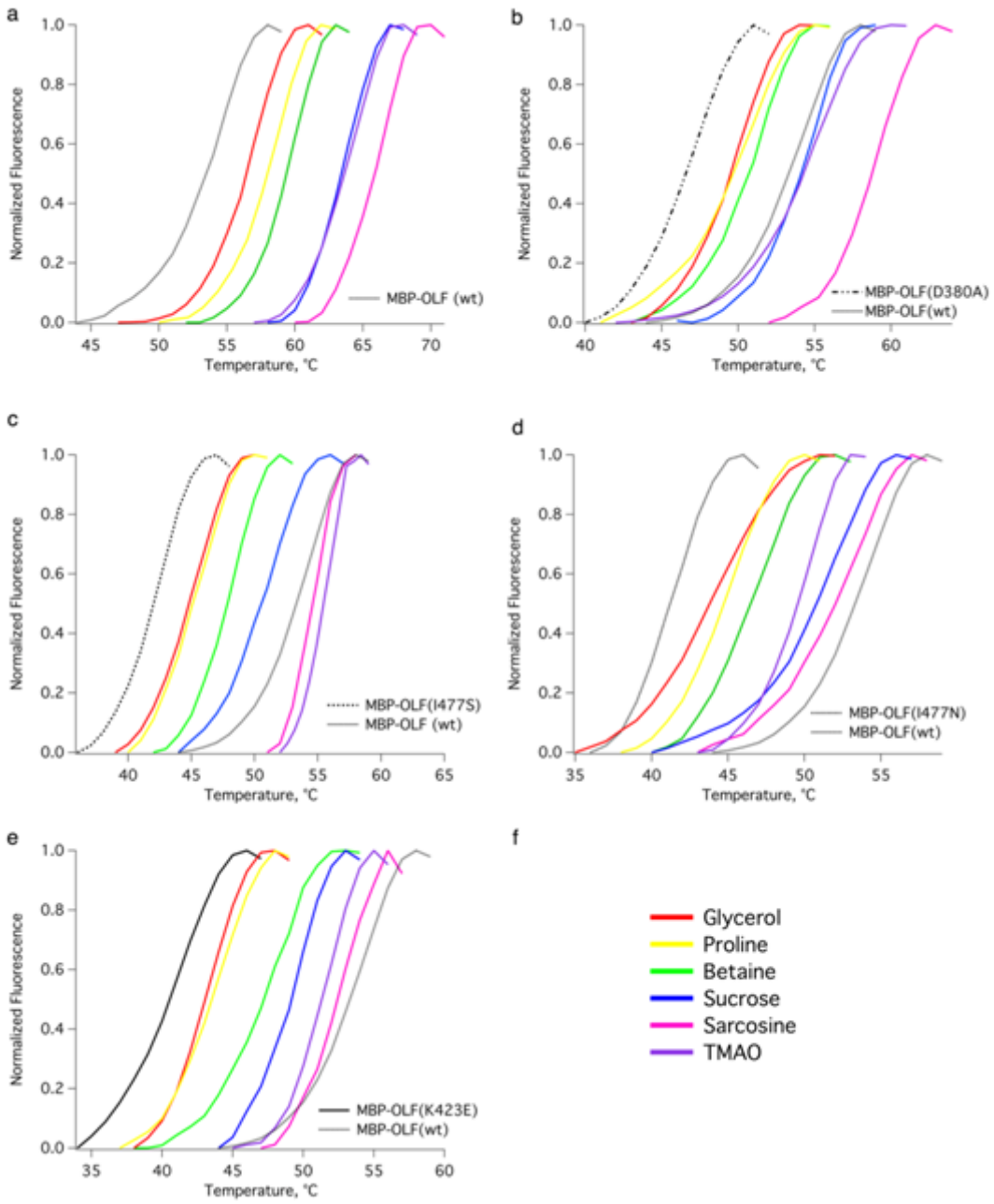

Figure 2.5. Effects of osmolytes on mutant myocilins. Key: pink, sarcosine; purple, TMAO; blue, sucrose; green, betaine; yellow, proline; orange, glycerol. (a) wild-type MBP-OLF, (b) MBP-OLF(D380A), (c) MBP-OLF(I477N), (d) MBP-OLF(I477S), (e) MBP-OLF(K423E). For (b)-(e), MBP-OLF mutant (no osmolyte) appears as the leftmost grey scale melting thermogram using the same scheme as in Fig 2D, and wild-type MBP-OLF appears as a grey thermogram.

zwitterionic, methylated analog of glycine that is highly stabilizing, is structurally similar to the less effective betaine and proline, illustrating the complexity of protein stabilization by osmolytes.

Sarcosine, TMAO, and to a lesser extent sucrose, were highly effective at 3 M in improving mutant MBP-OLF stability. For MBP-OLF(D380A), stability to better than wild-type (Fig. 2.5B) was achieved for all three osmolytes, a result that may not be surprising given that the ΔT_m between wild-type MBP-OLF and MBP-OLF(D380A) is smaller than the ΔT_m of wild-type MBP-OLF with the same osmolytes (Table 2.3). For both I477 variants (Fig. 2.5C, D), sarcosine gave the highest ΔT_m. Consistent with the proposed stabilizing mechanism of osmolytes, the OLF domain is not sensitive to side chain at this position, as it is stabilized to the same degree when substituted with either the small serine or similar-sized asparagine side chains. By contrast, MBP-OLF(K423E) (Fig. 2.5E) is relatively resistant to stabilization by chemical chaperones. For each, the extent of stabilization of MBP-OLF(K423E) was less than for wild-type and the other three mutants. Even in the presence of 5 M TMAO, the T_m could only be increased to a value between wild-type and MBP-OLF(D380A) without osmolytes (Table 2.3). Moreover, transitions observed for MBP-OLF(K423E) with TMAO and sarcosine, while shifted considerably, were correlated with more modest changes in Sypro Orange fluorescence signal in the assay. The effects of the strongly stabilizing osmolytes on MBP-OLF variants observed here are consistent with emerging evidence for more compact protein structures in osmolyte solutions [172], which is expected to be most challenging to accomplish for the charge inversion in MBP-OLF(K423E).

Compared to the transitions observed for osmolyte-stabilized wild-type MBP-OLF, all of which appear to have the same shape, those of the corresponding melting curves for mutants differ. In some cases, it was challenging to establish pre- and post-denaturation baselines, which were either broad or very short. This difficulty in evaluating the melting temperature of marginally stable proteins is documented [167]. A

shallow, broad pre-transition is observed for MBP-OLF(D380A) with proline and TMAO, whereas the remaining osmolytes follow closely the shape of the curve in the absence of osmolyte (Fig. 2.5B). Pre-transitions are also apparent for MBP-OLF(I477N) in the presence of glycerol and sucrose, which are both polyols (Fig. 2.5D). Conversely, sharper transitions are seen for MBP-OLF(I477S) in the presence of sarcosine compared to other osmolytes. These comparisons do not directly inform an unfolding pathway, but suggest a deviation from assumed two-state behavior of a single domain unfolding. For example, an unfolding intermediate may exist in which the mutated residue is accommodated by non-native interactions prior to full domain unfolding. Alternatively, two sub-domains may exist within OLF, one of which is stabilized better by the osmolyte than the other. In sum, the effects of osmolytes, which are generally believed to be an effect due to interactions with the protein backbone, may also be influenced by the side chains, either in terms of unfolding pathway or by unfavorable side chain environment such as charge inversion that limit the extent of stability achievable.

Our stabilization results differ from previous cellular trafficking studies using green fluorescence protein (GFP)-tagged mutant myocilin (C245Y, G364V, P370L, Y347H) [173] or peptide epitope (FLAG tag, used in D380N mutant myocilin) [174]. These studies monitored secretion in the presence of a single concentration (mM) of glycerol [173], 4-PBA [173] or TMAO [173] by immunoprecipitation/ Western blot of myocilin in the media, in combination with immunofluorescence to detect myocilin retained in the ER. Chaperones 4-PBA and TMAO showed a modest increase (~ 2x) in secretion. In cell studies, however, chemical chaperones can have stabilizing effects on numerous proteins, such as those involved in stress or the unfolded protein response, so they do not establish a direct stabilizing effect on myocilin. Whereas no effect on secretion was seen with glycerol in cell studies [173], this polyol results in a modest increase in mutant OLF stability, albeit at much higher concentrations that were not tested in cells. In addition, in contrast to two-fold rescue of mutant myocilin secretion

observed with 4-PBA, this compound had no direct stabilizing effect on wild-type myoc-OLF *in vitro* at low mM concentrations, and was strongly destabilizing above 10 mM (not shown). Only TMAO appears to both stabilize in our system and promote secretion from HTM cells, although the effects were observed with different mutants. This limited comparison stresses the need for complementary studies to evaluate molecules that stabilize mutant myocilins directly and promote its secretion in cells, both of which are key to developing a new treatment for myocilin glaucoma.

In conclusion, we have produced in soluble form and purified in high yield wild-type and four glaucoma-related mutant myoc-OLFs as MBP fusion proteins with a short intervening sequence. This advance enabled the adaptation of a facile stability assay for OLF without removal of MBP to both compare stability among mutants and examine the relative effects of chemical chaperones. All OLF mutants tested here are destabilized compared to wild-type myoc-OLF, includung D380A, which is associated with a mild OAG phenotype. Wild-type and mutant OLFs are stabilized by osmolytes, with several compounds capable of restoring mutant myocilin stability to an extent near wild-type. Our results further suggest that screening a library of potentially stabilizing compounds first against wild-type myoc-OLF, either as the readily available MBP fusion or in the cleaved form, will identify compounds of potential therapeutic interest that can then be tested in a more focused way on mutant myocilins associated with inherited OAG. These initial stability tests can then be followed by cellular studies to test for enhanced secretion. Small molecules capable of stabilizing myocilin hold promise for delaying the associated autosomal-dominant inherited forms of glaucoma, for which no specific treatment currently exists.

2.3 Methods

2.3.1 Molecular Biology

The OLF construct of the myocilin gene (myoc-OLF) was first amplified (5-PRIME Master Mix, Fisher Scientific) from a plasmid reported previously [147] and annealed into the pET-30 Xa/LIC vector (Novagen). Attempts to express the pET-30Xa/LIC OLF plasmid in *E. coli* did not yield sufficient soluble protein (not shown). OLF was then amplified from pET-30 Xa/LIC (retaining the N-terminal Factor Xa cleavage site) and ligated (Roche Quick Ligation Kit) into the pMAL-c4x vector using SacI and EcoRI (New England Biolabs) restriction sites, respectively. Primers used are listed in Table 2.4. The final pMAL-c4x construct incorporates an 8-amino acid linker between MBP and OLF (SSSEIGR), where the Factor Xa cleavage sequence is leftover from pET-30 Xa/LIC. After transformation into NovaBlue Gigasingles (Novagen) and overnight growth, the plasmid was isolated (Qiagen QIAPrep). Four mutant MYOC-OLF, constructs were generated by site directed mutagenesis (Stratagene QuikChange) according to the manufacturer's instructions. Each mutant was amplified from the wild-type OLF pMAL-c4x plasmid with complementary mutagenesis primers. After treatment with Dpn I to remove the parental strand, transformation into XL1-Blue cells and overnight growth, the mutant plasmid was isolated. Primers used in this study appear in Table 2.4. All plasmids were verified by DNA sequencing (MWG/Operon).

2.3.2 Protein Expression and Purification

Wild type and mutant plasmids were transformed into Rosetta-gami 2(DE3)pLysS (Novagen) cells for protein expression. Cells were cultured in Superior Broth (US

Table 2.4. Primers used in this study.

Plasmid Template	Target Vector		Primer Used
			Myoc-OLF cloning
pcDNA	pET - 30XaLIC	Forward	5’-GGTATTGAGGGTCGCTTGAAGGAGAGCCCATCTG
		Reverse	5’-AGAGGAGAGTTAGAGCCTTATCACATCTTGGAGAGCTTGATG
pET-30XaLIC	pMAL-c4x	Forward	5’-CGCCGAGCTCTATTGAGGGTCGC
		Reverse	5’-GCCGAATTCAGGAGAGTTAGAGCCTTATCA
			Mutagenesis
D380A			5’-GCTACACGGACATTGCCTTGGCTGTGGATG
K423E			5’-GGGAGACAAACATCCGTGAACAGTCAGTCGCCAATGCC
I477N			5’-GTACAGCAGCATGAATGACTACAACCCCCTGG
I477S			5’-GTACAGCAGCATGTCTGACTACAACCCCCTCG

Biological) to an optical density of 0.6 to 0.8 at 600 nm, cooled to 18 °C, and induced with 0.5 mM isopropyl β-D-thiogalactopyranoside (IPTG). They were grown overnight for 12-16 hours, pelleted by centrifugation, flash frozen with liquid nitrogen and stored at -80 °C. Cell pellets were lysed either by sonication or by French Press in the presence of 50 mM HEPES pH 7.5, 200 mM NaCl, 1 mM EDTA (Buffer A), supplemented with Roche Complete Protease Inhibitor. Cell debris was removed by centrifugation (5000 x g for 15 min) and supernatant loaded onto a 20 mL High Flow Amylose Resin (New England Biolabs) column equilibrated with Buffer A. The MBP-OLF protein was eluted with lysis buffer supplemented with 10 mM maltose, concentrated using an Amicon Ultra YM-10 or -30 centrifugation device, and either frozen in liquid nitrogen and stored at -80 °C, or further purified by gel filtration.

Gel filtration was carried out on a Superdex 75 Prep Grade resin equilibrated with 10 mM Phosphate (Na/K), 200 mM NaCl, pH 7.2 (Buffer B). Care was taken so that only those fractions corresponding to monomeric MBP-OLF were pooled and concentrated for further use. Samples were stored either at 4 °C or at -80 °C.

Cleavage was accomplished by overnight (~ 12 h) incubation with Factor Xa (New England Biolabs, 10 μg Factor Xa : 50 μg purified MBP-OLF) in 50 mM Tris pH 8, 100 mM NaCl, 5 mM $CaCl_2$. After capture of Factor Xa (Xarrest, Novagen), cleaved OLF was fractionated from uncleaved material and MBP by Superdex 75 prepared as above. MBP used in these studies were isolated from this cleavage protocol. Purified protein was either flash frozen in liquid nitrogen or stored at 4 °C. Samples were tested for melting properties within one week.

2.3.3 Disulfide Characterization

The oxidation state of the two cysteines present in wild type OLF, as well as the OLF mutants, was determined by utilizing a maleimide fluorogenic SH reagent, ThioGlo® 1 (Calbiochem). A stock solution of ThioGlo® 1 was prepared by dilution in

DMSO to a final concentration of 10 mM. ThioGlo® 1 was further diluted to 20 μM in Buffer B, along with 1-2 μM OLF with and without 5 mM tris(2-carboxyethyl)phosphine HCl (TCEP; Thermo Scientific). Fluorescence emission spectra of cysteine– ThioGlo® 1 protein adducts were recorded using excitation and emission wavelengths of 379 and 513 nm respectively, using a Shimadzu RF-5301 PC spectrofluorophotometer.

2.3.4 Circular Dichroism

Prior to CD scans, monomeric MBP-OLF samples were purified on an analytical Superdex 75 GL column and concentrated to 0.25-0.5 μM. CD spectra were acquired at 25 °C on a Jasco J-810 CD spectropolarimeter. Twenty consecutive scans ranging from 200 nm to 300 nm, using a bandwidth of 1 nm at a continuous scanning rate of 500 nm/min, were averaged for each sample.

2.3.5 *In Vitro* Thermal Stability Assay

The fluorescence stability assay was adapted from a thermal shift assay reported previously [148]. Sypro Orange dye (Invitrogen) was used to monitor the relative exposed hydrophobic protein regions. The dye, which is supplied as a 5,000X solution in DMSO, was diluted in the buffer solution (1:1000) and mixed well just prior to preparing samples for the assay. Total reaction volumes of 30 μL were prepared at room temperature and delivered to 96-well optical plates (Applied Biosystems) before sealing with optical film. To the protein solution (maltose binding protein, wild-type OLF cleaved or uncleaved, and mutant MBP-OLF) at a final concentration of 0.5-1.5 μM in Buffer B, 3 μL of diluted Sypro Orange were added. Except when indicated otherwise, maltose was added to a final concentration of 50 mM. Compounds tested for stability enhancement include betaine (trimethylglycine), glycerol, sucrose, TMAO, sarcosine (methylglycine), and 4-PBA, which were obtained from commercial sources. TMAO and sarcosine were tested at a final concentration of 5 M in the reaction buffer, and 4-PBA

was tested in a concentration range of 1 mM to 0.5 M. All others were tested at 3 M by diluting 5 M stock solutions in Buffer B. Test proteins citrate synthase and lysozyme were obtained in purified form from Sigma. All plates included a baseline blank control containing diluted Sypro Orange with no protein. The pH of the final solutions did not deviate significantly from 7.

Fluorescence data were acquired on an Applied Biosciences Step-One Plus RT-PCR instrument, which is equipped with fixed excitation wavelength (480 nm) and optional ROX® emission filter (610 nm) that can be used without a passive reference. Denaturation curves were conducted in the range of 25-95 °C at a rate of 1 °C per min, as no difference in T_m was observed when the rate of heating was decreased to 0.5 °C per min. In addition, above a minimum threshold of protein concentration required to observe a discrete transition, no dependence of protein concentration on T_m was observed. Data were processed using GraphPad Prism software. After baseline subtraction, data were trimmed to include the boundaries and the melting transition of interest and normalized. The reported melting temperature is the inflection point of the sigmoidal curve, which was fit as described previously [148].

CHAPTER 3

BIOPHYSICAL CHARACTERIZATION OF THE OLFACTOMEDIN DOMAIN OF MYOCILIN

3.1 Introduction

Myocilin, the protein most closely associated with inherited forms of open angle glaucoma (OAG) through genetic linkage studies, is a ~57 kDa glycoprotein composed of a secretion signal sequence, coiled-coil region, and a ~30 kDa olfactomedin (OLF) domain (Figure 3.1), which harbors 90% of all reported pathogenic lesions [110]. The molecular mechanisms that lead to glaucoma are not well established but are of significant biomedical interest given that glaucoma is a leading cause of blindness worldwide, and early-onset myocilin glaucoma accounts for 4% of glaucoma cases, primarily afflicting children.

Wild-type (WT) myocilin is secreted from human trabecular meshwork (HTM) cells to the trabecular meshwork extracellular matrix (TEM) [114, 175-176], the anatomical region believed to regulate intraocular pressure [114, 116]. By contrast, mutant myocilins aggregate in the endoplasmic reticulum (ER), leading to cell death and a malfunctioning matrix. The net result is an increase in intraocular pressure and retina degeneration, a hallmark of glaucoma [108]. Defects in protein stability and trafficking that lead to this gain-of-toxic-function have been shown to underlie the pathophysiology of myocilin glaucoma [121-122]. Temperature-sensitive secretion of some myocilin variants [125-126] indicates that when protein production is slowed, some mutant proteins appear native-like and competent for trafficking out of the cell and to the TEM. In cell culture, the toxicity of mutant myocilins can be reduced by the addition of certain chemical chaperones [174, 177], and in vitro, the compromised stability of mutant myoc-OLFs can be restored with some of the same compounds [178].

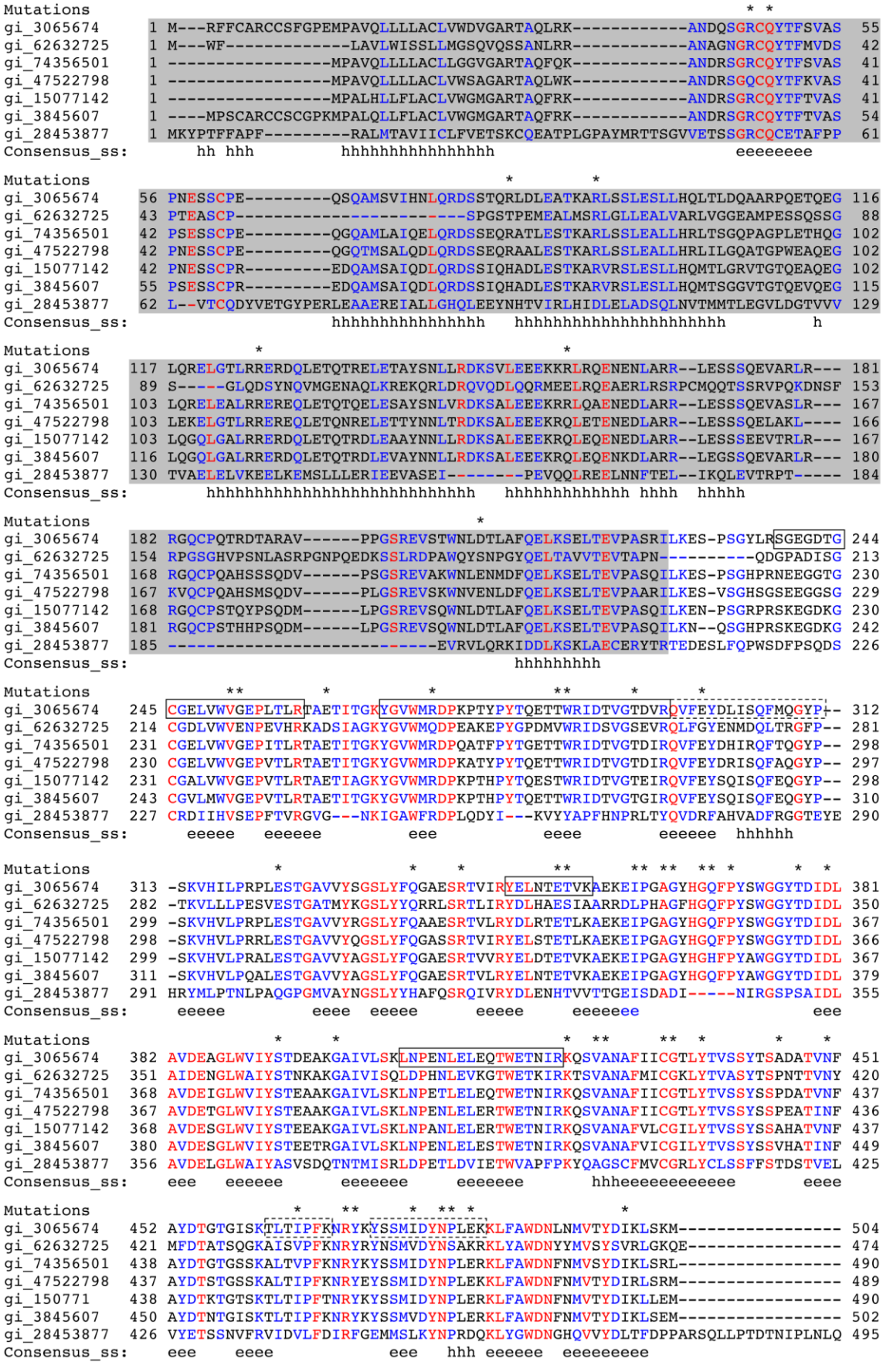
Mutations
gi_3065674 1 M---RFFCARCCSFGPEMPAVQLLLLACLVWDVGARTAQLRK----------ANDQSGRCQYTFSVAS 55
gi_62632725 1 M---WF----------LAVLWISSLLMGSQVQSSANLRR----------ANAGNGRCQYTFMVDS 42
gi_74356501 1 ----------MPAVQLLLLACLLGGVGARTAQFQK----------ANDRSGRCQYTFSVAS 41
gi_47522798 1 ----------MPAVQLLLLACLVWSAGARTAQLWK----------ANDRSGQCQYTFKVAS 41
gi_15077142 1 ----------MPALHLLFLACLVWGMGARTAQFRK----------ANDRSGRCQYTFTVAS 41
gi_3845607 1 ----MPSCARCCSCGPKMPALQLLFLACLVWGMGARTAQFRK----------ANDRSGRCQYTFTVAS 54
gi_28453877 1 MKYPTFFAPF---------RALMTAVIICLFVETSKCQEATPLGPAYMRTTSGVVETSSGRCQCETAFPP 61
Consensus_ss: hh hhh hhhhhhhhhhhhhhh eeeeeeee
Mutations
gi_3065674 56 PNESSCPE---------QSQAMSVIHNLQRDSSTQRLDLEATKARLSSLESLLHQLTLDQAARPQETQEG 116
gi_62632725 43 PTEASCP----------SPGSTPEMEALMSRLGLLEALVARLVGGEAMPESSQSSG 88
gi_74356501 42 PSESSCPE---------QGQAMLAIQELQRDSSEQRATLESTKARLSSLEALLHRLTSGQPAGPLETHQG 102
gi_47522798 42 PNESSCPE---------QGQTMSALQDLQRDSSEQRAALESTKARLSSLEALLHRLILGQATGPWEAQEG 102
gi_15077142 42 PNESSCPR---------EDQAMSAIQDLQRDSSIQHADLESTKARVRSLESLLHQMTLGRVTGTQEAQEG 102
gi_3845607 55 PSESSCPR---------EDQAMSAIQDLQRDSSIQHADLESTKARVRSLESLLHQMTSGGVTGTQEVQEG 115
gi_28453877 62 L--VTCQDYVETGYPERLEAAEREIALLGHQLEEYNHTVIRLHIDLELADSQLNVTMMTLEGVLDGTVVV 129
Consensus_ss: hhhhhhhhhhhhhhhh hhhhhhhhhhhhhhhhhhhhhh h
Mutations
gi_3065674 117 LQRELGTLRRERDQLETQTRELETAYSNLLRDKSVLEEEKKRLRQENENLARR--LESSSQEVARLR--- 181
gi_62632725 89 S-----GLQDSYNQVMGENAQLKREKQRLDRQVQDLQQRMEELRQEAERLRSRPCMQQTSSRVPQKDNSF 153
gi_74356501 103 LQRELEALRREREQLETQTQELESAYSNLVRDKSALEEEKRRLQAENEDLARR--LESSSQEVASLR--- 167
gi_47522798 103 LEKELGTLRREREQLETQNRELETTYNNLTRDKSALEEEKRQLETENEDLARR--LESSSQELAKL---- 166
gi_15077142 103 LQGQLGALRRERDQLETQTRDLEAAYNNLLRDKSALEEEKRQLEQENEDLARR--LESSSEEVTRLR--- 167
gi_3845607 116 LQGQLGALRRERDQLETQTRDLEVAYNNLLRDKSALEEEKRQLEQENKDLARR--LEGSSQEVARLR--- 180
gi_28453877 130 TVAELELVKEELKEMSLLLERIEEVASEI-------PEVQQLREELNNFTEL--IKQLEVTRPT----- 184
Consensus_ss: hhhhhhhhhhhhhhhhhhhhhhhhhhhh hhhhhhhhhhhhh hhhh hhhhh
Mutations
gi_3065674 182 RGQCPQTRDTARAV------PPGSREVSTWNLDTLAFQELKSELTEVPASRILKES-PSGYLRSGEGDTG 244
gi_62632725 154 RPGSGHVPSNLASRPGNPQEDKSSLRDPAWQYSNPGYQELTAVVTEVTAPN----------QDGPADISG 213
gi_74356501 168 RGQCPQAHSSSQDV------PSGSREVAKWNLENMDFQELKSELTEVPASQILKES-PSGHPRNEEGGTG 230
gi_47522798 167 KVQCPQAHSMSQDV------PLGSREVSKWNVENLDFQELKSELTEVPAARILKES-VSGHSGSEEGGSG 229
gi_15077142 168 RGQCPSTQYPSQDM------LPGSREVSQWNLDTLAFQELKSELTEVPASQILKEN-PSGRPRSKEGDKG 230
gi_3845607 181 RGQCPSTHHPSQDM------LPGSREVSQWNLDTLAFQELKSELTEVPASQILKN--QSGHPRSKEGDKG 242
gi_28453877 185 ----------EVRVLQRKIDDLKSKLAECERYTRTEDESLFQPWSDFPSQDS 226
Consensus_ss: hhhhhhhhh
Mutations
gi_3065674 245 CGELVWVGEPLTLRTAETITGKYGVWMRDPKPTYPYTQETTWRIDTVGTDVRQVFEYDLISQFMQGYP-- 312
gi_62632725 214 CGDLVWVENPEVHRKADSIAGKYGVWMQDPEAKEPYGPDMVWRIDSVGSEVRQLFGYENMDQLTRGFP-- 281
gi_74356501 231 CGELVWVGEPITLRTAETITGKYGVWMRDPQATFPYTGETTWRIDTVGTDIRQVFEYDHIRQFTQGYP-- 298
gi_47522798 230 CGELVWVGEPVTLRTAETITGKYGVWMRDPKATYPYTQETTWRIDTVGTDIRQVFEYDRISQFAQGYP-- 297
gi_15077142 231 CGALVWVGEPVTLRTAETIAGKYGVWMRDPKPTHPYTQESTWRIDTVGTEIRQVFEYSQISQFEQGYP-- 298
gi_3845607 243 CGVLMWVGEPVTLRTAETITGKYGVWMRDPKPTHPYTQETTWRIDTVGTGIRQVFEYSQISQFEQGYP-- 310
gi_28453877 227 CRDIIHVSEPFTVRGVG---NKIGAWFRDPLQDYI---KVYYAPFHNPRLTYQVDRFAHVADFRGGTEYE 290
Consensus_ss: eeeee eeeeee eee eeee eeeeee hhhhhh
Mutations
gi_3065674 313 -SKVHILPRPLESTGAVVYSGSLYFQGAESRTVIRYELNTETVKAEKEIPGAGYHGQFPYSWGGYTDIDL 381
gi_62632725 282 -TKVLLLPESVESTGATMYKGSLYYQRRLSRTLIRYDLHAESIAARRDLPHAGFHGQFPYSWGGYTDIDL 350
gi_74356501 299 -SKVHVLPRPLESTGAVVYRGSLYFQAAESRTVLRYDLRTETLKAEKEIPGAGYHGQFPYSWGGYTDIDL 367
gi_47522798 298 -SKVHVLPRRLESTGAVVYQGSLYFQGASSRTVIRYELSTETLKAEKEIPGAGYHGQFPYSWGGYTDIDL 366
gi_15077142 299 -SKVHVLPRALESTGAVVYAGSLYFQGAESRTVVRYELDTETVKAEKEIPGAGYHGHFPYAWGGYTDIDL 367
gi_3845607 311 -SKVHVLPQALESTGAVVYAGSLYFQGAESRTVLRYELNTETVKAEKEIPGAGYHGQFPYAWGGYTDIDL 379
gi_28453877 291 HRYMLPTNLPAQGPGMVAYNGSLYYHAFQSRQIVRYDLENHTVVTTGEISDADI-----NIRGSPSAIDL 355
Consensus_ss: eeeee eeee eeeee eeeee eeeeeee eee
Mutations
gi_3065674 382 AVDEAGLWVIYSTDEAKGAIVLSKLNPENLELEQTWETNIRKQSVANAFIICGTLYTVSSYTSADATVNF 451
gi_62632725 351 AIDENGLWAIYSTNKAKGAIVISQLDPHNLEVKGTWETKIRKTSVANAFMICGKLYTVASYTSPNTTVNY 420
gi_74356501 368 AVDEIGLWVIYSTEAAKGAIVLSKLNPETLELEQTWETNIRKQSVANAFIICGTLYTVSSYSSPDATVNF 437
gi_47522798 367 AVDETGLWVIYSTEAAKGAIVLSKLNPENLELERTWETNIRKQSVANAFIICGTLYTVSSYSSPEATINF 436
gi_15077142 368 AVDESGLWVIYSTEEAKGAIVLSKLNPANLELERTWETNIRKQSVANAFVLCGILYTVSSYSSAHATVNF 437
gi_3845607 380 AVDESGLWVIYSTEETRGAIVLSKLNPENLELESTWETNIRKQSVANAFVICGILYTVSSYSSVHATINF 449
gi_28453877 356 AVDELGLWAIYASVSDQTNTMISRLDPETLDVIETWVAPFPKYQAGSCFMVCGRLYCLSSFFSTDSTVEL 425
Consensus_ss: eee eeeeee eeeeeee eeeeeee hhheeeeeeeeeeee eeee
Mutations
gi_3065674 452 AYDTGTGISKTLTIPFKNRYKYSSMIDYNPLEKKLFAWDNLNMVTYDIKLSKM---------------- 504
gi_62632725 421 MFDTATSQGKAISVPFKNRYRYNSMVDYNSAKRKLYAWDNYYMVSYSVRLGKQE---------------- 474
gi_74356501 438 AYDTGTGSSKALTVPFKNRYKYSSMIDYNPLERKLFAWDNFNMVSYDIKLSRL---------------- 490
gi_47522798 437 AYDTSTGSSKALTIPFKNRYEYSSMIDYNPLEKKLFAWDNFNMVTYDIRLSRM---------------- 489
gi_150771 438 AYDTKTGTSKTLTIPFTNRYKYSSMIDYNPLERKLFAWDNFNMVTYDIKLLEM---------------- 490
gi_3845607 450 AYDTNTGISKTLTIPFKNRYKYSSMVDYNPLERKLFAWDNFNMVTYDIKLSEM---------------- 502
gi_28453877 426 VYETSSNVFRVIDVLFDIRFGEMMSLKYNPRDQKLYGWDNGHQVVYDLTFDPPARSQLLPTDTNIPLNLQ 495
Consensus_ss: eee eeee eee hhh eeeeee eeeeeeeee

Figure 3.1. Multiple sequence alignment for myocilin and non-ocular ortholog amassin. Alignment includes myocilin from *H. sapiens* (gi 3065674), *D. rerio* (gi 62632725), *B. taurus* (gi 74356501), *S. scrofa* (gi 47522798), *M. musculus* (gi 15077142), *R. norvegicus* (gi 3845607), and amassin from *S. purpuratus* (gi 28453877). The region shaded in grey contains the N-terminal signal sequence and coiled-coil region, whereas the OLF domain remains unshaded. The consensus predicted secondary structures are shown in the last line (h, alpha-helix; e, beta-strand). Blue, similar residues; red, conserved residues; asterisk, reported disease-causing mutation in human myocilin [179]. The alignment and predicted secondary structure were generated using PROMALS [180]. Solid black boxes enclose peptides identified in both core-OLF and myoc-OLF by mass spectrometry; whereas dashed boxes enclose peptides identified only in myoc-OLF (see text).

In spite of the importance of myocilin in inherited glaucoma pathogenesis, little is known about its normal biological function in the TEM, especially the OLF (myoc-OLF) domain. Full-length myocilin has been shown to bind to TEM proteins such as laminin and the Hep II domain of fibronectin [181-182], as well as the glycosaminoglycan (GAG) heparan sulfate, but these interactions are localized to the coiled-coil region of myocilin, and not myoc-OLF [113]. The normal biological roles of myocilin are further complicated by reports of myocilin localized to the mitochondria of HTM cells [175, 183], calpain-II dependent cleavage prior to secretion [184], as well as its expression in other ocular tissues including sclera, ciliary body, iris, retina and optic nerve head [185]. Moreover, beyond the eye, OLF domains are found in numerous multicellular organisms, and more than half of reported OLF domains are found in neural tissues. OLF domains are proposed to play roles in neurogensis, neural crest formation, dorsal ventral patterning, cell-cell adhesion, cell-cycle regulation, cell-cell signaling, tumorigenesis, and have been implicated in psychiatric disorders [119]. The explicit roles of myocilin in any of these tissues and processes, however, are not clear due to a lack of functional assays.

The objective of this study is to probe the molecular properties of myoc-OLF to gain insight into its function and structure. The study was enabled by our recent development of a preparative *in vitro* expression system in which myoc-OLF is closely fused to a cleavable maltose binding protein (MBP) [178]. Our current work places the OLF domain for the first time in the context of other known proteins. The analysis of myoc-OLF described herein also provides a biophysical basis for the development of a new therapeutic avenue for glaucoma in the context of a protein conformational disorder.

3.2 Results

3.2.1 pH Stability Profile of Myoc-OLF

We investigated the pH stability profile of myoc-OLF to elucidate any preferences of this domain as well as to gain insight into its resilience under different pH environments, such as low pH, that might be encountered under a known age-related TEM stressor, oxidative stress [186]. For the broad 96-well pH screen, we used the MBP-OLF fusion protein and adapted the differential scanning fluorimetry (DSF) technique used originally to assess thermal stability differences between WT and glaucoma-causing myoc-OLF variants [178]. The melting of MBP is deconvoluted from the melting of OLF by the addition of 50 mM maltose. The melting curves of MBP and OLF are readily distinguished in the stability assay throughout the pH range tested. MBP is stable from pH 4-10.5 [154], OLF is not affected by the presence of maltose [178], and Sypro Orange is not pH sensitive in the range 4-10 (not shown).

To cross-validate the results obtained using the MBP-OLF fusion protein, we subsequently tested cleaved myoc-OLF in a subset of stabilizing and destabilizing buffers (Table 3.1). There was no difference in melting temperature (T_m) between the MBP-OLF and cleaved myoc-OLF among the pHs tested (Table 3.1), reinforcing the independence of the domains in the fusion protein. Interestingly, myoc-OLF is stable in 100 mM buffers corresponding to a range in pH of 4.6 to 7.4, but specifically in sodium lactate, acetate, MES, phosphate and Hepes (Table 3.1-3.2). Bicine at pH 7.0 and glycine at pH 8.2 were also stabilizing buffers, albeit within a more limited pH range (Table 3.1-3.2). By contrast, OLF was destabilized in pH 4.0-4.6, as well as the full pH range tested of Bis-Tris, Imidazole, Tris, and CHES buffers (Table 3.1-3.2).

The concentration dependence of buffer stabilization or destabilization was further investigated using acetate buffer pH 4.6 or Tris buffer pH 7.5 as examples, respectively (Table 3.1). Myoc-OLF is more stable in 10 mM Tris pH 7.5 compared to

Table 3.1. Melting temperature of myoc-OLF and MBP-OLF in buffer.

Concentration	Buffer	pH	myoc-OLF T_m (°C)	MBP-OLF T_m (°C)	Δ T_m (°C) (myoc-OLF - MBP-OLF)
100 mM	Sodium Lactate/HCl	4.0		39.4 ± 0.5	
100 mM	Sodium Lactate/HCl	4.4		47.1 ± 0.3	
100 mM	Sodium Lactate/HCl	4.8		52.2 ± 0.0	
100 mM	Sodium Lactate/HCl	5.2		55.4 ± 0.1	
100 mM	Sodium Acetate/Acetic Acid	4.2	47.7 ± 0.0	47.6 ± 0.5	0.1
10 mM	**Sodium Acetate/Acetic Acid**	**4.6**	**49.8 ± 0.2**		
100 mM	Sodium Acetate/Acetic Acid	4.6	51.9 ± 0.3	50.8 ± 0.2	1.0
100 mM	Sodium Acetate/Acetic Acid	5.0	54.8 ± 0.3	54.0 ± 0.0	0.8
100 mM	Sodium Acetate/Acetic Acid	5.4	56.5 ± 0.4	55.8 ± 0.1	0.7
100 mM	Sodium Acetate/Acetic Acid	5.8	57.3 ± 0.1	56.2 ± 0.0	1.1
100 mM	Sodium Acetate/Acetic Acid	6.2	56.6 ± 0.0	55.7 ± 0.2	0.9
100 mM	MES/ NaOH	5.0	51.5 ± 0.2	51.3 ± 0.1	0.2
100 mM	MES/ NaOH	5.4	53.8 ± 0.1	53.3 ± 0.1	0.5
100 mM	MES/ NaOH	5.8	55.6 ± 0.1	54.7 ± 0.1	0.9
100 mM	MES/ NaOH	6.2	55.8 ± 0.3	54.6 ± 0.0	1.2
100 mM	MES/ NaOH	6.6	54.8 ± 0.2	53.9 ± 0.2	0.9
100 mM	MES/ NaOH	7.0	53.2 ± 0.2	53.0 ± 0.1	0.3
100 mM	MES/ NaOH	7.4	51.9 ± 0.0	52.1 ± 0.1	-0.1
100 mM	Bis-Tris/HCl	5.2		49.3 ± 0.1	
100 mM	Bis-Tris/HCl	5.6		50.8 ± 0.4	
100 mM	Bis-Tris/HCl	6.0		50.1 ± 0.1	
100 mM	Bis-Tris/HCl	6.4		48.6 ± 0.0	
100 mM	Bis-Tris/HCl	6.8		47.5 ± 0.2	
100 mM	Bis-Tris/HCl	7.2		46.7 ± 0.3	
100 mM	Bis-Tris/HCl	7.6		46.3 ± 0.1	
100 mM	Bis-Tris/HCl	8.0		46.2 ± 0.2	
100 mM	Imidazole/HCl	5.4		49.5 ± 0.4	
100 mM	Imidazole/HCl	5.8		49.4 ± 0.5	
100 mM	Imidazole/HCl	6.2		48.3 ± 0.5	
100 mM	Imidazole/HCl	6.6		47.0 ± 0.8	
100 mM	Imidazole/HCl	7.0		45.8 ± 0.2	
100 mM	Imidazole/HCl	7.4		45.4 ± 0.5	
100 mM	Imidazole/HCl	7.8		45.5 ± 0.6	
100 mM	Imidazole/HCl	8.2		45.9 ± 1.1	
10 mM	**K_2HPO_4/NaH_2PO_4**	**5.8**	**56.9 ± 0.2**		
100 mM	K_2HPO_4/NaH_2PO_4	5.8	56.1 ± 0.3	54.8 ± 0.0	1.2
100 mM	K_2HPO_4/NaH_2PO_4	6.2	55.2 ± 0.2	54.1 ± 0.1	1.0
100 mM	K_2HPO_4/NaH_2PO_4	6.6	54.3 ± 0.4	53.4 ± 0.1	0.9
100 mM	K_2HPO_4/NaH_2PO_4	7.0	51.8 ± 0.6	52.1 ± 0.3	-0.3
10 mM	**K_2HPO_4/NaH_2PO_4**	**7.2**	**55.3 ± 0.1**		
100 mM	K_2HPO_4/NaH_2PO_4	7.4	50.9 ± 0.9	51.0 ± 0.4	-0.1
100 mM	K_2HPO_4/NaH_2PO_4	7.8	49.3 ± 0.3	49.9 ± 0.0	-0.5
100 mM	K_2HPO_4/NaH_2PO_4	8.2	48.9 ± 0.0	49.4 ± 0.4	-0.4
100 mM	K_2HPO_4/NaH_2PO_4	8.6	48.3 ± 0.5	48.9 ± 0.2	-0.6
100 mM	Hepes/NaOH	6.0	54.3 ± 0.1	53.4 ± 0.0	0.9

100 mM	Hepes/NaOH	6.4	53.5 ± 0.0	52.7 ± 0.1	0.8
100 mM	Hepes/NaOH	6.8	52.2 ± 0.1	52.3 ± 0.0	-0.1
100 mM	Hepes/NaOH	7.2	51.2 ± 0.3	51.1 ± 0.1	0.1
100 mM	Hepes/NaOH	7.6	49.9 ± 0.3	50.4 ± 0.1	-0.5
100 mM	Hepes/NaOH	8.0	49.7 ± 0.3	49.7 ± 0.1	0.0
100 mM	Hepes/NaOH	8.4	48.9 ± 0.2	49.2 ± 0.1	-0.3
100 mM	Tris/HCl	6.6		48.0 ± 0.0	
100 mM	Tris/HCl	7.0		46.3 ± 0.5	
100 mM	Tris/HCl	7.4		44.7 ± 0.3	
100 mM	Tris/HCl	7.5	44.5 ± 0.1		
10 mM	Tris/HCl + 200 mM NaCl	7.5	52.4 ± 0.1		
100 mM	Tris/Cl + 200 mM NaCl	7.5	50.9 ± 0.1		
100 mM	Tris/HCl	7.8		45.1 ± 1.6	
100 mM	Tris/HCl	8.2		43.5 ± 0.1	
100 mM	Tris/HCl	8.6		43.8 ± 0.1	
100 mM	Bicine/NaOH	7.0	51.9 ± 0.3	52.2 ± 0.0	-0.2
100 mM	Bicine/NaOH	7.4	50.0 ± 0.0	50.4 ± 0.6	-0.4
100 mM	Bicine/NaOH	7.8	48.5 ± 0.7	48.7 ± 0.1	-0.2
100 mM	Bicine/NaOH	8.2	47.5 ± 0.7	48.2 ± 0.2	-0.7
100 mM	Bicine/NaOH	8.6	47.2 ± 0.7	47.5 ± 0.3	-0.4
50 mM	CHES/NaOH	8.0		50.0 ± 0.7	
50 mM	CHES/NaOH	8.4		48.3 ± 0.3	
50 mM	CHES/NaOH	8.8		47.0 ± 0.3	
100 mM	Glycine/NaOH	8.2	51.3 ± 0.0	52.3 ± 0.6	-1.0
100 mM	Glycine/NaOH	8.6	47.9 ± 0.1	47.5 ± 0.1	0.3

Table 3.2. Summary of stabilization of myoc-OLF by buffers of varying pH.

Buffer	**pH range**	**Stabilizing Buffer[a]**
Sodium Lactate/HCl	4.0-4.4	No
Sodium Lactate/HCl	**4.8-5.2**	**Yes**
Sodium Acetate/Acetic Acid	4.2	No
Sodium Acetate/Acetic Acid	**4.6-6.2**	**Yes**
MES/ NaOH	**5.0-7.4**	**Yes**
Bis-Tris/HCl	5.2-8.0	No
Imidazole/HCl	5.4-8.2	No
K_2HPO_4/NaH_2PO_4	**5.8-7.4**	**Yes**
K_2HPO_4/NaH_2PO_4	7.8-8.6	No
Hepes/NaOH	**6.0-7.2**	**Yes**
Hepes/NaOH	7.6-8.4	No
Tris/HCl	6.6-8.6	No
Bicine/NaOH	**7.0**	**Yes**
Bicine/NaOH	7.2-8.6	No
CHES/NaOH*	8.0-8.8	No
Glycine/NaOH	**8.2**	**Yes**
Glycine/NaOH	8.6	No

[a]No: T_m < 51.7 °C; Yes: T_m > 51.7 °C. The lower limit cutoff is 1 °C less than the originally reported T_m of myoc-OLF in phosphate buffer, using DSF [178]. Full data are presented in Table 3.1.

100 mM Tris pH 7.5. For Tris buffer, increasing the ionic strength by the addition of NaCl partially restores stability, suggesting that counterions may play a role in this buffer system. Conversely, for acetate buffer pH 4.6, a further increase of 2 °C in the T_m value for myoc-OLF is observed when 100 mM acetate buffer pH 4.6 is used compared to 10 mM (Table 3.1), with no additional effects due to the presence of NaCl.

Finally, to evaluate any further possible effects of counterions, a variety of salts (50 mM) were added to MBP-OLF in stabilizing buffers, specifically acetate pH 5.8, MES pH 6.6, phosphate 5.8, or Hepes pH 6.4, and the melting temperatures were calculated and compared (Table 3.3). Overall, the addition of counterions produced negligible to minor stabilizing effects. Magnesium salts consistently stabilized MBP-OLF by 1-4 °C whereas potassium phosphate dibasic had a destabilizing effect in acetate and MES buffers. Zinc acetate in all buffers and ammonium chloride in acetate yielded poor spectrums. Only one melt transition was observed for calcium chloride in all buffers tested, indicating either a complete destabilization of OLF or a possible overlap between the OLF and MBP melt curves. Further analysis of cleaved myoc-OLF in either 100 mM Tris pH 7.5 or 100 mM Hepes pH 7.5, revealed a substantial increase in the melting temperature (+10 °C) with only 10 mM $CaCl_2$ (Table 3.3).

3.2.2 Stability Analysis in the Presence of GAGs

Interestingly, the preferred buffers for myoc-OLF contain sulfate and acetate functional groups that are reminiscent of GAGs, whereas those that are destabilizing in an overlapping pH range harbor aliphatic amines (Table 3.2). Thus, we sought to evaluate the stability of myoc-OLF in the presence of individual GAGs found in the TEM [187] at physiologically relevant concentrations [188] (Table 3.4). Indeed, a modest (ΔT_m = 4.5 °C) stabilizing effect was observed for myoc-OLF in the presence of a relatively low concentration (0.75 mg/mL) of heparan sulfate, whereas a similar increase in stability for chondroitin sulfate and hyaluronic acid were observed only at higher concentrations of 10

Table 3.3. Melting temperatures of MBP-OLF in stabilizing buffer and salt[a].

	Sodium Acetate, pH 5.8		**MES, pH 6.6**		**K_2HPO_4/NaH_2PO_4, pH 5.8**		**Hepes, pH 6.4**	
	T_m (°C)	Δ T_m (°C)	T_m (°C)	Δ T_m (°C)	T_m (°C)	Δ T_m (°C)	T_m (°C)	Δ T_m (°C)
Ammonium Acetate	56.6	0.9	55.4	0.2	57.1	0.9	55.3	2.2
Magnesium Acetate	57.7	2.0	56.8	1.6	57.6	1.4	57.6	4.4
Sodium Acetate	56.1	0.4	55.8	0.6	57.1	0.9	55.3	2.1
Zinc Acetate Dihydrate	**N/A**	**N/A**	**N/A**	**N/A**	**N/A**	**N/A**	54.6	1.5
Potassium Bromide	55.4	-0.3	55.2	0.0	56.1	-0.1	53.5	0.4
Sodium Bromide	55.5	-0.2	55.2	0.0	55.9	-0.4	53.6	0.5
Ammonium Chloride	**N/A**	**N/A**	54.5	-0.7	56.5	0.3	53.3	0.1
Calcium Chloride[b]	**N/A**	**N/A**	**N/A**	**N/A**	**N/A**	**N/A**	**N/A**	**N/A**
Lithium Chloride	55.4	-0.3	55.0	-0.3	56.4	0.2	52.7	-0.4
Magnesium Chloride	56.4	0.7	56.7	1.5	57.3	1.1	55.3	2.1
Sodium Chloride	55.7	0.0	55.5	0.3	56.7	0.4	53.7	0.5
Sodium Citrate	56.0	0.3	55.2	0.0	56.8	0.5	54.7	1.5
Sodium Fluoride	56.2	0.5	55.5	0.3	57.0	0.8	54.6	1.5
Magnesium Formate	56.9	1.2	57.2	2.0	57.4	1.1	56.8	3.6
Potassium Iodide	55.0	-0.7	55.0	-0.2	56.4	0.2	53.7	0.5
Potassium Phosphate Dibasic	52.2	-3.5	53.0	-2.2	56.4	0.1	53.0	-0.1
Sodium Dihydrogen Phosphate	55.7	0.0	55.6	0.4	57.3	1.0	53.2	0.1
Ammonium Sulfate	55.6	-0.1	56.5	1.3	56.9	0.6	53.2	0.1
Lithium Sulfate	55.6	-0.1	54.0	-1.2	56.9	0.7	53.3	0.1
Potassium Sodium Tartrate	55.7	0.0	55.5	0.3	56.5	0.2	55.1	1.9
Potassium Thiocyanate	54.2	-1.5	54.1	-1.1	55.4	-0.9	52.3	-0.8

[a]Buffer (100 mM) and salt (50 mM) concentrations were consistent throughout the stability assay. ΔT_m represents the difference between T_m with and without salt in the specified buffer.

[b]Cleaved myoc-OLF melting temperatures were calculated in the presence of 10 mM $CaCl_2$ to be 60.0 °C (ΔT_m= 15.4 °C) in 100 mM Tris, pH 7.5 and 61.2 °C (ΔT_m= 10.6 °C) in 100 mM Hepes, pH 7.5.

Table 3.4. Stabilization of myoc-OLF by GAGs.

	T_m (°C)	ΔT_m (°C)
None	52.4 ± 0.1	0
Chondroitin Sulfate	57.7 ± 0.0	5.3
Dermatan Sulfate	52.7 ± 0.0	0.3
Heparan Sulfate [a]	57.2 ± 0.0	4.8
Hyaluronic Acid	55.4 ± 0.1	3.0

[a]For these experiments, heparan sulfate concentration was 0.75 mg/mL, whereas all other GAGs were present at 10 mg/mL.

mg/mL, at the outer limit of the physiological range, suggesting a weaker effect. The addition of dermatan sulfate did not change the T_m value of myoc-OLF in the full range tested.

3.2.3 Conformational Analysis of Myoc-OLF at pH 4.6, 5.8, and 7.2

In order to detect structural changes across the stable pH regime, we next compared the secondary structure of myoc-OLF by conducting circular dichroism (CD) melts in stabilizing buffers of varying pH. We measured the CD spectrum in 10 mM acetate buffer pH 4.6, below the calculated [189] pI = ~5 of myoc-OLF, at the lower end of the stable range, as well as in 10 mM phosphate buffer pH 5.8 where OLF was the most stable in our assay (Table 3.1-3.2), and at the physiological pH 7.2 expected in the TEM under normal conditions.

No major changes are observed among the three CD spectra at different pH values. The 200-210 nm range is more positive at pH 4.6 than the others, suggestive of non-native features of OLF in this buffer environment, but otherwise there are only slight differences in the intensity of the two major minima at ~217 and ~230 nm (Figure 3.2A). Component spectra, identified using singular value decomposition (SVD) analysis, reveal three significant spectral contributions. By far the most predominant component is one that contains both minima, followed by two minor contributions from spectra that resemble random coils (Figure 3.2B). Notably, there is no significant contribution from features at 208 nm and/or another at 222 nm; thus, there is no evidence of α-helices in myoc-OLF. The broad ~217 nm minimum, which is characteristic of antiparallel β-sheets, resembles the CD spectrum of a smaller OLF construct expressed in *P. pastoris* [135], but the prominent shoulder near 230 nm has not been seen previously. The lack of this latter feature in the *P. pastoris* OLF construct may have been a result of its N-terminal truncation or the use of Tris pH 8.0 [135], a destabilizing buffer (Table 3.1-3.2).

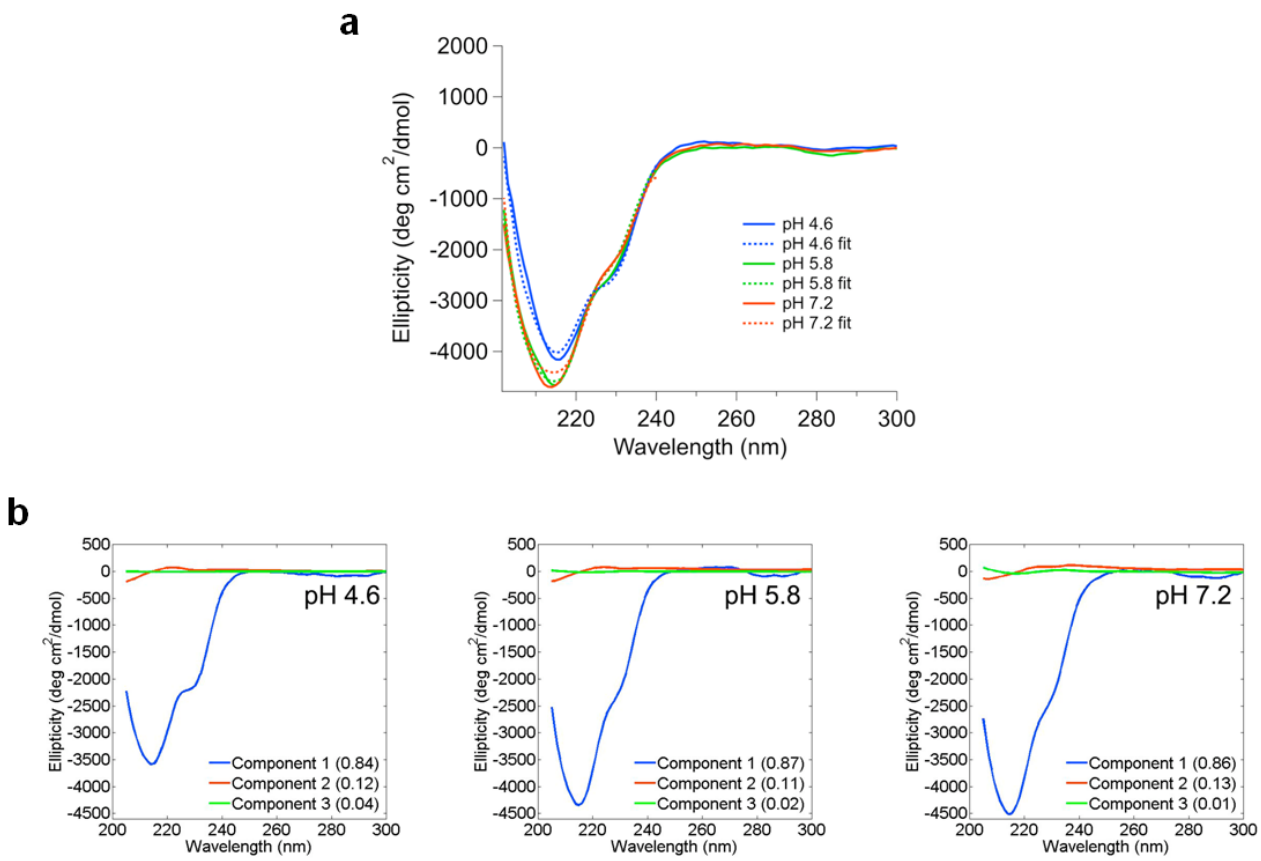

Figure 3.2. CD signatures of myoc-OLF domain at varying pH. A) Prominent minima are observed at ~217 nm and ~230 nm for both experimental spectra (solid) and reconstructed spectral fit from SVD analysis (dashed). B) Top component spectra from SVD analysis. Inset: relative contribution.

Consistent with the aggregation propensity observed in mutants that lead to myocilin glaucoma, the unfolding transitions of myoc-OLF are irreversible. Sample precipitation was seen under all experimental conditions tested, including all concentrations, pH and temperature ranges. Nevertheless, there is substantial evidence [190] for a highly cooperative transition. First, at all three pH values, a sharp transition and similar isodichroic point near 238 nm are observed for myoc-OLF (Figure 3.3). Second, the differences in T_m for the melting curves monitored at the two local minima are consistently within 1 °C of each other, and within error of the fit to the T_m obtained from the Boltzmann sigmoid equation, which assumes a two-state model (Table 3.5). Third, there is no obvious scan rate dependence of denaturation (not shown), suggesting that the melting transition is under thermodynamic, rather than kinetic control. Nevertheless, because we were not able to find experimental conditions of reversibility for myoc-OLF, the extent of the validity of thermodynamic parameters obtained using a two-state model cannot be assessed. We note, however, that thermodynamic parameters we obtained using this assumption with excellent error statistics (Figure 3.4, Table 3.5) are similar to those of α-chymotrypsin [191], a protein that exhibits both similar mass and CD spectrum as myoc-OLF (see Discussion).

The transition to the denatured state for myoc-OLF at pH 4.6 occurs between 40-50 °C (Figure 3.3A). Upon denaturation, the ellipticity is reduced by 50% and there is a shift in minimum at 216 nm in the folded state to 220 nm in the denatured state. SVD deconvolution (not shown) reveals a significant reduction in the β-sheet component and an increase in the random coil component, suggesting the precipitated sample is likely a molten globule with local secondary structure. By comparison, for both unfolding experiments conducted at pH 5.8 (Figure 3.3B) and pH 7.2 (Figure 3.3C), the transition occurs between 50 and 60 °C with a fourfold reduction in signal intensity between folded and unfolded states of myoc-OLF. Less residual secondary structure remaining in these higher pH experiments may be attributed to the difference in net charge per residue. In

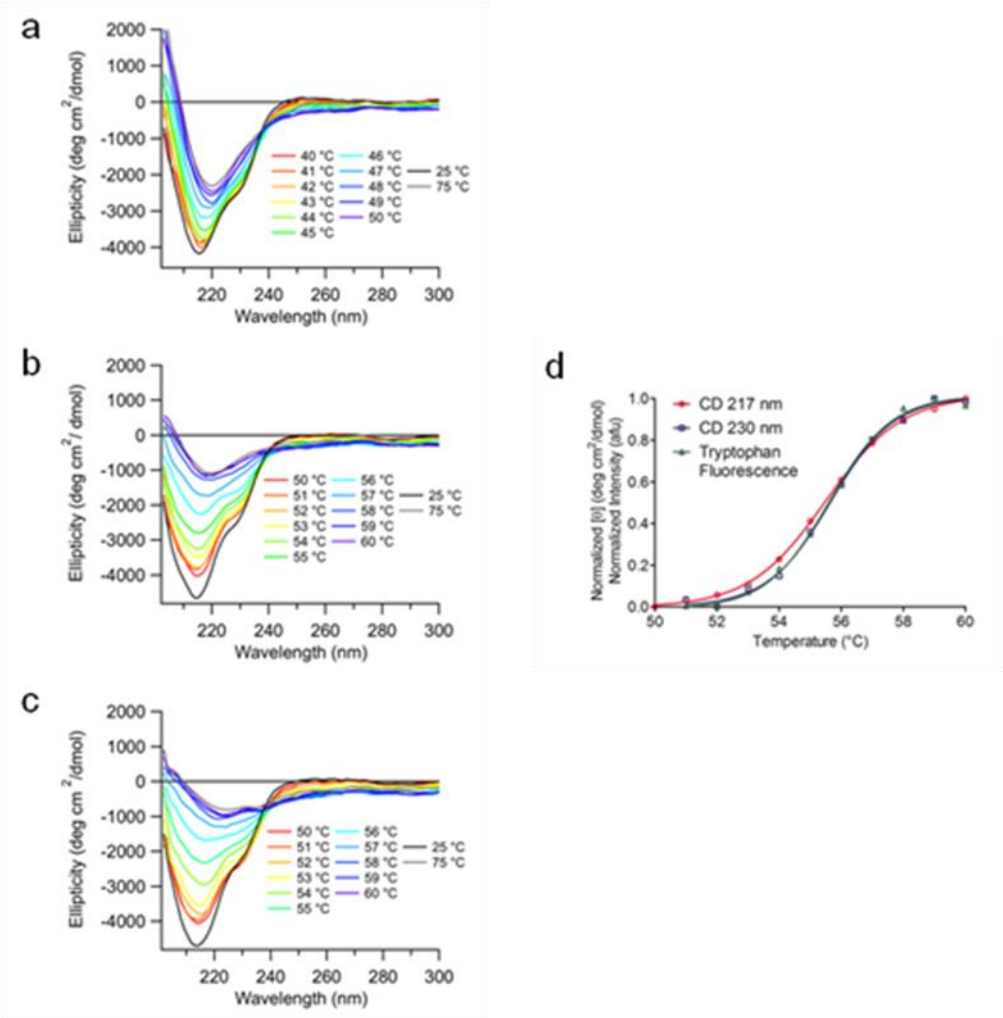

Figure 3.3. Thermal unfolding of myoc-OLF monitored by CD spectropolarimetry. Melts were conducted at (A) pH 4.6 (B) pH 5.8 and (C) pH 7.2. For each, 11 spectra are overlayed in the region of melting as well as two additional extrema. (D) Comparison of tryptophan fluorescence melt with CD melts from above. Each curve is normalized to the range of its respective signal.

Table 3.5. Thermodynamic data for myoc-OLF unfolding assuming a two-state transition.

pH	Technique	Boltzmann Equation		Van't Hoff Equation					
		T_m (°C)	R^2	T_m (°C)	ΔG (37 °C, kcal mol^{-1})	ΔH_m (kcal mol^{-1})	ΔS_m (cal $mol^{-1}K^{-1}$)	R^2	rmse
4.6	CD, 217 nm	46.1 ± 0.1	0.997 ± 0.001	46.5 ± 0.0	3.5 ± 0.4	118.4 ± 13.3	370.5 ± 41.7	0.954 ± 0.037	0.000 ± 0.001
	CD, 230 nm	46.9 ± 0.2	0.997 ± 0.003	47.0 ± 0.7	3.8 ± 0.6	120.9 ± 23.9	378.0 ± 75.0	0.997 ± 0.001	0.014 ± 0.007
5.8	CD, 216 nm	55.3 ± 0.1	0.997 ± 0.000	55.5 ± 0.0	9.0 ± 0.6	158.1 ± 11.0	481.0 ± 33.9	0.920 ± 0.015	0.001 ± 0.001
	CD, 230 nm	56.1 ± 0.1	0.997 ± 0.001	56.5 ± 0.0	9.7 ± 0.4	156.0 ± 8.0	474.0 ± 24.0	0.913 ± 0.017	0.001 ± 0.013
7.2	CD, 214 nm	55.2 ± 0.2	0.998 ± 0.000	55.5 ± 0.0	8.85 ± 1.1	159 ± 22.0	484.0 ± 67.9	0.953 ± 0.014	0.000 ± 0.002
	CD, 229 nm	55.8 ± 0.4	0.997 ± 0.004	56.0 ± 0.7	8.4 ± 0.2	146.4 ± 9.5	445.0 ± 29.7	0.903 ± 0.011	0.009 ± 0.005
	Fluorescence Stability Assay	52.7 ± 0.8	0.998 ± 0.001	N/A	N/A	N/A	N/A	N/A	N/A
	Tryptophan Fluorescence	55.6 ± 0.1	0.998 ± 0.001	55.0 ± 0.0	10.4 ± 0.1	180.5 ± 3.4	548.5 ± 10.6	0.991 ± 0.009	0.015 ± 0.005

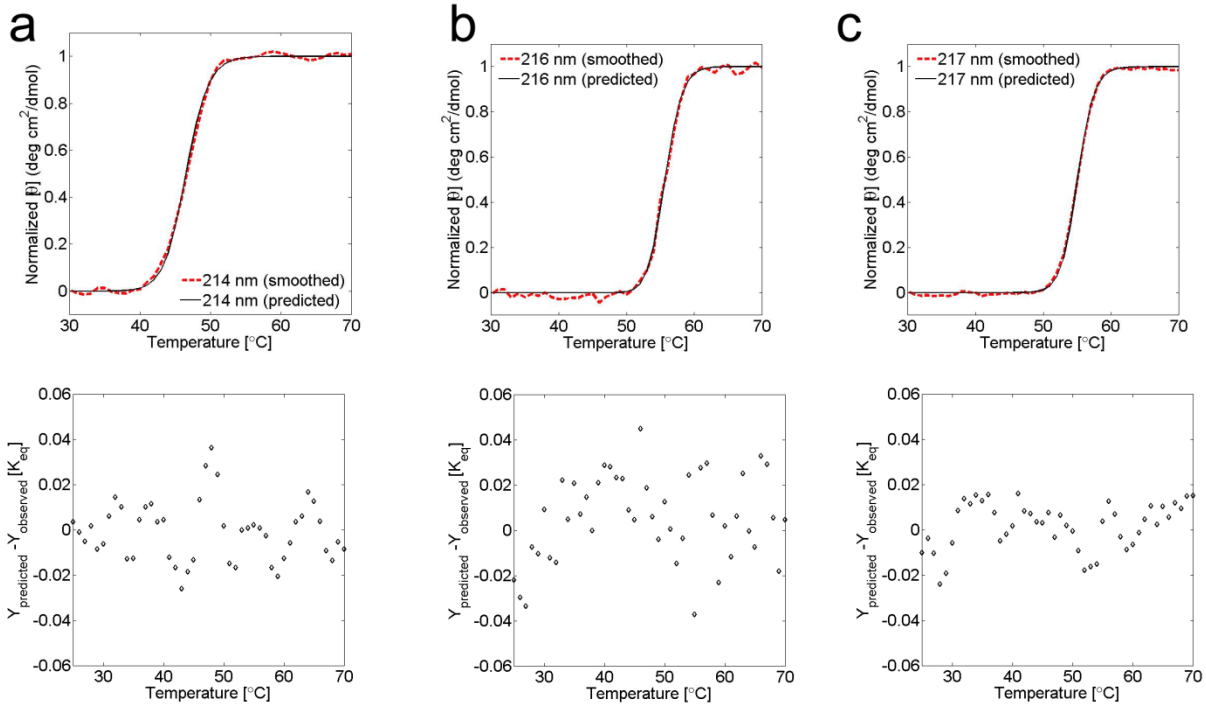

Figure 3.4. Melt data fit to a two-state transition. Melt curves and fitting residuals are presented. (A) pH 4.6, (B) pH 5.8, (C) pH 7.2. See values in Table 3.5.

conditions far from the pI of myoc-OLF, such as at pH 7.2, secondary structure would be expected to be disrupted due to the high net charge per residue. By contrast, at pH 4.6, myoc-OLF is closest to its pI where it may experience less repulsion and therefore retain secondary structure in the denatured state [192].

The T_m of myoc-OLF at pH 4.6 is nearly 10 °C lower than the T_m at pH 5.8 or 7.2, and ~3 °C lower than that measured by DSF using the same ionic strength buffer (Table 3.1). Using a two-state assumption (see caveats above), comparison of the free energy of unfolding, as well as both enthalpy and entropy components, also indicate a lower barrier to unfolding (Table 3.5). Nevertheless, even the values at pH 4.6 are well within parameters obtained from numerous other folded proteins [191]. The thermodynamic values fit for myoc-OLF above its pI indicate a larger energy barrier and more stable protein, consistent with the measured increase in T_m. Finally, the unfolding transition at neutral pH was further corroborated by a thermal melt in which intrinsic tryptophan fluorescence was monitored at pH 7.2 (Figure 3.3D). Indeed, the intrinsic T_m measured by both CD and Trp fluorescence melts is close to the T_m = 52.7 °C we previously reported using the more facile, if indirect, DSF technique [178]. The melting thermogram overlays particularly well with the curve obtained monitoring ~230 nm by CD, suggesting tryptophan residues contribute to this CD signal (see Discussion).

3.2.4 Limits of the Myoc-OLF Core Domain

We subjected myoc-OLF to limited proteolysis to identify its three dimensional core structure(s). In most constructs of myoc-OLF studied in the laboratory, a disulfide bond is formed between the only two available cysteine residues (Cys 245 and Cys 433) [135, 178], which are 189 residues apart. Yet, protein domains are typically composed of ~150 amino acids [193]. It is possible that the two cysteine residues, far apart in sequence, are nevertheless topologically close. This could lead to either two or more smaller structural domains or one larger than average single domain.

Overall, myoc-OLF is resistant to cleavage by proteases at room temperature, including trypsin, α-chymotrypsin, pepsin, and V_8 protease (not shown) suggesting that our construct consisting of residues 228-504 of myocilin, comprises a well folded, ~30 kDa protein. However, incubation with subtilisin A, a non-specific protease that cleaves after large uncharged residues, generated a smaller domain of ~25 kDa (Figure 3.5A). Similar results were obtained with the likewise promiscuous protease papain (not shown). The CD spectrum of core-OLF is similar to that of myoc-OLF with some minor exceptions, a 202 nm shoulder characteristic of a type I β-turn [194], and a more pronounced 230 nm shoulder (Figure 3.5B). As seen previously with myoc-OLF [178], the disulfide bond remains intact in core-OLF. Observed using the thiol-sensitive fluorogenic reagent, ThioGlo (see Materials and Methods), fluorescence increases only in samples in which the disulfide bond in core-OLF has been reduced with tris(2-carboxyethyl)phosphine (TCEP) (Table 3.6). Finally, the T_m is unchanged, 53.4 ± 0.2 °C measured by DSF.

Peptide mass fingerprinting reveals that the N- and C-termini of core-OLF are truncated compared to myoc-OLF (Figure 3.1, Table 3.7). For core-OLF, the most N-terminal fragment observed in the spectrum encompasses residues 238-258, the extreme C-terminal peptide observed for core-OLF comprises residues 408-422 (Table 3.7), whereas the peptides TLTIPFK (residues 462-468, Figure 3.5C, Table 3.7) and YSSMIDYNPLEK (residues 473-484, Figure 3.5D, Table 3.7) are absent. The truncated C-terminal 44 residues may form a motif not detected by SDS-PAGE due to its small size, or it may be largely unordered. In sum, consistent with the ~25 kDa fragment size, and digest analysis, the main structural domain of myoc-OLF harbors a disulfide bond and is likely inclusive of residues Ser 238 and Lys 461.

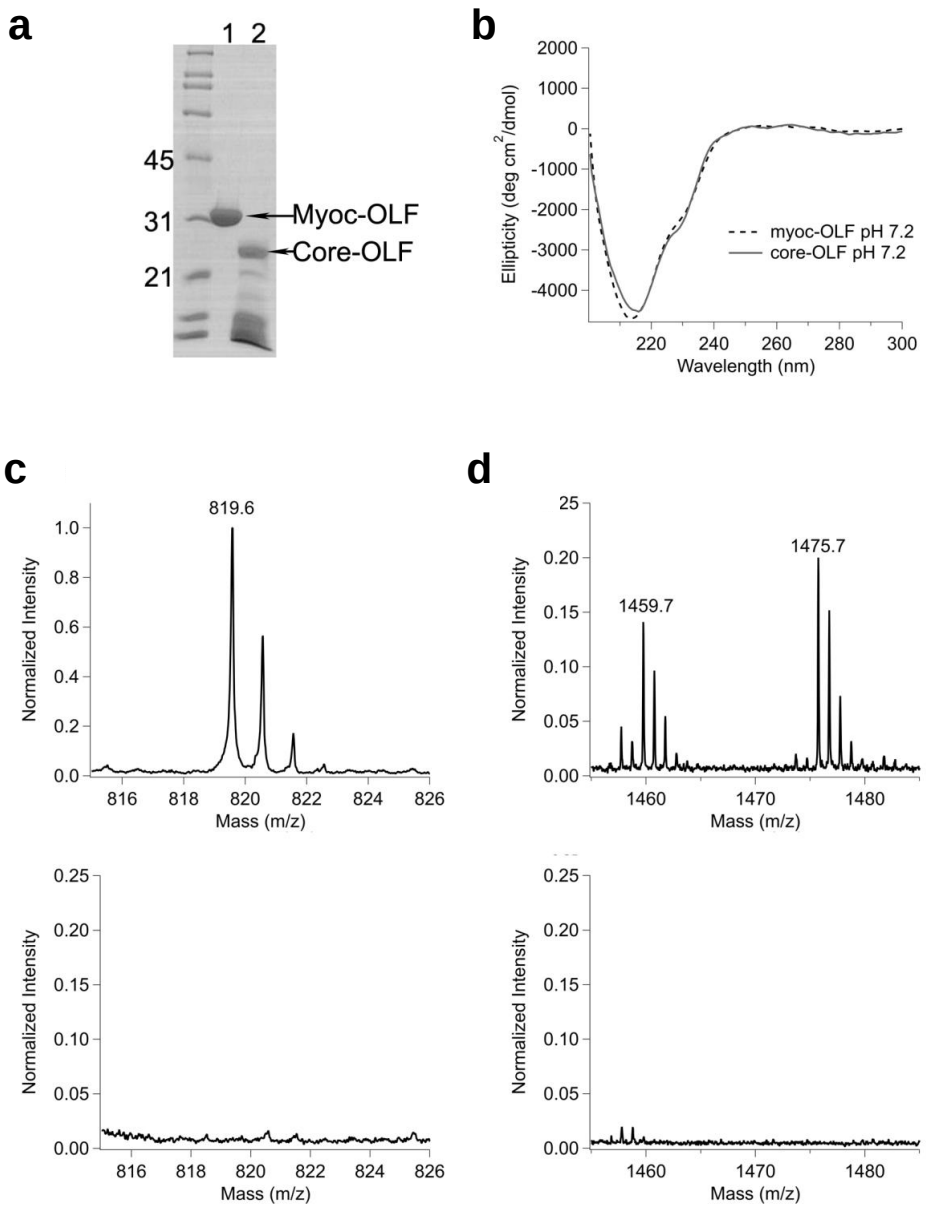

Figure 3.5. Analysis of core OLF domain. A) SDS-PAGE analysis of myoc-OLF before and after limited proteolysis by subtilisin A. Lane 1, myoc-OLF, Lane 2, core-OLF. Molecular mass markers denoted in kDa. B) Overlay of core-OLF and myoc-OLF CD spectra at pH 7.2. C, D) Comparison of trypsin digest/MALDI TOF/TOF mass spectra of myoc-OLF (top) and core OLF domain (bottom) in two key regions (see text, Table 3.7).

Table 3.6. Characterization of disulfide bond in core-OLF.

Sample	Fluorescence Intensity (513 nm)
core-OLF (6 μM)	0.7
core-OLF (6 μM), TCEP (5 mM)	184.4

Table 3.7. Observed and calculated mass spectrum peaks for myoc-OLF and core-OLF.

	Residue Range	Calculated Mass	Observed Mass	ΔMass	MS/MS	Sequence
Core-OLF	267-272	827.3868	827.3786	-0.0082		YGVWM[a]R
	288-296	975.5105	975.5100	-0.0005	yes	IDTVGTDVR
	347-355	1096.5521	1096.5477	-0.0044	yes	YELNTETVK
	273-287	1882.8970	1882.8944	-0.0026		DPKPTYPYTQETTWR
	406-422	2099.0403	2099.0400	-0.0003	yes	LNPENLELEQTWETNIR
	238-258	2232.0601	2232.0674	0.0073	yes	SGEGDTGC[b]GELVWVGEPLTLR
Myoc-OLF	462-468	819.4974	819.5486	0.0512		TLTIPFK
	267-272	843.3817	843.3954	0.0137		YGVWM[c]R
	288-296	975.5105	975.5311	0.0206		IDTVGTDVR
	347-355	1096.5521	1096.5712	0.0191		YELNTETVK
	473-484	1459.6672	1459.6852	0.0180		YSSMIDYNPLEK
	273-287	1882.8970	1882.9452	0.0482		DPKPTYPYTQETTWR
	406-422	2099.0403	2099.0972	0.0569		LNPENLELEQTWETNIR
	297-314	2180.0369	2180.0801	0.0432		QVFEYDLISQFMQGYPSK

[a]A indicates oxidation of methionine, [b]B designates carbamidomethyl cysteine, [c]C indicates methionine sulphone.

The first protein crystals for 3D structural determination were obtained with core-OLF after limited proteolysis *in situ*. Initial crystals were grown in the Cryo I/II screen (Emerald BioSystems) and partially optimized (see Methods). A full data set was collected using a piece of a crystal (Fig. 3.6A-B) grown in 3% PEG 3000, 39% PEG 200, and 100 mM MES, pH 6.0 and diffracted to 2.0 Å resolution. The data set was 100 % complete to 2.3 Å resolution with an R_{sym}= 8.9% (Table 3.8), indicating the intensity measurements are accurately reproducible. Since no OLF structure exists, a predicted structural homolog (PDB code 3NOK) [195] was used to obtain phases by molecular replacement, but yielded unsuccessful results.

We are currently investigating both multiple isomorphous replacement (MIR) and anomalous scattering (MAD) methods using heavy atoms. In particular, $YbNO_3$ and $MnCl_2$ have been identified by DSF and shown to stabilize myoc-OLF, indicating potential binding. However, due to a lack of single 3D crystals, growth conditions will have to be optimized prior to soaking with heavy atoms. Co-crystallization conditions have been attempted, but will also require further optimization. Once a data set is obtained, these heavy atoms can be located using SOLVE [196] or other similar programs, followed by model building and refinement using Coot [197] and Refmac [198]. One final technique includes incorporating selenomethionine substitutions into myoc-OLF to obtain experimental phases by MAD. However, this has not been attempted as creating the selenomethionine derivatives requires growth in minimal media, a condition known to produce little soluble myoc-OLF and also a contaminant binding heat-shock protein, GroEL.

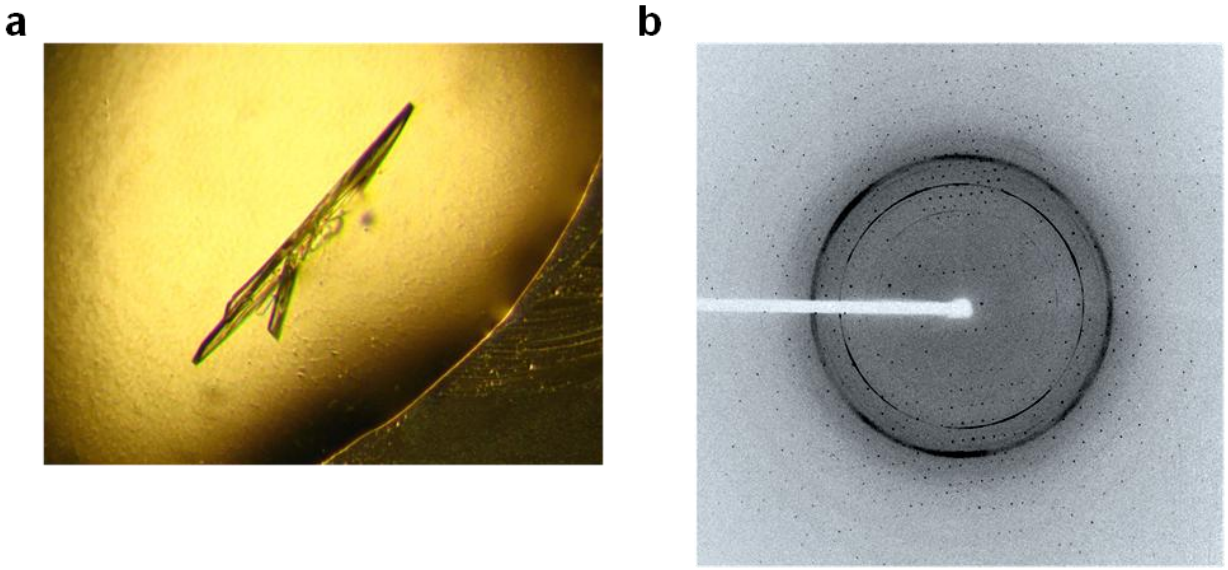

Figure 3.6. Crystal of core-OLF(A) and acquired diffraction pattern (B).

Table 3.8. Data collection statistics.

Data Statistics	
Space group	C2
Cell dimensions	
a, *b*, *c* (Å)	111.5, 85.8, 68.5
α, *β*, *γ* (deg)	90.0, 127.7, 90.0
Resolution (Å) [a]	61.5-1.9 (1.98-1.93)
R_{sym} [a]	8.9 (2.8)
Redundancy	5.4
Completeness (%)[a]	98.5 (58.3)

[a]Data for the highest-resolution shell given in parenthesis.

3.3 Discussion

3.3.1 Functional Significance

The human TEM, a microenvironment in the eye consisting of fibrillar and curly collagens, elastic fibrils, basement membrane and amorphous basement membrane-like materials, as well as other specific proteins, proteoglycans and GAGs, is the anatomical region that controls outflow of aqueous humor in the eye [187]. The structural and functional details of this interconnected matrix, its receptor-mediated interactions with HTM cells, and mechanisms leading to phenotypes observed in the diseased state, are poorly understood [110]. The proper functioning of this complex tissue involves adaptation to a host of cellular and environmental stressors over time, and cumulative long-term detrimental effects of oxidative stress have been implicated in decreased aqueous humor outflow. Eventually, poor flow control leads to an impaired ability to regulate eye pressure, and subsequently, glaucoma [186]. Changes in GAG composition have also been observed in glaucoma-patient derived samples [199-200], but the mechanisms that bring about these changes are unknown. In addition, the roles played by myocilin in the TEM, either normal or pathogenic, are not clear. In this study, we have unraveled some of the molecular characteristics of the myoc-OLF domain in the context of its TEM microenvironment, which will aid future functional characterization.

Several lines of evidence support the notion that GAGs provide a favorable environment for myoc-OLF to function, even though to date, no experiments have identified specific GAGs binders in the myoc-OLF region from any organism. Four GAG attachment sites to the myoc-OLF domain are predicted by the ELM database [201] within residues 232-235, 237-240, 330-333 and 443-446, suggesting that direct linkages are possible. The microenvironment of myoc-OLF in the TEM is also replete with GAGs at a total concentration of 1-2 mg/mL [202], with the approximate composition of 20-25% hyaluronic acid or hyaluronan, 40-60% chondroitin and dermatan sulfates, 5-10%

karatan sulfate, and 15-20% heparan sulfate [187]. Our experiments reveal a modest increase in stability for myoc-OLF in the presence of heparan sulfate, chondroitin sulfate, and hyaluronic acid. Although no change in T_m was observed in the presence of dermatan sulfate, no GAGs tested destabilized myoc-OLF. Interestingly, whereas direct binding of chondroitin sulfate to another OLF-containing protein, mouse photomedin, has been shown [203], the presence of chondroitin sulfate only weakly influences thermal properties of myoc-OLF. This result suggests that chondroitin sulfate may have different functional significance for related OLF-containing proteins.

By contrast, a more notable effect on myoc-OLF stability was observed in physiologically relevant concentrations of heparan sulfate. Even though direct binding to the OLF domain has been ruled out by a previous study demonstrating binding via the N-terminal coiled-coil domain of myocilin [113], the knowledge that heparan sulfate binds to myocilin indicates that this GAG is in the local milieu of myoc-OLF. The observation that heparan sulfate thermally stabilizes myoc-OLF should prompt experiments to further clarify the nature of this interaction.

In addition, although heparan sulfate appears to exert a modest stabilizing effect on myoc-OLF in the absence of other analytes, it seems plausible that cations might enhance the favorable specific interactions between the negatively charged GAGs and the negatively charged OLF domain under physiological conditions. For example, detailed functional studies of amassin, a related, but non-ocular, OLF-containing protein (Figure 1) from the invertebrate animal sea urchin, demonstrates the requirement of the amassin OLF domain for cell-cell adhesion in coelomocytes. This process also requires the presence of Ca^{2+}, and higher multimeric states of the amassin OLF domain [204]. To date, however, no canonical Ca^{2+}-binding sites have been identified in myoc-OLF, and to the best of our knowledge, Ca^{2+} has not been included in any assays. In our hands, myoc-OLF is significantly thermally stabilized in the presence of Ca^{2+}, but does not bind Tb^{3+}, a Ca^{2+} mimic [205] (not shown), and has only been isolated as a monomer by gel

filtration [178]. Although it is possible that these two related proteins have unique modes of interactions and binding partners, based on our study we raise the possibility that certain key components, such as GAGs and/or metal ions, may be missing from functional assays of myocilin attempted to date. Further studies are required to elucidate the potential role of Ca^{2+} with myoc-OLF.

Lastly, the importance of elucidating the mechanism by which GAGs stabilize myoc-OLF is underscored by the finding that the concentrations of GAGs in glaucomatous eyes deviate from those of healthy eyes [199-200]. Specifically, concentrations of sulfated GAGs, such as chondroitin sulfate, are higher in samples derived from early-onset glaucoma patients than from controls [200], and the concentration of hyaluronan decreases in adult-onset OAG patient-derived specimens compared to controls [199]. Given the connection between myocilin and early-onset glaucoma [206], an understanding of the nuances of different GAG interactions with myoc-OLF may pave the way to a better comprehension of myocilin glaucoma pathogenesis.

3.3.2 Structural Significance

Although predominantly β-sheet-containing proteins, such as the immunoglobulins [207], exhibit a trough at ~217 nm that is characteristic of antiparallel β-sheets [194], of particular interest is the prominent ~230 nm shoulder that had not been observed previously. One possibility is that a β-turn [208] is present, a hypothesis supported by prediction of β-turns in myoc-OLF by bioinformatics [209]. Alternatively, or in addition, the 230 nm feature may arise from aromatic residues, as observed in certain serine proteases. For example, a notable 230 nm band in α-chymotrypsin has been attributed to a tryptophan residue whose conformation is sensitive to changes in its environment upon activation of α-chymotrypsinogen to α-chymotrypsin [210]. In support of this assignment, the Trp fluorescence melt curve overlays closely with that

from 230 nm observed in CD (Figure 3D). Of the seven Trp residues in myoc-OLF, two, Trp 270 and Trp 286, are in and near, respectively, a proline-rich region. Alternatively, Trp 373 is within a region with significant disorder probability as predicted by GlobPlot [211]. Future studies involving systematic mutagenesis of each Trp residue may shed more light on the properties of this unusual feature of the CD spectrum.

Intriguingly, the CD spectrum of core-OLF is similar to that of the βγ-crystallin superfamily. Crystallins are cytoplasmic lens cell proteins associated with genetic forms of cataract, a condition in which the crystallins precipitate. Regardless of their quaternary structure, which often exhibits functionally significant polydisperse, domain-swapped oligomers [212], CD spectra of crystallins include the same features at ~202 nm, ~217 nm, and ~230 nm as seen with core-OLF [213], albeit with different relative intensities. Myoc-OLF exhibits no significant sequence homology with crystallins, is ~10 kDa larger, is not known to oligomerize, nor observed to harbor two structural domains [214]. Nevertheless, OLF likely shares structural features such as similar length or twist of its β-strands, and/or the unusually strained torsion angles in a β-hairpin. Further characterization of the three-dimensional structure of an OLF domain will help elucidate the extent of similarity of features with the crystallins, including repeat structures in myoc-OLF that may be important for myocilin self assembly and/or function in the TEM, or plausible molecular mechanisms for the severe aggregation properties observed upon thermal unfolding.

3.3.3 Implications for New Therapeutic Directions

The details of the unfolding mechanisms of WT and disease-causing myoc-OLF domains variants, particularly at physiological pH, are informative for a pharmacological chaperone therapeutic effort [215] for myocilin glaucoma. In this approach, the binding of small molecules will enhance the stability of the mutant myocilins to WT levels so that

after folding in the ER, mutant myocilins will meet quality control requirements and be competent for secretion to the TEM.

Both thermodynamics and kinetics may be important in chaperone therapy for myocilin glaucoma. The therapeutic small molecule might bind to a folded mutant protein to restore its stability to that of WT, and/or bind to a non-native conformation and accelerate folding to the native state. From this study we know that the ~31 kDa WT myoc-OLF domain is a stable entity that appears to unfold under thermodynamic control in a highly cooperative transition. We can now move forward to compare unfolding pathways of the numerous missense mutants of OLF. If mutant OLFs unfold in similarly cooperative transitions, thermal stabilization of the fully folded protein may be sufficient for preventing aggregation and improving secretion, and screening for candidate chaperone molecules would be based on thermal stability alone. However, a more likely scenario is that deviations from two-state unfolding exist for at least some of the reported mutants [179]. In this case, a pharmacological chaperone may need to be tailored in such a way that it alters the folding pathway back to a fully cooperative mechanism observed in WT myoc-OLF. Future studies will examine to what extent such unfolding intermediates exist for specific glaucoma-causing myoc-OLF mutants.

3.4 Methods

3.4.1 Expression and Purification of Myoc-OLF

The myoc-OLF gene was introduced into the MBP fusion vector, pMAL-c4x as described previously (see Chapter 2) [178]. Expression and purification of MBP-OLF followed previously described procedures, as did generation of cleaved myoc-OLF by incubation with Factor Xa and further purification [178]. SDS-PAGE analysis was conducted as described [216].

3.4.2 Thermal Stability Assay for Buffer and pH Analysis

Our fluorescence thermal stability assay [178] utilizing DSF (see Chapter 2) [148] was adapted to identify buffer and pH preferences for myoc-OLF. Reactions of 30 μL were prepared at room temperature and delivered to 96-well optical plates (Applied Biosystems) before sealing with optical film (Applied Biosystems). The reaction mixture consisted of 1 μM myoc-OLF or MBP-OLF in 10 mM sodium phosphate dibasic/ potassium phosphate monobasic, 200 mM NaCl pH 7.2 (Buffer A) and 5X Sypro Orange (Invitrogen). Buffers from pH 4 to pH 9 were obtained from the pHat™ Buffer screen (Emerald Biosciences) and added to each reaction at a final concentration of 100 mM, with the exception of N-Cyclohexyl-2-aminoethanesulfonic acid (CHES), which had a final concentration of 50 mM. The salt screen was conducted in a similar format, but with 50 mM salt added to each reaction. Only for the initial screen was MBP-OLF used and 50 mM maltose added to the reaction mixture. Selected DSF measurements were repeated with cleaved myoc-OLF in acetate, MES, phosphate, Tris, bicine, and glycine buffers. Fluorescence data were acquired on an Applied Biosciences Step-One Plus RT-PCR instrument equipped with a fixed excitation wavelength (480 nm) and a ROX emission filter (610 nm). Melts were conducted from 25-95 °C with a 1 °C per min increase. Collected data were baseline subtracted, trimmed to include both the boundaries and the transition of interest, and subjected to Boltzmann sigmoid analysis (see below).

3.4.3 Thermal Stability Assay in the Presence of GAGs

The thermal stability assay described above was employed to test for increased myoc-OLF stability in the presence of GAGs including chondroitin sulfate (shark cartilage, Sigma), dermatan sulfate (TCI America), heparan sulfate (bovine kidney, Sigma), and hyaluronic acid (rooster comb, Sigma) at concentrations ranging from 0 mg/ml to 10 mg/mL. Samples were prepared in 10 mM Tris, pH 7.5 and 200 mM NaCl, diluted from a 5X stock solution. GAGs were added from 20 mg/mL stock solutions in

water, keeping protein and Sypro Orange concentration the same as above. Data analysis was performed as described above.

3.4.4. Circular Dichroism (CD) Spectropolarimetry

CD was performed on a Jasco J-810 spectropolarimeter with purified myoc-OLF (8-10 μM) prepared in Buffer A, Buffer A adjusted to pH 5.8, as well as in 10 mM sodium acetate/acetic acid and 200 mM NaCl, pH 4.6. Melts were performed in triplicate on each of the samples by raising the temperature from 5 to 90 °C in 1 °C/min increments using a Neslab RTE-111 (Thermo Scientific) circulating water bath and monitoring the profiles between 200 and 300 nm in a 0.1 cm cuvette. Ten spectra, scanned from 300 to 200 nm at rate of 500 nm•min^{-1}, were then averaged at the designated temperature. Our attempts to acquire reliable data below 200 nm were not successful due to voltage limits of the instrument and available nitrogen flow rate. Temperature increase and spectra acquisition lasted about five minutes per degree Celsius, and no differences in melting transitions were observed when the scan rate was reduced to 0.5 °C/min (data not shown). In all cases, samples precipitated after melting, including reversibility tests in which the temperature was raised just to the T_m and then cooled (not shown).

Each averaged spectrum was background-corrected and converted to mean residue ellipticity

$$[\Theta] = \frac{M_{res} \times \Theta_{obs}}{10 \times d \times c}$$

where M_{res} = 112.9 is the mean residue mass calculated from the protein sequence; Θ_{obs} is the observed ellipticity (degrees) at wavelength λ; d is the pathlength (cm); and c is the protein concentration (g/mL). CD melt data from 205 – 300 nm were deconvoluted into component spectra using the singular value decomposition procedure in Matlab (The Mathworks), and their statistical significance was calculated based on singular values. The top three components comprising ≥ 95% of the CD signal were then selected for

reconstitution for the final fit plotted in Figure 3.2. Inspection of difference spectra confirmed that additional components consist of noise.

3.4.5 Tryptophan Fluorescence Spectroscopy

Measurements were carried out in triplicate on a FluoroMax-3 spectrofluorimeter (Horiba Scientific). Intrinsic tryptophan fluorescence of myoc-OLF (2 μM) in Buffer A was excited at 280 nm (slit width 1 nm) and emission recorded in the range 300-400 nm (slit width 5 nm) with a maximum at 340 nm corresponding to tryptophan fluorescence emission. Each sample was heated from 20 to 70 °C or 45 to 65 °C, with a rate of three minutes per degree Celsius, using a Neslab RTE-7 Digital Plus (Thermo Scientific) circulating water bath.

3.4.6 Boltzmann Sigmoid Analysis

The baseline-subtracted and trimmed melt curves acquired by the fluorescence thermal stability assay, CD, and intrinsic fluorescence were processed using GraphPad Prism. The reported T_m is the inflection point of the sigmoidal curve, and is calculated using the Boltzmann sigmoid equation

$$Y = \frac{LL + (UL - LL)}{1 + \exp((T_m - X)/Slope)}$$

where *UL* and *LL* are the values of minimum and maximum intensities, respectively [148].

3.4.7 Limited Proteolysis

Myoc-OLF was pre-screened at room temperature against a variety of proteases including trypsin, α-chymotrypsin, pepsin, papain, V_8 protease and subtilisin A to identify a protease and concentration capable of producing a discrete smaller construct detectable by SDS-PAGE. The optimal reaction condition consisted of a 1:200 dilution of subtilisin A (Sigma Aldrich, 1 mg/ml) in 0.2 mg/mL myoc-OLF in 10 mM Hepes pH 7.5

or 1:200 dilution of papain (Sigma, 1 mg/mL) in 0.2 mg/mL myoc-OLF in 10 mM MES pH 6.2. The reaction was incubated at room temperature for 30 mins followed by subsequent quenching by either the addition of Complete Protease Inhibitor Cocktail (Roche) or SDS-PAGE sample loading buffer for SDS-PAGE analysis and in-gel digestion for mass spectrometry analysis. The core OLF product was fractionated from smaller digestion products on a Superdex 75 GL column (GE Healthcare) equilibrated with Buffer A. The core-OLF sample was further analyzed by CD as described above. Disulfide bond formation was confirmed with ThioGlo (EMD Biosciences) and the T_m measured as described [178].

3.4.8 In-gel Digestion and MALDI-TOF/TOF MS Analysis

In-gel digestion of myoc-OLF and core-OLF was carried out as described previously [217]. Digested and dried samples were subjected to peptide mass fingerprinting analysis using the Georgia Institute of Technology Bioanalytical Mass Spectrometry Facility. Spectra were acquired on an Applied Biosystems 4700 Proteomics Analyzer MALDI-TOF/TOF tandem mass spectrometer. Core-OLF was also analyzed by MS/MS. Peaks were analyzed by using MASCOT (GPS Explorer, Applied Biosystems). Only identified peptide fragments with a >3:1 signal-to-noise intensity were included in analysis. Samples were analyzed in duplicate. Due to the nonspecific nature of subtilisin cleavage, N-/C-terminal sequencing was not undertaken.

3.4.9 Crystallization and Data Collection

Core-OLF was created repeating the limited proteolysis reaction in situ. In short, myoc-OLF (10 mg/mL) in 10 mM Hepes, pH 7.5 was mixed with a 1:200 dilution of fresh subtilisin A (Sigma Aldrich) immediately prior to crystal tray set up. Crystals of core-OLF were grown by vapor diffusion at 16 °C using a cocktail composed of 1-7% PEG 3000, 24-39% PEG 200, and 100 mM MES, pH 6.0. Generally, plate-like single and

clustered crystals are grown with this condition, but one well provided a more 3D plate cluster. Pieces of this crystal cluster were removed and cryocooled in liquid N_2. No cryoprotectant was needed as the crystallization cocktail served as one. Data were collected at the General Medical Sciences and National Cancer Institute Collaborative Access Team (GM/CA-CAT) Beamline 23-ID-B at the Advanced Photon Source at Argonne National Labs (Darien, IL). Data sets were indexed and scaled using the HKL2000 [218].

CHAPTER 4

APPLICATION OF SYPRO® ORANGE, A FLUORESCENT HYDROPHOBIC DYE, FOR A HIGH-THROUGHPUT LIGAND BINDING ASSAY FOR PROTEINS OF UNKNOWN STRUCTURE AND/OR FUNCTION, SUCH AS MYOCILIN

4.1 Introduction

Lead discovery, which is the intense search to find a drug-like small molecule or biological therapeutic that can progress into pre-clinical development, clinical development, and eventually to market, remains as the bottle neck to the drug development process [219]. In the late 1980's and 90's, the development of high-throughput screening (HTS) consisting of screens of random compounds in libraries to find hits showing an activity against or affinity for a selected target [220] was thought to overcome this bottle neck. Sophisticated large-scale automation was anticipated to generate an unprecedented number of novel leads [221]. Unfortunately, the opposite was the case. Despite the significant advancements in large-scale automation, the FDA approved only 21 new drugs in 2010, with an average of ~23 new molecular entities per year in the past ten years [222].

Of the 21,000 listed drug products in the US FDA's Orange Book and Center for Biologics Evaluation and Research website in 2006, only 1,357 are unique drugs and 1,204 are small-molecule drugs [223]. Surprisingly, more than 50% of these drugs target only four key gene families: class 1 G-protein coupled receptors, nuclear receptors, ligand-gated ion channels, and voltage-gated ion channels [223-224]. One reason for this is that development of a novel drug is risky and expensive, costing on average $860 million [225]. It is therefore much less risky to repackage an old drug by creating new

formulations, combining already approved agents, and making subtle chemical changes [225]. Due to the availability of the sequenced human genome in 2002, there has been a surge in validated therapeutic protein targets. However, limited knowledge about the biology of these targets and therefore the types of compounds that they may interact with prevent knowledge-based drug design approaches, such as focused screening and structure-based design. HTS is therefore relied upon for compound identification [226] and may also provide an excellent starting point for understanding the interaction or role of a particular biochemical process in biology [227-228].

HTS starts with testing hundreds of thousands to millions of compounds against the target of interest by virtual screening, cell-based assay, or a biochemical assay approach [227]. I*n silico* drug screening involves selecting compounds by predicting binding to a macromolecular target [221]. An estimate of the free-energy of binding is calculated and the compounds are ranked according to their scoring function [229], of which there are three types: force-field-based, empirical, or knowledge-based [230]. Force-field-based scoring involves quantifying the sum of the receptor-ligand interaction energy and internal ligand energy (i.e. steric strain induced by binding), and various scoring functions are based on different force field parameter sets. Empirical scoring functions are fit to reproduce experimental binding energies and/or conformations as a sum of several parameterized functions. Finally, knowledge-based scoring functions are designed to reproduce experimental structures rather than binding energies [230]. One of the main benefits to virtual screening is that the compounds tested may not actually exist and their testing does not consume material. However, knowledge of the target's 3D structure, either from X-ray crystallography, NMR, or homology modeling, is a prerequisite. Additional challenges associated with virtual screening include accounting for ligand flexibility, protein flexibility, protonation states, protein-ligand interactions, solvent effects, the role of individual water molecules and the decomposition of enthalpic versus entropic binding [229]. The scope of virtual screening is highly dependent on the

amount and quality of the information available about the target [221], specifically, knowledge of the binding pocket of the target, but this ligand-based approach provides the least value to drug discovery for novel targets as there is already a small-molecule start point [231].

Cell-based assays measure cell proliferation, toxicity, production of markers, motility, activation of specific signaling pathways and changes in morphology [232]. The main benefit to this type of assay is that the compounds tested would be interacting in a biological milieu and therefore may decrease the chances for cytotoxicity at a later stage in the drug development process. Many of these assays rely on reporter gene technology, which is the discovery of compounds that modulate a pathway resulting in changes in gene expression [233]. This technique can be very sensitive and thus ideal for miniaturization. However, these assays tend to be based on signal transduction events that occur downstream or receptor activation and require gene expression. This causes a long response time, which may span from hours to days for analysis and also introduces the possibility of interference from other intracellular pathways [232]. Also, for all cell-based assays, potential hits of interest may be missed due to an inability to cross the cell membrane [226].

An ideal biochemical assay is usually one in which all the components of the assay are added at once. Advantages include being able to pipette, incubate, and measure directly from the microplate, which in turn saves time and cost. A homogenous assay also eliminates coating and washing of the plates that are usually required for a cell-based assay, which may introduce variability into the readout [228]. Usually the assay depends on a fluorescent readout which allows for high sensitivity and is amendable to a homogenous high-throughput format [226, 234]. However, other optical methods may be utilized including absorbance, luminescence, or scintillation.

Despite the advantages of a biochemical assay, many soluble target proteins remain difficult to format for HTS; for example, enzymes whose activity involves

multiple substrates and/or cofactors and proteins that display multifaceted biological functions [235]. Furthermore, there is a narrow range of enzyme targets for which fluorogenic substrates are available. Non-enzymatic proteins could potentially be of therapeutic interest, but the ability to assay for a specific readout based on function is highly problematic because biochemical assay techniques require prior knowledge of the function of the target in order to design an assay. Unfortunately, for many known targets linked to disease, such as myocilin in primary open-angle glaucoma (POAG), the function of the protein is unknown. Furthermore, approximately half of the proteins expressed by the human genome are functionally unclassified, even though some might prove to be 'druggable' [236]. More importantly, compounds identified by HTS could provide valuable information into the function of these proteins. This underscores the necessity for an assay generally applicable to proteins of unknown structure and function and to help alleviate the bottle neck of the lead discovery process.

In this chapter, a high-throughput chemical stability assay was developed and validated. The assay is based on the premise that ligand binding confers conformational stability and overall compactness to its target protein, a known phenomenon for most proteins [237], and therefore the assay may be adapted essentially to any soluble protein, regardless of prior knowledge of structure and/or function. Here, we show substantial progress in assay development for both a model protein, maltose binding protein (MBP), and our protein of therapeutic interest, the olfactomedin domain of myocilin (myoc-OLF). The homogenous assay requires no incubation steps, and is rapid, robust with low variability, cost-effective, and capable of generating a high signal-to-noise/background to minimize false negatives or positives. During the validation process, a total of 14 potential drugs for myoc-OLF were identified that may provide not only a therapeutic effect on myocilin but also insights into its function.

4.2 Results

4.2.1 Assay Principle

The principle of the assay is based on the well established property that soluble proteins are thermally stabilized upon ligand binding. In our assay, the soluble protein is slightly destabilized by the addition of guanidine hydrochloride (Gnd HCl), a denaturant, and may be re-stabilized upon ligand binding (Fig. 4.1A). Our assay employs Sypro Orange, an extrinsic fluorescent dye that monitors protein unfolding by fluorescing in the presence of exposed hydrophobic residues [238]. When the soluble protein is destabilized, a high fluorescent signal is observed due to the dye's colloquial interactions with exposed hydrophobic residues. When stabilization occurs after ligand binding, there is a decrease in fluorescence (Fig. 4.1B), creating the signal window. The primary benefit of this assay is that no prior knowledge of the protein's structure and/or function is required. However, the assay is limited to soluble proteins that may be expressed and purified and potential interference of compounds with Sypro Orange dye.

4.2.2 Assay Optimization and Verification

The assay was first developed in a 96-well format with the well studied *E. coli* maltose binding protein (MBP). MBP was chosen because it binds to the disaccharide maltose as well as longer linear and some circular maltodextrins with K_d values in the low micromolar range [239], which is the high end of the typical hit potency range of 100 nM to 5 μM for HTS [219]. The concentration of the denaturant Gnd HCl to be used in the assay was first determined by conducting a chemical melt with MBP (Fig. 4.2A), and 0.6 M Gnd HCl was chosen as the concentration at the onset of unfolding (i.e. the most destabilized point without unfolding the protein). After conducting a serial dilution of the protein in 0.6 M Gnd HCl, a concentration of 2 μM MBP was determined to be the lowest that may be used and still provide a robust signal (Fig. 4.2B).

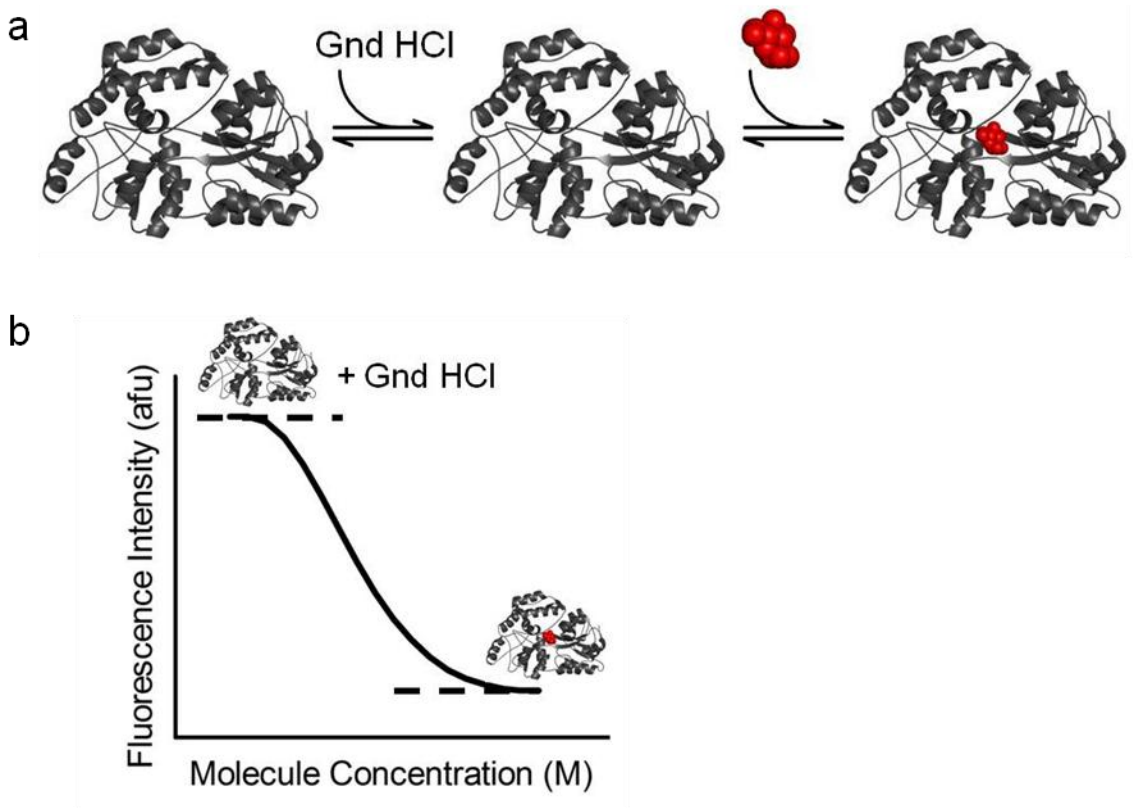

Figure 4.1. Schematic of chemical stability assay. A) Native protein (left) is destabilized by the addition of relatively low concentrations of chemical denaturant (middle) and is re-stabilized by binding of the ligand (red, right). B) Example of a typical fluorescence spectrum upon the addition of increasing amount of ligand. High signal is observed for the destabilized protein in the presence of the reporter dye, Sypro Orange, and a low signal is observed for the re-stabilized protein.

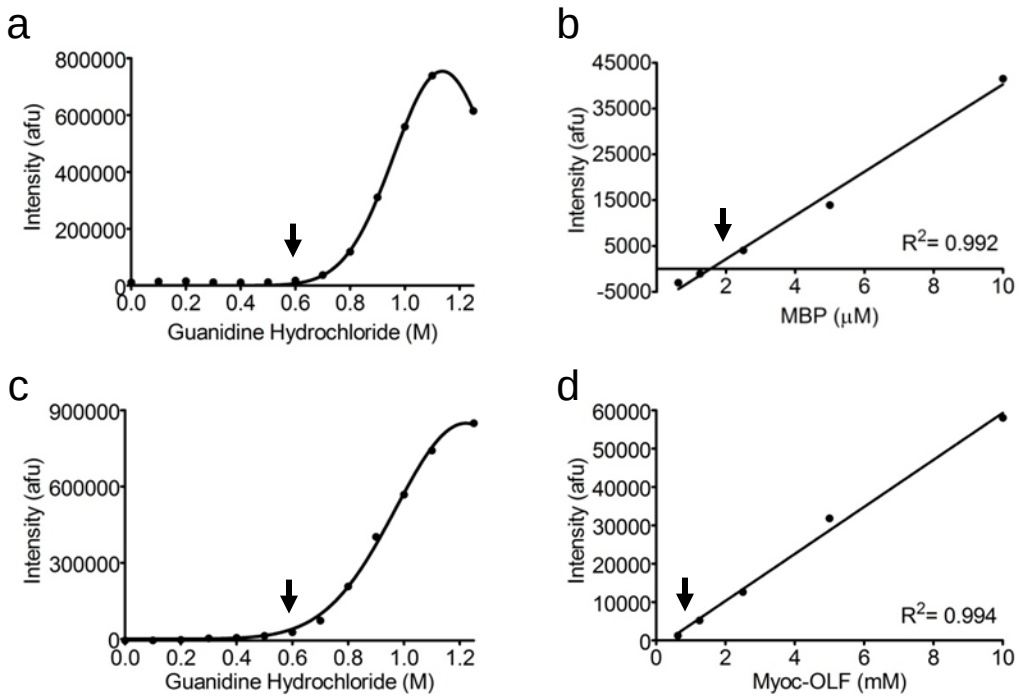

Figure 4.2. Concentration Optimization for MBP and myoc-OLF. Chemical melt of MBP (A) and myoc-OLF (C). Arrow denotes the Gnd HCl concentration at the onset of unfolding. Serial dilution of MBP (B) and myoc-OLF (D) to determine optimal concentration for subsequent assays (arrow).

Fluorescence assays were then conducted to test for a dose-dependent stabilization of MBP upon binding three known ligands: maltose, maltotetraose, and maltitol (Fig. 4.3A). All three sugars stabilized MBP in a dose-dependent manner in the assay. Maltose stabilized to the greatest degree with a 50% drop in fluorescence intensity at 10 μM (Fig. 4.3A). Maltitol stabilized to the lowest degree (Fig. 4.3A), but this was expected since the K_d = 50 μM [240]. All three sugars stabilize reproducibly day-to-day and plate-to-plate with a signal-to-background (S/B) of 2.1 (Fig. 4.3A,B), which describes the separation of the signal window. Phenylmethanesulfonylfluoride (PMSF), a known protease inhibitor, was tested as a negative control and no stabilization of MBP was observed (Fig. 4.3C).

Compounds in a small molecule library are generally dissolved in DMSO, thus it was necessary to determine the tolerance of the assay to DMSO. The dose-dependent maltose stabilization assay with MBP was repeated, but with 1% DMSO added to the reactions. An almost identical stability curve was collected and it was determined that the solvent does not appreciably affect the assay (Fig 4.3D).

Once the initial controls were completed, statistics for the assay were calculated. Destabilized MBP was added to 48 wells of a 96-well microplate, and the same mixture without protein was added to the remaining 48 wells. The assay was assessed using the Z' factor, which defines the difference between positive and the negative controls of the dynamic signal being measured and the variation of that signal [226]. The collected data exhibit a Z' factor of 0.76 (Fig. 4.3D), indicating an excellent assay with a large separation between signal and background populations [241]. The CV value, a variability measurement, from this plate was 4.0%, which is an acceptable value for HTS (i.e. less than 10%) [226, 242].

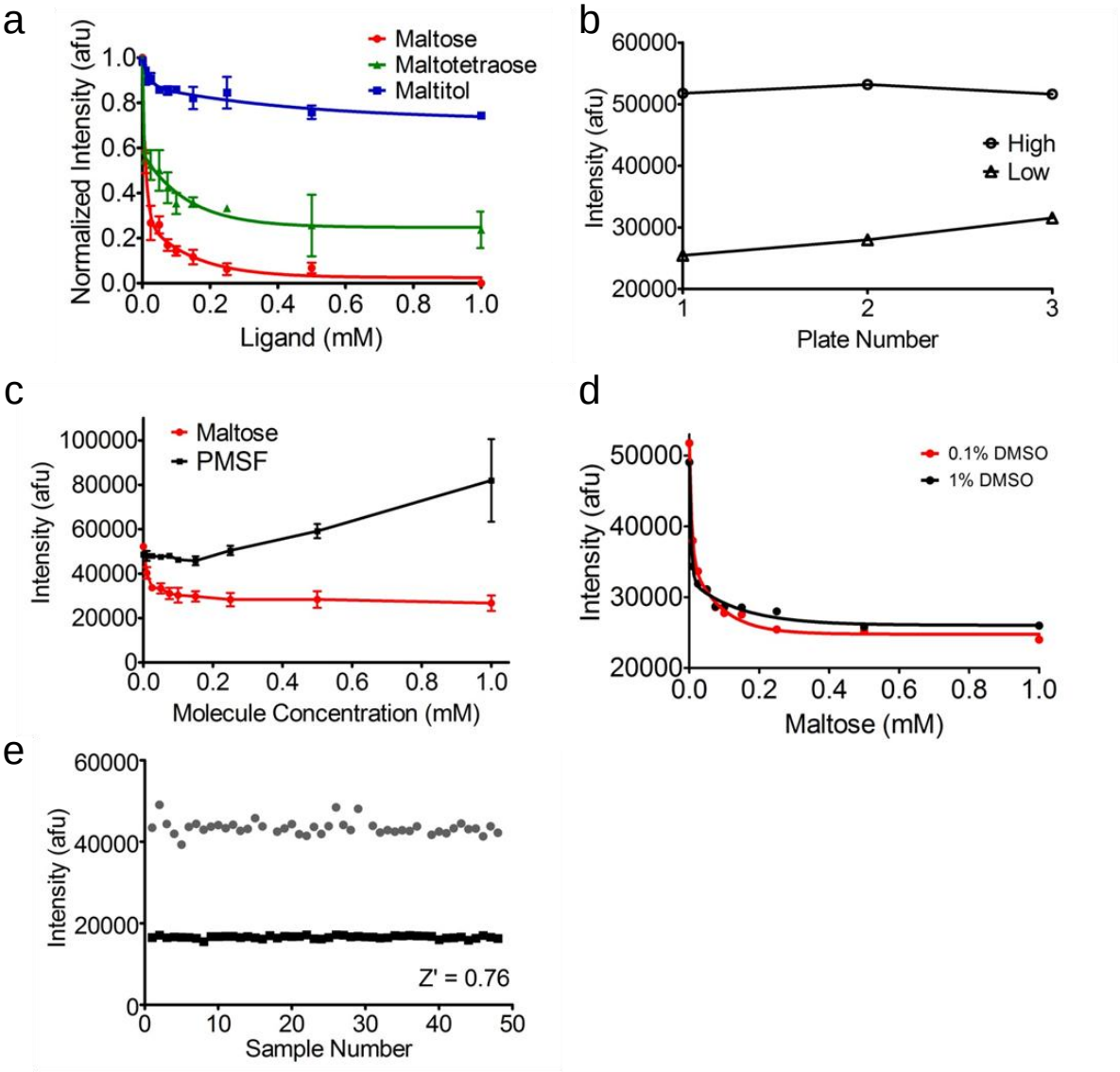

Figure 4.3. Assay verification with MBP. A) Dose-dependent stabilization of MBP by addition of ligand. Error bars denote standard deviation. B) Signal window of optimized assay with MBP. High signal (circles) corresponds to MBP in the presence of Gnd HCl, whereas low signal (triangles) corresponds to the same sample but with the addition of 1 mM maltose. C) Effect of the negative control, PMSF, when added to destabilized MBP. D) Stabilization of MBP by maltose in the presence of DMSO. E) Scatter plot of an equivalent amount of destabilized MBP (grey circles, n = 48) and background (black circles, n = 48) from a single 96-well plate. These data were used to calculate the Z′ value of the optimized assay.

4.2.3 Assay Adaptation to Myoc-OLF

After verification of the chemical stability assay with MBP, the assay was adapted to the protein of therapeutic relevance, myoc-OLF, also in a 96-well format. After performing concentration optimization tests as with MBP, it was determined by chemical melt that 0.6 M Gnd HCl was the concentration at the onset of unfolding (Fig. 4.2C), and 1 μM myoc-OLF from the serial dilution assay (Fig. 4.2D) provided the lowest amount of protein while still producing a measurable signal.

Since relatively little is known about structure or function of myocilin and no known ligands exist, trimethylamine N-oxide (TMAO) was chosen as a positive control to define the signal window. This was based on the results observed in Chapter 2 where myoc-OLF is thermally destabilized when a disease-causing mutation is introduced, and that these variants may be stabilized by the addition of non-specific small molecule chemical chaperones called osmolytes [243]. Both TMAO and sarcosine conferred a high degree of stabilization to WT and mutants increasing their melting temperatures [243]. Similar to MBP and maltose, TMAO stabilized myoc-OLF in a dose-dependent fashion (Fig. 4.4A), albeit at a 1,000-fold higher concentration range due to the nature of osmolytes. However, this stabilization effect provided an S/B = 7.7 (Fig. 4.4B), which is 4-fold higher than that observed for MBP with maltose (Fig. 4.3B).

The tolerance of the assay to DMSO was again tested, and no appreciable effect was observed (Fig. 4.4C). The assay was verified for a dose-dependent stabilization effect over the course of one hour at room temperature. The same stability trend was observed after three days of incubation in the dark at room temperature, but the fluorescence intensity increased over time (Fig. 4.4D). Therefore, the assay may be conducted at room temperature as long as a positive control is included on each plate. The assay with myoc-OLF was statistically evaluated as described above for MBP. Again, a Z' factor of 0.72 (Fig. 4.4E) was determined and a CV value of 3.3% was calculated.

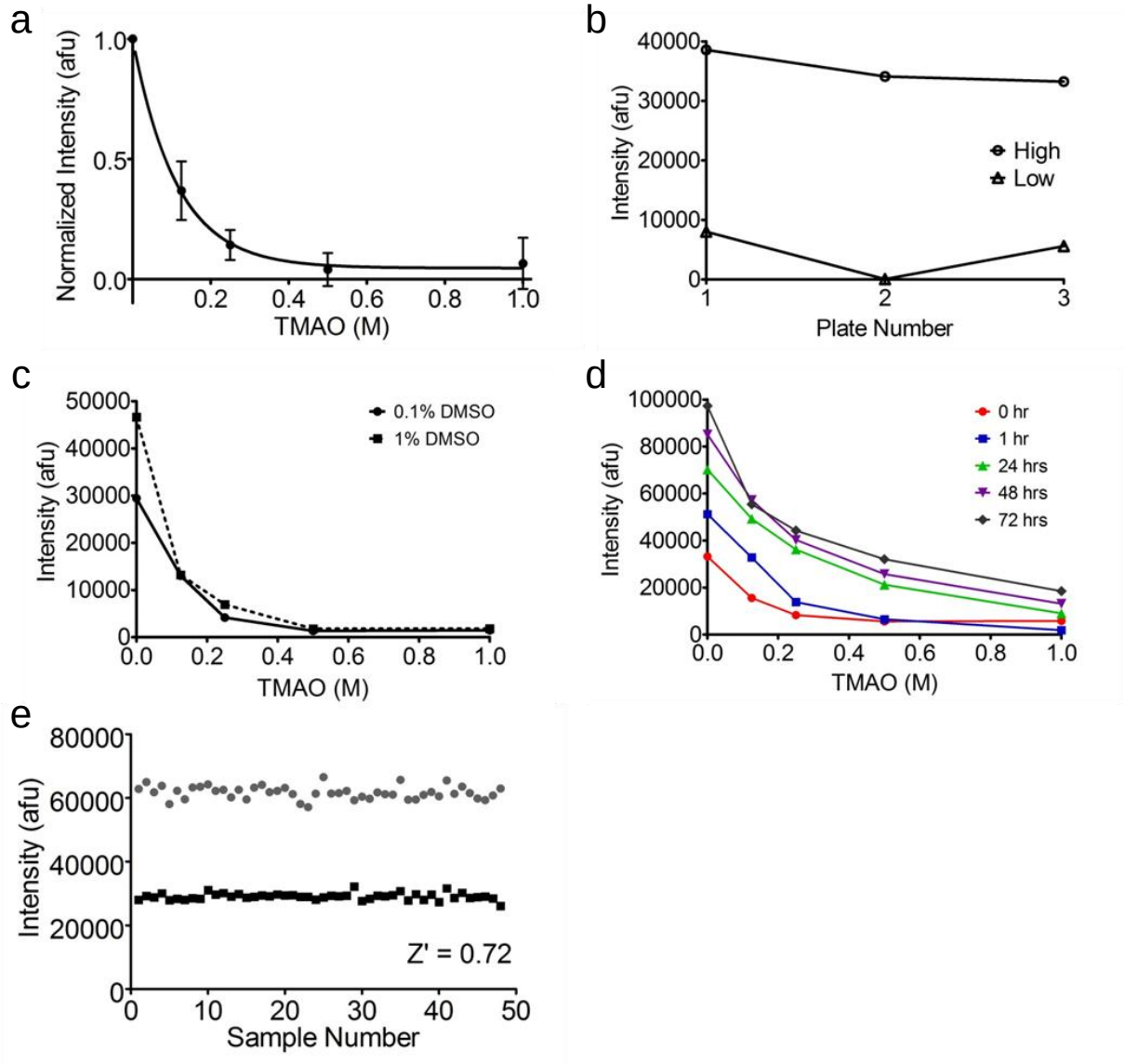

Figure 4.4. Assay verification with myoc-OLF. A) Dose-dependent stabilization of myoc-OLF in the presence of Gnd HCl by the addition of increasing amounts of the osmolyte, TMAO. B) Defined signal window for the myoc-OLF assay. High signal (circles) corresponds to destabilized myoc-OLF whereas low signal (triangles) corresponds to re-stabilized myoc-OLF by the addition of 1 M TMAO. C) Effect of DMSO on the stabilization curve of myoc-OLF. D) Effect of various incubation times on the assay output. E) Scatter plot of an equivalent amount of destabilized myoc-OLF (grey circles, n = 48) and background (black circles, n = 48) from a single 96-well plate. These data were used to calculate the Z′ value of the optimized assay.

4.2.4 Assay Validation

Before conducting the compound library pilot screen with the assay, the assay required validation for a 384-well format. The dose-dependent stabilization curve for MBP by the addition of maltose, as well as the stabilization curve for myoc-OLF by the addition of TMAO, were both repeated. However, in this miniaturized format, the S/B calculated for myoc-OLF was below a value of two, which is considered to be too low and may complicate the interpretation of the results. Optimization of the protein concentration was therefore conducted again in the 384-well plate, and it was found that 4 μM myoc-OLF provided the greatest S/B= 8. An S/B plateau was observed at higher protein concentrations, indicating no appreciable gain in the signal window upon the addition of more protein (Table 4.1).

At Emory University Chemical Biology Discovery Center, the optimized chemical stability assay in 384-well format was automated and used to test the LOPAC compound library (Sigma Aldrich), which includes 1,280 compounds known to be pharmacologically active or are currently approved drugs. Each compound was added at a single concentration (1 mM final). Destabilized myoc-OLF and re-stabilized myoc-OLF by TMAO (positive control) reactions were added to each plate to define the signal window, and allowed for calculation of plate-to-plate statistics to detect any irregularities in the assay. The HTS protocol is outlined in Table 4.2 and a scatter plot of the HTS results for the entire pilot screen is shown in Fig. 4.5. The performance of the screening assay was assessed using the average Z' value 0.78 (range of 0.76 to 0.83), consistent with a high-quality HTS assay. The S/B averaged between 4.2 and 5.5 and the CV value averaged between 4.3% and 6.1%, consistent with the values calculated in the 96-well format.

Molecules leading to a decrease in fluorescence intensity were considered as hits (Table 4.3). A total of 14 hits were identified during the pilot screen (Table 4.3, Fig. 4.6) and three molecules greatly destabilized myoc-OLF (Table 4.3, Fig. 4.7). It is possible

Table 4.1. Optimization of myoc-OLF concentration for 384-well format.

Myoc-OLF (μM)	S/B	Z′ Factor
1.0	3.9	-0.40
2.0	6.1	0.11
3.0	4.9	0.46
4.0	8.6	0.68
5.0	8.4	0.67
10.0	11.4	0.50

Table 4.2. Chemical stability assay HTS protocol.

Step	Parameter	Value	Description
1	Master Mix	20 μL	0.54 M Gnd HCl, 4.5X Sypro Orange, phosphate buffer, pH 7.2
2	Library Compounds	0.5 μL	1 mM in DMSO
3	Positive Control	4 μL	0.8 M TMAO
4	Protein	4 μL	4 μM in phosphate buffer, pH 7.2
5	Centrifugation	5 min	800 x g
6	Assay Readout	485 nm excitation /572 nm emission	2103 EnVision Multilabel Plate Reader (Perkin Elmer)

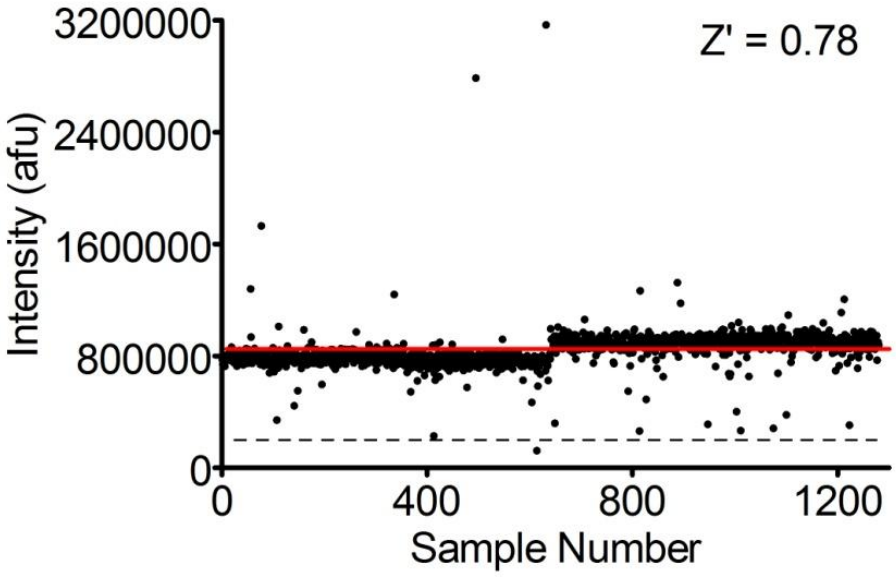

Figure 4.5. HTS results for the LOPAC compound library. The x axis represents the compounds screened (black circles). The solid red line represents the average signal for destabilized myoc-OLF without ligand and the dashed black line represents the average signal for re-stabilized myoc-OLF in the presence of TMAO. The Z′ stated is the average of the four plates tested.

Table 4.3. Compounds identified in myoc-OLF pilot screen.

Compound	Compound Class	Activity	Effect
Apigenin	Cell Cycle	Arrests cell cycle in G2/M phase	+
Aurintricarboxylic acid	Apoptosis	Topoisomerase inhibitor	+
GW5074	Phosphorylation	Kinase inhibitor	+
Isoliquiritigenin	Cyclic Nucleotides	Aldose reductase inhibitor	+
Morin	Cell Stress	Oxyradical scavenger	+
Myricetin	Phosphorylation	Kinase inhibitor	+
Niclosamide	Antibiotic	Uncouples oxidative phosphorylation	+
Phloretin	Ca^{2+} Channel	Blocks L-type Ca2+ channels	+
Piceatannol	Phosphorylation	Kinase inhibitor	+
Quercetin dihydrate	Cyclic Nucleotides	Mitochondrial ATPase and phosphodiesterase inhibitor	+
Reactive Blue 2	P2 Receptor	Antagonist for ATP-activated channels	+
Rottlerin	Phosphorylation	Kinase inhibitor	+
(R,R)-cis-Diethyl tetrahydro-2,8-chrysenediol	Hormone	Estrogen receptor beta antagonist	+
Tyrphostin AG 879	Phosphorylation	Tyrosine kinase nerve growth factor receptor inhibitor	+
4-Amino-1,8-naphthalimide	Apoptosis	Poly(ADP-ribose) polymerase inhibitor	-
Dequalinium analog, C-14 linker	Phosphorylation	Kinase inhibitor	-
Idarubicin	DNA Metabolism	Antineoplastic	-

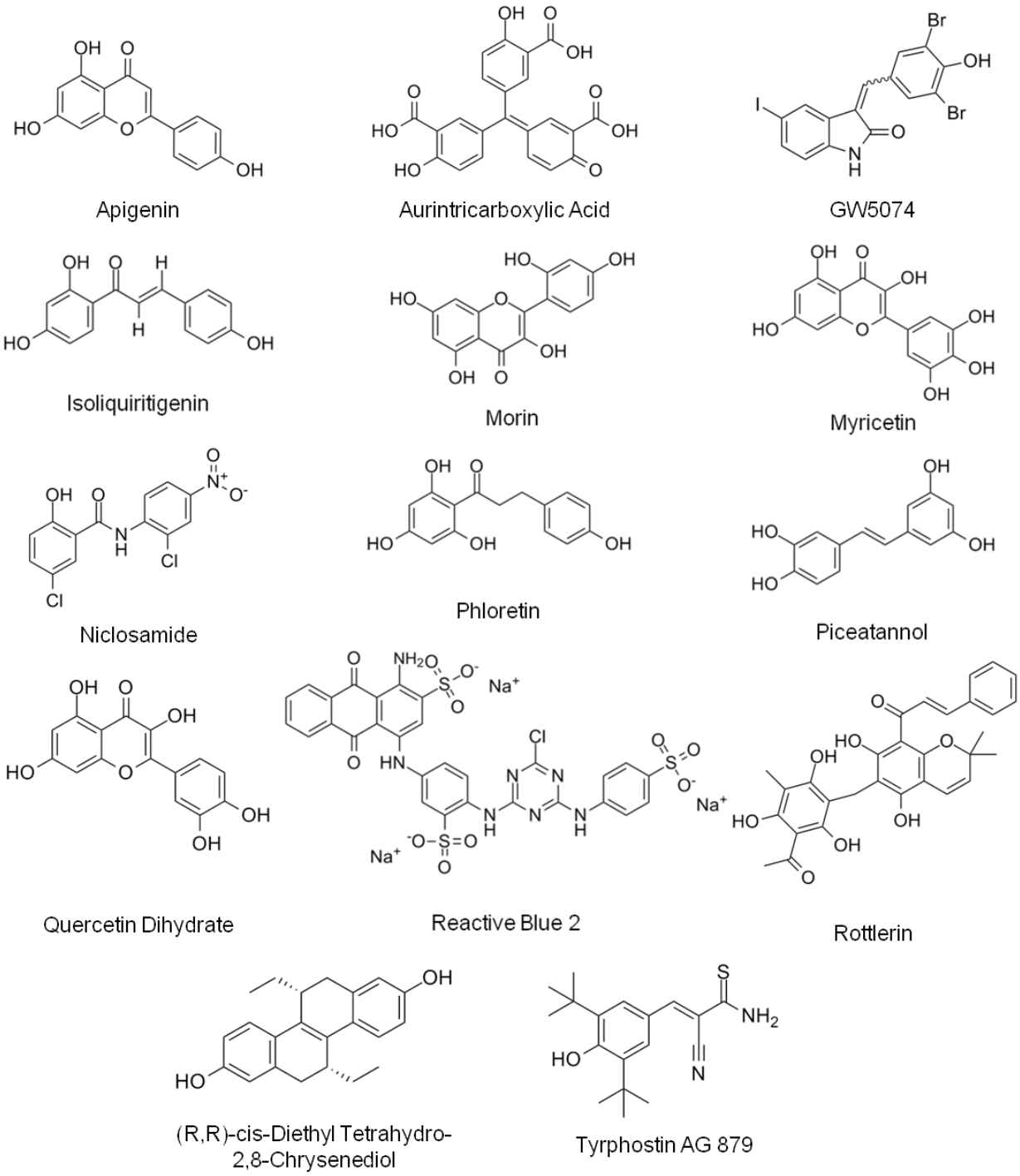

Figure 4.6. Compounds identified as hits from the LOPAC library screen that potentially stabilize myoc-OLF.

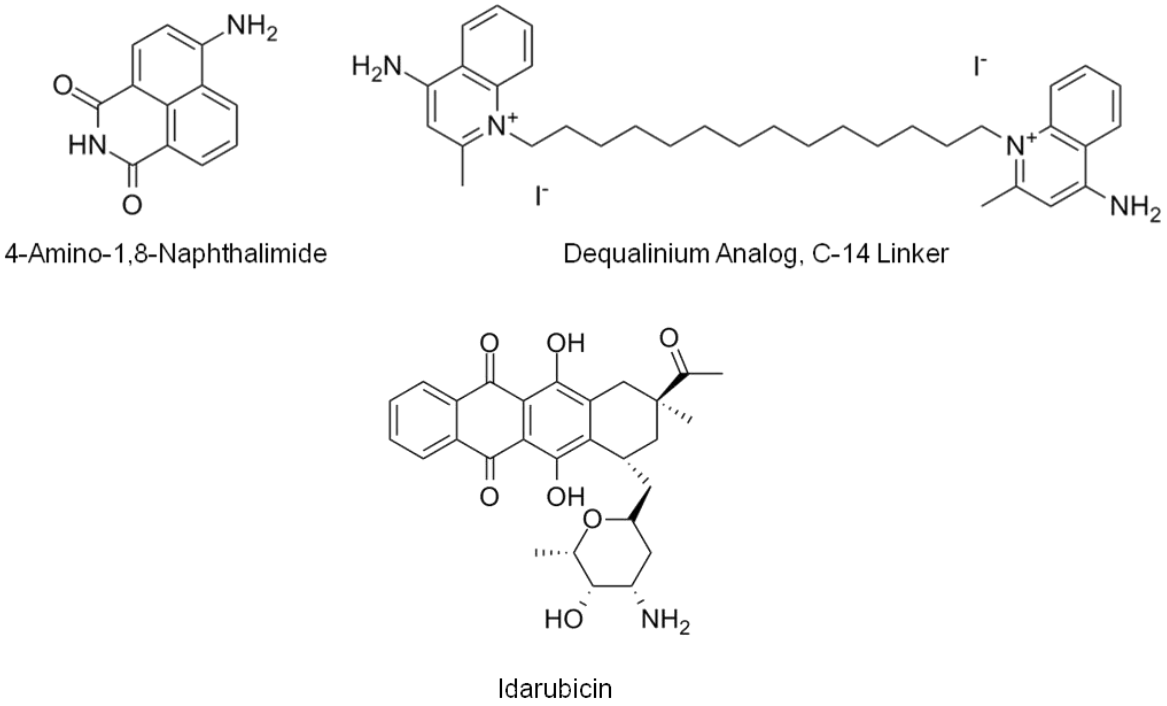

Figure 4.7. Identified compounds from the LOPAC library screen that may destabilize myoc-OLF significantly, as indicated by a substantial increase in Sypro Orange fluorescence.

that the high fluorescence intensity for the dequalinium analog in particular could be the result of Sypro Orange interacting with the alkyl linker and not the result of myoc-OLF destabilization. Interestingly, the stabilizing potential drug candidates include a variety of were the most predominant compound class accounting for ~36% of the total hits. The well containing the kinase inhibitor GW5074 yielded the lowest fluorescence intensity, indicating a potential stabilization effect that was greater than the positive control, TMAO. In previous work, myoc-OLF was shown to be stabilized in buffers with functional groups mimicking glycosaminoglycans (GAGs) (Chapter 3) [244]. In our assay, two compounds, aurintricarboxylic acid and reactive blue 2, also possess carboxylate and sulfate functional groups similar to GAGs (Fig. 4.6). While it is tempting to speculate the potential therapeutic relevance and functional importance of these molecules with myoc-OLF, the binding of these compounds must be verified first by conducting a dose-dependent assay for each hit to eliminate false positives, followed by isothermal titration calorimetry.

4.3 Discussion

HTS is the primary method used by pharmaceutical companies to generate leads in the drug discovery process, and starts by testing hundreds of thousands to millions of compounds against a target in an assay. However, this method requires tailored assays to the biological target of interest and many limitations arise, including most importantly, detailed knowledge of either the structure and/or function of the protein. This level of detail is not always available and may be costly and time-consuming to generate. Therefore, a generally applicable assay to detect ligand binding for essentially any soluble protein is needed.

The chemical stability assay was designed to be a ‘mix-and-measure’ homogenous assay with a facile, one-step readout. The premise of the assay is that a chemically destabilized protein is re-stabilized by ligand binding, and this occurs in a

dose-dependent fashion. The reporter dye, Sypro Orange, fluoresces only in the presence of a hydrophobic environment, i.e. in the presence of destabilized protein with exposed hydrophobic residues. Protein stabilization upon ligand binding is a general property of proteins and is not dependent on prior functional knowledge of the target of interest. Both enzymatic and non-enzymatic proteins may be equally screened in this assay, since activity and/or inhibition is not required to produce an optical signal for read out. In this work, the assay was first verified with the well characterized, non-enzymatic protein, MBP. Stabilization upon ligand binding was shown to occur in a dose-dependent fashion, and is not affected by the addition of DMSO. Since the compounds in this library are dissolved in this solvent, it is important to verify that the results obtained from the pilot screen were due to ligand-induced stabilization and not solvent effects.

The assay was next applied to myoc-OLF to identify potential ligands. Previously, we have shown that glaucoma-causing mutations in the myoc-OLF result in a destabilized protein, and that these variants retain similar secondary structure to wild-type [243, 245]. Instead of secretion to the human trabecular extracellular matrix (HTM), mutant myocilin has been shown to accumulate in the endoplasmic reticulum (ER) of HTM cells, triggering cell stress responses, and eventually leading to cell death [84-85, 97-98]. It has been hypothesized in our lab and others [76, 97] that if mutant myocilin could be stabilized endogenously and pass the ER quality control for subsequent trafficking, toxicity due to protein accumulation would be reduced, thus alleviating cell stress and delaying the onset of glaucoma. Pharmacological chaperones (PCs) are of particular interest as they are small molecule compounds capable of stabilizing endogenous mutant enzyme and lead to cellular trafficking, but design of such a beneficial molecule is hampered due to lack of knowledge of the myoc-OLF structure and function. A top-down approach is therefore required for the identification of molecules that may potentially act as PCs or provide clues to the biological function.

A total of 14 potential drug candidates from the LOPAC library were identified, with a hit rate of 1.25%. The chemical stability assay was amendable to miniaturization, easy to automate, and displayed excellent statistics, indicating a robust and reproducible assay. Further work will be required to verify the hits as potential drug candidates and would include generation of concentration response curves to eliminate false positives. Confirmation of binding should also be tested by isothermal titration calorimetry (ITC) or equilibrium dialysis. False positives due to the possible interference of the compounds with Sypro Orange should also be tested. Finally, myoc-OLF drug screening may be advanced by further miniaturizing to 1536-well format and screening hundreds of thousands of compounds at the National Institute of Health's Molecular Libraries Probe Production Center. Potential drug candidates identified by this chemical stability assay, and verified for binding by alternative methods, may yield further insight into the function of myoc-OLF as well as provide the first therapeutic molecules targeted at alleviating cell stress induced by mutant myocilin intracellular sequestration and accumulation.

4.4 Methods

4.4.1 Protein Purification

MBP was expressed in *E. coli* Rosetta-gami™ 2(DE3)pLysS competent cells (Novagen) using the pMAL-c4x vector (New England Biolabs) and purified on a 20 mL high-flow amylose resin (New England Biolabs) column. The myoc-OLF gene was introduced into the MBP fusion vector, pMAL-c4x, as described previously [178]. Expression and purification of MBP-OLF followed previously described procedures, as did generation of cleaved myoc-OLF by incubation with Factor Xa and further purification [178].

4.4.2 Chemical Stability HTS Assay

The optimal denaturant concentration was first determined by performing a chemical melt with Gnd HCl. Increasing concentrations of Gnd HCl (0-2 M) were added to 10 μM MBP or myoc-OLF in phosphate buffer (10 mM sodium phosphate dibasic/ potassium phosphate monobasic, 200 mM NaCl pH 7.2), and 5X Sypro Orange (Invitrogen). The reactions were assembled at room temperature and delivered to 96-well microplates (Grenier). Fluorescence data were acquired on a Biotek Synergy 2 instrument with a 485/20 nm excitation filter and a 590/35 nm emission filter. Data for each sample were taken in triplicate and blank subtracted. Protein concentration was then tested for by serial dilutions of the protein (0.625-10 μM) in the phosphate buffer, Sypro Orange, and optimized Gnd HCl concentration reaction. Fluorescence data was acquired and analyzed as before.

After optimal denaturant and protein concentrations were established, known ligands (maltose, maltotetraose, and maltitol) of MBP were added in a dose-dependent fashion (0-1 mM) to MBP in phosphate buffer, Gnd HCl, and Sypro Orange. Phenylmethylsulfonyl fluoride (PMSF), a known protease inhibitor, was also tested in a dose-dependent fashion (0-1 mM) as a negative control for MBP. In the case of myoc-OLF, TMAO (0-1 M) was added as a positive control and fluorescence data were acquired. In every case, the protein was added last and prior to fluorescence readings. All assays were conducted at room temperature in 100 μL reaction volumes.

4.4.3 Screening of Small Molecule Library

In the primary screen, approximately 1,280 compounds (LOPAC$^{®,\ 1280}$, Sigma Aldrich) were tested at the Emory University Chemical Biology Discovery Center. The assay volumes were adjusted to a 384-well format (25 μL reaction volume). Due to a low S/B value, myoc-OLF concentration (1-10 μM) was optimized for the 384-well format, and a concentration of 4 μM was utilized during the library screen. Master mix solution

(0.54 M Gnd HCl, 4.5X Sypro Orange, phosphate buffer, and water) was dispensed via a MultiDrop Combi (ThermoScientific) to a 384-well microtiter plate (Costar). The Sciclone ALH 3000 Workstation with 384-channel cannula array (Caliper LifeSciences) was used to transfer 0.5 μL of compound (1 mM final) to the dispensed master mix solution. Myoc-OLF was added last, again using the MultiDrop Combi. The plates were centrifuged for five minutes at 800 x g to remove air bubbles prior to fluorescence reading in a 2103 EnVision Multilabel Plate Reader (Perkin Elmer) (Exλ= 480 nm; Emλ= 572 nm).

4.4.4 Data Analysis

To validate the chemical stability assay, the Z′ factor (Eq. 1), the coefficient of variation (CV, Eq. 2), and signal-to-background ratio (S/B, Eq. 3) were calculated from a 96-well plate containing the destabilized sample in GndHCl and the same solution without protein:

$$Z' = 1 - 3 \times (SD_{signal} + SD_{background}) / \left| M_{signal} - M_{background} \right| \quad (1)$$

$$CV = 100 \times SD/M(\%) \quad (2)$$

$$S / B = M_{signal}/M_{background} \quad (3)$$

where SD is standard deviation and M is the mean.

CHAPTER 5

CHARACTERIZATION OF AMYLOID FIBRILS FORMED BY THE OLFACTOMEDIN DOMAIN OF MYOCILIN

5.1 Introduction

Amyloidoses are a subset of protein conformational disorders (PCDs) and a group of diverse diseases in which soluble polypeptides/proteins undergo a conformational change and accumulate to form stable, ordered filamentous protein aggregates, commonly referred to as amyloid fibrils [246]. These >20 diseases include such infamous disorders such as Huntington's disease, Alzheimer's disease, Parkinson's disease, and the prion diseases. Each disease involves predominantly the aggregation of a specific protein, but other additional proteins and carbohydrates, specifically glycosaminoglycans (GAGs) [247-248], have been identified in plaques and deposits *in vivo* [249-250]. Amyloid deposits may accumulate intracellularly leading to impaired organelle function and cell death [251-252], extracellularly resulting in disrupted tissue architecture and function [246, 253], or both [254].

Fibrils described for amyloidoses are structurally similar in spite of the fact constituent monomers exhibit diverse amino acid sequences and diverse tertiary structure. X-ray fiber diffraction reveals that the fibrils are composed of a cross-β-sheet structure in which the backbone hydrogen bonding is parallel to the fibril axis [255]. Fibrils are ~10 nm in diameter, un-branched, and mature fibrils have a twisted, rope-like appearance, as identified by transmission electron microscopy (TEM) and atomic force microscopy [256]. Mature fibrils also exhibit a green birefringence under polarized light when stained with Congo Red [257] and are resistant to proteolysis [258]. Formation of the fibrils is generally believed to follow the nidus theory, in which amyloid fibril fragments serve as templates for fibril growth [246]. Fibril extension is typically monitored with Thioflavin

T (ThT), which only fluoresces when bound to mature fibrils [259]. The dye binds rapidly to amyloid fibrils and produces an increase in fluorescence at 485 nm when excited at 440 nm [260]. Finally, polymerization may occur with a natively folded protein or unstable intermediates (i.e. mutated protein or protein altered by its environment) [261].

Amyloidogenic proteins are generally small in size (3-30 kDa) [246] and may be natively unfolded and prone to aggregate under physiological conditions, as is the case for huntingtin with polyQ expansion in Huntington's disease and amyloid-β peptide (Aβ) in Alzheimer's [262]. For vulnerable globular proteins, aggregation may be transmissible (prion), familial, or sporadic. Hereditary forms of the amyloidoses generally occur due to a genetic mutation that produces a less stable and less cooperative variant, and will therefore tend to fold and aggregate more readily. Familial forms usually have an early age of onset and higher severity than sporadic cases [254]; age of onset is generally closely related to the extent of destabilization by the mutation [263].

A large percentage of amyloid diseases occur sporadically and are observed in aged individuals. Premature aggregation earlier in life is prevented largely in part to the adapted mechanisms of the cell that serve to assist proteins to their native conformations and maintain them in a stable and controlled environment [264]. Intracellularly, molecular chaperones play a key role in protecting an incompletely folded polypeptide chain from non-productive interactions, including aggregation [249]. In the extracellular environment, abundantly secreted glycoproteins, including clusterin, α_2-macroglobulin, and haptoglobulin, act as extracellular molecular chaperones by protecting a range of proteins from stress-induced aggregation [261, 265]. It is likely that this control is lost in ageing in conjunction with environmental changes (such as oxidative damage) that may promote protein unfolding and aggregation.

Emerging evidence places myocilin-associated glaucoma in the context of a PCD. Similar to most neurodegenerative PCDs, there is a familial and sporadic form of the

disease. In particular, mutations in the secreted protein myocilin have been linked to inherited forms of glaucoma. To date, more than 70 glaucoma inducing mutations have been documented, located primarily in the C-terminal olfactomedin domain (myoc-OLF) [77]. Interestingly, missense mutations do not seriously compromise the overall tertiary structure of myoc-OLF, as *in vitro* studies for ~25 variants have shown that thermal unfolding occurs in a cooperative manner and variants retain similar secondary structure to wild-type (WT) by circular dichroism [243, 245]. However, these variants are thermally less stable than WT [243, 245] and in cell studies, are found to be sequestered within trabecular meshwork cells [266-267]. At physiological temperatures, the less stable mutant myocilin would be partially unfolded and therefore prone to aggregate. Moreover, diminished secretion of WT myocilin is observed when WT and mutant myocilin are co-expressed [80, 86, 268], suggesting that mutant myocilin can recruit WT to produce a pathogenic response even in the heterozygotes. In both human embryonic kidney (HEK) and human trabecular meshwork (HTM) cells expressing mutant myocilin, large juxtanuclear aggregates were observed and found to be primarily located in the ER, co-localizing with known ER chaperones [86, 97]. Aggregates of mutant myocilin have even been observed in transgenic flies [98]. These aggregates have been shown to be toxic, inducing the ER stress response [84-85, 98], and eventually cause cell death [86, 97-98, 269].

Although emerging clues to the pathogenesis of myocilin-induced inherited forms of glaucoma have come to light in the past decade, little progress has been made towards understanding the molecular mechanisms that lead to sporadic glaucoma, which may be due in part to the heterogeneity of the disorder. In this work, we initially sought to characterize the aggregated form of myoc-OLF and found that both WT and mutant variants of the protein form amyloid fibrils, similar to proteins in other PCDs described above. These fibrils are created under a variety of conditions *in vitro* and fibrillization

Table 5.1. Summary of experiments and results from this study.

Goal	Technique	Result Summary
Identification of Amyloid Fibrils	SEC	Void-volume peak corresponding to aggregated MBP-OLF
	ThT Fluorescence	WT and mutant olfactomedin domain fluoresce ThT
	TEM	Fibrils observed
	Proteolysis	Fibril core is resistant to PK
Determination of Conditions that Increase the Fibrillization Rate	Anionic Detergent	SDS promotes fibrillation
	Oxidizing Agent	<1.5% H2O2 promotes fibrillization
	Low pH	Incubation in citrate buffer, pH 3 promotes fibrillization
	Reducing Agent	BME, DTT, and TCEP promote fibrillization
Examination of Fibril Formation Kinetics	Seeding Assay	Fibril formation is self-propagating and the rate of fibrillization increases when the concentration of seeds is increased
	Multiple Round Seeding Assay	Fibrils are matured after three rounds of seeding
Identification of Amyloidogenic Core Sequence(s)	N-terminal Sequencing	Failed due to multiple N-termini
	Systematic Build-Up of Myoc-OLF	One amyloidogenic stretch is present within the first N-terminal 17 residues
	N-terminal and C-terminal truncations	The presence of other amyloid fibril forming regions, beyond the N-terminal 17 residues, are verified
Identification of Myocilin Amyloid in Cell Culture	Triton X-100 Extraction Followed by Gel-Boiling Analysis	P370L TX insoluble myocilin formed aggregates unable to migrate through the SDS-PAGE stacking gel. The aggregates were able to enter the gel after incubation over a boiling water bath and a second electrophoresis step.
	ThT Staining of CHO Cell Cultures	Intracellular deposits in the P370L myocilin transfected cells fluoresced ThT.

occurs in a nucleation dependent, self-propagating manner (Table 5.1). Mutant myocilin expressed in mammalian cells forms intracellular aggregates containing amyloid fibrils.Taken together, this work provides new insights into myocilin and suggests a novel molecular based hypothesis for pathogenesis.

5.2 Results

5.2.1 Identification of Amyloid Fibrils

5.2.1.1 Initial Identification of Aggregates by Size Exclusion Chromatography

During the original development of the myoc-OLF purification protocol, a void-volume peak corresponding to a large cytosolic MBP-OLF species was isolated by size-exclusion chromatography (SEC) from monomeric MBP-OLF (Fig. 2.1) after amylose affinity purification. Reducing SDS-PAGE revealed that the void-volume fractions are composed of MBP-OLF in an aggregated form (Table 5.1). The intensity of the void-volume peak compared to that of the monomer is not sensitive to incubation at 4 °C, freeze-thaw, or concentration loaded on the column. Furthermore, the species do not interconvert (Fig. 2.2). Indeed, a species eluting in the void-volume of the SEC chromatograph is observed for all variants of myoc-OLF studied in our lab. Even when subjected to fractionation on a column designed to fractionate much larger species (HiPrep 16/60 Sephacryl S-400 HR column; M_r 20,000–8,000,000), a distribution of high molecular weight species is observed (Fig. 5.1).

5.2.1.2 Identification of Amyloid Fibrils Formed from Olfactomedin Domain by ThT

Due to the observed unusual high molecular weight species observed for MBP-OLF by SEC, the high β-sheet content for the myoc-OLF [243-244] and its predicted amyloid propensity [270], we sought to test the hypothesis that the void-volume SEC peak constituted an amyloid. The fluorescent dye, ThT, undergoes characteristic spectral

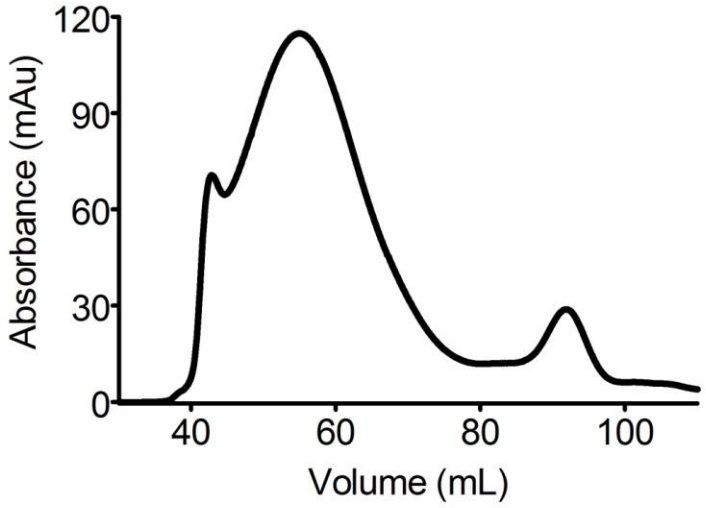

Figure 5.1. SEC chromatograph (M_r 20,000–8,000,000) of MBP-OLF aggregates.

alterations upon binding a variety of amyloid fibrils and not their precursor polypeptides, monomers, or amorphous aggregates of the protein [259, 271]. An increase of ThT fluorescence for MBP-OLF and full-length myocilin aggregates was observed but not in the presence of their respective monomers (Fig. 5.2A, Table 5.1). Similar to WT aggregates, all of the ~30 disease-causing MBP-OLF mutant aggregates studied in lab [243, 245] fluoresced with ThT (Fig. 5.2B, Table 5.1).

To rule out the possibility that MBP could be forming fibrils and contributing to the observed ThT signal, the MBP-OLF void-volume fraction was treated with Factor Xa and aggregates subjected to ThT fluorescence analysis. The cleaved aggregates were purified by an initial amylose affinity purification to remove any cleaved MBP or uncleaved MBP-OLF, followed by SEC to separate the fibrillar material from Factor Xa. Similarly, the small aggregate peak observed by SEC after the cleavage reaction for the monomeric fraction of MBP-OLF at 37 °C, was tested for ThT fluorescence. In both cases, a fluorescent signal for ThT was observed (Fig. 5.2C). No void-volume peak by SEC was observed when MBP was expressed and purified alone (data not shown). It was therefore concluded that the amyloidogenic region was contained to myoc-OLF and not MBP.

5.2.1.3 Proteolysis

The cross-β-sheet core of amyloid fibrils is resistant to proteinase K (PK), a protease highly active against globular or disordered conformations but not against densely packed cross-β regions [258, 272-273]. Treatment of MBP-OLF aggregate with PK followed by purification by SEC revealed a ThT positive void-volume elution peak (Fig. 5.2C, Table 1) adding further evidence that this species contains amyloids.

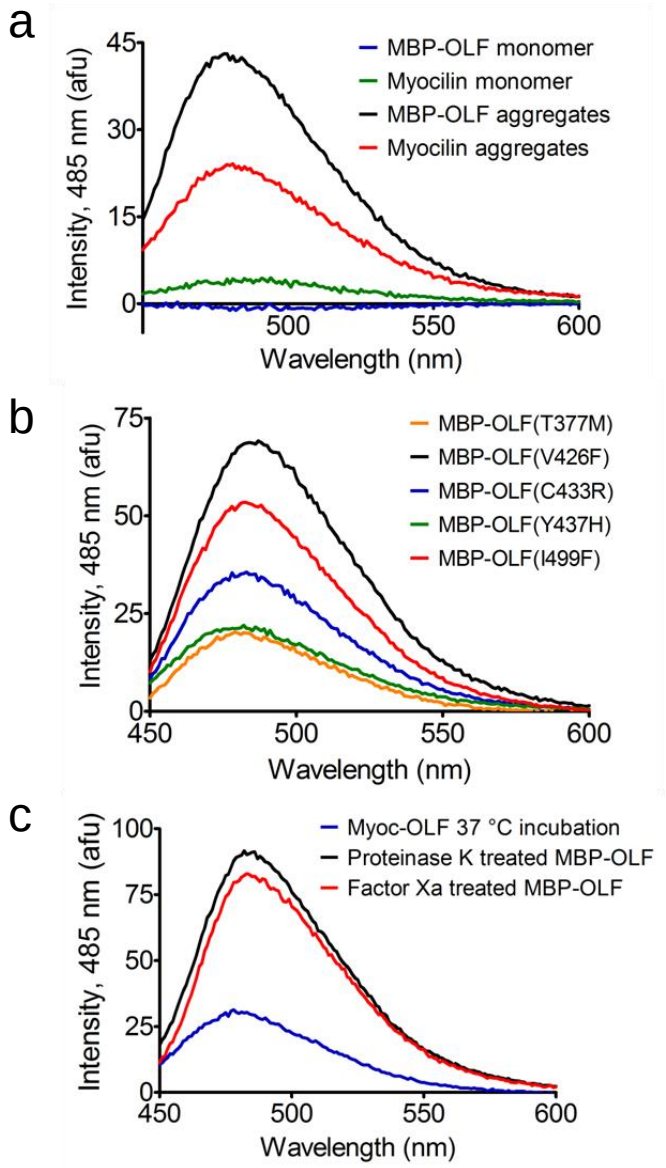

Figure 5.2. ThT fluorescence spectra in the presence of amyloid fibrils. A) Fluorescence emission increase in the presence of aggregated MBP-OLF (black) and aggregated myocilin (red) compared with the monomeric versions (blue, green, respectively). B) Emission spectra for selected aggregated OLF variants. C) ThT emission spectra for myoc-OLF aggregates obtained after incubation at 37 °C (blue), PK treated aggregates (black), and Factor Xa treated aggregates (red). All spectra collected at 25 μg/mL of protein and 5 μM ThT.

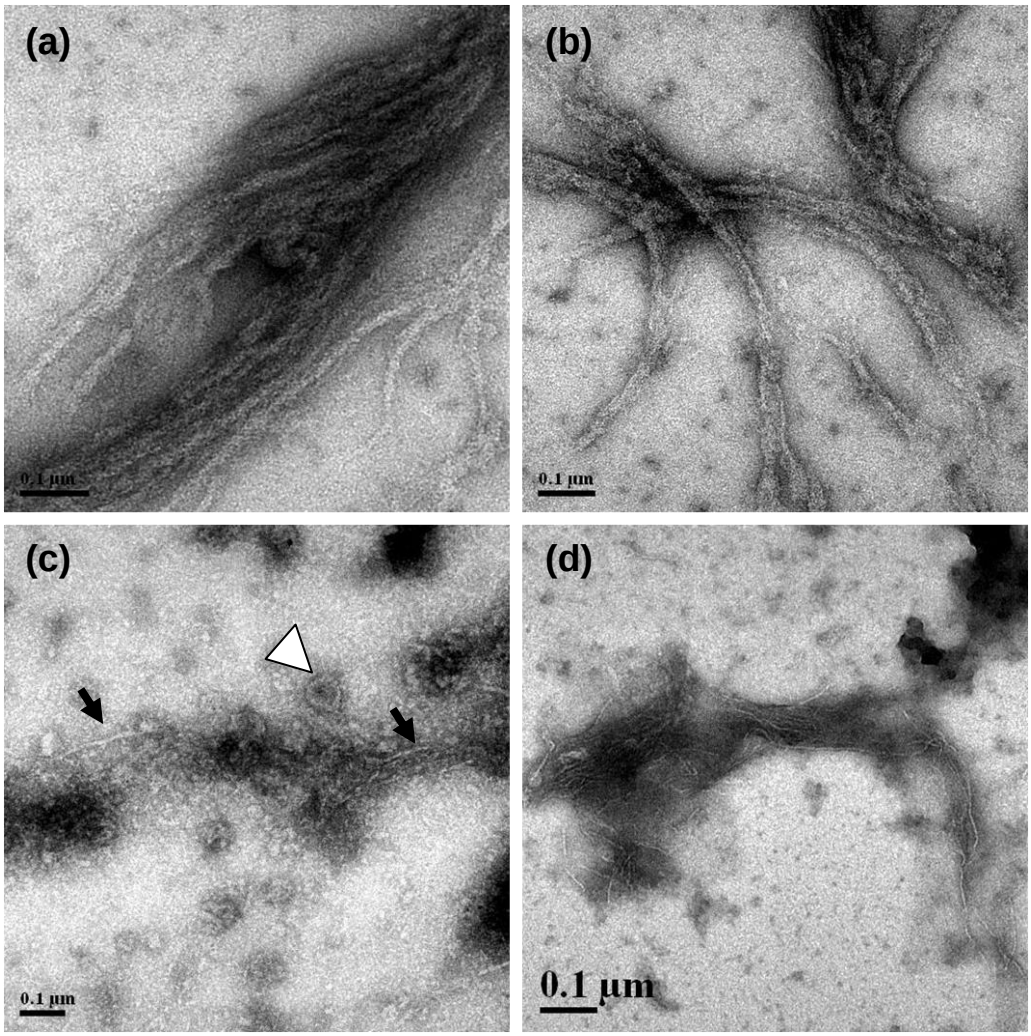

Figure 5.3. Electron micrographs of myoc-OLF amyloid fibrils. A-B) Myoc-OLF fibrils obtained after incubation at 37 °C for 95 hrs. C) Micrograph of myoc-OLF fibrils (black arrows) and torus-shaped oligomers (white arrowhead) formed after incubation at 37 °C in the presence of SDS. D) Myoc-OLF fibrils formed after incubation at 37 °C in the presence of 0.3% H_2O_2.

5.2.1.4 Amyloid Fibrils Visualized by TEM

Transmission electron microscopy was next employed to visualize myoc-OLF fibrils, which were formed *de novo* by incubation at 37 °C for 95 hrs as opposed to the fibrils isolated from *E. coli* by SEC described above. TEM revealed typical amyloid morphology: unbranched fibrils with a diameter of about 10 nm (Fig. 5.3 A-B, Table 5.1). Although amyloid fibril formation can be a generic property of the polypeptide backbone and that essentially any protein could form fibrils under the right destabilizing conditions, we believe this is not the case in our system as fibrils are observed after a long incubation of the OLF domain alone at physiological temperature. Taken together, although there is no definitive test for amyloid, the collection of evidence is strong for myoc-OLF.

5.2.2 Conditions That Promote Spontaneous Fibrillization *In Vitro*

In vitro fibril formation of myoc-OLF takes multiple days (with agitation of sample; Fig. 5.4) to weeks (no agitation of sample; data not shown) to occur because amyloid fibril formation is a nucleation-dependent process [274-275], consisting of both a nucleation phase and an extension phase. The nucleation process requires the self-assembly of monomers, and therefore is the rate-limiting step. However, as described below, the kinetics of myoc-OLF fibrillation can be accelerated by exposing the protein to slightly destabilizing conditions that allow the peptide backbone to be exposed and form the interchain hydrogen bonds associated with amyloid fibrils.

5.2.2.1 SDS, an Anionic Detergent, Promotes Fibrillization

Negatively charged GAGs, such as heparin and heparin sulfate, and anionic detergents accelerate the kinetics of amyloid fibril formation by serving as a nucleating surface [247, 250, 276-278]. In particular, SDS induces the extension of both β_2-microglobulin [279] and α-synuclein [280]. Therefore, the abilities of various SDS

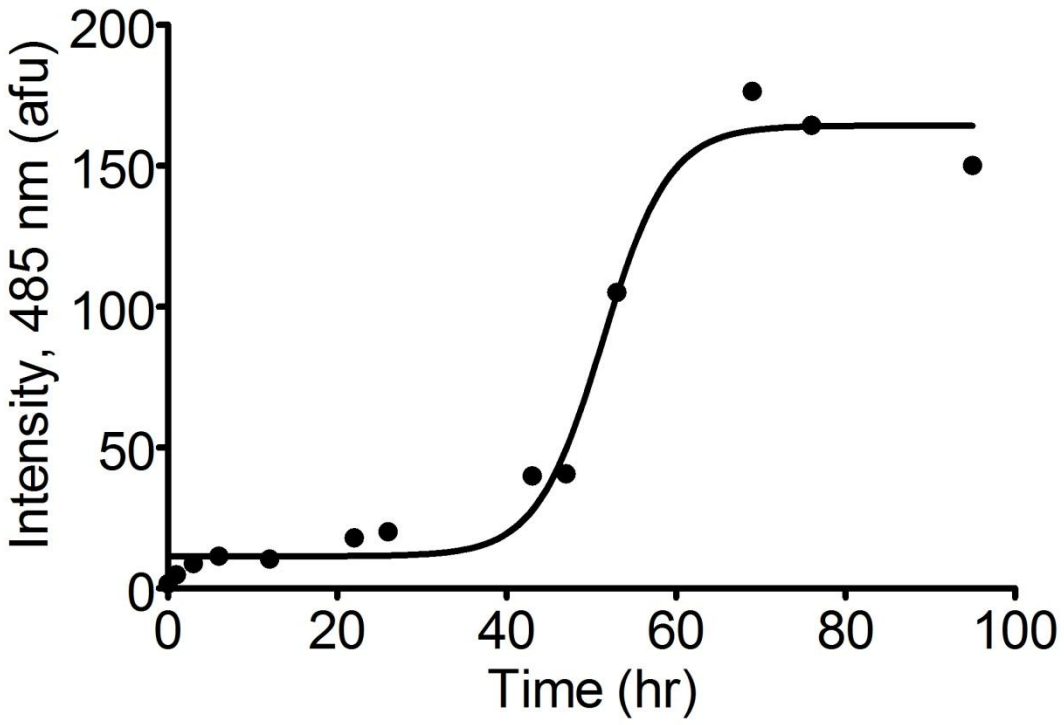

Figure 5.4. Myoc-OLF fibrillization monitored by ThT fluorescence. Myoc-OLF was incubated in phosphate buffer at 37 °C with agitation.

Table 5.2. Conditions that promote fibrillization[a].

Additive	ThT Intensity, 485 nm (afu)
Myoc-OLF (4 °C)	2.1
0 mM SDS	3.7
0.2 mM SDS	139.6
0.4 mM SDS	275.4
0.5 mM SDS	259.4
0.6 mM SDS	255.6
0.8 mM SDS	216.3
1.0 mM SDS	208.4
5.0 mM SDS	26.1
10.0 mM SDS	13.5
0% H_2O_2	21.4
0.03% H_2O_2	152.3
0.3% H_2O_2	313.8
1.5% H_2O_2	275.4
2.9% H_2O_2	32.6
50 mM Citrate, pH 3.0	57.6
5 mM BME	57.6
5 mM DTT	175.3
5 mM TCEP	124.4

[a]All fluorescence intensity readings were acquired with 30 μM OLF and 5 μM ThT.

concentrations to enhance myoc-OLF fibril formation were tested. SDS (0-10 mM) was incubated with 30 μM myoc-OLF without agitation for 95 hrs followed by measurement of ThT fluorescence. Consistent with previous results found with β_2-microglobulin and α-synuclein, SDS stimulates fibril formation at concentrations less than 0.8 mM (Fig. 5.2C, Table 5.1-5.2). This result is consistent with previous reports that concentrations of SDS at or below the critical micellar concentration (CMC) (0.67 mM) induce fibril growth as well as stabilize the fibrils [279]. At concentrations above 1.0 mM, fibrillization was vastly reduced (Table 5.2) most likely due to the formation of amorphous aggregates instead of fibrils. When monomeric myoc-OLF is incubated at 30 °C in the presence of 0.5 mM SDS, no lag phase is observed and a plateau in ThT fluorescence is observed after 30 hrs (Fig. 5.5B, black curve).

5.2.2.2 Oxidizing and Reducing Conditions Promote Fibrillization

We also attempted to mimic *in vitro* certain stresses myocilin is expected to encounter during the ageing process that may promote fibrillization, namely, oxidative stress and low pH. Accumulating evidence supports the role of oxidative stress in POAG [281-283] and it has already been shown to play a role in the development of cataracts, as reviewed by Sharma *et. al.* [284]. To test the effect of oxidative stress *in vitro*, various dilutions of hydrogen peroxide (up to ~3%) were added to monomeric myoc-OLF, followed by incubation at 37 °C for 95 hrs. Treated samples fluoresced with ThT (Table 2) and showed fibrils by TEM (Fig. 5.2D), except for the ~3% sample, which had a ThT signal similar to untreated myoc-OLF (Table 5.1-5.2) and displayed only amorphous aggregates by TEM (data not shown). Myoc-OLF at an identical concentration was also subjected to incubation in citrate buffer (pH 3.0) at 37 °C for 95 hrs. This sample fluoresced with ThT, but to a lesser extent than described for the conditions listed above (Table 5.1-5.2). Conversely, the effect of reductants, expected to reduce the single disulfide bond, on the fibrillization of myoc-OLF was tested. Fibrillization by disulfide

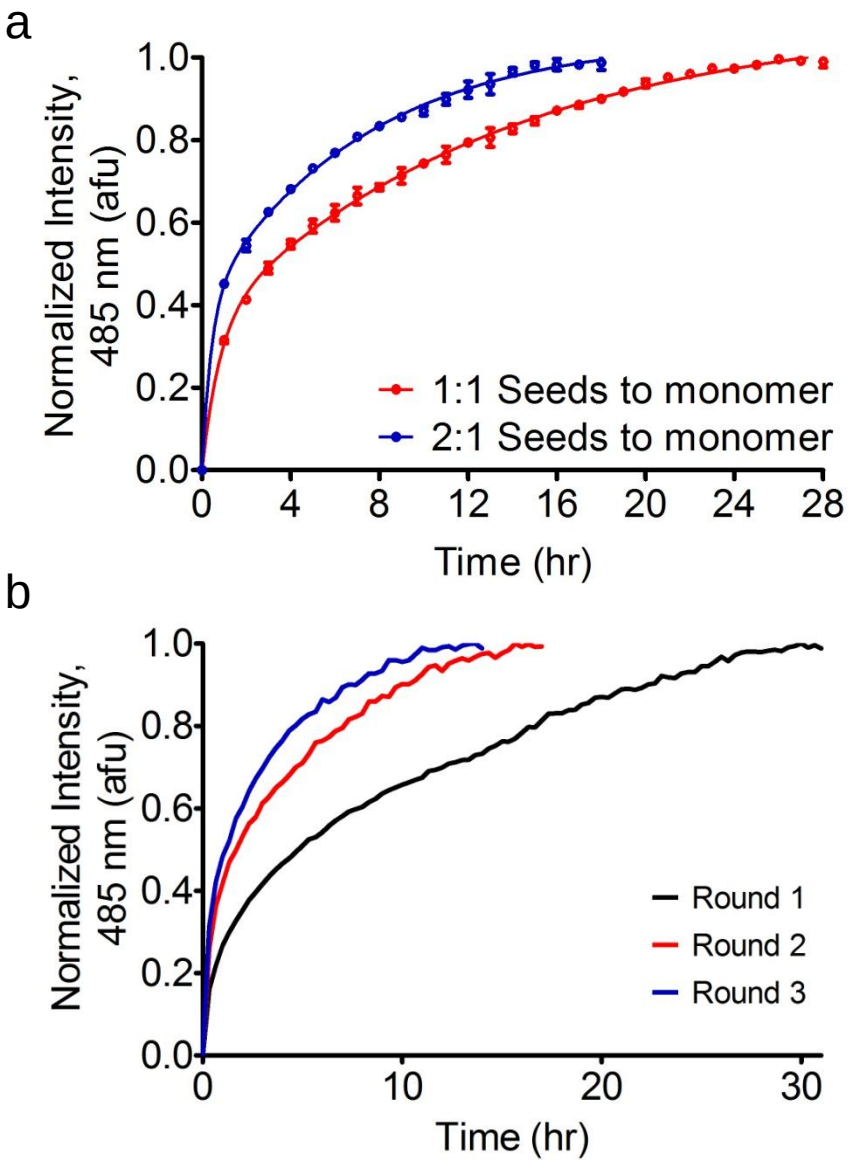

Figure 5.5. Extension of myoc-OLF fibrils in the presence of SDS. A) The formation of fibrils is accelerated by the addition of pre-formed fibrils (seeds). B) Self-seeding dependent maturation of myoc-OLF fibrils.

reduction is not unprecedented, as dithiothreitol (DTT) was shown to accelerate the fibril formation process for β_2-microglobulin [285]. Myoc-OLF was incubated in the presence of β-mercaptoethanol (BME), DTT, and tris(2-carboxyethyl)phosphine (TCEP). All three treated samples fluoresced with ThT (Table 5.1-5.2). The ThT signal was the lowest for BME and identical to that of the citrate (pH 3.0) sample (Table 5.2).

5.2.3 Myoc-OLF Forms Amyloid Fibrils by a Nucleation Dependent Mechanism

As mentioned above, *in vitro* amyloid fibril growth occurs with an initial lag phase, during which monomers assemble to form nuclei. Once the solution is nucleated, fibril extension occurs at a rapid rate by the addition of monomer to the fibril ends (elongation phase) until the solution is depleted of monomeric protein and a plateau is observed (Fig. 5.4) [286]. Fragmented amyloid fibrils may also serve as nuclei when added to globular protein and initiate rapid fibril growth in a process known as seeding.

5.2.3.1 Kinetics of Fibril Formation

In the seeding assay, myoc-OLF fibrils, formed *in vitro* by incubation at 37 °C in a water bath in the presence of 0.5 mM SDS, were verified by ThT fluorescence and fragmented by sonication. The 'seeds' were added at a 1:1 molar ratio with purified monomeric myoc-OLF in the presence of 0.5 mM SDS and incubated at 30 °C. ThT fluorescence was monitored and a rapid growth rate was observed with a $t_{1/2}$= ~3 hrs (Fig. 5.5A). Upon doubling the quantity of seeds, fibrillization occurred at a faster rate ($t_{1/2}$= ~1.5 hrs) (Fig. 5.5A, Table 5.1). This reaction reached a plateau presumably after the pool of globular myoc-OLF was depleted, about 10 hrs sooner than when fewer seeds were used. Both seeding experiments were performed in duplicate and rates were reproducible when the experiments were conducted at 30 °C.

5.2.3.2 Maturation of Fibrils by Multiple Seeding Rounds

The self-seeding propensity of myoc-OLF was analyzed by conducting multiple seeding rounds where the fibrillized material from a previous round was used to seed a subsequent round. To produce initial seeds, monomeric myoc-OLF was incubated alone in the presence of 0.5 mM SDS (Fig. 5.5B, black curve).The product was used to seed monomer in the second round (Fig. 5.5B, red curve), and the second round product was used to seed the third round (Fig. 5.5B, blue curve). An increase in the rate was observed each time (Fig. 5.5B). Subsequent seeding rounds did not yield an increase in rate of formation, indicating full maturation of the fibrils was achieved after three rounds (Table 5.1).

5.2.4 Identification of the Amyloidogenic Core

To identify the sequence(s) in myoc-OLF prone to forming amyloid fibrils, preformed fibrils were initially treated with PK, as described above, to digest any extraneous residues leaving only the core fibril, followed by N-terminal sequencing. Unfortunately, there was a heterogeneous mixture that did not allow for unambiguous determination of N-terminal sequence(s). As an alternative approach to identify the amyloidogenic core, we systematically assembled the myoc-OLF domain in ~20 residue segments by fusion to MBP (Fig. 5.6A). SEC was employed to identify which constructs contained the fibril forming sequence, as a void-volume peak would be present for those that did. Surprisingly, the construct containing the first 17 residues (MBP-$OLF_{228-244}$) (Fig. 5.6A, blue), as well as all subsequent constructs tested, yielded an aggregate void-volume peak (Fig. 5.6B, Table 1). All void-volume peaks fluoresced with ThT (Fig. 5.6C).

The sequence for MBP-$OLF_{228-244}$ was analyzed *in silico* for amyloid propensity by ZipperDB [287], and a predicted fibril forming region was located in the middle of this stretch (SGYLRSG). In an attempt to disrupt this amyloid fibril fragment, a stop

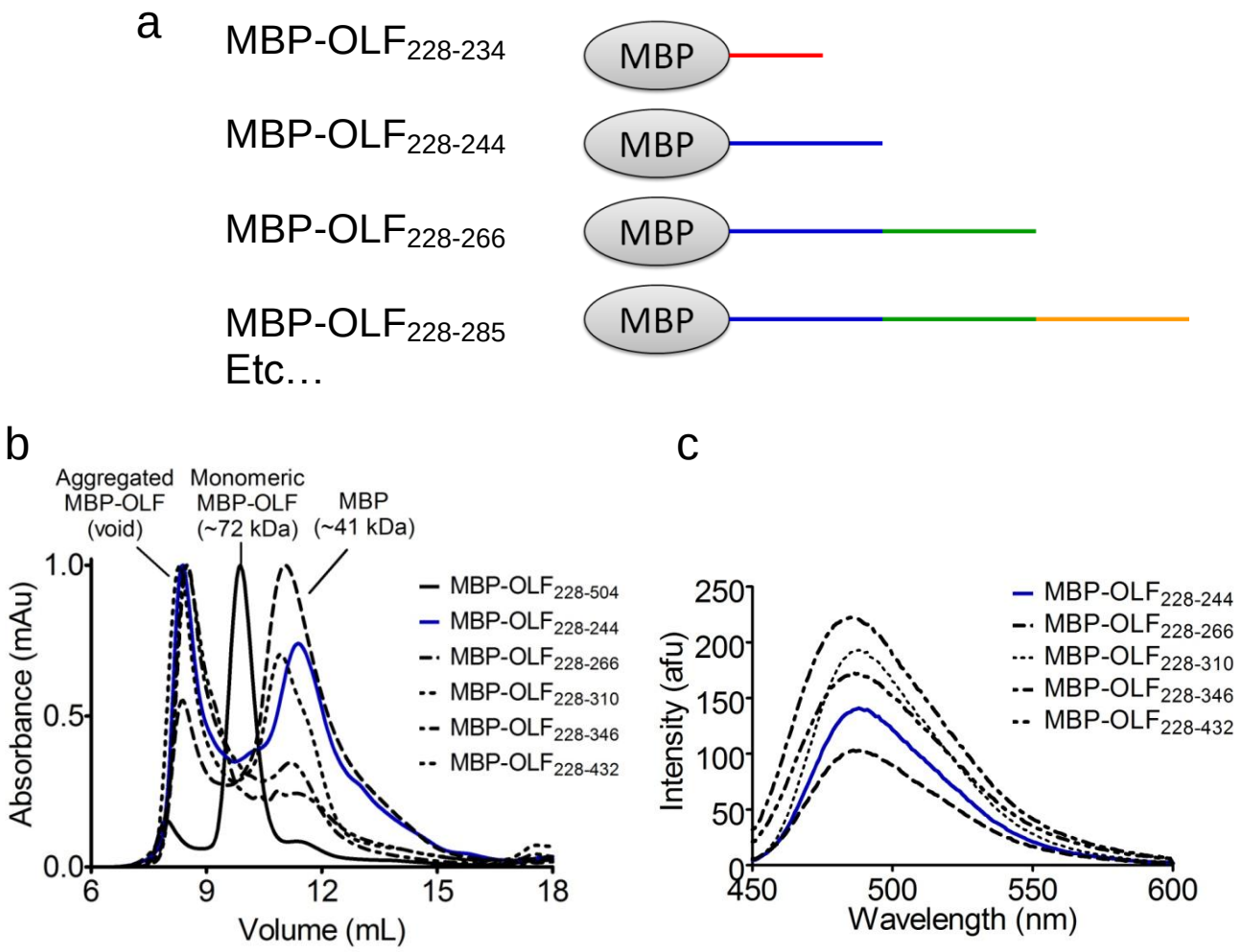

Figure 5.6. Systematic construction of the myoc-OLF domain. A) Schematic of constructs. B) SEC chromatograph of selected truncated constructs (dotted and dashed lines) including the construct containing the first 17 residues (solid blue) and full-length myoc-OLF (solid black). C) ThT fluorescence spectra for each selected construct's void-volume fraction isolated by SEC. Spectra were not acquired at equal concentrations, but all fluoresce positive with ThT.

a

```
1   MRFFCARCCS FGPEMPAVQL LLLACLVWDV GARTAQLRKA NDQSGRCQYT  50
51  FSVASPNESS CPEQSQAMSV IHNLQRDSST QRLDLEATKA RLSSLESLLH  100
101 QLTLDQAARP QETQEGLQRE LGTLRRERDQ LETQTRELET AYSNLLRDKS  150
151 VLEEEKKRLR QENENLARRL ESSSQEVARL RRGQCPQTRD TARAVPPGSR  200
201 EVSTWNLDTL AFQELKSELT EVPASRILKE SPSGYLRSGE GDTGCGELVW  250
251 VGEPLTLRTA ETITGKYGVW MRDPKPTYPY TQETTWRIDT VGTDVRQVFE  300
301 YDLISQFMQG YPSKVHILPR PLESTGAVVY SGSLYFQGAE SRTVIRYELN  350
351 TETVKAEKEI PGAGYHGQFP YSWGGYTDID LAVDEAGLWV IYSTDEAKGA  400
401 IVLSKLNPEN LELEQTWETN IRKQSVANAF IICGTLYTVS SYTSADATVN  450
451 FAYDTGTGIS KTLTIPFKNR YKYSSMIDYN PLEKKLFAWD NLNMVTYDIK  500
501 LSKM
```

b

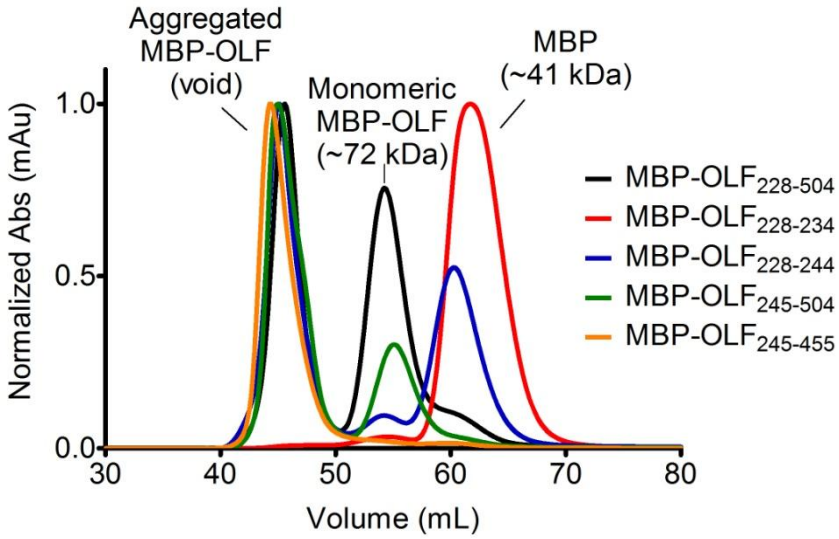

c

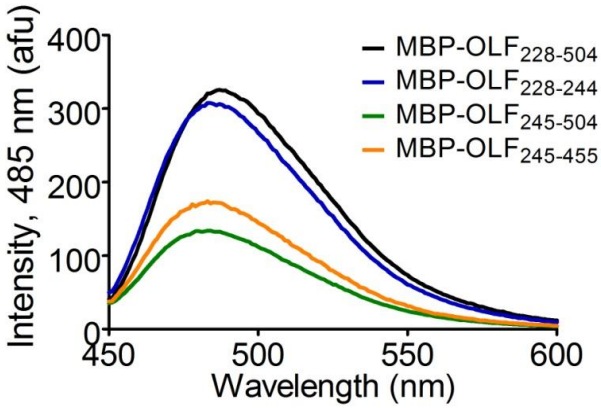

d

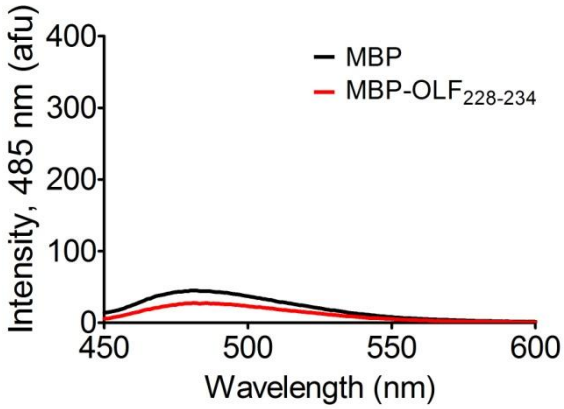

Figure 5.7. Identification of amyloidogenic regions in myoc-OLF. A) Myocilin sequence with various truncations tested in this study including the MBP-OLF construct containing the first 7 residues (red, MBO-$OLF_{228-234}$), containing the first 17 residues (blue, MBP-$OLF_{228-244}$), lacking the first 17 residues (green, MBP-$OLF_{245-504}$), and lacking the first 17 N-terminal residues and last 48 residues from the C-terminus (orange, MBP-$OLF_{245-455}$). The N-terminal region of myocilin eliminated in our myoc-OLF construct is grey. B) SEC chromatogram of the above listed constructs. C) ThT fluorescence spectra of the void-volume fractions isolated by SEC for each construct. D) ThT fluorescence spectra of monomeric MBP (black) and MBP-$OLF_{228-243}$ (red) after incubation in the presence of SDS for 95 hrs at 37 °C.

codon was introduced at Y235 to create MBP-$OLF_{228-234}$ (Fig. 5.7A, red). After expression and purification of MBP-$OLF_{228-234}$, no void-volume peak was observed by SEC (Fig. 5.7B, red curve, Table 5.1). To test whether the lack of aggregated MBP-$OLF_{228-234}$ material was due to a disruption in the fibril forming region and not a byproduct of folding in close proximity to the C-terminus of MBP, monomeric MBP-$OLF_{228-234}$ was incubated for 95 hrs at 37 °C in the presence of 0.5 mM SDS. The ThT fluorescence for MBP-$OLF_{228-234}$ was less than MBP treated in an identical manner (Fig. 5.7D) indicating that neither fibrillated, as the overall intensity was significantly lower than for MBP-$OLF_{228-244}$ and WT MBP-OLF (Fig. 5.7C).

The presence of additional fibril forming segments was tested in several ways, based on the knowledge of one fibril forming segment located in the first 17 residues (Table 5.1), and the identity of a core-OLF domain ($OLF_{228-455}$) (Chapter 3) [243]. First, a truncated construct lacking the first 17 residues (MBP-$OLF_{245-504}$) (Fig. 5.7A, green) was created. This construct displayed a void-volume peak isolated by SEC (Fig. 5.7B, green curve) that fluoresced strongly with the addition of ThT (Fig. 5.7C, green curve, Table 5.1). Thus, other amyloidogenic regions beyond the N-terminal 17 residues of myoc-OLF axist and need further identification.

Second, a variation of the core-OLF (see Chapter 3) sequence ($OLF_{228-455}$) was tested [244]. Previous attempts to generate core-OLF by *de novo* molecular biology yielded only a void-volume peak in the SEC chromatogram (Fig. 5.8). To test the presence of amyloidogenic sequences after the N-terminal 17 residues of myoc-OLF, but before the last ~50 C-terminal residues that are eliminated in the core-OLF domain, MBP-$OLF_{245-455}$ was expressed (Fig. 5.7A, orange). Again, only a void-volume peak was present in the SEC chromatogram (Fig. 5.7B) that also fluoresced in the presence of ThT (Fig. 5.7C). These results indicate that one or more amyloidogenic sequences are present within the structural core of the myoc-OLF domain, specifically residues 245-455 (Table

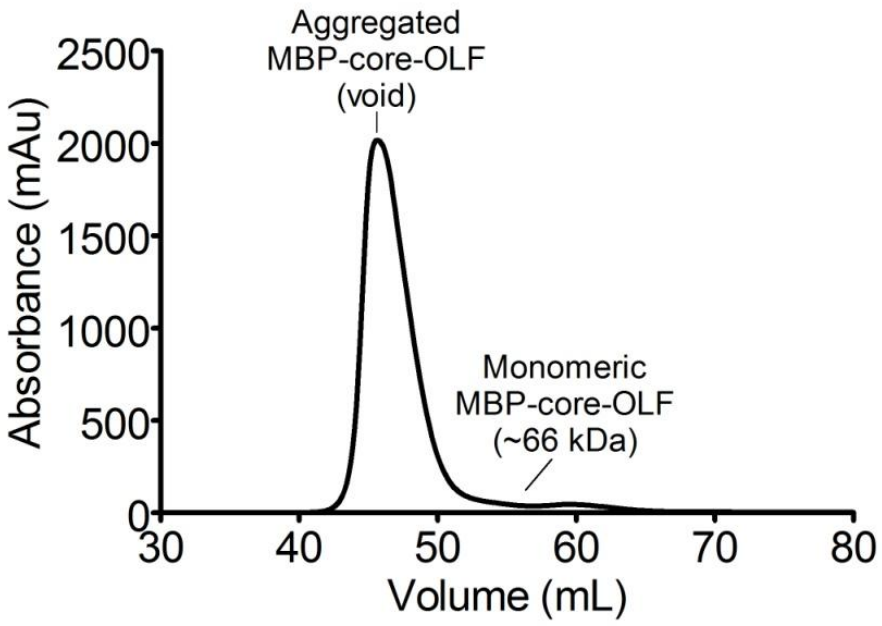

Figure 5.8. SEC chromatogram of MBP-core-OLF (MBP- $OLF_{228-455}$).

5.1), and does not exclude the possibility that an amyloidogenic stretch is present in the removed C-terminal residues (456-504).

5.2.5 Myocilin Amyloids in Cell Culture Model (Chinese Hamster Ovary Cells)

Previous work in the field has shown that disease-causing myocilin mutants are detergent insoluble [87], highly aggregation-prone, and accumulate in large aggregates in the ER of human embryonic kidney (HEK) cells and differentiated HTM cells [80, 84]. The possibility that aggregates found in cell models are amyloid fibrils was tested by expressing full-length myocilin in Chinese hamster ovary (CHO) cells for analysis by a gel-boiling assay and ThT staining of intact cells. CHO cells were transfected with either vector control, WT full-length myocilin, or a severe disease phenotype mutant myocilin, P370L, in the laboratory of Dr. Douglas Vollrath at Stanford University. All constructs possessed an N-terminal S-tag which was exploited for immunoblotting experiments. The cultured cells were harvested and myocilin was extracted by a previously reported Triton X-100 (TX) solubility assay, in which WT and non-glaucoma causing variants of myocilin are TX soluble, whereas disease causing variants are TX insoluble [87].

5.2.5.1 Triton X-100 Extraction and SDS-PAGE Gel-Boiling Analysis

Equivalent amounts from the TX soluble and insoluble fractions were analyzed by SDS-PAGE and immunoblotting. The samples were loaded into the SDS-PAGE gel in a loading buffer with a reduced amount of SDS (1% final) as opposed to the typical 2%. Due to their aggregated nature, amyloid fibrils are reluctant to enter polyacrylamide gels. This was indeed the case for the P370L TX insoluble sample, as aggregated material was present and unable to migrate through the stacking gel and enter the resolving gel (Fig. 5.9, left). This was also observed to a lesser extent in the P370L TX soluble and WT TX insoluble fractions (Fig. 9, left). As expected, neither vector control samples nor WT TX soluble sample exhibited evidence of aggregation (Fig. 5.9, left). Similar mobility trends

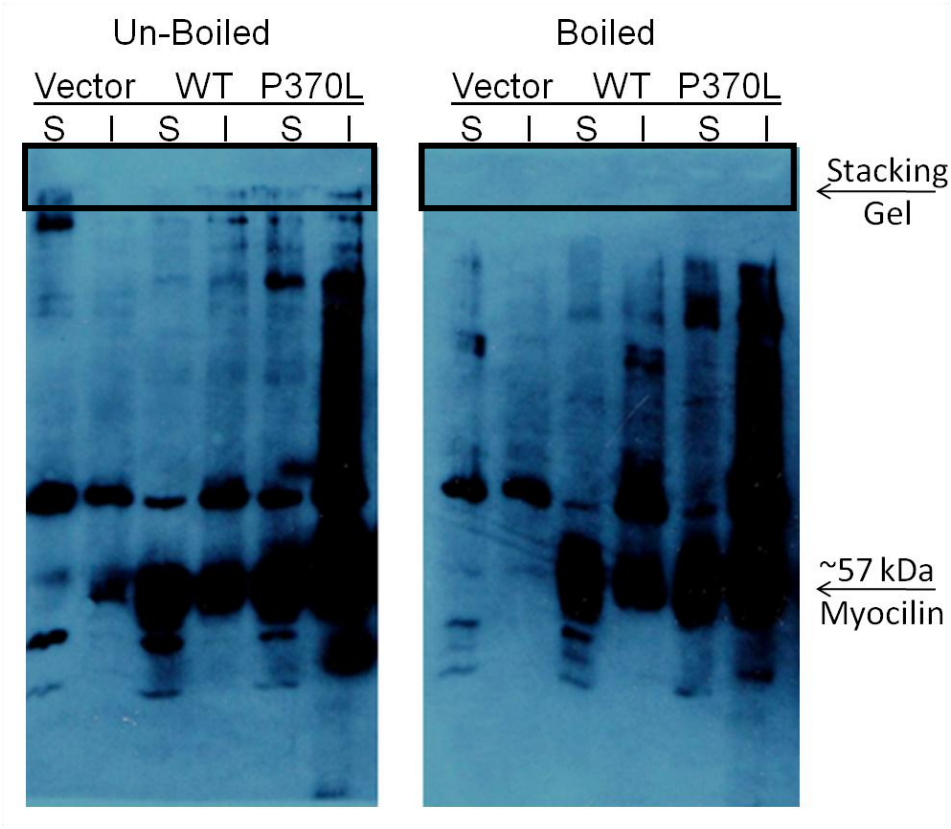

Figure 5.9. Boiled gel analysis of myocilin aggregates in transfected CHO cells. Left) Immunoblot of TX soluble (S) and insoluble (I) fractions. Stacking gel is outlined with a black box. Right) Immunoblot of same samples, however, the polyacrylamide gel was subjected to boiling and a second electrophoresis step before blotting.

have been observed for D380A, E323K, Y437H, G364V, and K423E glaucoma-causing myocilin variants [97]. Amyloid aggregates can be disrupted by boiling of the gel, allowing the constituent monomers to be released and enter the gel upon electrophoresis [288]. This was the case for our samples, as all aggregated samples entered the resolving gel after the gel was boiled for 10 minutes and a second electrophoresis step was performed (Fig. 5.9, right, Table 5.1).

5.2.5.2 ThT Staining of CHO Cell Cultures

Finally, to explicitly observe amyloid in cell culture and determine if the identified aggregated species were indeed forming amyloid fibrils, we stained the transfected CHO cells were stained with ThT. There was minimal ThT fluorescence in the WT sample (Fig. 5.10, top panels) signifying low levels of amyloid fibrils, a result consistent with the gel-boiling assay described above. Conversely, ThT staining of CHO cells transfected with P370L myocilin fluoresced (Fig. 5.10, bottom panels), indicating the presence of mature fibrils in the cells as predominantly intracellular deposits (Table 5.1). For this sample, there was no discernible extracellular staining.

5.3 Discussion

Amyloidoses display considerable heterogeneity and are influenced by various factors including inherited mutations in proteins [289], interactions with pathological molecular factors/environments [290], as well as by intracellular and extracellular quality control systems against misfolded proteins [261, 265, 291-292]. These factors, whether acquired or inherited, contribute to ER stress which may trigger apoptotic pathways. In inherited amyloidoses, the efficiency of the ER machinery to target destabilized mutant proteins for degradation is central to disease etiology, as well as the enhanced tendency of these variants to aggregate [289].

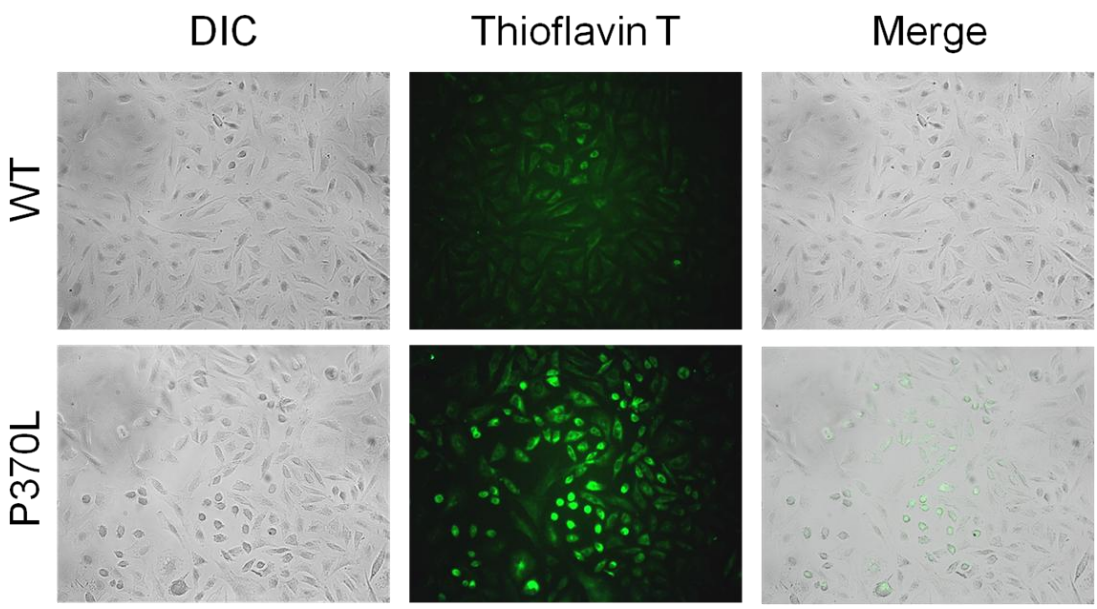

Figure 5.10. Comparison of ThT fluorescence in CHO cells transfected with WT or mutant (P370L) myocilin. Left) Differential interference contrast micrograph (DIC); middle) ThT fluorescence (green); right) merge of DIC and ThT.

In these inherited conformational disorders, intracellular accumulation of amyloidogenic protein due to point mutations in the amino acid sequence is a common phenomenon. For example, familial amyloidotic polyneuropathy and familial amyloidoticcardiomyopathy are autosomal dominant inherited diseases caused by genetic mutations in the transthyretin gene, of which over 100 variants have been described [289]. Another example includes familial Alzheimer's disease (AD), in which autosomal dominant inheritance of mutant genes that encode for either amyloid precursor protein (APP), presenilin 1, or presenilin 2 cause early-onset AD [293]. Amyloid deposits localized to the ER and Golgi have been identified in Type-II diabetes mellitus which occurs when human islet amyloid polypeptide aggregates in these organelles leading to apoptosis and β-cell death [294-296].

In familial forms of POAG, aggregation has been shown to occur in the ER of HTM cells expressing myocilin variants, which eventually leads to apoptosis [84, 97]. Large juxtanuclear aggregates have been observed in the ER of both human embryonic kidney and HTM cells [97]. Destabilizing point mutations have been shown to increase the aggregation propensity of myoc-OLF, as identified by an increased ratio of aggregate to monomer when purified from *E. coli* by SEC (Chapter 2) [243, 245]. In this work, we have shown that intracellular deposits present in CHO cells expressing mutant (P370L) myocilin fluoresce in the presence of ThT. Promiscuous β-strand interactions due to a destabilized or misfolded protein are a general feature of the protein aggregates that make up amyloidoses [297], as highlighted by multiple amyloidogenic regions, both identified and proposed, in the OLF domain of myocilin. *In vitro* characterization of recombinant myoc-OLF revealed that the OLF domain of myocilin, for both WT and mutant, is prone to fibril oligomerization, identifying glaucoma as a possible new amyloidosis. Structural analysis of the OLF fibrils showed that the recombinant myoc-OLF assembles *in vitro* into unbranched ~10 nm thick fibrils. Importantly, the fibrils show tinctorial affinity for ThT dye and are resistant to proteolysis by PK.

In addition to familial POAG, a novel hypothesis for the origin of pathogenesis of late-onset glaucoma has emerged from this work. *In vitro*, WT myoc-OLF fibril formation displays a lag phase of several days to weeks when incubated alone at physiological temperature but can be accelerated by the addition of destabilizing agents, and some WT myoc-OLF aggregates are present in CHO cells. However, the ability of myocilin to form fibrils in the trabecular extracellular matrix would be low under normal conditions in the eye, as homeostasis is tightly regulated and molecular chaperones are present to modulate the earliest aberrant protein interactions that lead to amyloid fibril formation [291]. In the aged eye, these regulations may not be as strictly controlled due to gradual deterioration of stress response mechanisms. Myocilin fibrillization and deposition could occur, seed other monomeric myocilin, which in turn could create a denser trabecular extracellular matrix and alter aqueous humor outflow leading to increased intra-ocular pressure (IOP). In addition, accumulating evidence has linked oxidative stress with glaucoma. Antioxidant enzymes, such as superoxide dismutase, malondialdehyde, and glutathione peroxidase, have been reported in aqueous humor and levels have been shown to be significantly higher in the aqueous humor of POAG patients [283]. In our study, monomeric myoc-OLF samples incubated with low levels of H_2O_2 formed amyloid fibrils, suggesting that oxidative stress may play a role in initiating the myoc-OLF fibrillization process in late-onset glaucoma. It is plausible that other proteins in the trabecular extracellular matrix, many of which are not well-characterized, might be similarly prone to fibrillization upon exposure to oxidative stress.

It should be noted that glaucoma is a very heterogeneous disorder, and that myocilin-associated POAG may be one of many origins of pathogenesis. Another amyloidogenic peptide, Aβ, has been identified to both colocalize with and induce apoptosis in retinal ganglion cells *in vivo*, and a compound used to reduce Aβ deposits in Alzheimer's disease was equally effective in treating glaucomatous degeneration [298]. Myocilin is also expressed in the optic nerve head [39], and it is possible, although

untested, that co-aggregation between myocilin and Aβ could occur. This "molecular cross-talk" is not unprecedented. Inoculation of an Alzheimer's transgenic mouse model with prions has been shown to lead to a dramatic acceleration and exacerbation of both pathologies, and *in vitro* protein misfolding could be enhanced by a cross-seeding mechanism [299]. Another example occurs in the case of familial amyloidosis of Finnish type (FAF), in which point mutations in plasma gelsolin cause aberrant cleavage that results in amyloidogenic fragments that fibrillize extracellularly [247]. However, mouse models for this disorder also experience a decline in cellular proteostasis, due to amyloid-like intracellular inclusions containing Aβ, APP, and other amyloidogenic polypeptides [300].

Taken together, this work provides a new hypothesis as to the role of myocilin in the pathogenesis of both familial and sporadic forms of glaucoma. Despite strong evidence that myoc-OLF forms amyloid fibrils both *in vitro* and in transfected CHO cells, the relevance to glaucoma is highly dependent on future experiments focused on studying fibril formation in HTM cells. Once this key experiment is established, a connection between raised myocilin expression levels and amyloid formation could be explored, as increased myocilin expression leads to elevated IOP and aqueous humor outflow resistance [67]. Finally, the exact identification of amyloidogenic sequences in the OLF domain could be achieved by optimizing the PK cleavage protocol and subjecting the treated aggregates to mass spectrometry or NMR analysis.

5.4 Methods

5.4.1 Protein Expression and Purification

The plasmid for MBP-OLF was cloned as described before (see Chapter 2) [243-244]. Myocilin mutants and truncated forms of myoc-OLF were generated by site-directed mutagenesis (QuikChange, Stratagene) of the MBP-OLF plasmid. Mutated

plasmids were verified by DNA sequencing (MWG Operon) and transformed into Rosetta-Gami 2(DE3)pLysS cells (Novagen), cultured, induced, harvested, and purified as described before [243-244]. In summary, all constructs were subjected to an initial purification over an amylose affinity column. Cytosolic aggregates and monomeric protein were further fractionated by size-exclusion chromatography (SEC). In the case of the truncated constructs, SEC was carried out on a Superdex 75 GL column (GE Healthcare). Cleavage of myoc-OLF from MBP was accomplished by incubating with Factor Xa by following the previously described protocol [243-244].

5.4.2. *In Vitro* Fibril Formation

Monomeric myoc-OLF (30 μM) was incubated in the presence of various destabilizing agents at 37 °C for 72-95 hrs. These agents included 50 mM citrate, pH 3.0, SDS (0-10 mM), H_2O_2 (0-2.9%), 5 mM β-mercaptoethanol (BME), 5 mM dithiothreitol (DTT), or 5 mM tris(2-carboxyethyl)phosphine (TCEP). The presence of amyloid fibrils was confirmed by monitoring the fluorescence intensity using a RF-5301 PC spectrofluorophotometer (Shimadzu) after 1 min incubation with 5 μM Thioflavin T (ThT, Ex λ: 440 nm; Em λ: 485 nm).

5.4.3 Spontaneous and Seeded Aggregation Assays

In the spontaneous aggregation assay, myoc-OLF was incubated in 0.5 mM SDS, phosphate buffer (10 mM Na_2H/KH_2PO_4, 200 mM NaCl, pH 7.2) and 40 μM ThT at 30 °C. Fibril formation of myoc-OLF without SDS was also monitored, in which 10 μM monomer was mixed with Buffer A and 5 μM ThT. In both cases, fibril formation was monitored by ThT fluorescence.

For seeding assays, preformed myoc-OLF fibrils (0.5 mM SDS, 37 °C incubation in a water bath for 72 hrs) were pelleted and washed in phosphate buffer to remove SDS. Afterwards, the fibrils were sonicated for 20 pulses at a 20% duty cycle using a Branson

Sonifier 450 (VWR). Monomeric myoc-OLF (15 μM) was inoculated with 15-30 μM seeds in a 100 μL reaction volume in the presence of 0.5 mM SDS, phosphate buffer, and 40 μM ThT. Fluorescence intensity was monitored while the sample incubated at 30 °C via a circulating water bath (VWR). In the case of the multiple round seeding assays, the fibrils of the previous round were used as seeds for the next round using a 1:1 ratio seeds to monomer (15 μM each). Fibril formation was followed by increase in ThT fluorescence.

5.4.4 Proteinase K Digestion

Proteinase K (2 μL of 20 mg/mL solution; New England Biolabs) was added to 2 mL of 8 μM MBP-OLF fibrils in 50 mM Tris HCl, pH 8.0 and 150 mM NaCl. The reaction was incubated for 1 hr at 37 °C. The reaction was then purified by amylose affinity resin, and the unbound flow through fractions were subjected to SEC on a Sup 75 column. The elution fractions corresponding to the void volume were concentrated and analyzed by SDS-PAGE and ThT fluorescence.

5.4.5 Transmission Electron Microscopy

Myoc-OLF fibrils were visualized by transmission electron microscopy. Sample volumes of 2 ul were pipette onto carbon-coated 400-mesh copper grids and blotted after 60s with Whatman #4 filter paper. Immediately after blotting, a 2 uL aliquot of 1% uranyl acetate was pipetted onto the grid and again blotted after 30 s. Images of negatively stained samples were collected with a JEOL JEM-1400 transmission electron microscope. Samples were screened at low magnification (20,000x – 30,000x) with an Orius SC1000 CCD camera. Once fibrils were identified, higher-magnification images were collected with an UltraScan1000 CCD camera.

5.4.6 Creation of Stable Cell Lines with Tetracycline Inducible Myocilin Expression

To place myocilin cDNAs under the control of a tetracycline-inducible promoter, DNA fragments encoding wild type or P370L mutant myocilin fused at the 3' end with a sequence encoding the 15 amino acid S-peptide from *E. coli* RNAse A [301] were inserted into the *PmeI* site of pcDNA4/TO (Invitrogen). DNA sequence analysis was performed to confirm that coding sequences were correct and in-frame with the S-peptide tag. To create stable cell lines with inducible myocilin expression, plasmids pcDNA4/TO-Myoc WT-S-tag and pcDNA4/TO-Myoc P370L-S-tag and the vector pcDNA4/TO control were individually transfected into T-REX-CHO cells (Invitrogen) using Lipofectamine plus. Two days after transfection, 50 μg/ml zeocin was added to select transfectants. Single cell colonies were picked following selection with zeocin for about two weeks. The expression of recombinant myocilin protein was induced by adding 1μg/ml tetracycline and verified by immunoblot at 48hr post-induction. Cloned cell lines were designated T-REX-CHO (pcDNA4/TO-Myoc WT-S-tag), T-REX-CHO (pcDNA4/TO-Myoc P370L-S-tag) and T-REX-CHO (pcDNA4/TO vector). For experiments, stable inducible cells were grown in Ham's F12 medium supplemented with 5% FBS, 1% penicillin-streptomycin, 2 mM glutamine, 10 μg/ml blasticidin, and 50 μg/ml zeocin.

5.4.7 Thioflavin T Staining for Amyloid Fibrils

6 X 10^4 cells were grown on poly-D-lysine-coated cover slips overnight and the expression of myocilin was then induced by adding 1 μg/ml tetracycline for 48 hr. Cells were processed for thioflavin T staining essentially as described [302]. Briefly, cells were fixed in 4% paraformaldehyde at room temperature for 15 min and washed in PBS three times. Cells were stained with Mayer's hematoxylin for 2 min, washed in water for 5 min, then incubated in 1% (w/v) thioflavin T for 3 min, rinsed in water again for 5 min, and finally incubated in 1% (v/v) acetic acid for 20 min. After the stained cells were

washed thoroughly in water, cover slips were mounted with FluorSave Reagent (Calbiochem) for 2 hr. Fluorescence microscopy was used to identify and quantify thioflavin T positive cells, which appeared green.

5.4.8 Triton X-100 Extraction and Boiled Gel Analysis

WT, P370L myocilin, and vector control cell pellets were thawed from -80 °C on ice, resuspended in 400 μL of extraction buffer (1X PBS, pH 7.4, 5 mM EDTA, 1% Triton X-100 (TX) with Complete protease inhibitor cocktail (Roche)), and incubated on ice for 30 minutes. The samples were centrifuged at 13,000 rpm for 15 minutes. After which, the supernatant was transferred to a new microcentrifuge tube and set aside as the TX soluble fraction. The pellet is the TX insoluble fraction and is solubilized in 100 μL of SDS buffer (1% SDS in PBS) for 10 minutes at room temperature. After addition of 300 μL extraction buffer, the sample was sonicated for 20 s with the output at 5.

The boiled gel protocol was adapted from a previously reported protocol for purification of yeast prion polymers from cell lysates [288]. In summary, TX soluble and insoluble samples containing 1% SDS and 40 μg total protein were loaded onto an SDS-PAGE gel and run for 45 minutes. The electrophoresis step was halted and the wells were sealed with a new portion of stacking gel. Once the newly added acrylamide was solidified, the gel was incubated over a boiling water bath for 10 minutes, cooled to room temperature, and then subjected to a second electrophoresis step. The proteins were transferred to Immun-Blot PVDF membrane (Bio-Rad) and then subjected to immunoblotting.

CHAPTER 6

THE ACID β-GLUCOSIDASE ACTIVE SITE EXHIBITS PLASTICITY IN BINDING 3,4,5,6-TETRAHYDROXYAZEPANE-BASED INHIBITORS: IMPLICATIONS FOR PHARMACOLOGICAL CHAPERONE DESIGN FOR GAUCHER DISEASE

6.1 Introduction

Gaucher disease (GD), the most common lysosomal storage disorder, is caused by inherited point mutations in alleles of acid-β-glucosidase (GCase), a lysosomal enzyme that hydrolyzes glucosylceramide (GlcCer) (Fig. 6.1) and related substrates [303]. GD-associated GCase variants exhibit endoplasmic reticulum (ER) folding and trafficking defects [304] and are either retained in the ER [305] and/or undergo ER-associated degradation (ERAD) [306-307]. As a result of decreased GCase function in the lysosome, GlcCer and other substrates accumulate, leading to GD-associated pathologies such as hepatomegaly, splenomegaly, anemia, a weakened skeleton, and in severe cases, central nervous system (CNS) complications [303, 308].

Although intravenous enzyme replacement therapy (ERT; imiglucerase, Cerezyme®, Genzyme; velaglucerase alfa, Vpriv®, Shire), the standard of care for Gaucher patients, significantly improves organ and blood parameters in non-neuronopathic GD [309], ERT does not improve pre-existing bone and lung disease. ERT also does not arrest neurological complications [310], due, at least in part, to the recombinant enzyme's inability to cross the blood-brain barrier. In addition, the cost of ERT ($90,000-$720,000 per patient per year [311]) is prohibitive for patients in

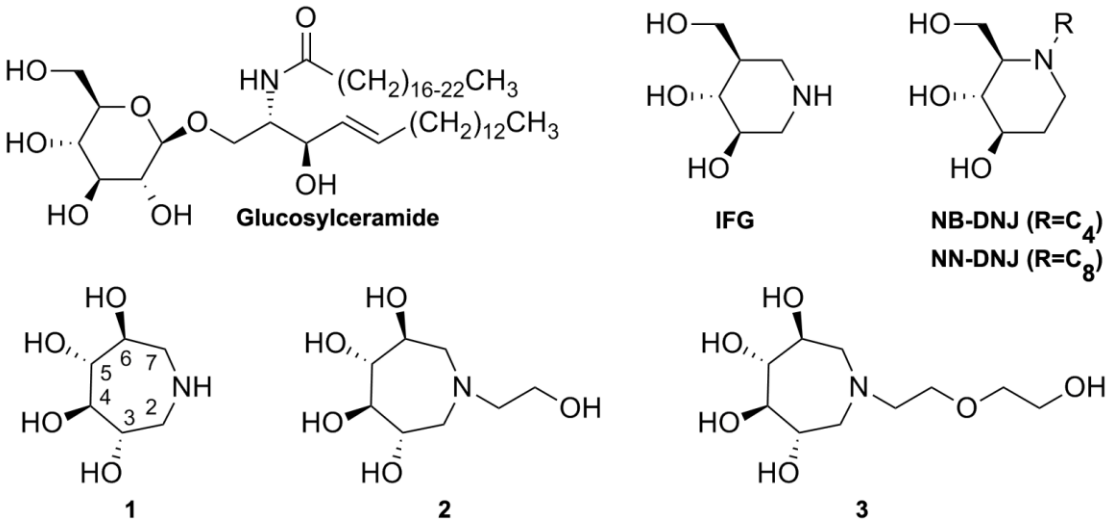

Figure 6.1. Chemical structure of the natural GCase substrate, GlcCer, representative azasugars investigated as pharmacologic chaperones, IFG, NB- and NN- DNJs, as well as the azepane compounds 1, 2, and 3 described in this study.

developing countries; only ~10% of GD patients worldwide are treated [309]. Due to these limitations, efforts to develop new therapeutic strategies have turned towards orally-available small molecules. Substrate reduction therapy (SRT), in particular, the FDA-approved miglustat (N-butyldeoxynojirimycin, NB-DNJ, Zavesca®; Acetlion), aims to reduce accumulation of GlcCer by inhibiting its synthesis. However, miglustat exhibits significant side effects and has therefore only been approved as a second-line therapy for patients with non-neuronopathic GD [309]. A second generation inhibitor [312], eliglustat (an analog of 1-phenyl-2-decanoylamino-3-morpholino-1-propanol; Genzyme), which passed Phase 2 clinical trials, may overcome some of the adverse reactions of miglustat [313-314], but does not reach the brain.

A promising therapeutic approach under development for GD is referred to as the pharmacological chaperone (PC) strategy, wherein a small molecule is designed to bind to and stabilize the native state ensemble of the endogenous mutant GCase enzyme in the ER. This allows more folded mutant GCase to engage its trafficking receptor LIMP-2 [315], increases its concentration in the lysosome which in turn increases overall cellular GCase activity [308]. The premise of the approach is based on the knowledge that missense mutations in GCase are not localized to its active site. Thus, while mutations diminish protein stability [158] and cellular trafficking, they do not completely abolish enzymatic activity [316-317]. As little as 1% GCase activity is thought to improve clinical symptoms of GD [318], but >10% of wild type GCase activity is generally required to prevent disease. Since small molecules are more likely to cross the blood-brain barrier than macromolecules, PCs hold promise for the treatment of neuronopathic variants of GD. In addition, PCs may be attractive in terms of cost, and may help overcome worldwide drug accessibility issues.

The desirable properties of a PC are in some ways contradictory. In the environment in which the target mutant enzyme folds (the ER), PCs must have high binding selectivity and affinity for the enzyme's folded or near-folded conformations to

increase the pool that is competent for trafficking. However, in the destination environment in which the target mutant enzyme is active, the lysosome, the PC must not bind so tightly to the active site that it cannot be displaced by the substrate. In GD, pH-dependent binding of the PC to GCase is one strategy to accomplishing these ideals. The chaperone should bind more tightly at the pH of the ER (~7) than the pH of the lysosome (~5). Administration of subinhibitory concentrations of these compounds is thought to be sufficient to achieve this goal, but the effective concentration needs to be optimized for each compound [319]. Nearly all compounds investigated to date are active-site directed, but achieving GCase-selective binding in the presence of other closely-related enzymes is an ongoing challenge [320-321]. Another approach to realize selective, pH-dependent GCase binders is to identify non-active-site directed binders for GCase, but these efforts are in the early stages of development [322-323].

One active-site-directed class of molecules investigated for GCase pharmacologic chaperoning activity is the deoxynojirimycins (Fig. 6.1), which have been studied extensively in relation to their inhibition of ceramide glucosyl transferase [320], the target enzyme of SRT. Some GCase PC activity was noted when 10 μM NB-DNJ was added to COS-7 cells expressing N370S-mutant GCase [324], but the same effect could not be replicated over a range of subinhibitory concentrations in patient-derived fibroblasts [325], indicating a weak chaperoning effect, if any. A more promising analog, *N*-(*n*-nonyl)deoxynojirimycin (NN-DNJ), with a 10-fold lower half maximal inhibitory concentration (IC_{50}), exhibited chaperoning capabilities for the non-neuronopathic N370S GCase variant, but not the neuronopathic L444P mutant of GCase [325]. Whereas these inhibitors were initially assumed to be transition-state-analog-based inhibitors mimicking the oxacarbenium-like transition state, it is notable that the crystal structures of GCase with either NB- or NN-DNJ bound later revealed that the endocyclic nitrogen mimics the ring oxygen of GlcCer [326]. Issues of enzyme selectivity of DNJ analogs [321] and

toxicity [327] linger and these compounds have not been tested in human clinical trials [328].

Other candidate GCase PCs such as (cyclic guanidine)-nojirimycin fused hybrids [329], bicyclic-NJ analogues [330], iminoxylitos [331], N-substituted δ-lactams [332], imino D-glucitols [325, 333], N-octyl-β-valienamine (NOV) aminocyclitols [334-335], the non-sugar Ambroxyl, an FDA-approved drug for an unrelated ailment [307, 336], and quinazoline analogues [337], have exhibited only limited promise as clinical candidates thus far. One initially promising clinical candidate is isofagomine, an active-site-directed [338] and selective [339] iminosugar analog (Fig. 6.1; IFG, Plicera), exhibiting an IC_{50} in the low nanomolar range. Isofagomine exhibited a cellular chaperoning effect for N370S- [340] and L444P- [339] mutant GCase, the two most prevalent GD variants. The latter variant was not responsive to numerous other chaperones [341], compared to better responses to a range of compounds observed for other GCase mutants [158, 333, 341], and the effect of IFG on L44P-mutant GCase was modest unless the enzyme was first enriched by immunoprecipitation [339]. IFG underwent clinical trials, and although the drug was well tolerated, the process was halted after Phase 2 in 2009 due to the lack of therapeutic effect [342]. The reason for the lack of effectiveness of this compound in patients is not clear at this time; inhibition of the mutant GCase due to high dosing, or off-target effects, are two of many possibilities [343].

Optimism for the PC approach remains high, but the example of IFG illustrates the complexities in design, development, and clinical application of a therapeutic GCase pharmacologic chaperone. In spite of a wide body of work detailing the design and synthesis of new candidate PCs for mutant GCase, as well as their characterization *in vitro*, in patient derived cell lines, and in some cases in animal models, the characteristics that make a PC a good clinical candidate are poorly understood. For example, the pH-dependent affinity of the candidate PC for GCase, the binding and inhibition kinetics of the compound, the ability to confer stability to the enzyme, and to what extent a

particular conformation of GCase might be required for a clinically effective PC, remain open questions.

In this study, we synthesized three GCase active-site-directed 3,4,5,6-tetrahydroxyazepane inhibitors (**1-3**; Fig. 6.1) that exhibit IC_{50} values in the low millimolar to micromolar range. While the synthesis of polyhydroxylated seven-membered ring structures has been known for over 40 years [344], exploration of these analogs as inhibitors of commercially available glycosidases has only more recently been investigated [1, 345-348]. Previous studies have not included human glycosidases like GCase, and no analogs previously synthesized contain alkyl ether substructures attached to the endocyclic nitrogen like the inhibitors described herein. The crystal structure of the core azepane (**1**) in complex with GCase reveals GCase in its proposed active conformation, albeit with nuances not observed previously, whereas the presence of a hydroxyethyl tail (**2**) results in an inactive GCase conformation. Compounds **1-3** thermally stabilize GCase at pH 7.4 but only **1** increases mutant GCase activity in an intact cell assay, the first indication that this scaffold holds promise as a pharmacological chaperone. Overall, our results demonstrate that probing the plasticity of the active site of GCase offers additional insight into possible molecular determinants that may be important factors leading to an effective PC for GD.

6.2 Results and Discussion

6.2.1 Inhibitor Design and Synthesis

To extend the previously studied 5-membered ring scaffolds and 6-membered glucose-derived analog PCs [158, 308, 325, 341], 7-membered 3,4,5,6-tetrahydroxyazepane iminosugar analogs (**1-3**; Fig. 6.1) were synthesized as potential GCase inhibitors and PCs by procedures slightly modified from those reported in the literature [349] (see Methods Section). We retained an endocyclic nitrogen because,

depending on their orientation, protonated iminosugars and azasugars can mimic the positive charge of the oxycarbenium-like transition state of glycosidases [350]. However, the new design potentially offers several advantages over the earlier scaffolds. First, seven-membered rings enable the installation of more functional groups, such as hydroxyl substituents, compared to smaller ring systems. This feature could be exploited to tune the hydrogen bonding network to select against unwanted inhibition of other glucosidases, a known problem [321]. Second, the larger ring structure has several options for the positioning of the endocyclic amine, as well as the positioning of the anomeric carbon. Finally, instead of the straight alkyl chains used previously, alkyl ether tails were installed to assist in discriminating between anomeric carbon configurations [351], to reduce the lipophilicity of the candidate PC, to better match the polarity of the ceramide component of the substrate to the GCase binding site, and to decrease the cytotoxicity found in related compounds [320].

6.2.2 Inhibition Profiles

The inhibitory activities of compounds **1**, **2**, and **3** toward GCase were determined using competition for the widely used fluorogenic substrate 4MU-β-Glc [352]. Compound **1** exhibited the strongest competitive inhibition, with an IC_{50} of 146 μM (Fig. 6.2A), a value slightly better than the previously characterized iminosugar analogs DNJ (IC_{50}= 240 μM) and NB-DNJ (IC_{50}= 270 μM) [353] but 10-fold weaker than NN-DNJ [325] and 250-fold weaker than IFG [338]. In contrast, compounds **2** and **3** exhibited weaker IC_{50} values of 3.4 mM and >15 mM, respectively (Fig. 6.2B, C). To address the possibility of slow binding kinetics, GCase was preincubated with **2** for 16 h prior to the addition of substrate. No change in the IC_{50} value was observed, suggesting that the on-rate is not slow (data not shown).

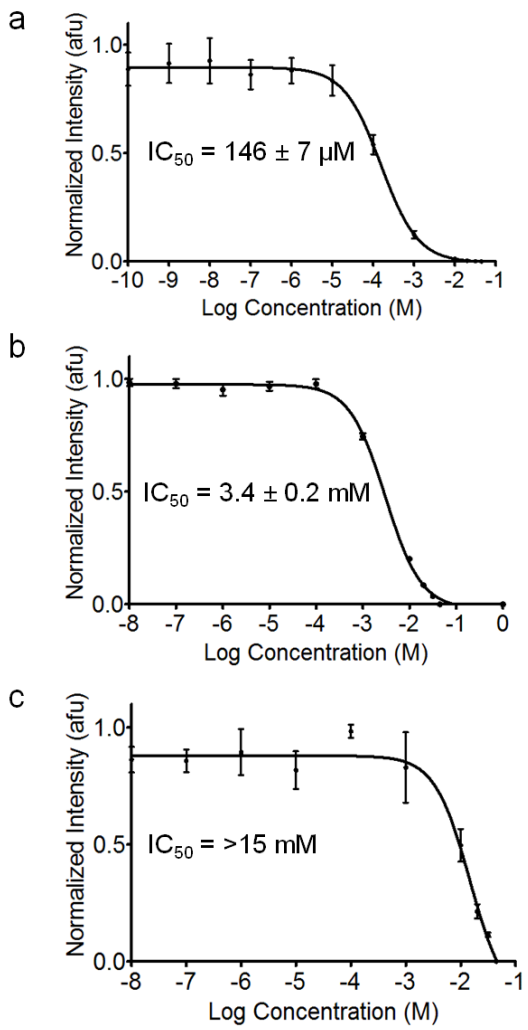

Figure 6.2. Competitive inhibition curves for 1, 2, and 3, respectively, toward GCase. Inset: IC_{50} values**.** Error bars indicate standard deviation.

6.2.3 Stability Profiles

The GCase stability change upon inhibitor binding to GCase was measured by differential scanning fluorimetry (DSF), which uses Sypro Orange as a reporter for. We chose the facile DSF method because GCase unfolding is not reversible when measured by differential scanning calorimetry (DSC), which precludes detailed thermodynamic insight [354-355], and DSF entails very low sample volume and GCase concentration. Melting temperatures (T_ms) recorded for GCase using DSF are within ~3 °C of those reported by DSC using similar concentrations of enzyme and inhibitor, but with slightly different buffers. All three inhibitors stabilize GCase at neutral pH with a ΔT_m of + 6-7.5 °C when added at mM concentrations (Table 6.1). At acidic pH, the inhibitors increased the T_m by only 1-3 °C, suggesting a lower affinity for GCase at pH 5.2. Thus, in terms of thermal stabilization, all three compounds are comparable over this concentration range, but binding confers more stability to GCase at a neutral pH (reflective of the pH in the ER) than at the lower lysosomal pH. We note that **1** increases the T_m of GCase slightly more than **2** and **3** at the highest concentrations, but it is a much better inhibitor of GCase than **2** and **3** (see above). Thus, it appears that inhibition at 37 °C and native state stabilization at higher temperatures are only partially correlated.

6.2.4 Structural Characterization

Next, we sought to investigate the structural changes that accompany binding of **1**, **2**, and **3** to GCase. We used a new vapor diffusion crystallization condition that requires a lower concentration of salt compared to most other conditions previously reported. We reasoned that the presence of PEG in the crystallization solution should enhance solubility of more hydrophobic compounds compared to molar concentrations of sulfate or phosphate salts. Interestingly, the lattice dimensions and space group remain the same. We obtained crystals with compounds **1** or **2** bound to GCase by soaking GCase crystals for five minutes or five days, respectively, but were unable to obtain a

Table 6.1. Stabilization of GCase with inhibitors at acidic and neutral pH.

		1		**2**		**3**		**IFG**	
	Inhibitor (mM)	T_m (°C)	ΔT_m (°C)	T_m (°C)	ΔT_m (°C)	T_m (°C)	ΔT_m (°C)	T_m (°C)	ΔT_m (°C)
pH 5.2		55.8 ± 0.0*							
	0.5	56.4 ± 0.0	0.6	55.9 ± 0.1	0.3	56.1 ± 0.0	0.3	68.0 ± 0.2	12.2
	1	56.6 ± 0.0	0.8	56.0 ± 0.0	0.3	56.1 ± 0.1	0.2	68.9 ± 0.3	13.0
	2	57.3 ± 0.1	1.5	56.7 ± 0.1	1.0	56.7 ± 0.1	0.8	69.7 ± 0.3	13.8
	5	58.4 ± 0.1	2.7	57.4 ± 0.1	1.7	57.2 ± 0.1	1.3	67.5 ± 0.3	11.6
	10	59.0 ± 0.1	3.2	57.4 ± 0.0	1.7	56.9 ± 0.0	1.0	63.7 ± 0.2	7.8
pH 7.2		47.1 ± 0.2*							
	0.5	48.5 ± 0.1	1.4	48.7 ± 0.1	1.7	50.7 ± 0.0	2.1	63.8 ± 0.3	16.9
	1	49.4 ± 0.1	2.3	49.3 ± 0.0	2.2	52.0 ± 0.1	3.3	65.4 ± 0.1	18.4
	2	49.9 ± 0.1	2.8	50.1 ± 0.1	3.1	52.6 ± 0.1	3.9	67.2 ± 0.2	20.2
	5	52.5 ± 0.1	5.4	52.1 ± 0.1	5.0	53.6 ± 0.1	5.0	70.3 ± 0.2	23.4
	10	54.6 ± 0.1	7.5	53.6 ± 0.1	6.5	54.5 ± 0.0	5.8	72.6 ± 0.2	25.7

* mean T_m measured for GCase at indicated pH value in the absence of inhibitor.

Table 6.2. Data collection and refinement statistics.

	3RIL (**1**)	3RIK (**2**)
Data Statistics		
space group	P2(1)	P2(1)
Cell dimensions		
a, *b*, *c* (Å)	109.2, 91.4, 152.7	108.0, 91.6, 152.2
α, β, γ (deg)	90.0, 110.95, 90.0	90.0, 110.70, 90.0
Resolution (Å)[a]	44.5-2.4 (2.49-2.40)	46.5-2.5 (2.55-2.48)
R_{sym}[a]	10.5 (35.7)	12.2 (47.8)
$\%>3\sigma$[a]	62.9 (38.3)	64.6 (40.7)
Completeness (%)[a]	96.3 (76.5)	94.3 (72.3)
redundancy	2.6	2.9
Refinement Statistics		
resolution (Å)	44.5-2.4	47-2.5
no. of reflections	100648 (5857)	88126 (4973)
R_{work}/R_{free}[a]	20.9/24.9	18.1/23.4
no. of molecules		
protein residues	1988	1988
N-acetylglucosamine (NAG)	4	4
sulfate anion (SO_4^{2-})	7	7
chaperone	4	2
water	1254	702
B-factor		
protein	23.6	26.6
NAG	29.7	50.4
SO_4^{2-}	60.8	38.1
chaperone	38.2	32.9
water	27.6	40.0
rmsd		
bond lengths (Å)	0.006	0.013
bond lengths (deg)	1.089	1.466

[a]Data for the highest-resolution shell given in parenthesis; 5% or reflections were selected for R_{free}.

crystal structure of **3**, also the weakest inhibitor, bound to GCase. Crystal structures were solved to 2.4 and 2.5 Å resolution (Table 6.2). The global structure of GCase does not change upon inhibitor binding, but adjustments are seen in the active site and surrounding loop residues, detailed below.

Both **1** and **2** bind in the GCase active site and are held in place by an extensive hydrogen bonding network (Fig. 6.3A, B). Notably, **1** is found in all four monomers of GCase in the asymmetric unit, compared to **2**, which is bound in the typical manner, in two of the four molecules. This result with **1** is surprising given that there is a 7-membered ring bound in a sugar pocket, and suggests that binding of **1** causes minimal distortion of the nearby loops that are involved in crystal packing. In the case of **2**, the hydroxyl substituents at positions 3, 4 and 5 (see Fig. 6.1) are within hydrogen bonding distance of Asp 127, Trp 179, Asn 234, Glu 340, and Trp 381 side chains on GCase whereas the 6-hydroxyl moiety is not involved. The endocyclic nitrogen and hydroxyethyl tail are also within hydrogen bonding distance with Glu 340, the catalytic nucleophile [356] (Fig. 6.3B). Similar interactions stabilize the hydroxyl groups of **1** in the GCase active site, but with the additional interaction of the 6-hydroxyl group with Tyr 313 (Fig. 6.3A). Notably, no hydrogen bonding interactions were observed for either compound with Glu 235, which, being the residue implicated as the general acid/base in catalysis [316, 357], is probably protonated in the resting state of the enzyme [358]. In the IFG-bound GCase structure (PDB code 2NSX, Fig. 6.3C), Glu 235 stabilizes the imino group of IFG, suggesting that Glu 235 may be deprotonated. However, an analogous shift of **1** or **2** to mimic the orientation of IFG is not compatible with the observed electron density. This configuration may not be preferred because the hydroxymethyl substituent on IFG, which interacts with Asn 396 and locks IFG into position, has been replaced with a shorter hydroxyl moiety in **1** and **2**.

The binding orientations of **1** and **2** are more similar to those found in NB-DNJ- (PDB code 2V3D) and NN-DNJ- (PDB code 2V3E; Fig. 6.4D) bound GCase [326], but

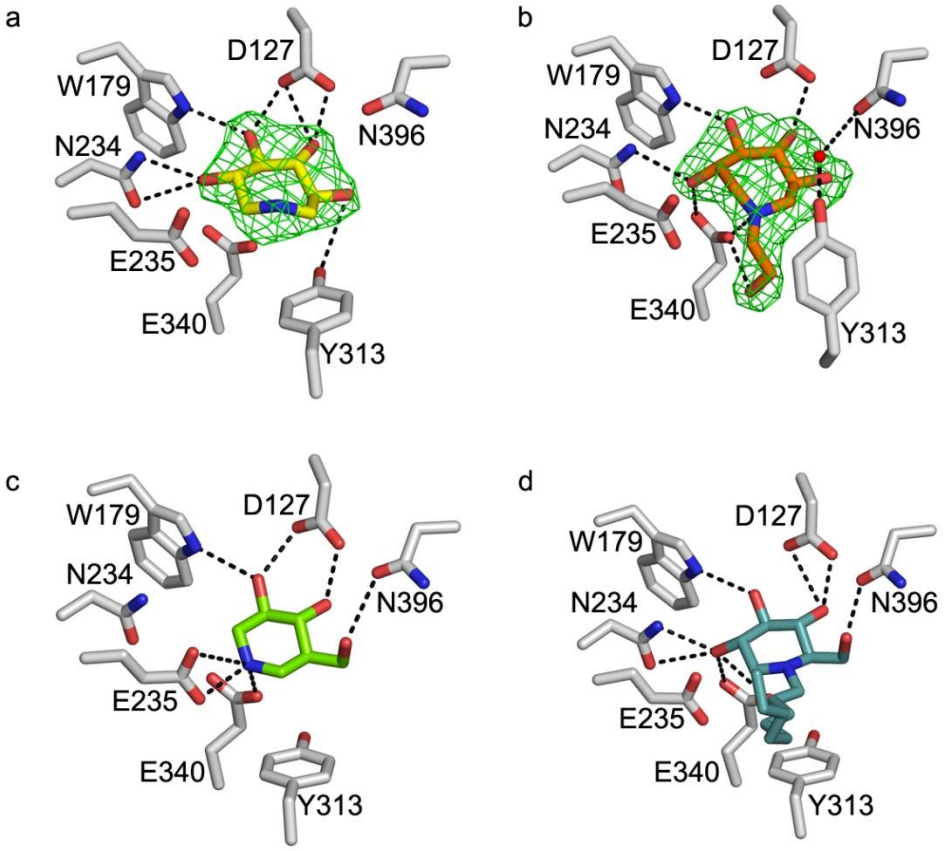

Figure 6.3. Ball-and-stick representation of the GCase active site upon compound binding. A) **1** B) **2** C) IFG (PDB code 2NSX) D) NN-DNJ (PDB code 2V3E). Difference (F_o-F_c) electron density for **1** and **2** was calculated from the initial phasing solution using only protein coordinates and is contoured to 3σ. Hydrogen bonding interactions are indicated by dashed black lines and represent distances between 2.5 Å- 3.5 Å.

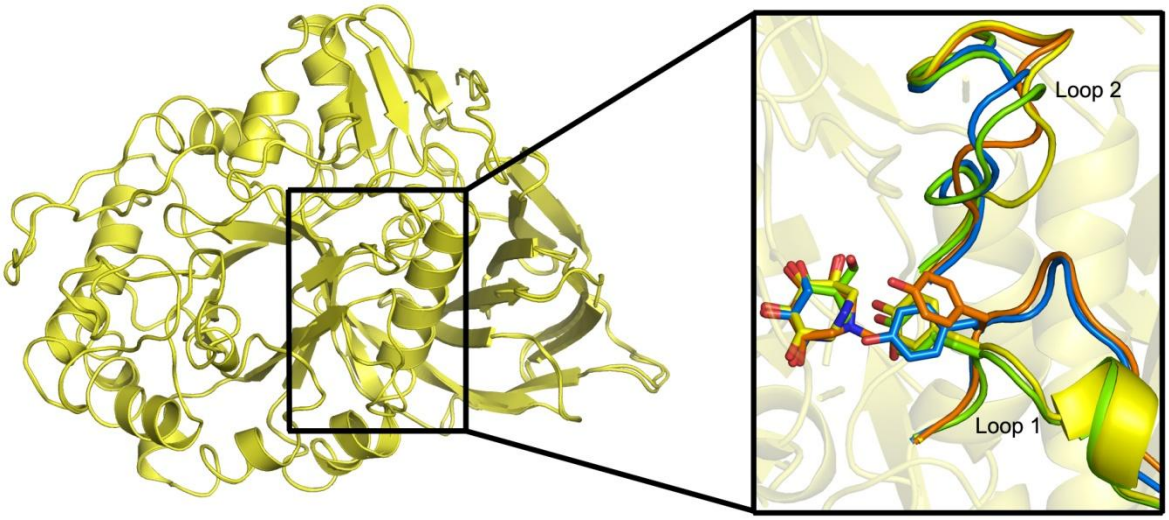

Figure 6.4. Superposition of 1 and 2 bound GCase structures and comparison of loops adjacent to the active site (inset). After binding, Loop 1 adopts either a helical turn as seen for compound **1** (yellow) and IFG (green), or an extended loop conformation seen in the compound **2** (orange) and glycerol (blue) bound structures. Changes in Loop 2 are due to crystal packing.

there are differences in interactions with GCase. One commonality is that in all four structures, Glu 235 is not involved in stabilizing **1** or **2** in the active site. Another share feature is that the position of the endocyclic nitrogens of **1**, **2**, NB- and NN-DNJ overlay well. However, the endocyclic nitrogens of NB- and NN- DNJ are held in place by a water-mediated hydrogen bond to the hydyroxyl group of Tyr 244. By comparison, for **2**, the endocyclic nitrogen is within hydrogen bonding distance of Glu 340 (Fig. 6.3B) whereas for **1**, the endocyclic nitrogen is not held by either water-mediated or direct interactions with any active site residues (Fig. 6.3A). Inspection of the F_o-F_c difference electron density in this region reveals that several pucker conformations for this location on the azepane ring of **1** are plausible. Lastly, like IFG (see above), NB- and NN-DNJ are also held in place by Asn 396, an interaction missing in **1** and **2** (compare Fig. 6.3A and B to Fig. 6.3C and D).

Notable differences in structure are observed in the active site loops (Loop 1: residues 311-319 and Loop 2: residues 342-354, Fig. 6.4) when comparing the binding modes of **1** (yellow) and **2** (orange) to each other and to previously reported GCase structures (green and blue). Loop 2 (residues 342-354) is shifted 3.2 Å from its position in the IFG or glycerol (PDB code 2NT0) bound GCase structures (Fig. 6.5). Movements in this loop have previously been implicated in crystal contacts, a conclusion supported by our observation that the same orientation of Loop 2 is seen in apo GCase crystallized under the conditions used here for azepane inhibitor soaking (data not shown), and thus is not a function of inhibitor binding. More important changes are observed in the well-defined conformation of Loop 1 (residues 311-319), which is in an extended conformation that covers the catalytic center when compound **2** binds, and is in an α-helical arrangement (Fig. 6.4, Fig. 6.6) that exposes the active site when **1** is bound. The extended Loop 1 has been observed when sulfate (PDB code 1OGS) [357], glycerol (PDB code 2NT0) [338], or the suicide inhibitor conduritol- β-epoxide (CBE, PDB code 1Y7V) [359] is bound in the active site, and is the only conformation observed in the

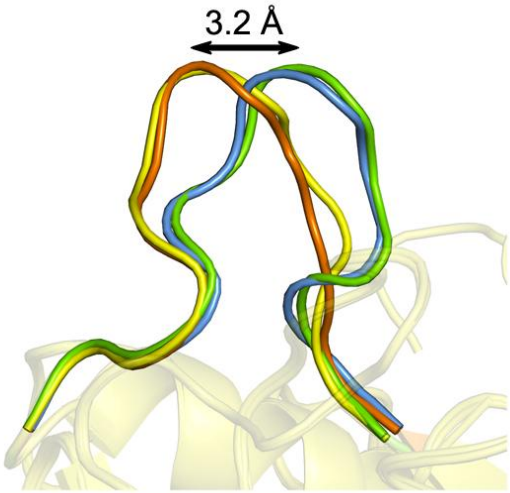

Figure 6.5. Comparison of Loop 2 orientation for 1- (yellow), 2- (orange), IFG- (green), and glycerol- (light blue) bound GCase.

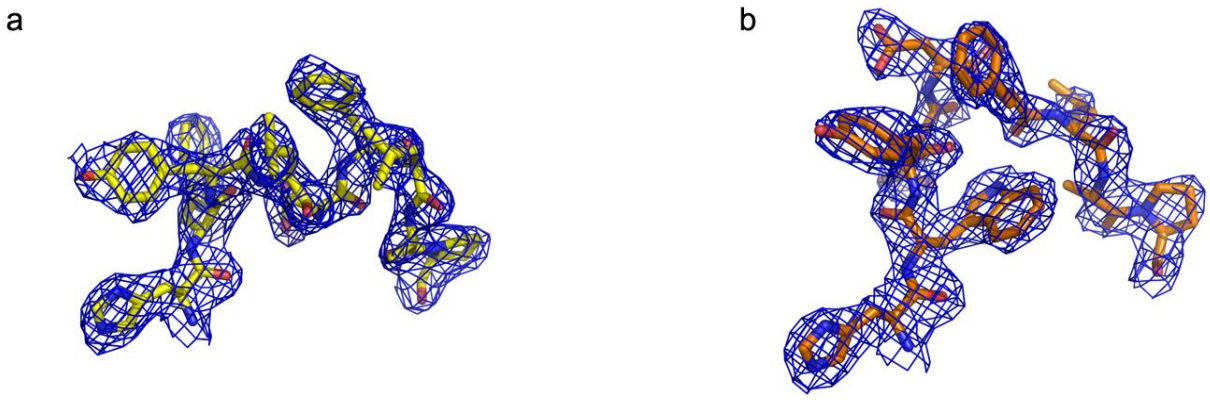

Figure 6.6. The final GCase Loop 1 model for 1 (left) and 2 (right) with $2F_o$-F_c electron density contoured to 1σ.

catalytically compromised N370S mutant GCase structure at either neutral or acidic pH (PDB codes 3KE0 and 3KEH) [355]. By contrast, the helical conformation of Loop 1 has been proposed to be the catalytically active form of GCase [338] and to date, has been observed only when a small molecule with chaperoning capabilities, namely NB-DNJ, NN-DNJ, or IFG, is bound to the GCase active site.

Although GCase adopts conformations that are related to those observed previously when bound to **1** and **2**, each is unique. Tyr 313 plays an important role in Loop 1 conformations. In crystal structures with an extended Loop 1 conformation, Tyr 313 is observed within hydrogen bonding distance to Glu 235, whereas when Loop 1 is helical, such as when IFG is bound (Fig. 6.7A), it interacts with Glu 340. As with IFG, when **1** binds to GCase, the helical Loop 1 is observed, with the same Glu 340 - Tyr 313 interaction (Fig. 6.7B). By contrast, when **2** binds in the GCase active site, neither of the two previously observed Loop 1 conformations is observed. Compound **2** interacts with Glu 340 via its hydroxyethyl substituent instead of Tyr 313 (Fig. 6.7C), which results in a new interaction between Tyr 313 and Asn 396 mediated by water (Fig. 6.3B) that caps the active site entrance. The extended Loop 1 seen with **2** (Fig. 6.7C, bottom panel) is otherwise similar to extended loop conformations observed previously, with minor alterations in the side chain orientation. We surmise that **3** does not bind well to GCase because the extra hydroxyethyl substituent of its tail is involved in steric clashes, or makes the compound too polar, which may account for our inability to obtain a bound crystal structure.

In addition to the particular configuration of the Tyr 313 side chain in the catalytic center, the helical turn in Loop 1 is stabilized by a network of water-mediated hydrogen bonds between residues on an interior helix of GCase (Fig 6.7, bottom panels). For the NB-DNJ, NN-DNJ, and IFG structures (see IFG: Fig. 6.6A, bottom panel), Asp 315 in Loop 1 is stabilized by electrostatic interactions with the guanidinium of Arg 285 (omitted in Fig. 6.7 for clarity) and is linked to Ser 366 and Asn 370 via a bound water

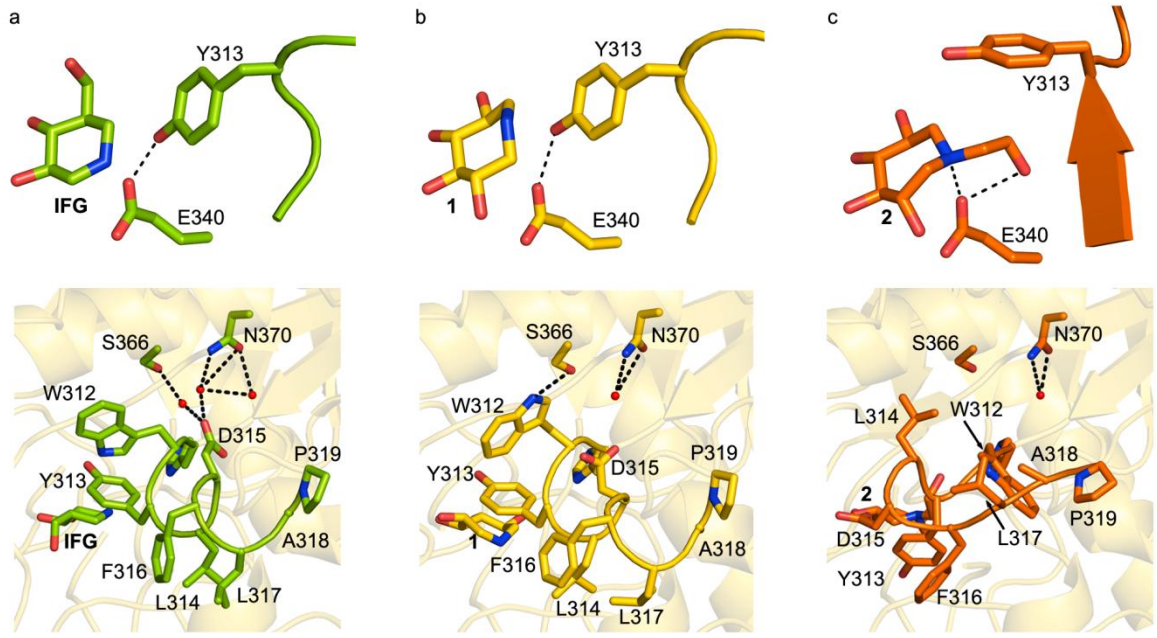

Figure 6.7. Comparison of Loop 1 configuration. A) IFG-, B) **1**-, and C) **2**- bound GCase. Top: orientation of Tyr 313 relative to Glu 340. Bottom: interactions of loop with interior GCase helix harboring Asn 370. Hydrogen bonding interactions are indicated by dashed black lines.

molecule, while the side chain of Trp 312 interacts with the carbonyl backbone of Cys 342, located on Loop 2. Unexpectedly, when **1** is bound, the side chain of Trp 312 is repositioned to form a new interaction with Ser 366 instead of Cys 342 (Fig. 6.7B, bottom panel). This change releases Asp 315 from the location seen in the other chaperone-bound structures, resulting in a more relaxed helix in Loop 1 and weaker electrostatic interaction with Arg 285.

6.2.5 Enhancement of Cellular Enzyme Activity

To evaluate the potential of **1**, **2**, and **3** for PC development, namely, their abilities to enhance mutant GCase activity in cells, were examined next. Patient-derived fibroblasts harboring either mutant G202R GCase (associated with the neuronopathic Type 2 GD) or mutant N370S/V394L GCase (associated with the non-neuronopathic Type 1 GD) were incubated with compounds **1**, **2**, or **3** for three days at varying concentrations. The upper limit tested was 100 μM due to cytotoxicity concerns. Compound **1** increased the cellular GCase activity of G202R fibroblasts by 20% at 100 μM, whereas **2** and **3** had no effect on activity in the concentration range tested (Fig. 6.8A). A similar but attenuated result was obtained for N370S/V394L GCase fibroblasts. A ~15% increase in activity was observed for cells treated with 10 mM of **1** (Fig. 6.8B), a lower concentration than was required for a similar effect with G202R and comparable to the optimal concentration observed for NN-DNJ [325]. The maximal 20% activity enhancement for G202R GCase is intermediate between the lack of activity enhancement seen for NB-DNJ and the 60-65% enhancement seen for NN-DNJ using the same enzyme variant and experimental setup [325]. The modest enhancement of the cellular activity of mutant GCase seen with the tetrahydroxyazepane core suggests that future optimization of this scaffold will be necessary for generating PCs for GCase with therapeutic potential.

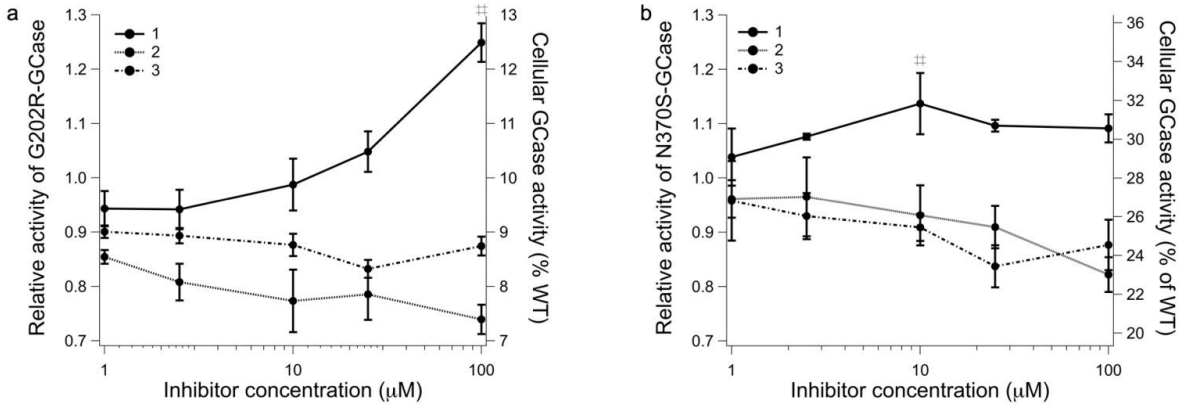

Figure 6.8. Effects of 1, 2, and 3 on mutant GCase activity in intact patient derived fibroblasts G202R. A) and N370S/V394L B). Enzyme activity is normalized to untreated and assigned a relative activity of **1**. The right-hand axis is the residual activity of the mutant expressed as the percentage of WT GCase activity. Mean values for triplicate experiments are shown. # = $p < 0.05$.

6.3 Conclusions and Future Outlook

In this study, we extended our set of potential pharmacological chaperone scaffolds for GCase to include hydroxy alkyl and alkyl ether azepanes **1**-**3**. The active site of GCase readily accommodates the larger 7-membered azepane ring, but the enzyme is exquisitely sensitive to binding and can propagate changes as far as ~ 13 Å away. The three compounds synthesized thermally stabilize GCase to approximately the same extent both at neutral and acidic pH. Only the tetrahydroxyl-substituted azepane, **1**, which exhibits a ~10x better competitive inhibition profile compared to **2** and **3**, enhances enzyme activity in fibroblasts expressing G202R- and N370S-mutant GCase. Combined with the crystal structures, the enhanced cellular enzyme activity of **1** correlates with the helical conformation in Loop 1 of GCase, whereas the corresponding extended conformation found with **2** bound does not. Therefore, **1**, the core azepane structure, qualifies as a lead as a potential PC. Based on our study and in line with our previous observations, it appears that competitive inhibition of the fluorogenic substrate in the 10-20 mM range is a lower limit for observing PC activity in cells, although cellular penetration and organelle distribution clearly also contribute.

Comparison of the crystal structures of **1** and **2** bound to GCase reveals that the cores of these two compounds are bound in a distinct fashion in the active site. First, whereas all four hydroxyl substituents of **1** are stabilized by hydrogen bonding interactions with active site residues, with **2** bound, one interaction is lost. Second, in terms of the endocyclic nitrogen, there is no stabilizing interaction for **1**, whereas that in **2** is held in place by Glu 340, a residue that also interacts with the hydroxyethyl substructure of **2**. It appears as if the latter set of interactions propagates to distinct loop

configurations for **1** or **2**, either helical, or extended, respectively, with nuances not previously observed in GCase structures. Presumably, other exocyclic substituents that can form favorable interactions with Glu 340 would likewise not prove to be effective chaperones. One method to improve the PC activity of **1** and/or convert **2** or **3** into a PC would be to replace the 6-hydroxyl with a hydroxymethyl or another subsituent that could compete favorably for stabilization by Asn 396. This approach could also prevent the ether-linked substructure from unintended interactions with catalytic residues, and subsequently enable direct evaluation of the effectiveness of the exocyclic substituents of **2** and **3** on their PC activity. The opening of the hydrophobic binding pocket is energetically demanding, but can be compensated by the favorable entropy increase due to water desolvation [350]; considerations for optimizing exocyclic substituent binding include tuning both lipophilicity and chain length.

Finally, even though **2** generates a GCase conformation thought to be inactive, **1** is a significantly better active-site-directed, competitive inhibitor in vitro. Competitive inhibition of GCase and the kinetics of such inhibition toward the hydrolysis of closely related natural substrates glucosylceramide and glucosylsphingosine in the context of the cell [360] may differ somewhat from that of a model substrate in vivo, but a link is emerging among the ability of a molecule to competitively inhibit GCase in vitro, nuances regarding the resulting conformation of Loop 1 that exposes the GCase active site, and its ability to increase mutant GCase activity in cell culture. Thermal stabilization, while typically a feature of a competitive inhibitor, is not a singular good predictor of cellular PC activity. We anticipate that GCase structures, in combination with biochemical studies of potential PCs, will continue to provide insight into the

connection between GCase loop structure and enhancement of cellular mutant enzyme activity. A better comprehension of these basic molecular determinants of PCs will ultimately lead to the identification of compounds worthy of detailed cellular trafficking and animal model studies, and eventually to a successful outcome of clinical trials of a therapeutic PC for GD.

6.4 Methods

6.4.1 Chemical Synthesis of Compounds 1, 2, and 3

6.4.1.1 (1R,1'R)-1,1'-((4R,5R)-2,2-dimethyl-1,3-dioxolane-4,5-diyl)bis(ethane-1,2-diol) (S-1)

2,2'-Dimethoxypropane (300 mL) was charged to a 1 L round bottom flask. D-Mannitol (20 g, 0.11 mol) and pyridinium *p*-toluenesulfonate (1 mol%, 0.27 g, 2.0 mmol) were added, and the resultant suspension was stirred at reflux. After 18 hours, the solution was allowed to cool to room temperature and concentrated under reduced pressure. The residue was dissolved in ethyl acetate (300 mL) and washed with water (2 x 100 mL) and brine (100 mL). The organic layer was taken, dried over $MgSO_4$, filtered and evaporated under reduced pressure. The resultant white solid was charged to a 1 L round bottom flask. Acetic acid (210 mL) and water (90 mL) were added and the suspension was stirred at 40 ˚C. After 2 hours, the mixture was concentrated under reduced pressure. The residue was suspended in acetone (100 mL) and stirred at room temperature. After 1 hour, the mixture was filtered and the filtrate was concentrated under reduced pressure to yield **S-1** as a white solid (17.1g, 70 %). ^{1}H NMR (300 MHz, $CDCl_3$) δ ppm 4.17-4.23 (m, 2H), 3.90-4.05 (m, 2H), 3.70-3.77 (m, 4H), 1.45 (s, 6H);

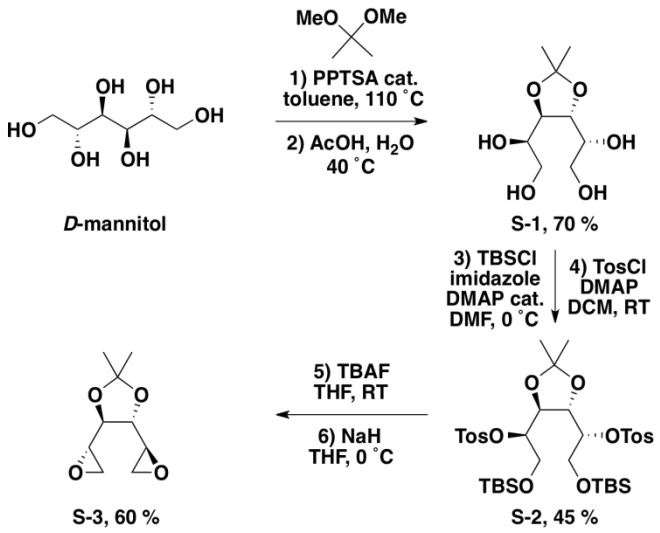

Scheme 6.1. Synthesis of Di-epoxide **S-3**

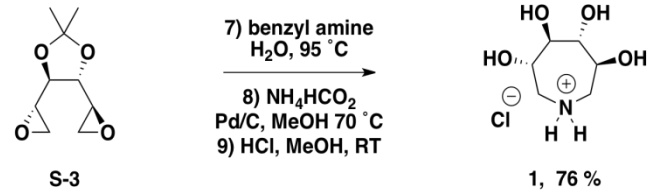

Scheme 6.2. Synthesis of Tetrahydroxyazepane **1**

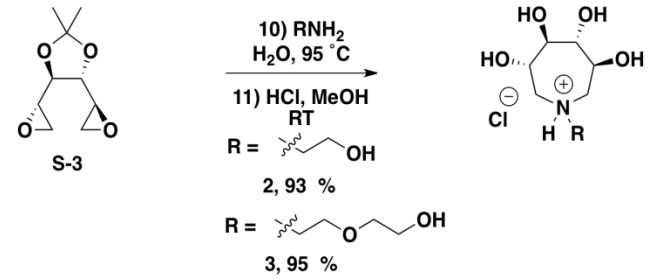

Scheme 6.3. Synthesis of Tetrahydroxyazepanes **2** and **3**

LCMS *m/z* 245.2 $[M + Na]^+$, calculated for $C_9H_{18}NaO_6^+$ 245.1. Data are consistent with literature [361].

6.4.1.2 (1R,1'R)-((4S,5S)-2,2-dimethyl-1,3-dioxolane-4,5-diyl)bis(2-((tert-butyldimethylsilyl)oxy)ethane -1,1-diyl) bis(4-methylbenzenesulfonate) (S-2)

S-1 (7.5 g, 33.8 mmol) was charged to a 500 mL round bottom flask under a nitrogen atmosphere. Anhydrous DMF (200 mL), imidazole (7.0 g, 100 mmol) and DMAP (0.16 g, 1.3 mmol) were added and the reaction was stirred at 0 ˚C. After 10 minutes, TBSCl (10.1 g, 68.0 mmol) was added portionwise and the solution was allowed to warm to room temperature. After 18 hours, the reaction mixture was diluted with ether/hexane (1:1, 500 mL), washed with water (3 x 100 mL), dried over $MgSO_4$ and concentrated under reduce pressure. Purification by flash column chromatography (silica, 9:1 hexane/ethyl acetate) afforded a colorless oil (8.0 g, 52 %). A sample (6.82 g, 15.15 mmol) was charged to a 500 mL round bottom flask. Anhydrous DCM (200 mL), DMAP (7.39 g, 60.5 mmol) and tosyl chloride were added and the mixture was stirred at room temperature. After 18 hours, the reaction was diluted with ethyl acetate (200 mL), washed with water (100 mL), aq. HCl (1 M, 100 mL), sat. aq. $NaHCO_3$ (100 mL) and brine (100 mL). The organic layer was taken dried over $MgSO_4$, filtered and concentrated under reduced pressure to afford **S-2** (10.0 g, 87 %) as a white solid. ^{1}H NMR (300 MHz, $CDCl_3$) δ ppm 7.81 (d, *J* = 8.4 Hz, 4H), 7.29 (d, *J* = 8.4 Hz, 4H), 4.68-4.72 (m, 2H), 4.36-4.40 (m, 2H), 3.83 (dd, *J* = 11.6, 4.6 Hz, 2H) 3.74 (dd, *J* = 11.6, 5.1 Hz, 2H), 2.43 (s, 6H), 1.14 (s, 6H), 0.83 (s, 18H), 0.1 (s, 12 H); LCMS *m/z* 781.4 $[M + Na]^+$, calculated for $C_{35}H_{58}NaO_{10}S_2Si_2^+$ 781.3.

6.4.1.3 (4R,5R)-2,2-dimethyl-4,5-di((S)-oxiran-2-yl)-1,3-dioxolane (S-3)

S-2 (10.0 g, 13.2 mmol) was charged to a 500 mL round bottom flask. THF (250 mL) and TBAF (1M in THF, 29.0 mL, 29.0 mmol) were added and the mixture was stirred at room temperature. After 2 hours, the reaction was concentrated under reduced pressure and the residues dissolved in ether (100 mL) and washed with sat. aq. $MgSO_4$ (3 x 100 mL), dried over $MgSO_4$, filtered and concentrated under reduced pressure. The residue was dissolved in anhydrous THF (120 mL), sealed under a nitrogen atmosphere and cooled 0 ˚C. Sodium hydride (60 % dispersion in mineral oil, 2.11 g, 52.7 mmol) was added portionwise. After 1 hour, the reaction was quenched with ice water (50 mL), and extracted with ether (3 x 20 mL). The organic layers were combined, dried over $MgSO_4$, filtered and concentrated under reduced pressure. Purification by flash column chromatography (silica, 8:2 hexane/ethyl acetate) afforded **S-3** (1.5 g, 60 %) as a white solid. ^{1}H NMR (300 MHz, $CDCl_3$) δ ppm 3.86 (dd, *J* = 3.2, 1.6 Hz, 2H), 3.04-3.10 (m, 2H), 2.85 (dd, *J* = 5.2, 4.1 Hz, 2H), 2.74 (2H, *J* = 5.2, 2.6 Hz, 2H), 1.41 (s, 6H); LCMS *m/z* 209.0 $[M + Na]^+$, calculated for $C_9H_{14}NaO_4^+$ 209.0. Data are consistent with literature [349].

6.4.1.4 (3*S*,4*R*,5*R*,6*S*)-3,4,5,6-tetrahydroxyazepan-1-ium chloride (**1**)

S-3 (120 mg, 0.64 mmol) was charged to a 5 mL round bottom flask. Water (2 mL) and benzylamine (freshly distilled, 69 mg, 70 µL, 0.64 mmol) were added and the mixture stirred at 95 ˚C. After 2 hours, the reaction was cooled to room temperature and concentrated under reduced pressure. Purification by flash chromatography (silica, 1:1 ethyl acetate/hexane) yielded a white solid which was charged to a 10 mL round bottom flask. Methanol (5 mL), palladium on carbon (10%, 60 mg) and ammonium formate (122

mg, 1.9 mmol) were added and the mixture stirred at 70 ˚C. After 2 hours, the reaction was cooled to room temperature and 1-heptene (1.86 g, 2.66 mL, 19.0 mmol) was charged to the vessel. After stirring at room temperature for 1 hour, the reaction was filtered through celite, and evaporated under reduced pressure. The residue was dissolved in methanol (5 mL) and methanolic HCl (1 M, 5 mL, 5 mmol) was added. The mixture was stirred at room temperature. After 1 hour, the reaction was evaporated under reduced pressure to yield **1** as a gummy colorless solid (100 mg, 76 % from **S-3**). ^{1}H NMR (300 MHz, D_2O) δ ppm 4.06-4.18 (m, 2H), 3.69-3.76 (m, 2H), 3.34-3.44 (m, 2H), 3.18-3.30 (m, 2H); LCMS *m/z* 164.3 $[M + H]^+$, calculated for $C_6H_{14}NO_4^+$ 164.1. Data consistent with literature [349].

6.4.1.5 (3*S*,4*R*,5*R*,6*S*)-3,4,5,6-tetrahydroxy-1-(2-hydroxyethyl)azepan-1-ium chloride (**2**)

S-3 (120 mg, 0.64 mmol) was charged to a 5 mL round bottom flask. Water (2 mL) and ethanolamine (39 mg, 39 µL, 0.64 mmol) were added, and the mixture was stirred at 95 ˚C. After 2 hours, the reaction was cooled to room temperature and concentrated under reduced pressure. The residue was dissolved in methanol (5 mL) and methanolic HCl (1 M, 5 mL, 5 mmol) was added, and the mixture stirred at room temperature. After 1 hour, the reaction was evaporated under reduced pressure to yield **2** as a gummy yellow solid (144 mg, 93 %). ^{1}H NMR (300 MHz, D_2O) δ ppm 4.07-4.24 (m, 2H), 3.87-4.01 (m, 2H), 3.61-3.77 (m, 4H), 3.44-3.58 (m, 4H); LCMS *m/z* 208.2 $[M + H]^+$, calculated for $C_8H_{18}NO_4^+$ 208.1.

6.4.1.6 (3S,4R,5R,6S)-3,4,5,6-tetrahydroxy-1-(2-(2-hydroxyethoxy)ethyl)azepan-1-ium chloride (**3**)

S-3 (120 mg, 0.64 mmol) was charged to a 5 mL round bottom flask. Water (2 mL) and 2-(2-aminoethoxy)ethanol (67 mg, 64 μL, 0.64 mmol) were added and the mixture was stirred at 95 ˚C. After 2 hours, the reaction was cooled to room temperature and concentrated under reduced pressure. The residue was dissolved in methanol (5 mL) and methanolic HCl (1 M, 5 mL, 5 mmol) was added, and the mixture stirred at room temperature. After 1 hour, the reaction was concentrated under reduced pressure to yield **3** as a gummy yellow solid (174 mg, 95 %). ^{1}H NMR (300 MHz, D_2O) δ ppm 4.10-4.23 (m, 2H), 3.92-3.99 (m, 2H), 3.61-3.80 (m, 4H), 3.34-3.57 (m, 8H); LCMS *m/z* 208.1 $[M + H]^+$, calculated for $C_8H_{18}NO_4^+$ 208.1.

6.4.2 *In Vitro* GCase Inhibition Assay

Approximately 15 ng of Cerezyme® (Genzyme corp.) was mixed with McIlvaine buffer (0.1 M citrate, 0.2 M phosphate, pH 5.4), 0.1% Triton X-100, 0.25% taurochloric acid, and various concentrations of compound (**1**, **2**, or **3**) on ice. A stock of 300 mM 4-methylumbelliferyl-β-glucopyranoside (4MU-β-Glc, Sigma) was freshly prepared in dimethylsulfoxide (DMSO), and added to the Cerezyme/inhibitor mixture at a final concentration of 3 mM. The reaction was then transferred into a microplate (Grenier), sealed, and incubated at 37 °C for 30 minutes. An equal volume of 0.4 M glycine and 0.4 M NaOH was added to each well to quench the reaction. The release of 4-methylumbelliferone (4MU) was measured by fluorescence (excitation 355 nm, emission 460 nm) on a BioTek microplate reader. Each reaction was set up in triplicate per plate, averaged, and background subtracted. Each plate was repeated in triplicate per inhibitor

and the averaged, normalized data was plotted against drug concentration and fitted to a log(inhibitor) vs response-variable slope curve in GraphPad Prism to estimate the IC_{50}. To investigate the effect of incubation time of premixed inhibitor and enzyme, the Cerezyme/**2** mixture was incubated at 4 °C for 16 hours. 4MU- β-Glc was then added and the assay carried out as described above. An inhibition assay with IFG (Toronto Research Chemicals) was also carried out as a positive control with a result similar to that previously published [338].

6.4.3 Thermal Stability Assay for GCase

Cerezyme was resuspended in 0.1 M citrate, 0.2 M phosphate, adjusted either to pH 5.2 or pH 7.2, and protein concentration was determined via Bradford assay [362]. A working stock of 10 μM Cerezyme was prepared by diluting in the appropriate buffer. Reactions of 30 μL were prepared at room temperature by diluting Cerezyme in water (1:10) along with various concentrations of inhibitor (0-10 mM), also prepared in water. This resulted in a final buffer concentration of 0.01 M citrate, 0.02 M phosphate, either at pH 5.2 or 7.2, and 1 μM protein. Finally, Sypro Orange (Invitrogen, supplied as 5000X solution in DMSO) was diluted in water and then added to each reaction with a final concentration of 5X. Each reaction was delivered to 96-well optical plates (Applied Biosystems) before sealing with optical film. Fluorescence data were acquired on an Applied Biosciences Step-One Plus RT-PCR instrument equipped with a fixed excitation wavelength (480 nm) and a ROX emission filter (610 nm). Melts were conducted from 25–95 °C with a 1 °C per min increase. Collected data were baseline subtracted, trimmed to include both the boundaries and the transition of interest, and subjected to Boltzmann sigmoid analysis as described previously [363].

6.4.4 Intact Cell GCase Activity Assay

Primary skin fibroblast culture was established from Gaucher patients homozygous for the G202R GC (c.721G>A) mutation. The heterozygous Gaucher fibroblasts containing the N370S/V394L GC mutation (GM01607) were obtained from the Coriell Cell Repositories (Camden, NJ). Fibroblasts were grown in minimal essential medium with Earle's salts (supplemented with 10 % heat-inactivated fetal bovine serum and 1 % glutamine Pen-Strep at 37 °C in 5 % CO_2). Cell culture media were obtained from Gibco (Grand Island, NY).

The intact cell assay was performed as described previously [325]. Briefly, cells were plated into 96-well plates (100 μL per well). After cell attachment, the media was replaced with fresh media containing small molecules and incubated at 37 °C for 3 days. The media was removed and cell monolayers washed with Dulbecco's phosphate buffered saline. The assay was started by the addition of 50 μl of 2.5 mM 4MU-β-Glc in 0.2 M acetate buffer (pH 4.0) to each well, followed by incubation at 37 °C for 1-4 hours. The extent of unspecific non-lysosomal GC activity was evaluated by adding CBE (Toronto Research Chemicals) to control wells. The reaction was stopped by the addition of 150 μL of 0.2 M glycine buffer (pH 10.8). Liberated 4MU was measured (excitation 365 nm, emission 445 nm) with a Molecular Devices SpectraMax Gemini fluorescence plate reader. Small molecules were assayed at least in triplicate at each concentration, and on three different days. Cells appeared intact when viewed under a light microscope. The data reported were normalized to the enzyme activity of cells of the same type treated with vehicle control (H_2O) and expressed as percentage of WT enzyme activity.

6.4.5 Crystallization, Data Collection, Structure Determination and Refinement

Cerezyme was partially deglycosylated with N-glycosidase F (Promega) as described previously [357] and concentrated to 3 mg/mL in 0.02% sodium azide, 10 mM citrate buffer, pH 5.5, 7% (v/v) ethanol. Crystals of GCase were grown by vapor diffusion at room temperature using a cocktail composed of 11-12% PEG 3350, 0.18-0.205 M ammonium sulfate, and 0.1 M acetate buffer, pH 4.6. Crystals with **1** and **2** were acquired by soaking crystals in the reservoir solution with 1 mM inhibitor for 5 minutes or 5 days, respectively. Crystals were cryoprotected with 20% ethylene glycol, cryocooled in liquid N_2. Data were collected at the Southeast Regional Collaborative Access Team (SER-CAT) Beamline 22-BM-C at the Advanced Photon Source at Argonne National Labs (Darien, IL). Data sets were indexed and scaled using the HKL2000 [218]. The structures were solved by rigid body refinement to 4 Å resolution in REFMAC5 [364] utilizing the IFG-bound protein structure as the initial model (PDB code 2NSX) after all waters, ligands, and N-acetyl-glucosamines were removed. Each of the four monomers in the asymmetric unit of 2NSX was defined as a rigid body. This procedure was followed by restrained refinement against the highest resolution of the data with REFMAC5 [364] and model rebuilding with Coot [365]. Models for **1** and **2** were generated using PRODRG [366] and figures generated using PyMOL [367]. For both structures, 99% of the residues lie in most favored and additionally allowed regions of the Ramachandran plot. Crystallographic statistics appear in Table 6.1.

APPENDIX A

EXPRESSION AND PURIFICATION OF THE LUMINAL DOMAIN OF LIMP-2

A.1 Introduction

Lysosomal storage disorders are 'loss of function' disorders, due to deficient lysosomal glycolipid hydrolase activity [368]. Gaucher disease (GD), the most common lysosomal storage disorder, is caused by inherited point mutations in acid-β-glucosidase (GCase), the enzyme that hydrolyzes glucosylceramide (GlcCer) in the lysosome. These point mutations result in GCase degradation in the endoplamic reticulum (ER) by ER associated degradation instead of trafficking to the lysosome. This results in an accumulation of GlcCer in the lysosome and leads to the many symptoms of Gaucher disease including hepatomegaly, splenomegally, anemia, weakened skeleton, and in severe cases, central nervous system (CNS) complications [369].

As part of our long-term drug discovery efforts, we are working to understand the molecular details of GCase as it is trafficked to the lysosome. Although most lysosomal proteins are synthesized in the ER and are selectively transported via the Golgi complex to the lysosome by the mannose-6-phosphate receptor (MPR) pathway, GCase does not [370-371]. Until 2007, the trafficking mechanism of GCase remained unclear when the 477 residue lysosomal integral membrane protein 2 (LIMP-2), of no known definitive function [372], was shown to be a trafficking partner of GCase. The LIMP-2/GCase complex was identified by affinity chromatography, and the role of LIMP-2 as a sorting receptor for GCase was verified by immunoprecipitation and fluorescence studies *in vitro*. GCase activity, level, and localization correlated with the presence or absence of LIMP-2. *In vivo* studies involving LIMP-2 knockout mice, revealed 50% or less wild type GCase activity in its vital organs. GCase was shown to interact with the soluble

luminal domain of LIMP-2, specifically a coiled-coiled motif, and disruption of this domain eliminated the interaction. Complex formation is pH dependent, with association occurring at the neutral pH similar to that in the ER, and dissociation occurring at acidic pH corresponding to that of the lysosome. This is the first time that a lysosomal membrane protein has been shown to be a trafficking receptor. Not only is this complex a novel pathway for protein sorting, but over expression of LIMP-2 has been shown to enhance trafficking of mutant GCase [373]. The aim of the project originally was to characterize the LIMP-2/GCase complex utilizing biophysical methods and identify compounds that stabilize this interaction. Unfortunately, purification of a stable construct in sufficient quantities for biophysical studies was unattainable and the project was abandoned.

A.2 Methods and Discussion

A.2.1 LIMP-2/ pET-30 (-32) Xa/LIC Constructs

LIMP-2 is a 477 residue lysosomal membrane protein that is composed of a 400 residue luminal domain, two transmembrane domains, and a 20 amino acid cytoplasmic domain [373]. As membrane-bound proteins are notoriously difficult to purify and analyze by typical biophysical methods, we chose to express only the soluble luminal domain of LIMP-2 (L2LD). We initially annealed L2LD into the pET-30 Xa/LIC vector which provided a poly-histidine affinity tag for subsequent purifications and a Factor Xa cleavage site for removal of this tag. In an effort to yield a more soluble construct, L2LD was also annealed into the pET-32 Xa/LIC vector which contains the same affinity tag, but also encodes for a thioredoxin fusion protein for better folding. As detailed below, other vectors, including those for periplasmic expression and N-terminal MBP tag, were also evaluated for their ability to generate soluble L2LD.

A.2.1.1 Molecular Biology

L2LD was first amplified (5-PRIME Master Mix, Fisher Scientific) from a plasmid containing the gene purchased from Origene and annealed into the pET-30 Xa/LIC (L2LD30; Novagen) or pET-32 Xa/LIC vector (L2LD32; Novagen). The pET-30 Xa/LIC vector encodes for the following features: N-terminal hexa-histidine and S-tags, a Factor Xa cleavage site, and a C-terminal hexa-histidine tag. The pET-32 Xa/LIC vector encodes for the same features as pET-30 Xa/LIC with the addition of a thioredoxin fusion protein encoded at the N-terminus. Both constructs eliminated the C-terminal histidine tag. After plasmid replication in NovaBlue Giga Singles *E. coli* (Novagen), the entire coding region was verified by DNA sequencing (MWG Operon) and compared to the sequence deposited in the NCBI repository.

A.2.1.2 Protein Expression and Purification

Since LIMP-2 is a human protein possessing five cysteine residues in the luminal domain, expression trials of both L2LD plasmids were conducted in a bacterial strain that corrects for rare codons and favors disulfide bond formation, specifically Rosetta-Gami 2(DE3)pLysS (Novagen). When protein expression, induced by isopropyl β-D-1-thiogalactopyranoside (IPTG, 0.1-1 mM), was carried out at 37 °C, inclusion bodies were formed. However, when cultures were induced overnight at 17 °C with the same concentrations of IPTG, L2LD30 was expressed in the soluble *E. coli* fraction. Liter cultures were grown to an OD_{600}= 0.6, induced with 0.1 mM IPTG, and incubated for 15 hours at 17 °C while shaking. The cells were harvested by centrifugation, resuspended in lysis buffer (50 mM Hepes, 0.2 M NaCl, 40 mM Imidazole, pH 7.5) and lysed by French press. The suspension was centrifuged at 8,000 x g to remove cell debris.

Initial purification attempts were conducted with the L2LD30 construct in which the soluble fraction of the cell lysate was loaded onto a 1 mL HisTrap FF crude column attached to an AKTA FPLC system (GE Life Sciences). A combination of a 100 column-

volume (CV) wash with lysis buffer containing 0.1% Triton X-100 and an elution gradient of 40 mM to 200 mM imidazole over 25 CVs was necessary to resolve L2LD30 from most of the contaminants. Elution fractions were visualized by sodium dodecylsulfate polyacrylamide electrophoresis (SDS-PAGE). Coomassie staining revealed that the fraction containing L2LD30 (MW ~53 kDa) was still contaminated with an ~60 kDa impurity (Fig. A.1A, lane 2). Attempts to remove the ~60 kDa protein from L2LD30 by ion exchange and size-exclusion chromatography failed to separate the two proteins.

Cleavage of L2LD30 was achieved by incubating 1 U Factor Xa (NEB) per 50 μg of protein at room temperature overnight. Cleavage was confirmed by SDS-PAGE (Fig. A.1A, lane 3). Cleaved L2LD30 was initially purified over a nickel affinity column to remove any uncleaved protein as well as the cleaved tags. A final purification by size-exclusion on a HiLoad 16/60 Superdex 75 prep grade column was employed to remove L2LD from Factor Xa. However, cleaved L2LD30 co-eluted with the ~60 kDa protein in the void volume.

This purification protocol was also repeated for the L2LD32 construct. However, SDS-PAGE followed by coomassie staining revealed a doublet of bands corresponding to the L2LD32 (MW 64 kDa) protein and the ~60 kDa impurity seen in the L2LD30 purifications (Fig. A.1B). Due to the close proximity of the L2LD32 band with this contaminate, this construct was abandoned and further attempts to remove the impurity were focused on the L2LD30 construct.

A.2.1.3 Verification of L2LD30 and L2LD32 Expression and Identification of GroEL

The presence of both L2LD30 and L2LD32 was confirmed by western blot analysis using a 1:2000 dilution of Penta-His mouse monoclonal antibody (Invitrogen) followed by incubation with a 1:2000 dilution of rabbit anti-mouse IgG1-HRP antibody

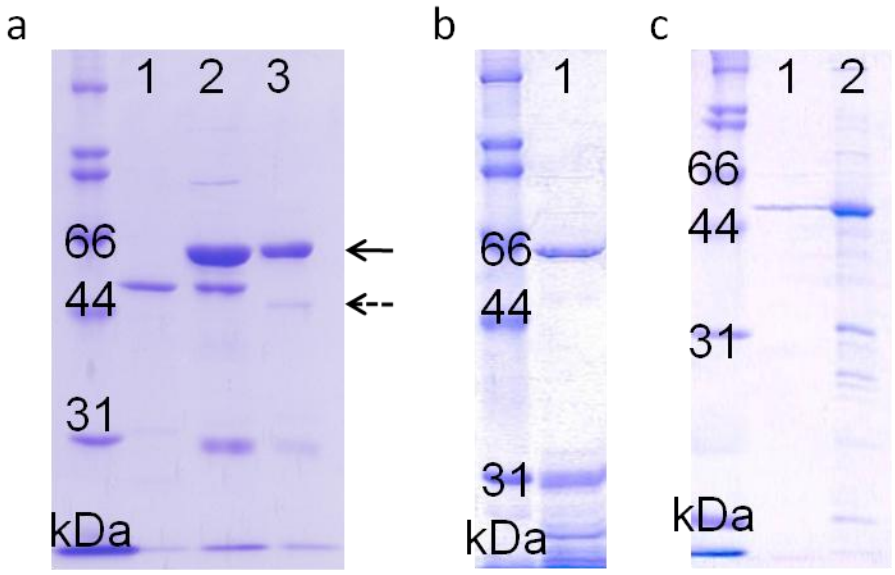

Figure A.1. SDS-PAGE analysis of L2LD30 and L2LD32 constructs. A) Lane 1, L2LD30 inclusion bodies; lane 2, L2LD30 uncleaved and GroEL; lane 3, L2LD30 cleaved (dashed arrow) and GroEL (solid arrow). B) Lane 1, purified L2LD32. C) Lane 1, purified L2LD30; lane 2, L2LD30 inclusion bodies.

(Invitrogen). Both blots were recorded on a Typhoon imager (GE Healthcare) (Fig.A. 2A-B).

The identification of L2LD in both constructs, as well as the ~60 kDa contaminate protein, was further verified by in-gel trypsin digestion and MALDI-TOF mass spec analysis. The protocol was carried out as described in Chapter 3. L2LD was confirmed and the ~60 kDa impurity was identified to be the bacterial heat shock protein GroEL (monomer MW 57 kDa).

A.2.1.4 Removal of GroEL

Attempts to remove GroEL included optimizing the expression conditions of L2LD30. An overnight culture of LB was inoculated and incubated overnight at 37 °C while shaking. This was used to inoculate various nutrient-rich broths, including Power, Turbo, Hyper, Superior, Glucose M9Y, Terrific +4% glycerol, and LB broths (Athena Enzyme Systems). Cultures were grown to an OD_{600} of 0.6 to 0.8 and protein expression was induced by 0.2 mM IPTG and incubated at either 17 °C overnight or for three hours at 37 °C. Nickel affinity batch purification of the soluble fraction followed by SDS-PAGE analysis revealed GroEL to be present in all samples.

Ultimately, purification from the ~60 kDa contaminate was achieved by conducting an initial nickel affinity purification as described above. The elution was then concentrated to 250 µL and then diluted to 10 mL in 5% milk and incubated on ice for 3 minutes followed by the addition of 10 mM ATP and 5 mM $MgSO_4$. During this step, ATP binds to active GroEL and induces the release of L2LD. The free GroEL then preferentially binds to casein, a highly abundant protein in milk that contains a considerable amount of exposed hydrophobic residues in its native state [374]. The reaction was incubated while rocking at 37 °C for 1 hr, ultracentrifuged for 30 minutes at 42,000 rpm, and then subjected to another nickel affinity purification step. SDS-PAGE

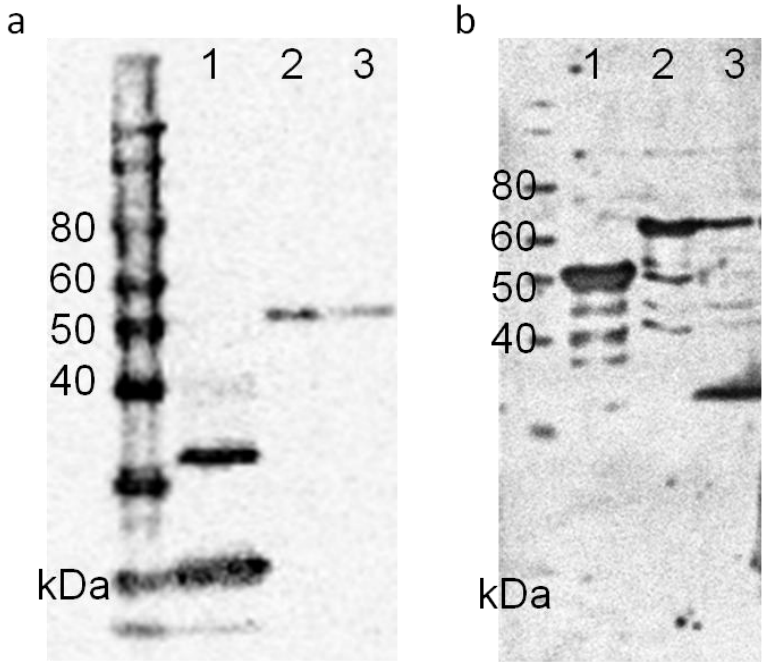

Figure A.2. Western blot analysis of L2LD30 and L2LD32. A) Benchmark his-tag protein standard; lane 1, *A. fulgidus* signal peptide peptidase possessing an N-terminal his-tag as a positive control; lane 2, L2LD30 inclusion bodies; lane 3; batch purified L2LD30. B) Benchmark his-tag protein standard; lane 1, L2LD30 inclusion bodies; lane 2, L2LD32 inclusion bodies; lane 3, batch purified L2LD32.

analysis of the eluted sample revealed a ~99% pure sample (Fig. A.1C, lane 1). Unfortunately, the yield was very low and attempts to scale-up the procedure failed. Therefore, other constructs to increase the solubility of L2LD and minimize GroEL content were created, as described below.

A.2.2 LIMP-2/ pET-22b(+) Construct

We next sought to express L2LD in the periplasmic space of *E. coli*. This was believed to reduce, if not eliminate, GroEL contamination as GroEL is a cytoplasmic protein and would be physically separated from L2LD in the periplasmic space by the inner membrane.

A.2.2.1 Molecular Biology

L2LD was amplified from the original PCR product used to create the pET-30 and -32 Xa/LIC constructs and ligated (Roche Quick Ligation Kit) into the pET-22b(+) (L2LD22; Novagen) vector using SacI and EcoRI (New England Biolabs) endonuclease restriction sites, respectively. The final L2LD22 construct encodes for an N-terminal *pelB* signal sequence for periplasmic localization and a C-terminal His-tag. After transformation into NovaBlue Giga Singles and overnight growth, the plasmid was isolated, and its sequence verified. An N386D mutation was present in the final construct, which was corrected by site-directed mutagenesis (Stratagene QuikChange) according to the manufacturer's instructions. After treatment with Dpn I to remove the parental strand, transformation into XL1-Blue cells and overnight growth, the mutant plasmid was isolated and sequenced, as above.

A.2.2.2 Protein Expression and Purification

The L2LD22 plasmid was transformed into Rosetta-Gami 2(DE3)pLysS. Liter cultures were grown to an OD_{600}= 0.6, induced with 1 mM IPTG, and incubated for 3 hours at 37 °C while shaking. The cells were harvested by centrifugation.

Initially, the L2LD22 construct was purified as described above for L2LD30. However, GroEL was present after elution from the nickel affinity column. Spheroplasting, a lysis method which removes only the outer membrane of gram-negative bacteria was then used to purify L2LD22 expressed only in the periplasmic space. The procedure was adapted from a previously published protocol [375] in which about three grams of cell pellet were thawed and resuspended in 5 mL ice-cold spheroplast buffer (40% sucrose, 33 mM Tris HCl, pH 8.0). Lysozyme and EDTA were then added at 5 μg/mL and 1 mM, respectively. The reaction was incubated on ice for 1 hr and then subjected to ultracentrifugation at 42,000 rpm. The supernatant was loaded onto a 1 mL HisTrap FF crude column and the elution fractions were analyzed by SDS-PAGE (Fig. A.3A). GroEL was again present in the elution and the yield of L2LD22 was low. One likely source of error was the use of frozen cells, as it is possible that some cells lysed in the thawing procedure, thus releasing GroEL from the cytoplasm and allowing it to bind to the otherwise isolated L2LD22. Therefore, the spheroplasting procedure should be conducted the same day as cell growth.

A.2.3 LIMP-2/ pMAL-c4x Construct

We next sought to test the *E. coli* maltose binding protein (MBP) as a fusion partner with L2LD. MBP is reported to be a more effective solubilizing agent than the thioredoxin tag and can promote the proper folding of the attached protein into its biologically active conformation [376].

A.2.3.1 Molecular Biology

L2LD was amplified from pET-30 Xa/LIC (retaining the N-terminal Factor Xa cleavage site) and ligated into the pMAL-c4x vector (New England Biolabs) using SacI and EcoRI restriction sites, respectively. Our pMAL-c4x construct (L2LDc4x) incorporates an 8-amino acid linker between MBP and L2LD (NSSSEIGR), where the

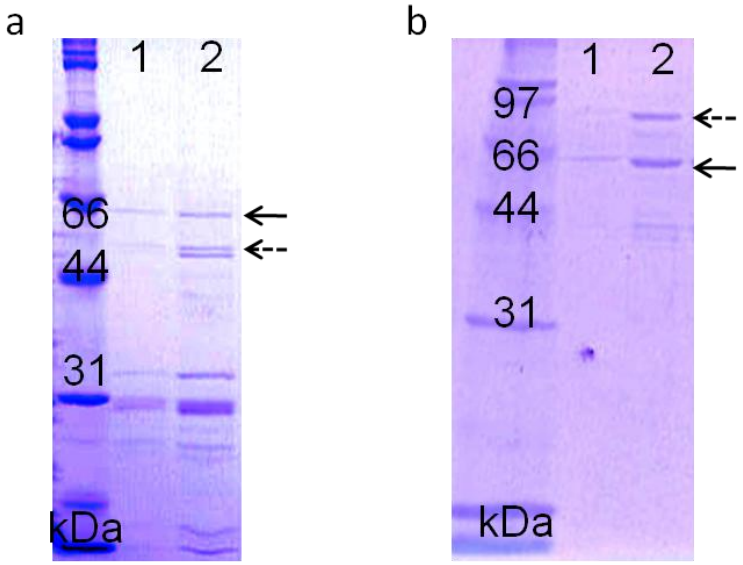

Figure A.3. SDS-PAGE analysis of L2LD22 and L2LDc4x constructs. A) Lane 1, purified L2LD22 and GroEL; lane 2, concentrated purified L2LD22 (dashed arrow) and GroEL (solid arrow). B) Lane 1, purified L2LDc4x; lane 2, concentrated purified L2LDc4x (dashed arrow) and GroEL (solid arrow).

Factor Xa cleavage sequence is leftover from pET-30 Xa/LIC. After transformation into NovaBlue Giga Singles and overnight growth, the plasmid was isolated, and its sequence verified.

A.2.3.2 Protein Expression and Purification

As described above, the L2LDc4x plasmid was transformed into Rosetta-gami 2(DE3)pLysS. Cells were cultured in Superior Broth (US Biological) to an optical density of 0.6 at 600 nm, induced with 0.1 mM IPTG, and incubated for three hours at 37 °C. The cells were pelleted by centrifugation, flash frozen with liquid nitrogen and stored at -80 °C.

Approximately 3 g of cell pellet were lysed by sonication in the presence of 50 mM HEPES, pH 7.5, 200 mM NaCl, 1 mM EDTA (Buffer A), supplemented with Roche Complete Protease Inhibitor. Cell debris was removed by ultracentrifugation (42,000 rpm for 20 min) and supernatant loaded onto a 20 ml High Flow Amylose Resin (New England Biolabs) column equilibrated with Buffer A. The MBP-L2LDc4x protein (MW ~96 kDa) was eluted with Buffer A supplemented with 10 mM maltose. The elution fractions were analyzed by SDS-PAGE and GroEL was found to be present in each sample (Fig. A.3B).

A.2.4 LIMP-2/ pPICZα-C Construct

Finally, expression in the methylotropic yeast, *Pichia pastoris*, was attempted as L2LD may be better expressed in a eukaryotic system. *P. pastoris* was chosen as it has several advantages over other eukaryotic and prokaryotic expression systems including rapid growth rate, ease of high cell-density fermentation, high levels of productivity in an almost protein-free medium, diverse posttranslational modifications, and the ability to engineer secreted proteins that can be purified from growth medium [377].

A.2.4.1 Molecular Biology

L2LD was amplified from pET-30 Xa/LIC and ligated into the pPICZα C vector (L2LD αC; Invitrogen) using EcoRI and Kpn I (New England Biolabs) restriction sites, respectively. This vector encodes for an α-factor secretion signal, a C-terminal myc eptiope and polyhistidine tag. The ligated plasmid was transformed into NovaBlue Giga Singles to propogate the plasmid, and transformants were selected for on low salt Luria–Bertani (LB) agar plates supplemented with the antibiotic Zeocin (25 μg/ml). The L2LDαC transformants were subjected to overnight growth, isolated by mini-prep, and the sequence was verified.

A.2.4.2 Protein Expression and Purification

The L2LDαC plasmid was linearized after digestion with SacI followed by heat inactivation of the restriction enzyme. The digestion reaction was immediately transformed into the X-33 wild-type strain using the EasyComp (Invitrogen) method and propagated on YPD medium (1% (w/v) yeast extract, 2% (w/v) peptone, 2% (w/v) dextrose, 1 M sorbitol, 2% (w/v) agar) containing Zeocin (100 μg/ml). A small-scale expression trial was then conducted in which 25 mL of BMGY (buffered glycerol-complex medium; 1% (w/v) yeast extract, 2% (w/v) peptone, 100 mM potassium phosphate, pH 6.0, 1.34% (w/v) yeast nitrogen base, 4 x 10^{-5}% (w/v) biotin, 1% glycerol) was inoculated and grown at 30 °C for 16 hrs while shaking. The cells were pelleted and induced by resuspension in BMMY (buffered methanol-complex medium; 1% (w/v) yeast extract, 2% (w/v) peptone, 100 mM potassium phosphate, pH 6.0, 1.34% (w/v) yeast nitrogen base, 4 x 10^{-5}% (w/v) biotin, 0.5% methanol) to an OD_{600}= 1.0 and the culture was returned to 30 °C for continued growth. Methanol was added every 24 hrs to a final concentration of 0.5% to maintain induction. A 1 mL aliquot of the culture was removed every 6 hrs for the first day and then every 12 hrs for a total of 4 days (96 hrs) to determine the optimal time post-induction to harvest. Each aliquot was pelleted and the

supernatant was transferred to a separate microcentrifuge tube. Both pellet and supernatant were frozen in liquid nitrogen and stored at -80 °C.

Each supernatant fraction was thawed, and batch purified with Nickel Sepharose High Performance resin (GE Life Sciences). Unfortunately the samples were too dilute to be visualized by SDS-PAGE or western blot. Therefore, all samples were pooled and concentrated (Fig. A.4A). A western blot was performed with the Penta-His monoclonal antibody as described above and an 80 kDa band consistent with a glycosylated L2LD was observed (Fig. A.4B). To confirm the band was corresponding to a glycosylated L2LD, the sample was subjected to PNGase F cleavage, an amidase that cleaves between the innermost GlcNAc and asparagine residues of high mannose, hybrid, and complex oligosaccharides from N-linked glycoproteins. The cleavage reaction was incubated at room temperature for 80 hrs, resulting in a lower molecular weight species consistent with the L2LD with affinity tags (Fig. A.4C). However, attempts to scale-up this protocol failed.

A.2.5 Conclusions

Ultimately, we were unable to generate soluble L2LD for further characterization in spite of repeated attempt to optimize expression conditions, cellular distribution, fusion tags, and eukaryotic expression. Incubation with milk, ATP and Mg^{2+} allowed for the removal of GroEL, however this procedure failed to scale-up.

Analysis of the L2LD sequence by the DAS transmembrane prediction server predicts a hydrophobic region in the area of the coiled-coil domain of LIMP-2, which may explain GroEL binding. However, this is the identified potential binding region of GCase [373] and decreasing the hydrophobic nature of this region by site-directed mutagenesis may also impact its ability to bind to GCase as well. Ultimately, it may be necessary to express this protein in mammalian cells such as Chinese hamster ovary, human embryonic kidney, or insect cells.

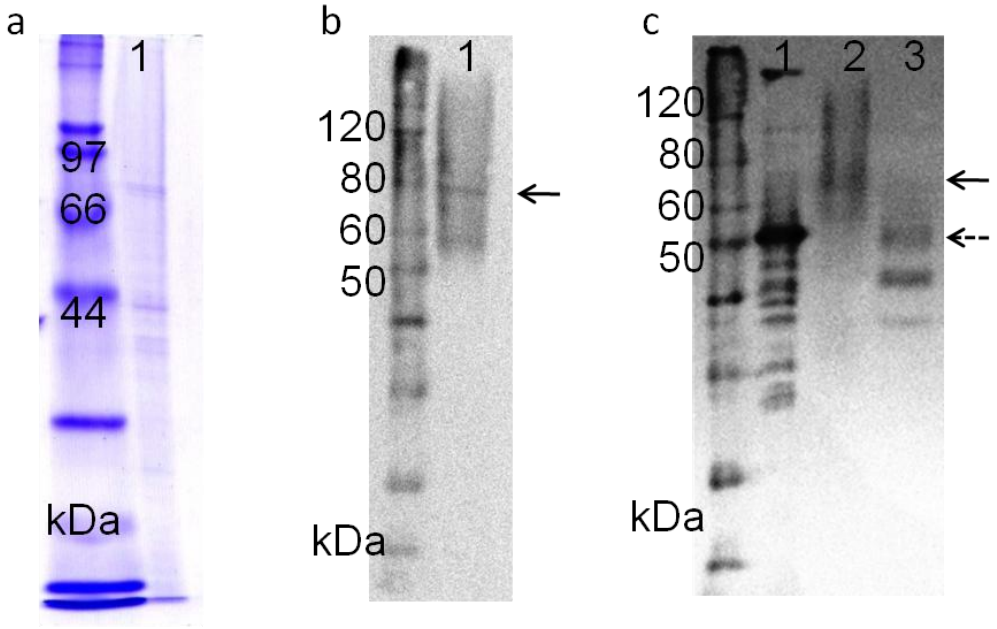

Figure A.4. SDS-PAGE and western blot analysis of glycosylated and de-glycosylated L2LDαC. A) SDS-PAGE: Lane 1, L2LDαC. B) Western blot: Benchmark his-tag protein standard; lane 1, L2LDαC (solid arrow). C) Western blot: Benchmark his-tag protein standard; lane 1, L2LD30; lane 2, glycosylated L2LDαC (solid arrow); lane 3, de-glycosylated L2LDαC (dashed arrow).

REFERENCES

1. RESNIKOFF, S., *et al.*, "Global data on visual impairment in the year 2002," Bulletin of the World Health Organization, vol. 82, pp. 844-851, 2004.

2. QUIGLEY, H.A., "Glaucoma," Lancet, vol. 377, pp. 1367-1377, 2011.

3. BURGOYNE, C.F., *et al.*, "The optic nerve head as a biomechanical structure: A new paradigm for understanding the role of iop-related stress and strain in the pathophysiology of glaucomatous optic nerve head damage," Progress in Retinal and Eye Research, vol. 24, pp. 39-73, 2005.

4. QUIGLEY, H.A., "Medical progress - open-angle glaucoma," New England Journal of Medicine, vol. 328, pp. 1097-1106, 1993.

5. SARFARAZI, M., "Recent advances in molecular genetics of glaucomas," Human Molecular Genetics, vol. 6, pp. 1667-1677, 1997.

6. KIM, B.S., *et al.*, "Targeted disruption of the myocilin gene (myoc) suggests that human glaucoma-causing mutations are gain of function," Molecular and Cellular Biology, vol. 21, pp. 7707-7713, 2001.

7. BILL, A., "Drainage of aqueous-humor," Investigative Ophthalmology, vol. 14, pp. 1-3, 1975.

8. YUE, B., "The extracellular matrix and its modulation in the trabecular meshwork," Survey of Ophthalmology, vol. 40, pp. 379-390, 1996.

9. HEIJL, A., *et al.*, "Reduction of intraocular pressure and glaucoma progression - results from the early manifest glaucoma trial," Archives of Ophthalmology, vol. 120, pp. 1268-1279, 2002.

10. KASS, M.A., *et al.*, "The ocular hypertension treatment study - a randomized trial determines that topical ocular hypotensive medication delays or prevents the onset of primary open-angle glaucoma," Archives of Ophthalmology, vol. 120, pp. 701-713, 2002.

11. GOLDMANN, H., "Cortisone glaucoma," Archives of Ophthalmology, vol. 68, pp. 621-&, 1962.

12. STERN, J.J., "Acute glaucoma during cortisone therapy," American Journal of Ophthalmology, vol. 36, pp. 389-390, 1953.

13. COVELL, L.L., "Glaucoma induced by systemic steroid therapy," American Journal of Ophthalmology, vol. 45, pp. 108-109, 1958.

14. POLANSKY, J.R., *et al.*, "Isolation of messenger rna and secreted proteins following dexamethasone treatment of cultured human trabecular meshwork cells," Investigative Ophthalmology and Visual Science, vol. 30, pp. 223, 1989.

15. TRIPATHI, B.J., MILLARD, C.B., and TRIPATHI, R.C., "Corticosteroids induce a sialated glycoprotein (cort-gp) in trabecular cells-invitro," Experimental Eye Research, vol. 51, pp. 735-736, 1990.

16. PARTRIDGE, C.A., *et al.*, "Dexamethasone induces specific proteins in human trabecular meshwork cells," Investigative Ophthalmology & Visual Science, vol. 30, pp. 1843-1847, 1989.

17. KWON, Y.H., *et al.*, "Mechanisms of disease: Primary open-angle glaucoma," New England Journal of Medicine, vol. 360, pp. 1113-1124, 2009.

18. NGUYEN, T.D., *et al.*, "Gene structure and properties of tigr, an olfactomedin-related glycoprotein cloned from glucocorticoid-induced trabecular meshwork cells," Journal of Biological Chemistry, vol. 273, pp. 6341-6350, 1998.

19. POLANSKY, J.R., *et al.*, "Cellular pharmacology and molecular biology of the trabecular meshwork inducible glucocorticoid response gene product," Ophthalmologica, vol. 211, pp. 126-139, 1997.

20. KIRSTEIN, L., *et al.*, "Regulation of human myocilin/tigr gene transcription in trabecular meshwork cells and astrocytes: Role of upstream stimulatory factor," Genes to Cells, vol. 5, pp. 661-676, 2000.

21. SHEPARD, A.R., *et al.*, "Delayed secondary glucocorticoid responsiveness of myoc in human trabecular meshwork cells," Investigative Ophthalmology & Visual Science, vol. 42, pp. 3173-3181, 2001.

22. SHEFFIELD, V.C., *et al.*, "Genetic-linkage of familial open-angle glaucoma to chromosome-1q21-q31," Nature Genetics, vol. 4, pp. 47-50, 1993.

23. STONE, E.M., *et al.*, "Identification of a gene that causes primary open angle glaucoma," Science, vol. 275, pp. 668-670, 1997.

24. KUBOTA, R., *et al.*, "A novel myosin-like protein (myocilin) expressed in the connecting cilium of the photoreceptor: Molecular cloning, tissue expression, and chromosomal mapping," Genomics, vol. 41, pp. 360-369, 1997.

25. FAN, B.J., *et al.*, "Gene mapping for primary open angle glaucoma," Clinical Biochemistry, vol. 39, pp. 249-258, 2006.

26. REZAIE, T., *et al.*, "Adult-onset primary open-angle glaucoma caused by mutations in optineurin," Science, vol. 295, pp. 1077-1079, 2002.

27. MONEMI, S., *et al.*, "Identification of a novel adult-onset primary open-angle glaucoma (poag) gene on 5q22.1," Human Molecular Genetics, vol. 14, pp. 725-733, 2005.

28. ALDRED, M.A., *et al.*, "Low prevalence of myoc mutations in uk primary open-angle glaucoma patients limits the utility of genetic testing," Human Genetics, vol. 115, pp. 428-431, 2004.

29. FINGERT, J.H., *et al.*, "Analysis of myocilin mutations in 1703 glaucoma patients from five different populations," Human Molecular Genetics, vol. 8, pp. 899-905, 1999.

30. WIGGS, J.L., *et al.*, "Prevalence of mutations in tigr/myocilin in patients with adult and juvenile primary open-angle glaucoma," American Journal of Human Genetics, vol. 63, pp. 1549-1552, 1998.

31. ORTEGO, J., ESCRIBANO, J., and COCAPRADOS, M., "Cloning and characterization of subtracted cdnas from a human ciliary body library encoding tigr, a protein involved in juvenile open angle glaucoma with homology to myosin and olfactomedin," Febs Letters, vol. 413, pp. 349-353, 1997.

32. MUKHOPADHYAY, A., *et al.*, "Did myocilin evolve from two different primordial proteins?," Molecular Vision, vol. 8, pp. 271-279, 2002.

33. FAUTSCH, M.P. and JOHNSON, D.H., "Characterization of myocilin-myocilin interactions," Investigative Ophthalmology & Visual Science, vol. 42, pp. 2324-2331, 2001.

34. RUSSELL, P., *et al.*, "The presence and properties of myocilin in the aqueous humor," Investigative Ophthalmology & Visual Science, vol. 42, pp. 983-986, 2001.

35. GOLDWICH, A., SCHOLZ, M., and TAMM, E.R., "Myocilin promotes substrate adhesion, spreading and formation of focal contacts in podocytes and mesangial cells," Histochemistry and Cell Biology, vol. 131, pp. 167-180, 2009.

36. FILLA, M.S., *et al.*, "In vitro localization of tigr/myoc in trabecular meshwork extracellular matrix and binding to fibronectin," Investigative Ophthalmology & Visual Science, vol. 43, pp. 151-161, 2002.

37. KARALI, A., *et al.*, "Localization of myocilin/trabecular meshwork-inducible glucocorticoid response protein in the human eye," Investigative Ophthalmology & Visual Science, vol. 41, pp. 729-740, 2000.

38. RAO, P.V., ALLINGHAM, R.R., and EPSTEIN, D.L., "Tigr/myocilin in human aqueous humor," Experimental Eye Research, vol. 71, pp. 637-641, 2000.

39. TAMM, E.R., "Myocilin and glaucoma: Facts and ideas," Progress in Retinal and Eye Research, vol. 21, pp. 395-428, 2002.

40. TAMM, E.R., *et al.*, "Modulation of myocilin/tigr expression in human trabecular meshwork," Investigative Ophthalmology & Visual Science, vol. 40, pp. 2577-2582, 1999.

41. ADAM, M.F., *et al.*, "Recurrent mutations in a single exon encoding the evolutionarily conserved olfactomedin-homology domain of tigr in familial open-angle glaucoma," Human Molecular Genetics, vol. 6, pp. 2091-2097, 1997.

42. RESCH, Z.T., *et al.*, "Aqueous humor rapidly stimulates myocilin secretion from human trabecular meshwork cells," Experimental Eye Research, vol. 91, pp. 901-908, 2010.

43. SOHN, S., *et al.*, "Expression of wild-type and truncated myocilins in trabecular meshwork cells: Their subcellular localizations and cytotoxicities," Investigative Ophthalmology & Visual Science, vol. 43, pp. 3680-3685, 2002.

44. CLARK, A.F., *et al.*, "Expression of the glaucoma gene myocilin (myoc) in the human optic nerve head," Faseb Journal, vol. 15, pp. 1251-1253, 2001.

45. CLARK, A.F., *et al.*, "Glucocorticoid induction of the glaucoma gene myoc in human and monkey trabecular meshwork cells and tissues," Investigative Ophthalmology & Visual Science, vol. 42, pp. 1769-1780, 2001.

46. O'BRIEN, E.T., REN, X.O., and WANG, Y.H., "Localization of myocilin to the golgi apparatus in schlemm's canal cells," Investigative Ophthalmology & Visual Science, vol. 41, pp. 3842-3849, 2000.

47. SANCHEZ-SANCHEZ, F., *et al.*, "Characterization of the intracellular proteolytic cleavage of myocilin and identification of calpain ii as a myocilin-processing protease," Journal of Biological Chemistry, vol. 282, pp. 27810-27824, 2007.

48. AROCA-AGUILAR, J.D., *et al.*, "Myocilin mutations causing glaucoma inhibit the intracellular endoproteolytic cleavage of myocilin between amino acids arg(226) and ile(227)," Journal of Biological Chemistry, vol. 280, pp. 21043-21051, 2005.

49. GOLDWICH, A., *et al.*, "Perfusion with the olfactomedin domain of myocilin does not affect outflow facility," Investigative Ophthalmology & Visual Science, vol. 44, pp. 1953-1961, 2003.

50. SAKAI, H., *et al.*, "Mitochondrial association of myocilin, product of a glaucoma gene, in human trabecular meshwork cells," Journal of Cellular Physiology, vol. 213, pp. 775-784, 2007.

51. UEDA, J., *et al.*, "Ultrastructural localization of myocilin in human trabecular meshwork cells and tissues," Journal of Histochemistry & Cytochemistry, vol. 48, pp. 1321-1329, 2000.

52. WENTZ-HUNTER, K., *et al.*, "Myocilin is associated with mitochondria in human trabecular meshwork cells," Journal of Cellular Physiology, vol. 190, pp. 46-53, 2002.

53. WENTZ-HUNTER, K., SHEN, X., and YUE, B., "Distribution of myocilin, a glaucoma gene product, in human corneal fibroblasts," Molecular Vision, vol. 9, pp. 308-314, 2003.

54. MERTTS, M., *et al.*, "Identification of the region in the n-terminal domain responsible for the cytoplasmic localization of myoc/tigr and its association with microtubules," Laboratory Investigation, vol. 79, pp. 1237-1245, 1999.

55. ALVARADO, J., MURPHY, C., and JUSTER, R., "Trabecular meshwork cellularity in primary open-angle glaucoma and nonglaucomatous normals," Ophthalmology, vol. 91, pp. 564-579, 1984.

56. TAWARA, A., *et al.*, "Immunohistochemical localization of myoc/tigr protein in the trabecular tissue of normal and glaucomatous eyes," Current Eye Research, vol. 21, pp. 934-943, 2000.

57. UEDA, J., WENTZ-HUNTER, K., and YUE, B., "Distribution of myocilin and extracellular matrix components in the juxtacanalicular tissue of human eyes," Investigative Ophthalmology & Visual Science, vol. 43, pp. 1068-1076, 2002.

58. UEDA, J. and YUE, B., "Distribution of myocilin and extracellular matrix components in the corneoscleral meshwork of human eyes," Investigative Ophthalmology & Visual Science, vol. 44, pp. 4772-4779, 2003.

59. PETERS, D.M., *et al.*, "Myocilin binding to hep ii domain of fibronectin inhibits cell spreading and incorporation of paxillin into focal adhesions," Experimental Cell Research, vol. 303, pp. 218-228, 2005.

60. SHEN, X., *et al.*, "Rho gtpase and camp/protein kinase a signaling mediates myocilin-induced alterations in cultured human trabecular meshwork cells," Journal of Biological Chemistry, vol. 283, pp. 603-612, 2008.

61. O'BRIEN, T.E., METHENEY, C.D., and POLANSKY, J.R., "Immunofluorescence method for quantifying the trabecular meshwork

glucocorticoid response (tigr) protein in trabecular meshwork and schlemm's canal cells," Current Eye Research, vol. 19, pp. 517-24, 1999.

62. SAGE, E.H. and BORNSTEIN, P., "Extracellular proteins that modulate cell-matrix interactions - sparc, tenascin, and thrombospondin," Journal of Biological Chemistry, vol. 266, pp. 14831-14834, 1991.

63. BORNSTEIN, P., "Diversity of function is inherent in matricellular proteins - an appraisal of thrombospondin-1," Journal of Cell Biology, vol. 130, pp. 503-506, 1995.

64. MURPHY-ULLRICH, J.E., "The de-adhesive activity of matricellular proteins: Is intermediate cell adhesion an adaptive state?," Journal of Clinical Investigation, vol. 107, pp. 785-790, 2001.

65. LUTJEN-DRECOLL, E., *et al.*, "Localization of the stress proteins alpha b-crystallin and trabecular meshwork inducible glucocorticoid response protein in normal and glaucomatous trabecular meshwork," Investigative Ophthalmology & Visual Science, vol. 39, pp. 517-525, 1998.

66. RESCH, Z.T. and FAUTSCH, M.P., "Glaucoma-associated myocilin: A better understanding but much more to learn," Experimental Eye Research, vol. 88, pp. 704-712, 2009.

67. FAUTSCH, M.P., *et al.*, "Recombinant tigr/myoc increases outflow resistance in the human anterior segment," Investigative Ophthalmology & Visual Science, vol. 41, pp. 4163-4168, 2000.

68. NASKAR, R. and THANOS, S., "Retinal gene profiling in a hereditary rodent model of elevated intraocular pressure," Molecular Vision, vol. 12, pp. 1199-1210, 2006.

69. MACKAY, E.O., *et al.*, "Myocilin protein levels in the aqueous humor of the glaucomas in selected canine breeds," Veterinary Ophthalmology, vol. 11, pp. 234-241, 2008.

70. MACKAY, E.O., KALLBERG, M.E., and GELATT, K.N., "Aqueous humor myocilin protein levels in normal, genetic carriers, and glaucoma beagles," Veterinary Ophthalmology, vol. 11, pp. 177-185, 2008.

71. SAWAGUCHI, K., *et al.*, "Myocilin gene expression in the trabecular meshwork of rats in a steroid-induced ocular hypertension model," Ophthalmic Research, vol. 37, pp. 235-242, 2005.

72. CABALLERO, M., ROWLETTE, L.L.S., and BORRAS, T., "Altered secretion of a tigr/myoc mutant lacking the olfactomedin domain," Biochimica Et Biophysica Acta-Molecular Basis of Disease, vol. 1502, pp. 447-460, 2000.

73. WIGGS, J.L. and VOLLRATH, D., "Molecular and clinical evaluation of a patient hemizygous for tigr/myoc," Archives of Ophthalmology, vol. 119, pp. 1674-1678, 2001.

74. LAM, D.S.C., *et al.*, "Truncations in the tigr gene in individuals with and without primary open-angle glaucoma," Investigative Ophthalmology & Visual Science, vol. 41, pp. 1386-1391, 2000.

75. ALLINGHAM, R.R., LIU, Y.T., and RHEE, D.J., "The genetics of primary open-angle glaucoma: A review," Experimental Eye Research, vol. 88, pp. 837-844, 2009.

76. VOLLRATH, D. and LIU, Y.H., "Temperature sensitive secretion of mutant myocilins," Experimental Eye Research, vol. 82, pp. 1030-1036, 2006.

77. GONG, G., *et al.*, "Genetic dissection of myocilin glaucoma," Human Molecular Genetics, vol. 13, pp. R91-R102, 2004.

78. "Myocilin allele specific phenotype database " 07/24/2011; Available from: www.myocilin.com.

79. MORISSETTE, J., *et al.*, "A common gene for juvenile and adult-onset primary open-angle glaucomas confined on chromosome 1q," American Journal of Human Genetics, vol. 56, pp. 1431-1442, 1995.

80. JACOBSON, N., *et al.*, "Non-secretion of mutant proteins of the glaucoma gene myocilin in cultured trabecular meshwork cells and in aqueous humor," Human Molecular Genetics, vol. 10, pp. 117-125, 2001.

81. KANAGAVALLI, J., *et al.*, "In vitro and in vivo study on the secretion of the gly367arg mutant myocilin protein," Molecular Vision, vol. 13, pp. 1161-1168, 2007.

82. CABALLERO, M. and BORRAS, T., "Inefficient processing of an olfactomedin-deficient myocilin mutant: Potential physiological relevance to glaucoma," Biochemical and Biophysical Research Communications, vol. 282, pp. 662-670, 2001.

83. GOBEIL, S., *et al.*, "Intracellular sequestration of hetero-oligomers formed by wild-type and glaucoma-causing myocilin mutants," Investigative Ophthalmology & Visual Science, vol. 45, pp. 3560-3567, 2004.

84. JOE, M.K., *et al.*, "Accumulation of mutant myocilins in er leads to er stress and potential cytotoxicity in human trabecular meshwork cells," Biochemical and Biophysical Research Communications, vol. 312, pp. 592-600, 2003.

85. WANG, L., *et al.*, "Pro370leu mutant myocilin disturbs the endoplasm reticulum stress response and mitochondrial membrane potential in human trabecular meshwork cells," Molecular Vision, vol. 13, pp. 618-625, 2007.

86. YAM, G.H.F., *et al.*, "Aggregated myocilin induces russell bodies and causes apoptosis - implications for the pathogenesis of myocilin-caused primary open-angle glaucoma," American Journal of Pathology, vol. 170, pp. 100-109, 2007.

87. ZHOU, Z.H. and VOLLRATH, D., "A cellular assay distinguishes normal and mutant tigr/myocilin protein," Human Molecular Genetics, vol. 8, pp. 2221-2228, 1999.

88. ELLGAARD, L. and HELENIUS, A., "Quality control in the endoplasmic reticulum," Nature Reviews Molecular Cell Biology, vol. 4, pp. 181-191, 2003.

89. ELLGAARD, L., MOLINARI, M., and HELENIUS, A., "Setting the standards: Quality control in the secretory pathway," Science, vol. 286, pp. 1882-1888, 1999.

90. KOPITO, R.R., "Er quality control: The cytoplasmic connection," Cell, vol. 88, pp. 427-430, 1997.

91. CIECHANOVER, A. and SCHWARTZ, A.L., "The ubiquitin-proteasome pathway: The complexity and myriad functions of proteins death," Proceedings of the National Academy of Sciences of the United States of America, vol. 95, pp. 2727-2730, 1998.

92. KOPITO, R.R. and SITIA, R., "Aggresomes and russell bodies - symptoms of cellular indigestion?," Embo Reports, vol. 1, pp. 225-231, 2000.

93. PAHL, H.L., "Signal transduction from the endoplasmic reticulum to the cell nucleus," Physiological Reviews, vol. 79, pp. 683-701, 1999.

94. SIDRAUSKI, C., CHAPMAN, R., and WALTER, P., "The unfolded protein response: An intracellular signalling pathway with many surprising features," Trends in Cell Biology, vol. 8, pp. 245-249, 1998.

95. MUNRO, S. and PELHAM, H.R.B., "An hsp70-like protein in the er - identity with the 78 kd glucose-regulated protein and immunoglobulin heavy-chain binding-protein," Cell, vol. 46, pp. 291-300, 1986.

96. LABOISSIERE, M.C.A., STURLEY, S.L., and RAINES, R.T., "The essential function of protein-disulfide isomerase is to unscramble nonnative disulfide bonds," Journal of Biological Chemistry, vol. 270, pp. 28006-28009, 1995.

97. LIU, Y.H. and VOLLRATH, D., "Reversal of mutant myocilin non-secretion and cell killing: Implications for glaucoma," Human Molecular Genetics, vol. 13, pp. 1193-1204, 2004.

98. CARBONE, M.A., *et al.*, "Overexpression of myocilin in the drosophila eye activates the unfolded protein response: Implications for glaucoma," Plos One, vol. 4, pp. 12, 2009.

99. WILKINSON, C.H., *et al.*, "Tonography demonstrates reduced facility of outflow of aqueous humor in myocilin mutation carriers," Journal of Glaucoma, vol. 12, pp. 237-242, 2003.

100. RUTISHAUSER, J. and SPIESS, M., "Endoplasmic reticulum storage diseases," Swiss Medical Weekly, vol. 132, pp. 211-222, 2002.

101. HERCZENIK, E. and GEBBINK, M., "Molecular and cellular aspects of protein misfolding and disease," Faseb Journal, vol. 22, pp. 2115-2133, 2008.

102. YAM, G.H.T., *et al.*, "Sodium 4-phenylbutyrate acts as a chemical chaperone on misfolded myocilin to rescue cells from endoplasmic reticulum stress and apoptosis," Investigative Ophthalmology & Visual Science, vol. 48, pp. 1683-1690, 2007.

103. JIA, L.Y., *et al.*, "Correction of the disease phenotype of myocilin-causing glaucoma by a natural osmolyte," Investigative Ophthalmology & Visual Science, vol. 50, pp. 3743-3749, 2009.

104. ARAKAWA, T., *et al.*, "Small molecule pharmacological chaperones: From thermodynamic stabilization to pharmaceutical drugs," Biochimica Et Biophysica Acta-Proteins and Proteomics, vol. 1764, pp. 1677-1687, 2006.

105. BERNIER, V., *et al.*, "Pharmacological chaperones: Potential treatment for conformational diseases," Trends in Endocrinology and Metabolism, vol. 15, pp. 222-228, 2004.

106. VALENZANO, K.J., *et al.*, "Identification and characterization of pharmacological chaperones to correct enzyme deficiencies in lysosomal storage disorders," Assay and Drug Development Technologies, vol. 9, pp. 213-235, 2011.

107. HERCZENIK, E. and GEBBINK, M., "Molecular and cellular aspects of protein misfolding and disease," FASEB J., vol. 22, pp. 2115, 2008.

108. KWON, Y.H., *et al.*, "Primary open-angle glaucoma," N. Engl. J. Med., vol. 360, pp. 1113-24, 2009.

109. ALWARD, W.L., "Medical management of glaucoma," N. Engl. J. Med., vol. 339, pp. 1298-307, 1998.

110. RESCH, Z. and FAUTSCH, M., "Glaucoma-associated myocilin: A better understanding but much more to learn," Exp. Eye Res., vol. 88, pp. 704-12, 2009.

111. GASIOROWSKI, J. and RUSSELL, P., "Biological properties of trabecular meshwork cells," Exp. Eye Res., vol. 88, pp. 671-675, 2009.

112. FAUTSCH, M.P., *et al.*, "In vitro and in vivo characterization of disulfide bond use in myocilin complex formation," Mol. Vis., vol. 10, pp. 417-25, 2004.

113. GOLDWICH, A., SCHOLZ, M., and TAMM, E.R., "Myocilin promotes substrate adhesion, spreading and formation of focal contacts in podocytes and mesangial cells," Histochem. Cell Biol., vol. 131, pp. 167-80, 2009.

114. FILLA, M.S., *et al.*, "In vitro localization of tigr/myoc in trabecular meshwork extracellular matrix and binding to fibronectin," Invest. Ophthalmol. Vis. Sci., vol. 43, pp. 151-61, 2002.

115. FAUTSCH, M.P. and JOHNSON, D.H., "Characterization of myocilin-myocilin interactions," Invest. Ophthalmol. Vis. Sci., vol. 42, pp. 2324-31, 2001.

116. WENTZ-HUNTER, K., *et al.*, "Extracellular myocilin affects activity of human trabecular meshwork cells," J. Cell. Physiol., vol. 200, pp. 45-52, 2004.

117. TAMM, E.R., *et al.*, "Modulation of myocilin/tigr expression in human trabecular meshwork," Invest. Ophthalmol. Vis. Sci., vol. 40, pp. 2577-82, 1999.

118. KARAVANICH, C.A. and ANHOLT, R.R., "Molecular evolution of olfactomedin," Mol. Biol. Evol., vol. 15, pp. 718-26, 1998.

119. TOMAREV, S.I. and NAKAYA, N., "Olfactomedin domain-containing proteins: Possible mechanisms of action and functions in normal development and pathology," Mol. Neurobiol., vol. 40, pp. 122-38, 2009.

120. ZENG, L.-C., HAN, Z.-G., and MA, W.-J., "Elucidation of subfamily segregation and intramolecular coevolution of the olfactomedin-like proteins by comprehensive phylogenetic analysis and gene expression pattern assessment," FEBS Lett., vol. 579, pp. 5443-53, 2005.

121. KIM, B.S., *et al.*, "Targeted disruption of the myocilin gene (myoc) suggests that human glaucoma-causing mutations are gain of function," Mol. Cell. Biol., vol. 21, pp. 7707-13, 2001.
122. LAM, D.S., *et al.*, "Truncations in the tigr gene in individuals with and without primary open-angle glaucoma," Invest. Ophthalmol. Vis. Sci., vol. 41, pp. 1386-91, 2000.

123. JOE, M.K., *et al.*, "Accumulation of mutant myocilins in er leads to er stress and potential cytotoxicity in human trabecular meshwork cells," Biochem. Biophys. Res. Commun., vol. 312, pp. 592-600, 2003.

124. LIU, Y. and VOLLRATH, D., "Reversal of mutant myocilin non-secretion and cell killing: Implications for glaucoma," Hum. Mol. Genet., vol. 13, pp. 1193-204, 2004.

125. VOLLRATH, D. and LIU, Y., "Temperature sensitive secretion of mutant myocilins," Exp. Eye Res., vol. 82, pp. 1030-6, 2006.

126. GOBEIL, S., LETARTRE, L., and RAYMOND, V., "Functional analysis of the glaucoma-causing tigr/myocilin protein: Integrity of amino-terminal coiled-coil regions and olfactomedin homology domain is essential for extracellular adhesion and secretion," Exp. Eye Res., vol. 82, pp. 1017-29, 2006.

127. VAN ANKEN, E. and BRAAKMAN, I., "Versatility of the endoplasmic reticulum protein folding factory," Crit. Rev. Biochem. Mol. Biol., vol. 40, pp. 191-228, 2005.

128. ELLGAARD, L. and HELENIUS, A., "Quality control in the endoplasmic reticulum," Nat. Rev. Mol. Cell. Biol., vol. 4, pp. 181-191, 2003.

129. YAM, G.H.-F., *et al.*, "Aggregated myocilin induces russell bodies and causes apoptosis: Implications for the pathogenesis of myocilin-caused primary open-angle glaucoma," Am. J. Pathol., vol. 170, pp. 100-9, 2007.

130. WANG, L., *et al.*, "Pro370leu mutant myocilin disturbs the endoplasm reticulum stress response and mitochondrial membrane potential in human trabecular meshwork cells," Mol. Vis., vol. 13, pp. 618-25, 2007.

131. CARBONE, M.A., *et al.*, "Overexpression of myocilin in the drosophila eye activates the unfolded protein response: Implications for glaucoma," PLoS ONE, vol. 4, pp. e4216, 2009.

132. WUSTMAN, B., *et al.*, "114. Pharmacological chaperone therapy for gaucher disease: Mechanism of action, a survey of responsive mutations and phase i clinical trial results," Mol. Genet. Metab., vol. 93, pp. S46, 2008.

133. RUBENSTEIN, R. and ZEITLIN, P., "A pilot clinical trial of oral sodium 4-phenylbutyrate (buphenyl) in δ f508-homozygous cystic fibrosis patients partial restoration of nasal epithelial cftr function," Am. J. Resp. Crit. Care Med., vol. 157, pp. 484-490, 1998.

134. COHEN, F.E. and KELLY, J.W., "Therapeutic approaches to protein-misfolding diseases," Nature, vol. 426, pp. 905-9, 2003.

135. NAGY, I., TREXLER, M., and PATTHY, L., "Expression and characterization of the olfactomedin domain of human myocilin," Biochem. Biophys. Res. Commun., vol. 302, pp. 554-61, 2003.

136. PETERS, D.M., *et al.*, "Myocilin binding to hep ii domain of fibronectin inhibits cell spreading and incorporation of paxillin into focal adhesions," Exp. Cell. Res., vol. 303, pp. 218-28, 2005.

137. PARK, B.C., *et al.*, "Optimized bacterial expression of myocilin proteins and functional comparison of bacterial and eukaryotic myocilins," Mol. Vis., vol. 12, pp. 832-40, 2006.

138. ESWARI PANDARANAYAKA, P.J., *et al.*, "Over expression and purification of recombinant human myocilin," World J. Microbiol. Biotechnol., vol. 24, pp. 903-907, 2008.

139. DI GUAN, C., *et al.*, "Vectors that facilitate the expression and purification of foreign peptides in escherichia coli by fusion to maltose-binding protein," Gene, vol. 67, pp. 21-30, 1988.

140. MONNÉ, M., *et al.*, "Crystal structure of the zp-n domain of zp3 reveals the core fold of animal egg coats," Nature, vol. 456, pp. 653-657, 2008.

141. YAM, G., GAPLOVSKA-KYSELA, K., and ZUBER, C., "Aggregated myocilin induces russell bodies and causes apoptosis: Implications for the …," American Journal Of Pathology, 2007.

142. TROVATO, A., SENO, F., and TOSATTO, S.C., "The pasta server for protein aggregation prediction," Protein Eng. Des. Sel., vol. 20, pp. 521-3, 2007.

143. KENNAN, A.M., *et al.*, "A novel asp380ala mutation in the glc1a/myocilin gene in a family with juvenile onset primary open angle glaucoma," J Med Genet, vol. 35, pp. 957-60, 1998.

144. STOILOVA, D., *et al.*, "Novel tigr/myoc mutations in families with juvenile onset primary open angle glaucoma," J Med Genet, vol. 35, pp. 989-92, 1998.

145. RICHARDS, J.E., *et al.*, "Novel trabecular meshwork inducible glucocorticoid response mutation in an eight-generation juvenile-onset primary open-angle glaucoma pedigree," Ophthalmology, vol. 105, pp. 1698-707, 1998.
146. MORISSETTE, J., *et al.*, "A common gene for juvenile and adult-onset primary open-angle glaucomas confined on chromosome 1q," Am J Hum Genet, vol. 56, pp. 1431-42, 1995.

147. ZHOU, Z. and VOLLRATH, D., "A cellular assay distinguishes normal and mutant tigr/myocilin protein," Hum. Mol. Genet., vol. 8, pp. 2221-8, 1999.

148. NIESEN, F.H., BERGLUND, H., and VEDADI, M., "The use of differential scanning fluorimetry to detect ligand interactions that promote protein stability," Nat. Protoc., vol. 2, pp. 2212-21, 2007.

149. VEDADI, M., *et al.*, "Chemical screening methods to identify ligands that promote protein stability, protein crystallization, and structure determination," Proc. Natl. Acad. Sci. U S A, vol. 103, pp. 15835-40, 2006.

150. GIULIANI, S.E., FRANK, A.M., and COLLART, F.R., "Functional assignment of solute-binding proteins of abc transporters using a fluorescence-based thermal shift assay," Biochemistry, vol. 47, pp. 13974-84, 2008.

151. MUNSON, M., *et al.*, "What makes a protein a protein? Hydrophobic core designs that specify stability and structural properties," Protein Sci., vol. 5, pp. 1584-93, 1996.

152. LAVINDER, J.J., *et al.*, "High-throughput thermal scanning: A general, rapid dye-binding thermal shift screen for protein engineering," J Am Chem Soc, vol. 131, pp. 3794-5, 2009.

153. NOVOKHATNY, V. and INGHAM, K., "Thermodynamics of maltose binding protein unfolding," Protein Sci, vol. 6, pp. 141-6, 1997.

154. GANESH, C., *et al.*, "Thermodynamic characterization of the reversible, two-state unfolding of maltose binding protein, a large two-domain protein," Biochemistry, vol. 36, pp. 5020-8, 1997.

155. ROSENBLUTH, R.F. and FATT, I., "Temperature measurements in the eye," Exp Eye Res, vol. 25, pp. 325-41, 1977.

156. SAWKAR, A.R., D'HAEZE, W., and KELLY, J.W., "Therapeutic strategies to ameliorate lysosomal storage disorders – a focus on gaucher disease," Cell. Mol. Life Sci., vol. 63, pp. 1179-1192, 2006.

157. LIEBERMAN, R.L., *et al.*, "Effects of ph and iminosugar pharmacological chaperones on lysosomal glycosidase structure and stability," Biochemistry, vol. 48, pp. 4816-4827, 2009.
158. SAWKAR, A.R., *et al.*, "Chemical chaperones and permissive temperatures alter localization of gaucher disease associated glucocerebrosidase variants," ACS Chem. Biol., vol. 1, pp. 235-51, 2006.

159. LOO, T.W., BARTLETT, M.C., and CLARKE, D.M., "Correctors promote folding of the cftr in the endoplasmic reticulum," Biochem. J., vol. 413, pp. 29-36, 2008.

160. POWERS, E.T., *et al.*, "Biological and chemical approaches to diseases of proteostasis deficiency," Annu Rev Biochem, vol. 78, pp. 959-91, 2009.

161. JOHNSON, S.M., *et al.*, "Native state kinetic stabilization as a strategy to ameliorate protein misfolding diseases: A focus on the transthyretin amyloidoses," Acc. Chem. Res., vol. 38, pp. 911-21, 2005.

162. BALCH, W.E., *et al.*, "Adapting proteostasis for disease intervention," Science, vol. 319, pp. 916-919, 2008.

163. BOLEN, D.W. and ROSE, G.D., "Structure and energetics of the hydrogen-bonded backbone in protein folding," Annu. Rev. Biochem., vol. 77, pp. 339-62, 2008.

164. BOLEN, D.W. and BASKAKOV, I.V., "The osmophobic effect: Natural selection of a thermodynamic force in protein folding1," Journal of Molecular Biology, vol. 310, pp. 955-963, 2001.

165. ARAKAWA, T. and TIMASHEFF, S.N., "The stabilization of proteins by osmolytes," Biophysical J., vol. 47, pp. 411-414, 2005.

166. ARAKAWA, T., *et al.*, "Small molecule pharmacological chaperones: From thermodynamic stabilization to pharmaceutical drugs," Biochem. Biophys. Acta., vol. 1746, pp. 1677-1687, 2006.

167. WU, P. and BOLEN, D.W., "Osmolyte-induced protein folding free energy changes," Proteins, vol. 63, pp. 290-296, 2006.

168. WANG, A. and BOLEN, D.W., "A naturally occurring protective system in urea-rich cells: Mechanism of osmolyte protection of proteins against urea denaturation," Biochemistry, vol. 36, pp. 9101-8, 1997.

169. RUBENSTEIN, R.C., EGAN, M.E., and ZEITLIN, P.L., "In vitro pharmacologic restoration of cftr-mediated chloride transport with sodium 4-phenylbutyrate in

cystic fibrosis epithelial cells containing delta f508-cftr," J. Clin. Invest., vol. 100, pp. 2457-65, 1997.

170. WANG, A., ROBERTSON, A.D., and BOLEN, D.W., "Effects of a naturally occurring compatible osmolyte on the internal dynamics of ribonuclease a," Biochemistry, vol. 34, pp. 15096-104, 1995.

171. LIU, Y. and BOLEN, D.W., "The peptide backbone plays a dominant role in protein stabilization by naturally occurring osmolytes," Biochemistry, vol. 34, pp. 12884-91, 1995.

172. STREET, T.O., *et al.*, "Osmolyte-induced conformational changes in the hsp90 molecular chaperone," Protein Sci., 2009.

173. YAM, G.H.-F., *et al.*, "Sodium 4-phenylbutyrate acts as a chemical chaperone on misfolded myocilin to rescue cells from endoplasmic reticulum stress and apoptosis," Invest. Ophthalmol. Vis. Sci., vol. 48, pp. 1683-90, 2007.

174. JIA, L.-Y., *et al.*, "Correction of the disease phenotype of myocilin-causing glaucoma by a natural osmolyte," Invest. Ophthalmol. Vis. Sci., vol. 50, pp. 3743-9, 2009.

175. UEDA, J., WENTZ-HUNTER, K., and YUE, B.Y., "Distribution of myocilin and extracellular matrix components in the juxtacanalicular tissue of human eyes," Invest. Ophthalmol. Vis. Sci., vol. 43, pp. 1068-76, 2002.

176. TAWARA, A., *et al.*, "Immunohistochemical localization of myoc/tigr protein in the trabecular tissue of normal and glaucomatous eyes," Curr. Eye Res., vol. 21, pp. 934-43, 2000.

177. YAM, G.H.-F., ZUBER, C., and ROTH, J., "A synthetic chaperone corrects the trafficking defect and disease phenotype in a protein misfolding disorder," FASEB J., vol. 19, pp. 12-8, 2005.

178. BURNS, J.N., *et al.*, "Rescue of glaucoma-causing mutant myocilin thermal stability by chemical chaperones," ACS Chem. Biol., vol. 5, pp. 477-87, 2010.

179. GONG, G., *et al.*, "Genetic dissection of myocilin glaucoma," Hum. Mol. Genet., vol. 13 Spec No 1, pp. R91-102, 2004.

180. PEI, J. and GRISHIN, N.V., "Promals: Towards accurate multiple sequence alignments of distantly related proteins," Bioinformatics, vol. 23, pp. 802-8, 2007.

181. FAUTSCH, M.P., VRABEL, A.M., and JOHNSON, D.H., "The identification of myocilin-associated proteins in the human trabecular meshwork," Exp. Eye Res., vol. 82, pp. 1046-52, 2006.

182. PETERS, D.M., *et al.*, "Myocilin binding to hep ii domain of fibronectin inhibits cell spreading and incorporation of paxillin into focal adhesions," Exp. Cell Res., vol. 303, pp. 218-28, 2005.

183. MERTTS, M., *et al.*, "Identification of the region in the n-terminal domain responsible for the cytoplasmic localization of myoc/tigr and its association with microtubules," Lab. Invest., vol. 79, pp. 1237-45, 1999.

184. SANCHEZ-SANCHEZ, F., *et al.*, "Characterization of the intracellular proteolytic cleavage of myocilin and identification of calpain ii as a myocilin-processing protease," J. Biol. Chem., vol. 282, pp. 27810-24, 2007.

185. TAMM, E.R., "Myocilin and glaucoma: Facts and ideas," Prog. Retin. Eye Res., vol. 21, pp. 395-428, 2002.

186. LITON, P.B., GONZALEZ, P., and EPSTEIN, D.L., "The role of proteolytic cellular systems in trabecular meshwork homeostasis," Exp. Eye Res., vol. 88, pp. 724-8, 2009.

187. ACOTT, T.S. and KELLEY, M.J., "Extracellular matrix in the trabecular meshwork," Exp. Eye Res., vol. 86, pp. 543-61, 2008.

188. KNEPPER, P.A., *et al.*, "Reconstitution of trabecular meshwork gags: Influence of hyaluronic acid and chondroitin sulfate on flow rates," J. Glaucoma, vol. 14, pp. 230-8, 2005.

189. GASTEIGER, E., *et al.*, *Protein identification and analysis tools on the expasy server*, in *The proteomics protocol handbook*, WALKER, J.M., Editor. 2005, Humana Press: Totowa, NJ. p. 571-607.

190. GREENFIELD, N.J., "Analysis of circular dichroism data," Methods Enzymol., vol. 383, pp. 282-317, 2004.

191. ROBERTSON, A.D. and MURPHY, K.P., "Protein structure and the energetics of protein stability," Chem. Rev., vol. 97, pp. 1251-1268, 1997.

192. PACE, C.N., *et al.*, "Urea denatured state ensembles contain extensive secondary structure that is increased in hydrophobic proteins," Protein Sci., vol. 19, pp. 929-943, 2010.

193. XU, D. and NUSSINOV, R., "Favorable domain size in proteins," Fold. Des., vol. 3, pp. 11-7, 1998.

194. WU, J., YANG, J.T., and WU, C.S., "Beta-ii conformation of all-beta proteins can be distinguished from unordered form by circular dichroism," Anal. Biochem., vol. 200, pp. 359-64, 1992.

195. SODING, J., BIEGERT, A., and LUPAS, A.N., "The hhpred interactive server for protein homology detection and structure prediction," Nucleic Acids Research, vol. 33, pp. W244-W248, 2005.

196. TERWILLIGER, T.C. and BERENDZEN, J., "Automated mad and mir structure solution," Acta Crystallographica Section D-Biological Crystallography, vol. 55, pp. 849-861, 1999.

197. P. EMSLEY, K.C., Acta Crystallogr D vol. D60, pp. 2126-2132, 2004.

198. 4, C.C.P.N., Acta Crystallogr D Biol Crystallogr, vol. D50, pp. 760, 1994.

199. KNEPPER, P.A., *et al.*, "Glycosaminoglycans of the human trabecular meshwork in primary open-angle glaucoma," Invest. Ophthalmol. Vis. Sci., vol. 37, pp. 1360-7, 1996.

200. KULESHOVA, O.N., ZAIDMAN, A.M., and KOREL, A.V., "Glycosaminoglycans of the trabecular meshwork of the eye in primary juvenile glaucoma," Bull. Exp. Biol. Med., vol. 143, pp. 381-4, 2007.

201. GOULD, C.M., *et al.*, "Elm: The status of the 2010 eukaryotic linear motif resource," Nucleic Acids Res., vol. 38, pp. D167-80, 2010.

202. KNEPPER, P.A., *et al.*, "Hypophosphorylation of aqueous humor scd44 and primary open-angle glaucoma," Invest. Ophthalmol. Vis. Sci., vol. 46, pp. 2829-37, 2005.

203. FURUTANI, Y., *et al.*, "Identification and characterization of photomedins: Novel olfactomedin-domain-containing proteins with chondroitin sulphate-e-binding activity," Biochem. J., vol. 389, pp. 675-84, 2005.

204. HILLIER, B.J. and VACQUIER, V.D., "Structural features and functional domains of amassin-1, a cell-binding olfactomedin protein," Biochem. Cell Biol., vol. 85, pp. 552-562, 2007.

205. RAJINI, B., *et al.*, "Stability, homodimerization, and calcium-binding properties of a single, variant betagamma-crystallin domain of the protein absent in melanoma 1 (aim1)," Biochemistry, vol. 42, pp. 4552-9, 2003.

206. STONE, E.M., *et al.*, "Identification of a gene that causes primary open angle glaucoma," Science, vol. 275, pp. 668-70, 1997.

207. JOHNSON, P.M., *et al.*, "A comparison of the circular dichroism spectra of the subclasses of human immunoglobulin g," Immunology, vol. 27, pp. 27-31, 1974.

208. BRAHMS, S. and BRAHMS, J., "Determination of protein secondary structure in solution by vacuum ultraviolet circular dichroism," J. Mol. Biol., vol. 138, pp. 149-78, 1980.

209. FUCHS, P.F. and ALIX, A.J., "High accuracy prediction of beta-turns and their types using propensities and multiple alignments," Proteins, vol. 59, pp. 828-39, 2005.

210. MORRISETT, J.D. and BROOMFIELD, C.A., "Active site spin-labeled alpha-chymotrypsin. Guanidine hydrochloride denaturation studies using electron paramagnetic resonance and circular dichroism," J. Am. Chem. Soc., vol. 93, pp. 7297-304, 1971.

211. LINDING, R., *et al.*, "Globplot: Exploring protein sequences for globularity and disorder," Nucleic Acids Res., vol. 31, pp. 3701-8, 2003.

212. BLOEMENDAL, H., *et al.*, "Ageing and vision: Structure, stability and function of lens crystallins," Prog. Biophys. Mol. Biol., vol. 86, pp. 407-85, 2004.

213. EVANS, P., *et al.*, "A reference dataset for circular dichroism spectroscopy tailored for the betagamma-crystallin lens proteins," Exp. Eye Res., vol. 84, pp. 1001-8, 2007.

214. MANDAL, K., *et al.*, "Structure and stability of gamma-crystallins. Denaturation and proteolysis behavior," J. Biol. Chem., vol. 262, pp. 8096-102, 1987.

215. CHAUDHURI, T.K. and PAUL, S., "Protein-misfolding diseases and chaperone-based therapeutic approaches," FEBS J., vol. 273, pp. 1331-49, 2006.

216. SAMBROOK, J. and RUSSELL, D.W., *Molecular cloning : A laboratory manual*. 3rd ed. 2001, Cold Spring Harbor, N.Y.: Cold Spring Harbor Laboratory Press. 3 v.

217. SHEVCHENKO, A., *et al.*, "Mass spectrometric sequencing of proteins from silver stained polyacrylamide gels," Analytical Chemistry, vol. 68, pp. 850-858, 1996.

218. OTWINOWSKI, Z. and MINOR, W., "Processing of x-ray diffraction data collected in oscillation mode," Methods Enzymol., vol. 276, pp. 307-326, 1997.

219. HUGHES, J.P., *et al.*, "Principles of early drug discovery," British Journal of Pharmacology, vol. 162, pp. 1239-1249, 2011.

220. GIACOMOTTO, J. and SEGALAT, L., "High-throughput screening and small animal models, where are we?," British Journal of Pharmacology, vol. 160, pp. 204-216, 2010.

221. KLEBE, G., "Virtual ligand screening: Strategies, perspectives and limitations," Drug Discovery Today, vol. 11, pp. 580-594, 2006.

222. 02/17/2011 07/18/2011]; Available from: http://www.fda.gov/Drugs/DevelopmentApprovalProcess/HowDrugsareDevelopedandApproved/DrugandBiologicApprovalReports/ucm242674.htm.

223. OVERINGTON, J.P., AL-LAZIKANI, B., and HOPKINS, A.L., "Opinion - how many drug targets are there?," Nature Reviews Drug Discovery, vol. 5, pp. 993-996, 2006.

224. LANDRY, Y. and GIES, J.P., "Drugs and their molecular targets: An updated overview," Fundamental & Clinical Pharmacology, vol. 22, pp. 1-18, 2008.

225. WOOD, A.J.J., "A proposal for radical changes in the drug-approval process," New England Journal of Medicine, vol. 355, pp. 618-623, 2006.

226. MACARRON, R. and HERTZBERG, R.P., "Design and implementation of high throughput screening assays," Molecular Biotechnology, vol. 47, pp. 270-285, 2011.

227. WAWER, M. and BAJORATH, J., "Extraction of structure-activity relationship information from high-throughput screening data," Current Medicinal Chemistry, vol. 16, pp. 4049-4057, 2009.

228. CHAKRABORTY, C., *et al.*, "Recent advances of fluorescent technologies for drug discovery and development," Current Pharmaceutical Design, vol. 15, pp. 3552-3570, 2009.

229. GREEN, D.V.S., "Virtual screening of chemical libraries for drug discovery," Expert Opinion on Drug Discovery, vol. 3, pp. 1011-1026, 2008.

230. KITCHEN, D.B., *et al.*, "Docking and scoring in virtual screening for drug discovery: Methods and applications," Nature Reviews Drug Discovery, vol. 3, pp. 935-949, 2004.

231. BILLINGSLEY, M.L., "Druggable targets and targeted drugs: Enhancing the development of new therapeutics," Pharmacology, vol. 82, pp. 239-244, 2008.

232. MICHELINI, E., *et al.*, "Cell-based assays: Fuelling drug discovery," Analytical and Bioanalytical Chemistry, vol. 398, pp. 227-238, 2010.

233. HILL, S.J., BAKER, J.G., and REES, S., "Reporter-gene systems for the study of g-protein-coupled receptors," Current Opinion in Pharmacology, vol. 1, pp. 526-532, 2001.

234. EGGELING, C., *et al.*, "Highly sensitive fluorescence detection technology currently available for hts," Drug Discovery Today, vol. 8, pp. 632-641, 2003.

235. PATEL, R., *et al.*, "Atlas - a high-throughput affinity-based screening technology for soluble proteins: Technology application using p38 map kinase," Assay and Drug Development Technologies, vol. 6, pp. 55-68, 2008.

236. FREIRE, E., *Thermal denaturation methods in the study of protein folding*, in *Energetics of biological macromolecules*. 1995, Academic Press Inc: San Diego. p. 144-168.

237. BULAJ, G. and OTLEWSKI, J., "Ligand-induced changes in the conformational stability of bovine trypsinogen and their implications for the protein function," Journal of Molecular Biology, vol. 247, pp. 701-716, 1995.

238. NIESEN, F.H., BERGLUND, H., and VEDADI, M., "The use of differential scanning fluorimetry to detect ligand interactions that promote protein stability," Nature Protocols, vol. 2, pp. 2212-2221, 2007.

239. HALL, J.A., GEHRING, K., and NIKAIDO, H., "Two modes of ligand binding in maltose-binding protein of escherichia coli - correlation with the structure of ligands and the structure of binding protein," Journal of Biological Chemistry, vol. 272, pp. 17605-17609, 1997.

240. HALL, J.A., *et al.*, "Two modes of ligand binding in maltose-binding protein of escherichia coli - functional significance in active transport," Journal of Biological Chemistry, vol. 272, pp. 17615-17622, 1997.

241. ZHANG, J.H., CHUNG, T.D.Y., and OLDENBURG, K.R., "A simple statistical parameter for use in evaluation and validation of high throughput screening assays," Journal of Biomolecular Screening, vol. 4, pp. 67-73, 1999.

242. ACHYUTHAN, K.E. and WHITTEN, D.G., "Design considerations for high throughput screening and in vitro diagnostic assays," Combinatorial Chemistry & High Throughput Screening, vol. 10, pp. 399-412, 2007.

243. BURNS, J.N., *et al.*, "Rescue of glaucoma-causing mutant myocilin thermal stability by chemical chaperones," Acs Chemical Biology, vol. 5, pp. 477-487, 2010.

244. ORWIG SD, L.R., "Biophysical characterization of the olfactomedin domain of myocilin, an extracellular matrix protein implicated in inherited forms of glaucoma," PLoS ONE, vol. 6, pp. e16347, 2011.

245. BURNS, J.N., *et al.*, "The stability of myocilin olfactomedin domain variants provides new insight into glaucoma as a protein misfolding disorder," Biochemistry, vol. 50, pp. 5824-5833, 2011.

246. SIPE, J.D., "Amyloidosis," Annual Review of Biochemistry, vol. 61, pp. 947-975, 1992.

247. SOLOMON, J.P., *et al.*, "Heparin binds 8 kda gelsolin cross-beta-sheet oligomers and accelerates amyloidogenesis by hastening fibril extension," Biochemistry, vol. 50, pp. 2486-2498, 2011.

248. SNOW, A.D., WILLMER, J., and KISILEVSKY, R., "Sulfated glycosaminoglycans - a common constituent of all amyloids," Laboratory Investigation, vol. 56, pp. 120-123, 1987.

249. DOBSON, C.M., "Protein folding and misfolding," Nature, vol. 426, pp. 884-890, 2003.

250. ALEXANDRESCU, A.T., "Amyloid accomplices and enforcers," Protein Science, vol. 14, pp. 1-12, 2005.

251. GLABE, C., "Intracellular mechanisms of amyloid accumulation and pathogenesis in alzheimer's disease," Journal of Molecular Neuroscience, vol. 17, pp. 137-145, 2001.

252. WALSH, D.M. and SELKOE, D.J., "Deciphering the molecular basis of memory failure in alzheimer's disease," Neuron, vol. 44, pp. 181-193, 2004.

253. QUIST, A., *et al.*, "Amyloid ion channels: A common structural link for protein-misfolding disease," Proceedings of the National Academy of Sciences of the United States of America, vol. 102, pp. 10427-10432, 2005.

254. SOTO, C., "Protein misfolding and disease; protein refolding and therapy," Febs Letters, vol. 498, pp. 204-207, 2001.

255. EANES, E.D. and GLENNER, G.G., "X-ray diffraction studies on amyloid filaments," Journal of Histochemistry & Cytochemistry, vol. 16, pp. 673-&, 1968.

256. SUNDE, M., *et al.*, "Common core structure of amyloid fibrils by synchrotron x-ray diffraction," Journal of Molecular Biology, vol. 273, pp. 729-739, 1997.

257. PUCHTLER, H., SWEAT, F., and LEVINE, M., "On binding of congo red by amyloid," Journal of Histochemistry & Cytochemistry, vol. 10, pp. 355-&, 1962.

258. BALGUERIE, A., *et al.*, "Domain organization and structure-function relationship of the het-s prion protein of podospora anserina," Embo Journal, vol. 22, pp. 2071-2081, 2003.

259. LEVINE, H., "Thioflavine-t interaction with synthetic alzheimers-disease beta-amyloid peptides - detection of amyloid aggregation in solution," Protein Science, vol. 2, pp. 404-410, 1993.

260. NAIKI, H., *et al.*, "Fluorometric-determination of amyloid fibrils invitro using the fluorescent dye, thioflavine-t," Analytical Biochemistry, vol. 177, pp. 244-249, 1989.

261. NAIKI, H. and NAGAI, Y., "Molecular pathogenesis of protein misfolding diseases: Pathological molecular environments versus quality control systems against misfolded proteins," Journal of Biochemistry, vol. 146, pp. 751-756, 2009.

262. CHITI, F. and DOBSON, C.M., "Protein misfolding, functional amyloid, and human disease," Annual Review of Biochemistry, vol. 75, pp. 333-366, 2006.

263. DOBSON, C.M., "Protein-misfolding diseases: Getting out of shape," Nature, vol. 418, pp. 729-730, 2002.

264. DOBSON, C.M., "Protein misfolding, evolution and disease," Trends in Biochemical Sciences, vol. 24, pp. 329-332, 1999.

265. WILSON, M.R., YERBURY, J.J., and POON, S., "Potential roles of abundant extracellular chaperones in the control of amyloid formation and toxicity," Molecular Biosystems, vol. 4, pp. 42-52, 2008.

266. ZHOU, Y., GRINCHUK, O., and TOMAREV, S.I., "Transgenic mice expressing the tyr437his mutant of human myocilin protein develop glaucoma," Investigative Ophthalmology & Visual Science, vol. 49, pp. 1932-1939, 2008.

267. SENATOROV, V., *et al.*, "Expression of mutated mouse myocilin induces open-angle glaucoma in transgenic mice," Journal of Neuroscience, vol. 26, pp. 11903-11914, 2006.

268. AROCA-AGUILAR, J.D., *et al.*, "Heterozygous expression of myocilin glaucoma mutants increases secretion of the mutant forms and reduces extracellular processed myocilin," Molecular Vision, vol. 14, pp. 2097-2108, 2008.

269. JOE, M.K. and TOMAREV, S.I., "Expression of myocilin mutants sensitizes cells to oxidative stress-induced apoptosis implication for glaucoma pathogenesis," American Journal of Pathology, vol. 176, pp. 2880-2890, 2010.

270. TROVATO, A., SENO, F., and TOSATTO, S.C.E., "The pasta server for protein aggregation prediction," Protein Engineering Design & Selection, vol. 20, pp. 521-523, 2007.

271. LEVINE, H., *Quantification of beta-sheet amyloid fibril structures with thioflavin t*, in *Amyloid, prions, and other protein aggregates*. 1999, Academic Press Inc: San Diego. p. 274-284.

272. DE GROOT, N.S., SABATE, R., and VENTURA, S., "Amyloids in bacterial inclusion bodies," Trends in Biochemical Sciences, vol. 34, pp. 408-416, 2009.

273. CAUGHEY, B.W., *et al.*, "Secondary structure-analysis of the scrapie-associated protein prp 27-30 in water by infrared-spectroscopy," Biochemistry, vol. 30, pp. 7672-7680, 1991.

274. NAIKI, H., *et al.*, "Kinetic-analysis of amyloid fibril polymerization invitro," Laboratory Investigation, vol. 65, pp. 104-110, 1991.

275. NAIKI, H. and NAKAKUKI, K., "First-order kinetic model of alzheimer's beta-amyloid fibril extension in vitro," Laboratory Investigation, vol. 74, pp. 374-383, 1996.

276. RELINI, A., *et al.*, "Heparin strongly enhances the formation of beta(2)-microglobulin amyloid fibrils in the presence of type i collagen," Journal of Biological Chemistry, vol. 283, pp. 4912-4920, 2008.

277. MCLAURIN, J., *et al.*, "Interactions of alzheimer amyloid-beta peptides with glycosaminoglycans - effects on fibril nucleation and growth," European Journal of Biochemistry, vol. 266, pp. 1101-1110, 1999.

278. NECULA, M., CHIRITA, C.N., and KURET, J., "Rapid anionic micelle-mediated alpha-synuclein fibrillization in vitro," Journal of Biological Chemistry, vol. 278, pp. 46674-46680, 2003.

279. YAMAMOTO, S., *et al.*, "Low concentrations of sodium dodecyl sulfate induce the extension of beta(2)-microglobulin-related amyloid fibrils at a neutral ph," Biochemistry, vol. 43, pp. 11075-11082, 2004.

280. GIEHM, L., *et al.*, "Sds-induced fibrillation of alpha-synuclein: An alternative fibrillation pathway," Journal of Molecular Biology, vol. 401, pp. 115-133, 2010.

281. SACCA, S.C. and IZZOTTI, A., *Oxidative stress and glaucoma: Injury in the anterior segment of the eye*, in *Glaucoma: An open window to neurodegeneration and neuroprotection*. 2008, Elsevier Science Bv: Amsterdam. p. 385-407.

282. IZZOTTI, A., BAGNIS, A., and SACCA, S.C., "The role of oxidative stress in glaucoma," Mutation Research-Reviews in Mutation Research, vol. 612, pp. 105-114, 2006.

283. GHANEM, A.A., ARAFA, L.F., and EL-BAZ, A., "Oxidative stress markers in patients with primary open-angle glaucoma," Current Eye Research, vol. 35, pp. 295-301, 2010.

284. SHARMA, K.K. and SANTHOSHKUMAR, P., "Lens aging: Effects of crystallins," Biochimica Et Biophysica Acta-General Subjects, vol. 1790, pp. 1095-1108, 2009.

285. LIU, C., SAWAYA, M.R., and EISENBERG, D., "Beta(2)-microglobulin forms three-dimensional domain-swapped amyloid fibrils with disulfide linkages," Nature Structural & Molecular Biology, vol. 18, pp. 49-+, 2011.

286. WETZEL, R., "Kinetics and thermodynamics of amyloid fibril assembly," Accounts of Chemical Research, vol. 39, pp. 671-679, 2006.

287. GOLDSCHMIDT, L., *et al.*, "Identifying the amylome, proteins capable of forming amyloid-like fibrils," Proceedings of the National Academy of Sciences of the United States of America, vol. 107, pp. 3487-3492, 2010.

288. KUSHNIROV, V.V., *et al.*, "Purification and analysis of prion and amyloid aggregates," Methods, vol. 39, pp. 50-55, 2006.

289. SEKIJIMA, Y., *et al.*, "The biological and chemical basis for tissue-selective amyloid disease," Cell, vol. 121, pp. 73-85, 2005.

290. NAIKI, H., *et al.*, "Molecular interactions in the formation and deposition of beta(2)-microglobuhn-related amyloid fibrils," Amyloid-Journal of Protein Folding Disorders, vol. 12, pp. 15-25, 2005.

291. MUCHOWSKI, P.J. and WACKER, J.L., "Modulation of neurodegeneration by molecular chaperones," Nature Reviews Neuroscience, vol. 6, pp. 11-22, 2005.

292. LI, X., LI, H., and LI, X.J., "Intracellular degradation of misfolded proteins in polyglutamine neurodegenerative diseases," Brain Research Reviews, vol. 59, pp. 245-252, 2008.

293. VETRIVEL, K.S.T., GOPAL *Neurobiology of alzheimer's disease: Molecular and cellular neurobiology*, in *Presenilins* DAWBARN, D.A., SHELLEY J Editor. 2007, Oxford University Press.

294. HIDDINGA, H.J. and EBERHARDT, N.L., "Intracellular amyloidogenesis by human islet amyloid polypeptide induces apoptosis in cos-1 cells," American Journal of Pathology, vol. 154, pp. 1077-1088, 1999.

295. WESTERMARK, P., ANDERSSON, A., and WESTERMARK, G.T., "Islet amyloid polypeptide, islet amyloid, and diabetes mellitus," Physiological Reviews, vol. 91, pp. 795-826, 2011.

296. AHMAD, E., *et al.*, "A mechanistic approach for islet amyloid polypeptide aggregation to develop anti-amyloidogenic agents for type-2 diabetes," Biochimie, vol. 93, pp. 793-805, 2011.

297. CHOW, M.K.M., LOMAS, D.A., and BOTTOMLEY, S.P., "Promiscuous beta-strand interactions and the conformational diseases," Current Medicinal Chemistry, vol. 11, pp. 491-499, 2004.

298. GUO, L., *et al.*, "Targeting amyloid-beta in glaucoma treatment," Proceedings of the National Academy of Sciences of the United States of America, vol. 104, pp. 13444-13449, 2007.

299. MORALES, R., *et al.*, "Molecular cross talk between misfolded proteins in animal models of alzheimer's and prion diseases," Journal of Neuroscience, vol. 30, pp. 4528-4535, 2010.

300. PAGE, L.J., *et al.*, "Secretion of amyloidogenic gelsolin progressively compromises protein homeostasis leading to the intracellular aggregation of proteins," Proceedings of the National Academy of Sciences of the United States of America, vol. 106, pp. 11125-11130, 2009.

301. KIM, J.S. and RAINES, R.T., "Ribonuclease s-peptide as a carrier in fusion proteins," Protein Science, vol. 2, pp. 348-356, 1993.

302. WESTERMARK, G.T., JOHNSON, K.H., and WESTERMARK, P., "Staining methods for identification of amyloid in tissue," Amyloid, Prions, and Other Protein Aggregates, vol. 309, pp. 3-25, 1999.

303. BEUTLER, E. and GELBART, T., "Glucocerebrosidase (gaucher disease)," Hum. Mutat., vol. 8, pp. 207-13, 1996.

304. SCHMITZ, M., *et al.*, "Impaired trafficking of mutants of lysosomal glucocerebrosidase in gaucher's disease," Int. J. Biochem. Cell Biol., vol. 37, pp. 2310-20, 2005.

305. ZIMMER, K.P., *et al.*, "Intracellular transport of acid beta-glucosidase and lysosome-associated membrane proteins is affected in gaucher's disease (g202r mutation)," J. Pathol., vol. 188, pp. 407-14, 1999.

306. RON, I. and HOROWITZ, M., "Er retention and degradation as the molecular basis underlying gaucher disease heterogeneity," Hum. Mol. Genet., vol. 14, pp. 2387-98, 2005.

307. BENDIKOV-BAR, I., *et al.*, "Characterization of the erad process of the l444p mutant glucocerebrosidase variant," Blood Cells Mol. Dis., vol. 46, pp. 4-10, 2011.

308. YU, Z., SAWKAR, A.R., and KELLY, J.W., "Pharmacologic chaperoning as a strategy to treat gaucher disease," FEBS J., vol. 274, pp. 4944-50, 2007.

309. COX, T.M., "Gaucher disease: Clinical profile and therapeutic developments," Biologics, vol. 4, pp. 299-313, 2010.

310. MICHELAKAKIS, H., *et al.*, "Early-onset severe neurological involvement and d409h homozygosity in gaucher disease: Outcome of enzyme replacement therapy," Blood Cells Mol. Dis., vol. 28, pp. 1-4, 2002.

311. WRAITH, J.E., "Limitations of enzyme replacement therapy: Current and future," J. Inherit. Metab. Dis., vol. 29, pp. 442-7, 2006.

312. LEE, L., ABE, A., and SHAYMAN, J.A., "Improved inhibitors of glucosylceramide synthase," J. Biol. Chem., vol. 274, pp. 14662-9, 1999.

313. LUKINA, E., *et al.*, "A phase 2 study of eliglustat tartrate (genz-112638), an oral substrate reduction therapy for gaucher disease type 1," Blood, vol. 116, pp. 893-9, 2010.

314. LUKINA, E., *et al.*, "Improvement in hematological, visceral, and skeletal manifestations of gaucher disease type 1 with oral eliglustat tartrate (genz-112638) treatment: 2-year results of a phase 2 study," Blood, vol. 116, pp. 4095-8, 2010.

315. RECZEK, D., *et al.*, "Limp-2 is a receptor for lysosomal mannose-6-phosphate-independent targeting of beta-glucocerebrosidase," Cell, vol. 131, pp. 770-83, 2007.

316. LIOU, B., *et al.*, "Analyses of variant acid beta -glucosidases: Effects of gaucher disease mutations," J. Biol. Chem., vol. 281, pp. 4242-4253, 2006.

317. GRACE, M.E., *et al.*, "Analysis of human acid beta-glucosidase by site-directed mutagenesis and heterologous expression," J. Biol. Chem., vol. 269, pp. 2283-91, 1994.

318. DESNICK, R.J. and FAN, J.Q., *Pharmacologic chaperone therapy for lysosomal diseases*, in *Gaucher disease*, FUTERMAN, A.H. and ZIMRAN, A., Editors. 2006, CRC Press: Boca Raton. p. 377-397.

319. BUTTERS, T.D., "Gaucher disease," Curr. Opin. Chem. Biol., vol. 11, pp. 412-8, 2007.

320. BUTTERS, T.D., *et al.*, "Molecular requirements of imino sugars for the selective control of n-linked glycosylation and glycosphingolipid biosynthesis," Tetrahedron: Asymmetry, vol. 11, pp. 113-124, 2000.

321. MELLOR, H.R., *et al.*, "Cellular effects of deoxynojirimycin analogues: Inhibition of n-linked oligosaccharide processing and generation of free glucosylated oligosaccharides," Biochem. J., vol. 381, pp. 867-75, 2004.

322. LANDON, M.R., *et al.*, "Detection of ligand binding hot spots on protein surfaces via fragment-based methods: Application to dj-1 and glucocerebrosidase," J. Comput. Aided Mol. Des., vol. 23, pp. 491-500, 2009.

323. ZHENG, W., *et al.*, "Three classes of glucocerebrosidase inhibitors identified by quantitative high-throughput screening are chaperone leads for gaucher disease," Proc. Natl. Acad. Sci. U S A, vol. 104, pp. 13192-7, 2007.

324. ALFONSO, P., *et al.*, "Miglustat (nb-dnj) works as a chaperone for mutated acid beta-glucosidase in cells transfected with several gaucher disease mutations," Blood Cells Mol. Dis., vol. 35, pp. 268-76, 2005.

325. SAWKAR, A.R., *et al.*, "Chemical chaperones increase the cellular activity of n370s beta -glucosidase: A therapeutic strategy for gaucher disease," Proc. Natl. Acad. Sci. U.S.A., vol. 99, pp. 15428-33, 2002.

326. BRUMSHTEIN, B., *et al.*, "Crystal structures of complexes of n-butyl- and n-nonyl-deoxynojirimycin bound to acid beta-glucosidase: Insights into the mechanism of chemical chaperone action in gaucher disease," J Biol Chem, vol. 282, pp. 29052-8, 2007.

327. CHANG, H.H., *et al.*, "Hydrophilic iminosugar active-site-specific chaperones increase residual glucocerebrosidase activity in fibroblasts from gaucher patients," Febs J., vol. 273, pp. 4082-92, 2006.

328. SAWKAR, A.R., D'HAEZE, W., and KELLY, J.W., "Therapeutic strategies to ameliorate lysosomal storage disorders--a focus on gaucher disease," Cell. Mol. Life Sci., vol. 63, pp. 1179-92, 2006.

329. BRUMSHTEIN, B., *et al.*, "6-amino-6-deoxy-5,6-di-n-(n'-octyliminomethylidene)nojirimycin: Synthesis, biological evaluation, and crystal

structure in complex with acid beta-glucosidase," Chembiochem, vol. 10, pp. 1480-5, 2009.

330. LUAN, Z., *et al.*, "Chaperone activity of bicyclic nojirimycin analogues for gaucher mutations in comparison with n-(n-nonyl)deoxynojirimycin," Chembiochem, vol. 10, pp. 2780-92, 2009.

331. OULAIDI, F., *et al.*, "Second-generation iminoxylitol-based pharmacological chaperones for the treatment of gaucher disease," ChemMedChem, vol. 6, pp. 353-61, 2011.

332. WANG, G.N., *et al.*, "Rational design and synthesis of highly potent pharmacological chaperones for treatment of n370s mutant gaucher disease," J. Med. Chem., vol. 52, pp. 3146-9, 2009.

333. YU, Z., *et al.*, "Isofagomine- and 2,5-anhydro-2,5-imino-d-glucitol-based glucocerebrosidase pharmacological chaperones for gaucher disease intervention," J. Med. Chem., vol. 50, pp. 94-100, 2007.

334. SANCHEZ-OLLE, G., *et al.*, "Promising results of the chaperone effect caused by imino sugars and aminocyclitol derivatives on mutant glucocerebrosidases causing gaucher disease," Blood Cells Mol. Dis., vol. 42, pp. 159-66, 2009.

335. DIAZ, L., *et al.*, "Click chemistry approach to new n-substituted aminocyclitols as potential pharmacological chaperones for gaucher disease," J. Med. Chem., vol. 53, pp. 5248-55, 2010.

336. MAEGAWA, G.H., *et al.*, "Identification and characterization of ambroxol as an enzyme enhancement agent for gaucher disease," J. Biol. Chem., vol. 284, pp. 23502-16, 2009.

337. MARUGAN, J.J., *et al.*, "Evaluation of quinazoline analogues as glucocerebrosidase inhibitors with chaperone activity," J Med. Chem., vol. 54, pp. 1033-58, 2011.

338. LIEBERMAN, R.L., *et al.*, "Structure of acid beta-glucosidase with pharmacological chaperone provides insight into gaucher disease," Nat. Chem. Biol., vol. 3, pp. 101-7, 2007.

339. KHANNA, R., *et al.*, "The pharmacological chaperone isofagomine increases the activity of the gaucher disease l444p mutant form of beta-glucosidase," FEBS J., vol. 277, pp. 1618-38, 2010.

340. STEET, R.A., *et al.*, "The iminosugar isofagomine increases the activity of n370s mutant acid beta-glucosidase in gaucher fibroblasts by several mechanisms," Proc. Natl. Acad. Sci. U.S.A., vol. 103, pp. 13813-8, 2006.

341. SAWKAR, A.R., *et al.*, "Gaucher disease-associated glucocerebrosidases show mutation-dependent chemical chaperoning profiles," Chem. Biol., vol. 12, pp. 1235-44, 2005.

342. THERAPEUTICS, A. [cited 2011 January 28]; Available from: http://www.amicustherapeutics.com/clinicaltrials.

343. SUN, Y., *et al.*, "Isofagomine in vivo effects in a neuronopathic gaucher disease mouse," PLoS ONE, vol. 6, pp. e19037, 2011.

344. PAULSEN, H. and TODT, K., "[on monosaccharides with nitrogen-yielding seven membered rings]," Chem. Ber., vol. 100, pp. 512-20, 1967.

345. PAINTER, G.F., ELDRIDGE, P.J., and FALSHAW, A., "Syntheses of tetrahydroxyazepanes from chiro-inositols and their evaluation as glycosidase inhibitors," Bioorg. Med. Chem., vol. 12, pp. 225-32, 2004.

346. QIAN, X., *et al.*, "C2-symmetrical tetrahydroxyazepanes as inhibitors of glycosidases and hiv/fiv proteases," Bioorg. Med. Chem., vol. 4, pp. 2055-69, 1996.

347. MORIS-VARAS, F., QIAN, X., and WONG, C.H., "Enzymatic/chemical synthesis and biological evaluation of seven-membered iminocyclitols," J. Am. Chem. Soc., vol. 118, pp. 7647-7652, 1996.

348. MARKAD, S.D., *et al.*, "Polyhydroxylated homoazepanes and 1-deoxy-homonojirimycin analogues: Synthesis and glycosidase inhibition study," Org. Biomol. Chem., vol. 4, pp. 3675-80, 2006.

349. LOHRAY, B.B., JAYAMMA, Y., and CHATTERJEE, M., "Unprecedented selectivity in the reaction of 1,2:5,6-dianhydro-3,4-o- isopropylidenehexitols with benzylamine: A practical synthesis of 3,4,5,6-tetrahydroxyazepanes," J. Org. Chem., vol. 60, pp. 5958-5960, 1995.

350. GLOSTER, T.M. and DAVIES, G.J., "Glycosidase inhibition: Assessing mimicry of the transition state," Org. Biomol. Chem., vol. 8, pp. 305-320, 2010.

351. AGUILAR-MONCAYO, M., *et al.*, "Glycosidase inhibition by ring-modified castanospermine analogues: Tackling enzyme selectivity by inhibitor tailoring," Org. Biomol. Chem., vol. 7, pp. 2738-47, 2009.

352. STRASBERG, P.M. and LOWDEN, J.A., "The assay of glucocerebrosidase activity using the natural substrate," Clin. Chim. Acta, vol. 118, pp. 9-20, 1982.

353. YU, L., *et al.*, "Alpha-1-c-octyl-1-deoxynojirimycin as a pharmacological chaperone for gaucher disease," Bioorg. Med. Chem., vol. 14, pp. 7736-44, 2006.

354. LIEBERMAN, R.L., *et al.*, "The effects of ph and iminosugar pharmacological chaperones on lysosomal glycosidase structure and stability," Biochemistry, vol. 48, pp. 4816-4827, 2009.

355. WEI, R.R., *et al.*, "X-ray and biochemical analysis of n370s mutant human acid beta-glucosidase," J. Biol. Chem., vol. 286, pp. 299-308, 2011.

356. MIAO, S., *et al.*, "Identification of glu340 as the active-site nucleophile in human glucocerebrosidase by use of electrospray tandem mass spectrometry," J. Biol. Chem., vol. 269, pp. 10975-8, 1994.

357. DVIR, H., *et al.*, "X-ray structure of human acid-beta-glucosidase, the defective enzyme in gaucher disease," EMBO Rep., vol. 4, pp. 704-9, 2003.

358. SINNOTT, M.L., "Catalytic mechanisms of enzymic glycosyl transfer," Chem. Rev., vol. 90, pp. 1171-1202, 1990.

359. PREMKUMAR, L., *et al.*, "X-ray structure of human acid-beta-glucosidase covalently bound to conduritol-b-epoxide. Implications for gaucher disease," J. Biol. Chem., vol. 280, pp. 23815-9, 2005.

360. BEUTLER, E. and GRABOWSKI, G.A., *Gaucher disease*, in *Metabolic and molecular bases of inherited disease*, SCRIVER, C.R., et al., Editors. 2001, McGraw Hill: New York. p. 3635-3667.

361. XIAO, X. and BAI, D., "An efficient and selective method for hydrolysis of acedonides," Synlett, vol. 4, pp. 535-537, 2001.

362. BRADFORD, M.M., "A rapid and sensitive method for the quantitation of microgram quantities of protein utilizing the principle of protein-dye binding," Anal. Biochem., vol. 72, pp. 248-54, 1976.

363. ORWIG, S.D. and LIEBERMAN, R.L., "Biophysical characterization of the olfactomedin domain of myocilin, an extracellular matrix protein implicated in inherited forms of glaucoma " PLoS ONE, vol. 6, pp. e16347, 2011.

364. 4, C.C.P.N., Acta Crystallogr., vol. D50, pp. 760, 1994.

365. EMSLEY, P., *et al.*, "Features and development of coot," Acta Crystallogr D Biol Crystallogr, vol. 66, pp. 486-501, 2010.

366. SCHUTTELKOPF, A.W. and VAN AALTEN, D.M., "Prodrg: A tool for high-throughput crystallography of protein-ligand complexes," Acta Crystallogr. , vol. D60, pp. 1355-63, 2004.

367. DELANO, W.L., *The pymol molecular graphics system*. 2002, DeLano Scientific: San Carlos, CA.

368. M. ROHRBACH, J.T.R.C., "Treatement of lysosomal storage disorders: Progress with enzyme replacement therapy," Drugs, vol. 67, pp. 2697-2716, 2007.

369. Z. YU, A.R.S., J.W. KELLY, "Pharmacologic chaperoning as a strategy to treat gaucher disease," FEBS Journal, vol. 274, pp. 4944-4950, 2007.

370. VELLODI, A., "Lysosomal storage disorders," British Journal of Haematology, vol. 128, pp. 413-431, 2004.

371. S. RIJNBOUTT, H.M.F.G.A., H.J. GEUZE, J.M. TAGER, G.J. STROUS, "Mannose 6-phosphate-independent membrane association of cathepsin d, glucocerebrosidase and sphingolipid-activating protein in hepg2 cells," The Journal of Biological Chemistry, vol. 266, pp. 4862-4868, 1991.

372. W. HUNZIKER, H.J.G., "Intracellular trafficking of lysosomal membrane proteins," Bioessays, vol. 18, pp. 379-389, 1996.

373. D. RECZEK, M.S., J SCHRÖDER, H. HUGHES, J. BLANZ, X. JIN, W. BRONDYK, S. VAN PATTEN, T. EDMUNDS, P. SAFTIG, "Limp-ii is a receptor for lysosomal mannose-6-phosphate independent targeting of beta-glucocerebrosidase," Cell, vol. 131, pp. 770-783, 2007.

374. MARTIN, J., *et al.*, "Chaperonin-mediated protein folding at the surface of groel through a molten globule-like intermediate," Nature, vol. 352, pp. 36-42, 1991.

375. FACEY, S.J. and KUHN, A., "The sensor protein kdpd inserts into the escherichia coli membrane independent of the sec translocase and yidc," European Journal of Biochemistry, vol. 270, pp. 1724-1734, 2003.

376. KAPUST, R.B. and WAUGH, D.S., "Escherichia coli maltose-binding protein is uncommonly effective at promoting the solubility of polypeptides to which it is fused," Protein Science, vol. 8, pp. 1668-1674, 1999.

377. LI, P.Z., *et al.*, "Expression of recombinant proteins in pichia pastoris," Applied Biochemistry and Biotechnology, vol. 142, pp. 105-124, 2007.

VITA

Susan D. Orwig

Susan was born in Atlanta, Georgia. She graduated in 2002 from Tuacahn High School for the Arts, Ivins, Utah where she studied theatrical lighting design. She served as Student Body President, Junior class vice president, secretary for the National Honor Society, treasurer for the environmental club, technical coordinator and member for the Dance Company, and won 2nd in the Utah State Drama Competitions for pantomime. Afterwards, she received a B.S. in Chemistry with a minor in Biology from North Georgia College and State University, Dahlonega, Georgia in 2006. During her undergraduate career, Susan was in the presidency of Phi Eta Sigma Honor Society, as well as a member of Mu Epsilon Delta Honor Society, Society of Chemistry Students, Ambassadors, and Kappa Delta sorority. Susan then went Georgia Tech to pursue a doctorate in Chemistry where she was a member of Women in Chemistry, American Chemical Society, and American Crystallographic Association. Susan was also a Drug Design, Development, and Delivery GAANN Fellow twice.